JUSTUS-LIEBIG-UNIVERSITÄT GIESSEN

DISSERTATION

CeO_2-basierte Nanostrukturen als Modellkatalysatoren für die HCl-Oxidation

Pascal Cop

2020

Inauguraldissertation zur Erlangung des Doktorgrades der Naturwissenschaftlichen Fachbereiche im Fachgebiet Physikalische Chemie (Fachbereich 08) an der Justus-Liebig-Universität Gießen

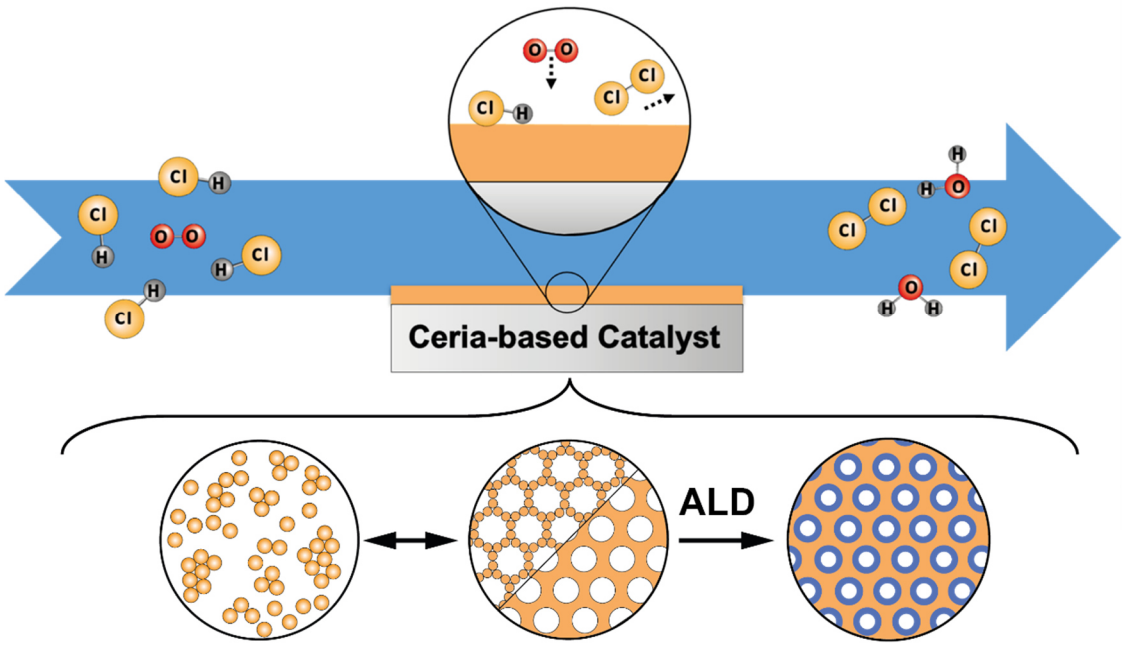

CeO_2-basierte Nanostrukturen als Modellkatalysatoren für die HCl-Oxidation

Vorgelegt von Pascal Cop

Betreuer Prof. Dr. Bernd M. Smarsly

Physikalisch-Chemisches Institut

Justus-Liebig-Universität Gießen

Abgabedatum 29. April 2020

Selbstständigkeitserklärung

Ich erkläre: Ich habe die vorgelegte Dissertation selbstständig und ohne unerlaubte fremde Hilfe und nur mit den Hilfen angefertigt, die ich in der Dissertation angegeben habe. Alle Textstellen, die wörtlich oder sinngemäß aus veröffentlichten Schriften entnommen sind, und alle Angaben, die auf mündlichen Auskünften beruhen, sind als solche kenntlich gemacht. Ich stimme einer evtl. Überprüfung meiner Dissertation durch eine Antiplagiat-Software zu. Bei den von mir durchgeführten und in der Dissertation erwähnten Untersuchungen habe ich die Grundsätze guter wissenschaftlicher Praxis, wie sie in der „Satzung der Justus-Liebig-Universität Gießen zur Sicherung guter wissenschaftlicher Praxis“ niedergelegt sind, eingehalten.

_____ _____

Datum Unterschrift

Dekan: Prof. Dr. Jürgen Janek

Erstgutachter: Prof. Dr. Bernd M. Smarsly

Zweitgutachter: Prof. Dr. Herbert Over

Disputation: 16. Juli 2020

“Above all, do not fear difficult moments. The best comes from them.”

Rita Levi-Montalcini

Danksagung

An dieser Stelle soll zunächst allen Personen gedankt werden, die mich auf meinem wissenschaftlichen Weg begleitet haben. Dies schließt zuallererst die kompletten Arbeitsgruppen von Prof. Bernd Smarsly und Prof. Herbert Over ein. Egal ob sie mittlerweile ihren eigenen industriellen oder akademischen Weg gehen, ob sie mich nur als kleinen Bachelor-Studenten wahrgenommen oder aber bis jetzt zusammen mit mir an der Promotion gearbeitet haben. Ich bin froh und stolz auf all die Erfahrungen, die ich mit Euch machen durfte – sowohl positive als auch negative.

Im Nachfolgenden möchte ich mich noch bei speziellen Personen bedanken, die mich besonders geprägt haben:

- *Prof. Bernd Smarsly* hat mich damals 2014 als Bachelor-Studenten in seiner AG aufgenommen und mir das Element gezeigt, mit dem ich mich nun ca. 6 Jahre beschäftigen durfte: Cer. An dieser Stelle der Dissertation kann ich ja bekanntlich schreiben, was immer ich auch möchte. Normalerweise wird sich hier bedankt, dass man seine Promotion in der Arbeitsgruppe anfertigen durfte, interessante wissenschaftliche Diskussion hatte etc… Aber, wenn Du das hier liest, Bernd, dann weißt Du das doch sowieso alles. Ich möchte mich eher persönlicher an Dich wenden. Dank Dir durfte ich in zahlreiche Länder reisen, dank Dir konnte ich ein Auslandssemester in Japan durchführen, dank Dir hatte ich wissenschaftlich nahezu alle Freiheiten und wenn es nötig war, hast Du mich hier auch hin und wieder gebremst; mir gesagt, dass die Idee zwar toll ist, aber nicht klappen wird. Insbesondere im letzten Jahr der Promotion hast Du mir viel Vertrauen geschenkt, was meine Betreuung von nationalen und internationalen Studenten betrifft und mir in der Tat hilfreiche und unterstützende Tipps für meinen weiteren beruflichen Weg gegeben, die ich definitiv verfolgen werde. Ich werde Dir zwar jetzt noch für ein paar Monate zur Seite stehen, aber ich denke, dass wir auch in Zukunft weiterhin miteinander *Cop-erieren* werden. Die Zeit in Deiner AG hat mich geprägt und ich hoffe, ich auch Deine AG.

- *Prof. Herbert Over* hat mich während meiner Studienzeit in zahlreichen Prüfungen wirklich zum Schwitzen gebracht. Die direkte Art gepaart mit Deinen unverwechselbaren Sprüchen fühlt einem bei jeder Paper-Besprechung auf den Zahn, ermittelt die vorzutragende Quintessenz der Publikation und kommentiert sie komödiantisch. Dieser Satz klingt vermutlich total wirr für viele Personen, aber bestimmte Dinge versteht man besser, wenn man sie erlebt. Ich möchte Dir danken, dass ich viele Deiner Instrumente für meine Forschung bis zuletzt verwenden durfte, auch wenn der eine oder andere Aufbau von Reaktoren leider nicht von Erfolg gekrönt war. Auf meinem zukünftigen Weg werde ich viele von Deinen Ratschlägen mitnehmen und höchstwahrscheinlich auch die eine oder andere Anekdote erzählen. Vielen Dank für zahlreiche Diskussionen, bei denen Du nur „kurz“ Zeit hattest, Du

Dir dann jedoch oft mehr als eine Stunde Zeit für einen genommen hast. Dies und Weiteres verleihen Dir nicht umsonst die verdiente Anerkennung Deiner jetzigen Arbeitsgruppe.

- *Prof. Hiromitsu Kozuka* is one of the persons I need to thank in English. However, even if I have written it in German, I know you would try to decipher it. As I do not want to waste your precious time, I would like to officially thank you in English for taking me as one of your students in 2015 and for 1 month also in 2019. Both of my stays were despite the absence of my wife, one of the best times of my life showing me the beauty of another country with all its facets. My short period as an international student at the Kansai University in Osaka, Japan really changed my life and is now dictating my future academic career. My thanks also go to your students which I have met during my two stays with special thanks to: Takashi Ito, Tsubasa Sakamoto, Shintaro Sumida, Kaede Fukui, Yuki Nishimura, Tsutsui Ryo and Masumi Kubota. I hope, we will meet each other in the future again and eat some gyoza at the Chinese restaurant, which name I always forget. See you soon!

- *Sebastian Werner* ist einer der wenigen Kommilitonen, der mich bis auf mein Auslandssemester doch ständig verfolgt hat. Obwohl wir uns anfangs nur über die fälligen „Physikalische Chemie I“ Übungen unterhalten haben, wurde aus der gemeinsamen Promotionszeit auch eine starke Freundschaft. Wir beide haben viel erlebt: Lissabon, Trieste Jelena, Milena und Katarina, sogar den Turke (siehe einen der nächsten Paragraphen) haben wir überlebt. An dieser Stelle muss ich mich auch nochmal für alle Taxifahrten bzw. Fahrgemeinschaften bedanken. Aber hey, Du weißt ja, hätte ich ein Auto, würde ich Dich auch nach Dautphe fahren. Selbst unter pandemischen Zeiten waren wir nahezu täglich im Kontakt, was mir bei der Anfertigung dieser Arbeit sehr geholfen hat.

- *Felix Matthias/Marius Badaczewski* war eines der versteckten Talente, die man als Fußballtrainer erst entwickeln musste. Als schüchterner Junge im 2. Stock des alten Chemiegebäudes wuchs er zum Spruchgaranten mit hoher Gag-Dichte auf. Neben zahlreichen Mitfahrgelegenheiten, die teilweise als unverschämt und schmarotzerhaft meinerseits gesehen werden können, half er mir sehr bei wissenschaftlichen Fragestellungen und brachte immer Komik und Harmonie in konfliktreiche Situationen.

- *Kevin H. (steht für Hammer) Turke* studierte mit mir seit dem 1. Semester zusammen. Er bestach vor allem durch unpassende jedoch lustige Kommentare während der zahlreichen Kaffeerunden. Obwohl ich Deine Leidenschaft für Mass Effect und Witcher 3 nicht nachvollziehen konnte, möchte ich Dir dennoch für unsere Videospieldiskussionen und Popkultur-/Serienreferenzen danken, in denen Du am Ende

auch einsehen konntest, dass Konsolen besser als PCs sind. Bis heute habe ich allerdings nicht verstanden, was manchmal in Deinem Kopf so vor sich geht und ich glaube, das ist auch ganz gut so. Denn das sorgt bekanntlich für so manche Überraschungen.

- *Christoph Seitz* war mein inoffizieller Betreuer während meiner Bachelor- und Master-Thesis. Deine immer freundliche Art und Weise auch komplett neue Studenten in die Arbeitsgruppe aufzunehmen, überzeugte mich von Beginn an und ließ mich Teil der „AG-Familie“ sein. Bis heute habe ich keine Person getroffen, die einen nur durch seine Erscheinung so Willkommen heißt wie Du. Ich meine, jeder Hund auf der Straße liebt Dich auf Anhieb. Selbst mein Hund rannte einmal eher zu Dir als zu mir ;). Nach Deinem Abschluss bist Du jetzt in der Nähe von Hannover gelandet und lebst mit Frau, Kind, Hund und „Basteljob“ Deinen Traum. Einen ähnlichen Traum werde ich mir auch bald erfüllen und ich hoffe, dass wir dann auch trotz 9000 km Entfernung den Kontakt aufrechterhalten.

- *Rüdiger Ellinghaus*… Während ich Dich anfangs zu fürchten gelernt habe, warst Du mir wissenschaftlich und persönlich ein sehr guter Ratgeber für meine Promotionszeit. Wenn wir bei der „AG-Familie“-Analogie bleiben, warst Du der große Bruder, der mit mehr Erfahrung die kleineren Geschwister berichtigt und auch hier und da gemaßregelt hat. Ich glaube nicht, dass jemand ein besser auf das Promotions- und Laborleben vorbereiten kann als Du. Deine wortreichen Korrekturen bei Protokollen, die meist die Anzahl der Wörter im eigentlichen Text überstiegen, verdienen Anerkennung, auch wenn der Studierende es nicht auf Anhieb zu schätzen weiß. Ich danke Dir hier somit noch einmal als Student, (Büro-)Kollege und als Freund.

- *Dr. Daniel Langsdorf* stand mir insbesondere in den letzten beiden Jahren stets zur Seite, wenn es sowohl um die Diskussion wissenschaftlicher Ergebnisse aber auch die neuesten Trends in der Popkultur-Branche ging. Dein breitgefächertes Wissen und Dein Talent, Leute zu motivieren, um das Beste aus ihnen in zahlreichen Lebenslagen herauszukitzeln, sorgte in den letzten Tagen für die Vollendung dieser Arbeit. Auch wenn ich Dich eventuell enttäuscht habe, indem ich den Thron der Mario-Kart-Turniere nicht erneut besteigen konnte, wird dies in den kommenden Monaten noch forciert. Ich danke Dir für Deine immense Unterstützung in den letzten Tagen und für Dein offenes Ohr für allerlei Themen, die in den Jahren für Diskussionsbedarf sorgten.

- *Dr. Rafael Meinusch* ist wohl einer der stillsten aber effizientesten wissenschaftlichen Kollegen, die ich kenne. Obwohl ich anfangs nur mit ihm über die neuesten Fußballereignisse diskutierte, rückte dies wie die momentanen Leistungen des

BVBs in den Hintergrund. Stattdessen lernte ich Dich während meiner Promotion als fähigen Kollegen kennen, der zusammen mit seiner Frau meine Begeisterung für die japanische Küche teilt. In den letzten Wochen standst Du mir bei der Anfertigung der Dissertation mit präzisem Feedback zu den wissenschaftlichen Ergebnissen zur Seite. Nun darf ich Dich während Deiner Elternzeit ersetzen, obwohl wir beide Wissen, dass es im Prinzip doch gar nicht möglich ist.

- Meine Promotion wäre nur halb so spaßig geworden, wäre ich nicht in den Genuss gekommen, zahlreiche Studenten zu betreuen. Dazu zählen: *David Specht*, *Hendrik Hemmelmann, Ruben Maile*, *Kevin Hess*, *Nina Herrmann*, *Felix Boll* und zuletzt *Lysander Q. Wagner*. Ehrlich gesagt, waren die Zusammenarbeiten mit den Studenten immer meine absoluten Lieblingsmomente. Zum einen durfte ich die Entwicklung der Studenten vom unsicheren Bachelorkandidaten zu nun promovierenden Kollegen beobachten; zum anderen genoss ich die Erfahrungsberichte der Studenten, die unter meiner wissenschaftlichen Betreuung ein Auslandsjahr in Japan bestritten.

Obwohl es eingangs bereits angesprochen wurde, möchte ich die anderen (auch ehemaligen) AG-Mitglieder noch namentlich erwähnen*: Dr. Christian Suchomski, Julia Schulze, Elifkübra Özkan, Melanie Sieland, Fabian Schmitz, Dr. Teresa Gatti, Eric Prates da Costa, Raoul Brand, Torben Pfaff, Dr. Giuliana Beck, Dr. Kristin Kirchberg, Dr. Tobias Weller, Marc Loeh, Dr. Pascal Vöpel, Dr. Marcus Einert, Dr. Julia Migenda* und alle, die ich hier nun vergessen habe.

Zudem geht ein Dank an alle arbeitsgruppen- und institutsübergreifenden Kollegen raus, die zusammen mit mir an den zahlreichen Projekten zusammengearbeitet haben: *Dr. Matthias Elm*, *Erdogan Celik*, *Omeir Khalid*, *Carl-Christian Sack*, *Yu Sun*, *Tim Weber*, *Volkmar Koller*, *Andreas Ringleb*, *Thi Hai Ouyen Nguyen*, *Yannik Moryson*, *Philip Klement*, *Dr. Anja Henss*, *Felix Walther*, *Adrian Schürmann*, *Kathrin Michel* und weitere :). Und natürlich noch *Antonella D'Ambrosio* und *Gabi Scheller* für die tatkräftige Unterstützung in administratorischen Dingen und Reiseangelegenheiten.

Schlussendlich geht mein größter Dank aber an Jasmin Cop (geb. Wolters), welche mich mittlerweile seit über 10 Jahren begleitet und die ich während der Promotion auch heiraten durfte. Ich habe sie gefragt und sie hat „Ja!" gesagt. Ich kann mich echt glücklich schätzen, Dich bereits so früh kennen gelernt zu haben. Trotz stressiger Phasen hast Du mir immer Mut zugesprochen; hast gesagt, dass ich das packe und dass wir das schaffen. Und nun liest Du diese Zeilen und hattest Recht. Nun stehen wir vor einem unserer wichtigsten Schritten, die wir gemeinsam bestreiten werden. Ich bin so unfassbar stolz und glücklich, dass Du mit mir zusammen nach Japan auswanderst, um dort meine Karriere zu unterstützen und Deine zu kreieren. Ich bin mir sicher, dass wir später einmal zu diesem Augenblick zurückschauen und uns zu denken: „Hier hat alles begonnen!"

Zusammenfassung

CeO_2 ist ein vielversprechendes Material für die katalytische Rückgewinnung von Chlor aus der heterogen katalysierten Umsetzung von Chlorwasserstoff und Sauerstoff (Deacon-Prozess). Sowohl die hohe thermische Stabilität als auch die Fähigkeit Sauerstoff leicht ein- und auszubauen, ermöglichten CeO_2 sich in den letzten Jahren als potenzielle Alternative für den momentan eingesetzten und kostenintensiven RuO_2-Katalysator zu etablieren. Obwohl die Sauerstoffspeicherkapazität (engl. *oxygen storage capacity*, kurz: OSC) von CeO_2 oftmals eng mit den katalytischen Eigenschaften in Oxidationsreaktionen verknüpft wird, fehlen grundlegende Untersuchungen um den Einfluss der OSC auf den Deacon-Prozess aufzuklären. Eine Herausforderung ist hierbei, ein geeignetes Modellsystem zu finden, mit welchem sowohl die OSC als auch die katalytische Aktivität und Stabilität unter realen Bedingungen gezielt getestet und evaluiert werden können. Hierfür wurden innerhalb des Promotionsprojektes CeO_2-basierte Mesostrukturen hergestellt, welche einerseits über eine hohe spezifische Oberfläche und andererseits über eine hohe Zugänglichkeit für gasförmige Reaktanden verfügen. Dabei wurden innerhalb der Promotion zwei Teilziele verfolgt:

Als erstes wurden mit einer neuartigen Präparationsmethode auf Basis der Sol-Gel-Synthese und dem eingesetzten Templat Poly(isobuten)-*block*-Poly(ethylenoxid) (PIB-*b*-PEO) mesoporöse CeO_2-Materialien hergestellt, die über eine kubische Porenstruktur mit Mesoporendurchmessern von ca. 12-14 nm verfügen. Die anschließende Dotierung von alio-/isovalenten Metallionen (Gd^{3+}, Zr^{4+}, $Pr^{3+/4+}$, $Tb^{3+/4}$) zeigte, dass keine direkte Korrelation zwischen der OSC und der katalytischen Aktivität im Deacon-Prozess besteht. Anders als die Aktivität, kann die beobachtete mangelnde katalytische Stabilität der auch nur teilweise aliovalent-dotierten CeO_2-Mesostrukturen über die zu hohe Anzahl von Sauerstoffstellen erklärt werden, die die Formation von inaktivem $CeCl_3$ fördern. Im Vergleich dazu erwiesen sich die Zr-dotierten CeO_2-Strukturen aufgrund ihrer hohen katalytischen Stabilität als vielversprechend. Das zuvor entwickelte Synthesekonzept wurde erweitert, um neben molekularen Präkursoren auch vorgefertigte Nanopartikel für den Templatierungsprozess zu verwenden. So konnte in einem zweiten Projekt der Einfluss der Mesostrukturierung auf die OSC und die katalytischen Eigenschaften in der HCl-Oxidation untersucht werden. Anders als die identisch behandelten aber nicht mesostrukturierten Nanopartikel, ermöglicht die kontrollierte Anordnung solcher Nanopartikel – rundum sphärischer Mesoporen – einen besseren Zugang zur aktiven Oberfläche, was durch die erhöhte dynamische Sauerstoffspeicherkapazität und spezifische Produktbildungsrate in der HCl-Oxidation (engl. *space time yield*, kurz: STY) verifiziert wurde.

Das zweite Teilziel beinhaltet die Deposition von definierten CeO_2-Schichten in mesoporösen ZrO_2-Substraten mithilfe der Atomlagenabscheidung (engl. *atomic layer deposition*, kurz: ALD), um in zukünftigen Projekten die Abhängigkeit der OSC von der CeO_2-Schichtdicke unter realen Bedingungen zu studieren. Hierzu wurden die instrumentellen Parameter der ALD sowie die möglichen Charakterisierungsoptionen auf Basis der bereits in der Literatur umfassend untersuchten Abscheidung von TiO_2 getestet und auf poröse CeO_2-ZrO_2-Substrate übertragen. Des Weiteren wurde die Präparation von mesoporösen ZrO_2-

Dünnschichten anhand mechanischer Verspannungsstudien optimiert, welche als Substrate für die CeO_2-Abscheidung mittels ALD dienten. Obwohl die mesoporösen Dünnschichten ideale Modellsysteme sind, um den Wachstumsprozess mittels ALD zu verfolgen, verfügen sie nicht über eine ausreichend hohe absolute Oberfläche um die OSC im Flussreaktor zu vermessen. Da die OSC ähnlich wie die ionische und elektronische Leitfähigkeit von der Anzahl der Sauerstoffleerstellen und deren Mobilität bei gegebener Temperatur abhängt, wurde die Gesamtleitfähigkeit der CeO_2/ZrO_2-ALD-Schichten mithilfe der Impedanzspektroskopie untersucht. Hiermit konnte demonstriert werden, dass ein Leitfähigkeitsmaximum bei einer Schichtdicke von 3,4 nm vorliegt, welches sehr gut mit theoretischen Berechnungen zum energetischen Minimum der Sauerstoffvakanzbildungsenthalpien in der Literatur übereinstimmt.

Das vorgelegte Promotionsprojekt demonstriert, dass sich mesoporöse CeO_2-Katalysatoren dank ihrer hohen spezifischen Oberfläche und guten Zugänglichkeit für gasförmige Reaktanden ideal als Modellsysteme sowohl für die katalytischen Untersuchungen in der HCl-Oxidation als auch für *conformality*[1]-Studien zur Abscheidung von Metalloxiden mittels ALD eignen. In einem nächsten Schritt sollen die beiden Teilziele verknüpft werden, indem die CeO_2-Abscheidung mittels ALD auf mesoporöse Pulvermaterialien übertragen wird und die entstehenden Modellkatalysatoren für OSC- und katalytische Untersuchungen unter realen Bedingungen verwendet werden. Zukünftige Studien sollten bevorzugt mesoporöse CeO_2-Materialien als Modellkatalysatoren einsetzen, um den Einfluss der OSC nicht nur auf die HCl-Oxidation, sondern auch auf andere Oxidationsreaktionen aufzuklären. Dabei ist die hier beschriebene Herstellung innovativer MO_x-CeO_2 Kern-Schale-Modellsysteme durch die ALD zukunftsweisend, um nicht nur das Verständnis der OSC und der katalytischen Eigenschaften zu vertiefen, sondern auch um neuartige Metalloxidkatalysatoren mit hoher gemeinsamer Grenzfläche zu entwickeln.

[1] Es existiert für diesen Begriff keine direkte Übersetzung in die deutsche Sprache. Es ist hiermit die gleichmäßige Abscheidung eines Materials auf gekrümmten Oberflächen gemeint. Obwohl umgangssprachlich häufig das Wort „konform“ in diesem Zusammenhang genutzt wird, ist das zugehörige Substantiv „Konformität“ von seiner eigentlichen Bedeutung in der Bildungssprache oder Technik nichtzutreffend.

Publikationsliste

Folgende Publikationsbeiträge sind während des Promotionsprojektes von 2016-2020 entstanden:

1. **P. Cop**, S. Kitano, K. Niinuma, B. M. Smarsly, H. Kozuka, In-plane stress development in mesoporous thin films, *Nanoscale* **2018**, *10*, 7002–7015.

2. **P. Cop**, M. Göttlicher, J. Schörmann, C. Boissiere, A. Beyer, C. Becker, K. Volz, H. Over, B. M. Smarsly, Atomic Layer Deposition of Titania in Ordered Mesoporous Cerium Zirconium Oxide Thin Films: A Case Study, *J. Phys. Chem. C* **2019**, *123*, 12851–12861.

3. **P. Cop**, K. Hess, S. Werner, R. Meinusch, B. M. Smarsly, H. Kozuka, Comparison of In-Plane Stress Development in Sol-Gel- and Nanoparticle-Derived Mesoporous Metal Oxide Thin Films, *Langmuir,* **2019**, *35* (50)*, 16427-16437.*

4. **P. Cop**, E. Celik, K. Hess, Y. Moryson, P. Klement, M. T. Elm, B. M. Smarsly, Atomic Layer Deposition of Defined Thin CeO_2 Layers in Ordered ZrO_2 Films and Their Impact on the Ionic/Electronic Conductivity, *ACS Applied Nano Materials,* **2020**, *submitted.*

5. **P. Cop**, R. Maile, Y. Sun, I. Djerdj, O. Khalid, H. Over, B. M. Smarsly, The Impact of Alio-/Isovalent Ions (Gd, Zr, Pr and Tb) on the Catalytic Stability of Mesoporous CeO_2 in the HCl Oxidation Reaction, *ACS Applied Nano Materials,* **2020**, *accepted.* https://pubs.acs.org/doi/abs/10.1021/acsanm.0c00994

6. **P. Cop**, R. Maile, Y. Sun, F. Badaczewski, E. Özkan, C. Sack, H. Over, B. M. Smarsly, Connectivity Matters: Comparison of Nanoparticle vs. Nanoparticle-Derived Mesoporous Ceria-Zirconia Structures in the HCl Oxidation Reaction, *Chemistry of Materials,* **2020**, *to be submitted.*

7. M. Möller, S. Urban, **P. Cop**, T. Weller, R. Ellinghaus, M. Kleine-Boymann, C. Fiedler, J. Sann, J. Janek, L. Chen, et al., *ChemCatChem* **2015**, *7*, 3738–3747.
8. C. Li, Y. Sun, F. Hess, I. Djerdj, J. Sann, P. Voepel, **P. Cop**, Y. Guo, B. M. Smarsly, H. Over, *Appl. Catal. B Environ.* **2018**, *239*, 628–635.
9. Y. Sun, C. Li, I. Djerdj, O. Khalid, **P. Cop**, J. Sann, T. Weber, S. Werner, K. Turke, Y. Guo, et al., *Catal. Sci. Technol.* **2019**, *9*, 2163–2172.
10. Y. Sun, **P. Cop**, I. Djerdj, X. Guo, T. Weber, O. Khalid, Y. Guo, B. M. Smarsly, H. Over, *ACS Catal.* **2019**, *9*, 10680–10693.
11. J. Bijelić, A. Stanković, B. Matasović, B. Marković, M. Bijelić, Ž. Skoko, J. Popović,

G. Štefanić, Z. Jagličić, S. Zellmer, **P. Cop**, B. M. Smarsly, I. Djerdj, *CrystEngComm* **2019**, *21*, 218–227.

12. R. A. Henning, P. Uredat, C. Simon, A. Bloesser, **P. Cop**, M. T. Elm, R. Marschall, *J. Phys. Chem. C* **2019**, *123*, 18240–18247.
13. M. F. Zscherp, J. Glaser, C. Becker, A. Beyer, **P. Cop**, J. Schörmann, K. Volz, M. T. Elm, *Cryst. Growth Des.* **2020**, *20* (4), 2194–2201.
14. E. Özkan, **P. Cop**, F. Benfer, A. Hofmann, M. Votsmeier, J. M. Guerra, M. Giar, C. Heiliger, H. Over, B. M. Smarsly, *J. Phys. Chem. C* **2020**, *124* (16), 8736–8748.
15. J. Bijelić, A. Stanković, M. Medvidović-Kosanović, B. Marković, **P. Cop**, Y. Sun, S. Hajra, M. Sahu, J. Vukmirović, D. Marković, Á. Kukovecz, Z. Jagličić, B. M. Smarsly and I. Djerdj, *J. Phys. Chem. C* **2020**, *124* (23), 12794–12807.
16. C. Li, C. Seitz, I. Djerdj, **P. Cop**, J. Yue, P. Vöpel, F. Bertolotti, A. Guagliardie, Y. Guo, H. Over, B. M. Smarsly, *Crystal Growth* & *Design*, *to be submitted*.
17. E. Özkan, F. Badaczewski, **P. Cop**, S. Werner, A. Hofmann, M. Votsmeier, H. Amenitsch, B. M. Smarsly, *Langmuir*, **2020**, *Accepted*.

Die erzielten Erkenntnisse wurden auf folgende externen Veranstaltungen präsentiert:

P. Cop, Y. Sun, H. Over, B. M. Smarsly, CeO_2-based Nanostructures as Promising Model Catalysts for the HCl Oxidation, 12th International Symposium on the "Scientific Bases for the Preparation of Heterogeneous Catalysts", Louvain-La-Neuve, Belgium. **2018**

Vortragspräsentation

P. Cop, R. Maile, Y. Sun, H. Over, B. M. Smarsly, Influence of the Oxygen Storage Capacity of Mesoporous Doped CeO_2 on the Catalytic Activity in the HCl Oxidation, 3rd Fundamentals and Applications of Cerium Dioxide in Catalysis, Barcelona, Spain. **2018**

Posterpräsentation

P. Cop, M. Göttlicher, J. Schörmann, C. Boissiere, C. Becker, H. Over, B. M. Smarsly, Atomic Layer Deposition of Titania in Mesoporous Cerium Zirconium Oxide Thin Films: A Case Study, 6th Nano Today Conference, Lisbon, Portugal. **2019**

Posterpräsentation

P. Cop, K. Hess, S. Werner, B. M. Smarsly, H. Kozuka, Comparison of In-Plane Stress Development in Sol-Gel- and Nanoparticle-Derived Mesoporous Metal Oxide Thin Films, 20th International Sol-Gel Conference, St. Petersburg, Russia. **2019**

Posterpräsentation

P. Cop, R. Maile, Y. Sun, H. Over, B. M. Smarsly, Nanoparticle vs. Nanoparticle-derived Mesoporous Ceria-Zirconia Structures as Model Catalysts in the HCl Oxidation, 29th ATC: Industrial Inorganic Chemistry - Materials and Processes, Frankfurt, Germany. **2020**

Posterpräsentation

Inhaltsverzeichnis

1. Einleitung

Die Chlorchemie ist untrennbar mit modernen Syntheseverfahren in der heutigen chemischen Industrie verknüpft. Mit einer Produktion von mehr als 60 Millionen Tonnen pro Jahr ist Chlor eine wichtige Basischemikalie für zahlreiche organische und anorganische Produkte.[1] Obwohl Chlor in Form von chlorhaltigen Verbindungen oder über chlorierte Zwischenstufen direkt am Herstellungsprozess beteiligt ist, sind eine Vielzahl von Endprodukten wie Polyurethane oder Teflon® in der Kunststoffindustrie (siehe Abbildung 1) schlussendlich chlorfrei.[2] Bei diesen Synthesen kommt es zur Bildung von Chlorwasserstoff (HCl) als unerwünschtes toxisches Nebenprodukt, welches nur begrenzt weiterverwendet werden kann. Die chemische Industrie ist daher bestrebt elementares Chlor aus HCl zurückzugewinnen, um Prozesskreisläufe zu schließen und damit die Nachhaltigkeit solch großtechnischer Prozesse zu erhöhen.

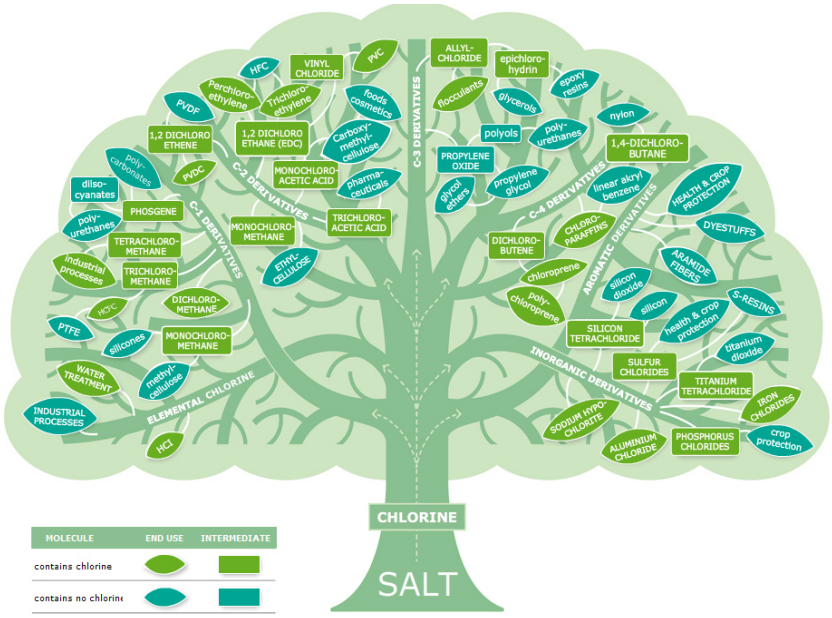

Abbildung 1: Schematische Darstellung der Chloranwendungen innerhalb der chemischen Industrie.[2]

Bereits vor 150 Jahren hat sich der englische Chemiker Henry Deacon erstmalig mit der katalytischen Umsetzung von HCl zu Chlor beschäftigt.[3] Der sogenannte Deacon-Prozess war der erste Versuch, Chlor aus seinem unerwünschten Nebenprodukt wiederzugewinnen. Obwohl das Verfahren einen bedeutenden Schritt zur Nachhaltigkeit darstellte, blieb ein großtechnischer Einsatz aufgrund des verwendeten instabilen CuO-$CuCl_2$-Katalysators aus. Erst 1999 entwickelte *Sumitomo Chemical*[4] einen stabilen Katalysator auf der Basis von RuO_2/TiO_2 (Rutil) für die HCl-Oxidation, der 85 % des HCl-Gases zu Chlor umsetzte.[5] Dabei erfüllt das Katalysatormaterial zwei essentielle Eigenschaften: *Stabilität* und hohe *Aktivität.*

Die begrenzte Verfügbarkeit und der hohe Rohstoffpreis von Ruthenium erschweren jedoch einen großtechnischen Einsatz. Aus diesem Grund begann die Suche nach kostengünstigeren, alternativen Katalysatormaterialien, die eine ähnliche katalytische Stabilität

und Aktivität wie RuO_2 aufweisen. Eines dieser Materialien ist CeO_2, dessen Aktivität im Vergleich zu RuO_2 zwar deutlich geringer ausfällt, allerdings auch bei höheren Reaktionstemperaturen eine hohe Cl_2-Ausbeute zulässt und dabei chemisch stabil ist.[6]

Der einfache Wechsel zwischen den beiden Oxidationsstufen Ce^{3+} und Ce^{4+} ermöglicht den Ein- und Ausbau von Sauerstoff bereits bei niedrigen Temperaturen um 300 °C.[7] Es lassen sich vor allem solche Redoxreaktionen mit Cerdioxid als Katalysator durchführen, die bedingt durch den Reaktionsmechanismus von der hohen Sauerstoffspeicherkapazität (engl. *oxygen storage capacity*, kurz: OSC) des CeO_2 profitieren.[8] Die OSC hängt von dem Ce^{3+}/Ce^{4+}-Verhältnis und der damit verbundenen Bildung von Sauerstoffleerstellen ab, welche aktiv an der Reaktion beteiligt sind. Sowohl die Partikelgröße[9] von CeO_2 als auch die Dotierung mit zum Beispiel Seltenerdoxiden verändern das Ce^{3+}/Ce^{4+}-Verhältnis und folglich die Sauerstoffspeicherkapazität. Granozzi *et al.* zeigten, dass ultradünne Cerdioxid-Schichten von wenigen Atomlagen auf oxidischen Trägermaterialien die Bildung von Ce^{3+}-Kationen an einer TiO_2-Oberfläche signifikant verstärken.[10] Des Weiteren konnte eine Studie von Sun *et al.*[11] verdeutlichen, dass dünne CeO_2-Schichten mit erhöhtem Ce^{3+}-Gehalt die katalytische Aktivität und die Stabilität in der HCl-Oxidation gegenüber entsprechenden CeO_2-Partikeln verbessern konnten.

Um all die genannten Einflüsse unter realen Bedingungen systematisch zu untersuchen, ist ein CeO_2-basiertes Modellsystem notwendig, was einerseits eine hohe spezifische Oberfläche besitzt und andererseits eine hohe Zugänglichkeit für gasförmige Reaktanden bietet. Im Gegensatz zu zufällig agglomertieren Nanopartikeln mit ähnlich großen Oberflächen ist die katalytisch-aktive Oberfläche in einem Material mit definierten Mesoporen besser für die Reaktanden zugänglich. Mögliche morphologische Veränderungen in Folge der HCl-Oxidation können zudem leicht anhand der Umorganisation bzw. Beschädigung der geordneten Mesoporen-Strukturen mit mikroskopischen Methoden (Rasterkraft- (AFM), Rasterelektronen- (REM) und Transmissionselektronenmikroskopie (TEM)) verfolgt werden. Solche morphologischen Veränderungen ermöglichen einen direkten Bezug zur katalytischen Stabilität der Cerdioxid-Nanokomposite. Dabei stellt in erster Linie die Synthese dieser Mesostrukturen als Dünnschichten und Pulver mit untereinander verknüpften Poren eine Herausforderung dar, die eine präzise Kontrolle des Templatierungsprozesses voraussetzt.

Die Promotion befasst sich demnach mit der Entwicklung von CeO_2-Mesostrukturen, um den Einfluss von der Sauerstoffspeicherfähigkeit auf die katalytische Aktivität und Stabilität in der HCl-Oxidation zu untersuchen und zu verbessern. Während in der Literatur der Mechanismus und die Eignung von CeO_2 als Katalysator für die HCl-Oxidation im Detail beschrieben ist, fehlen grundlegende Untersuchungen und Erkenntnisse, um den Zusammenhang zwischen dem Ce^{3+}/Ce^{4}-Verhältnis und der Sauerstoffspeicherfähigkeit zu verstehen. Daher werden im Rahmen des Promotionsprojektes einerseits die Einflüsse der

Seltenerdmetall-Dotierungen sowie der Mesostrukturierung - durch Einsatz von molekularen Präkusoren bzw. Nanopartikeldispersionen – von porösen CeO_2-Strukturen auf die Sauerstoffspeicherkapazität untersucht (siehe Abbildung 2, linker Pfad). Andererseits werden neuartige MOx/CeO_2 Kern/Schale-Modellsysteme mittels der Atomlagenabscheidung (ALD) entwickelt. Hierbei werden die Studien von Granozzi *et al.* und Sun *et al*. systematisch erweitert, indem definiert dünne CeO_2-Schichten in mesoporöse Trägersubstrate aufgewachsen werden (siehe Abbildung 2, rechter Pfad).

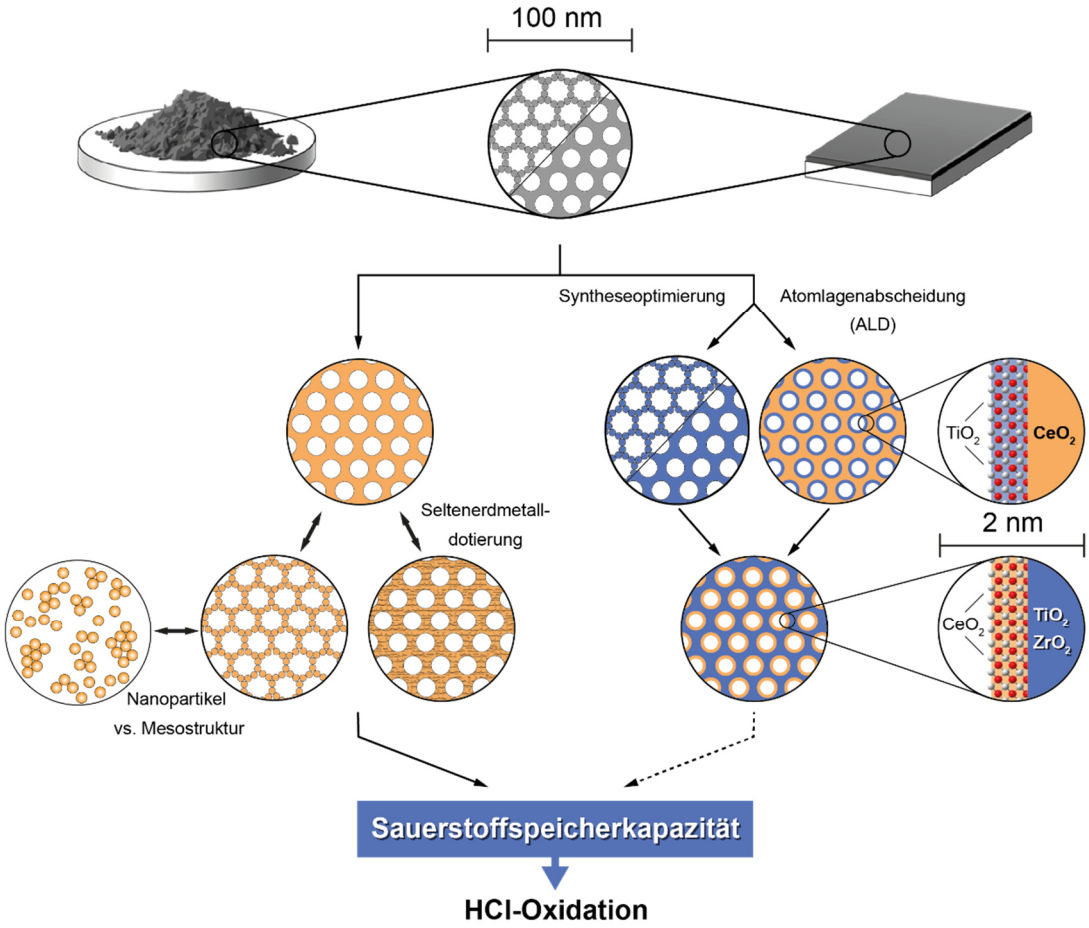

Abbildung 2: Schematische Darstellung des Ablaufs des Promotionsprojektee, welches sich auf die Herstellung und Verwendung mesoporöser Dünnschichten und Pulver mit jeweils geordneten mesoporösen Strukturen als Modellsysteme für die HCl-Oxidation fokussiert. Diese werden zum einen aus Cerdioxid hergestellt, um den Einfluss der Porenstruktur sowie Seltenerdoxid-Dotierungen auf die Sauerstoffspeicherkapazität zu untersuchen. Zum anderen werden durch die Methode der Atomlagenabscheidung (ALD) die Poren mit definierten Schichten von Cerdioxid funktionalisiert, um den Zusammenhang zwischen Schichtdicke und Sauerstoffspeicherkapazität aufzuklären. Hierzu wird in einem ersten Schritt die Synthese von mesoporösen TiO_2- und ZrO_2-Schichten optimiert und die Abscheidung via ALD in porösen Schichten mit einem Beispielsystem getestet.

Alle Teilziele arbeiten daraufhin, mesoporöse CeO_2-Materialien als Dünnfilme sowie Pulver zu synthetisieren und als Modellsysteme zu etablieren, um die mit der OSC zusammenhängenden katalytischen Eigenschaften in der HCl-Oxidation auf mikroskopischer Ebene aufzuklären. In den nachfolgenden Kapiteln werden zum einen die Eignung von CeO_2 als Deacon-Katalysator und die Einflussfaktoren auf die Sauerstoffspeicherkapazität

beschrieben (Kapitel 2.1). Zum anderen wird der momentane Stand der ALD-Beschichtung auf poröse Substrate berichtet (Kapitel 2.2), welcher als Ausgangspunkt für den in der Promotion erarbeiteten Entwicklungsprozess dient (Kapitel 3).

2. Nanostrukturierte CeO_2-Modellkatalysatoren in der HCl-Oxidation

2.1. CeO_2 im Deacon Prozess

Da es sich bei der HCl-Oxidation um einen schwach exothermen Prozess handelt, ist die Reaktionstemperatur ein entscheidender Faktor für die Wahl des Katalysators. Gemäß dem Prinzip des kleinsten Zwanges können nur geringe Ausbeuten bei höherer Betriebstemperatur erreicht werden. Aus diesem Grund muss die Reaktion bei möglichst niedrigen Temperaturen ablaufen.[12–14]

$$4\ \mathrm{HCl} + \mathrm{O_2} \rightarrow 2\ \mathrm{Cl_2} + 2\ \mathrm{H_2O} \qquad \Delta_r H^\circ = -118\,\frac{\mathrm{kJ}}{\mathrm{mol}}$$

Bei CuO, dem originären Deacon Katalysator, bilden sich beispielsweise unter dem Einfluss von HCl/Cl_2 die zugehörigen Kupferchloride, welche bei den notwendigen Reaktionstemperaturen von 430 °C flüchtig sind. Dies führt zum Verlust der aktiven Phase und zu einer unzureichenden Katalysatorstabilität.[15–17] Die Stabilität hinsichtlich der Chlorierung ist folglich ein wichtiger Parameter bei der Auswahl eines geeigneten Katalysators.[18]

Ein Oxid, welches diese Bedingung erfüllt, ist Rutheniumoxid.[1,12,19–22] Aufgrund seiner hohen Aktivität, kann die katalysierte Reaktion bereits bei niedrigeren Temperaturen (350 °C) durchgeführt werden, woraus auch eine erhöhte katalytischen Stabilität resultiert. Die begrenzte Verfügbarkeit von Ruthenium ließ Material- und Katalyseforscher nach entsprechenden Alternativen suchen. Schomäcker *et al.* postulierten mithilfe der Sauerstoffdissoziationsenergie geeignete Oxidmaterialien, um für den Deacon-Prozess einen idealen Katalysator zu finden.[12]

Die Untersuchungen zeigen, dass RuO_2 bereits die höchste katalytische Aktivität im Deacon-Prozess unter Oxiden der Zusammensetzung MO_x besitzt. Die Aktivität von anderen geeigneten Metalloxiden kann jedoch durch Dotierungen oder die Bildung von Mischoxiden gesteigert werden.[23–25] Neben seinem großen Vorkommen gilt CeO_2 aufgrund seiner ausgeprägten Redoxchemie als vielsprechende Katalysatoralternative für die HCl-Oxidation.[26] Es besitzt zwar eine geringeren katalytischen Aktivität im Deacon-Prozess, die eine höhere Reaktionstemperatur (430 °C) im Vergleich zum RuO_2 (350 °C) erfordert[13] und dadurch mit einer herabgesetzten HCl-zu-Cl_2-Konversion verbunden ist, jedoch besitzt CeO_2 eine höhere thermische Stabilität als RuO_2.[27] Zudem konnten Kanzler *et al.*[28] demonstrieren, dass polykristalline RuO_2-Nanofasern anders als einkristalline (100)- und (110)-RuO_2-Katalysatoren unter den harschen Bedingungen des Deacon-Prozesses nicht stabil sind.

Bei CeO_2-Katalysatoren ist das als Nebenprodukt entstehende $CeCl_3$ bei höheren Temperaturen nicht flüchtig im Vergleich zum $CuCl_2$ in CuO-basierten Katalysatoren. Dennoch ist $CeCl_3$ im Deacon-Prozess inaktiv, so dass die vermehrte Bildung während des Katalysevorganges vermieden werden soll. Amrute *et al.*[26] postulierten 2012 einen Reaktionsmechanismus für die HCl-Oxidation über CeO_2-Materialien. Er beinhaltet: (i) die Adsorption von

HCl-Wasserstoff an einem Oberflächensauerstoffatom unter Bildung einer Hydroxlgruppe sowie einer adsorbierten Chlorspezies, (ii) Aufnahme eines weiteren Wasserstoffatoms von HCl-Molekülen aus der Gasphase unter Bildung von H_2O, (iii) Desorption des gebildeten Wassers, (iv) Auffüllen der Sauerstoffleerstellen mit dissoziativ adsorbiertem Sauerstoff und (v) die Rekombination von einem Chloratom in einer Sauerstoffvakanz mit einem Chloratom auf der Oberfläche zu molekularem Chlor. Beim Reaktionsmechanismus auf RuO_2 besitzt die Abspaltung von molekularem Chlor die höchste Energiebarriere.[29] Im Falle des CeO_2-Katalysators liegt der ratenbestimmende Schritt bei der Chloraktivierung von einer Gitterleerstelle zu einem Oberflächenplatz[26], welcher im Folgenden näher erläutert wird. In einem ersten Schritt wird HCl (HCl_{ext}) unter Besetzung einer Sauerstoffleerstelle ($V_O^{\bullet\bullet}$) und der Protonierung eines benachbarten Sauerstoffions (O_O) an der CeO_2-Oberfläche adsorbiert (siehe Gleichung (1)).

$$\mathrm{HCl_{ext}} + \mathrm{O_O} + \mathrm{V_O^{\bullet\bullet}} \rightarrow \mathrm{OH^{\bullet}} + \mathrm{Cl_O^{\bullet}} \qquad (1)$$

Gleichung (1) zeigt, dass Sauerstoffleerstellen im nicht-stöchiometrischen CeO_2 essentiell für die katalytische Performance sind. Da dies zu anderen Oxidationsreaktionen[30–32] analog verläuft, ist es von höchster Priorität, die Bildung von Sauerstoffleerstellen zu verstehen und diese experimentell steuern zu können, um die katalytische Aktivität und Stabilität von CeO_2 in der HCl-Oxidation gezielt zu beeinflussen.

2.1.1 Sauerstoffspeicherkapazität (OSC)

Die Anwendungsmöglichkeiten von CeO_2 im Bereich der Katalyse sind sehr vielfältig. Der Einsatz von Cerdioxid als Träger, Additiv oder aktive Phase in einer katalytischen Reaktion ist durch den einfachen Aus- und Einbau von Sauerstoff begründet. Mittlerweile liegen Forschungsergebnisse für die SO_2-Oxidation, Wassergas-Shift-Reaktion, CO-Oxidation sowie für die hier beschriebene HCl-Oxidation vor.[30,31,33,34] In allen katalysierten Oxidationsreaktionen scheint die beobachtete Aktivität eng mit der Sauerstoffspeicherfähigkeit zu korrelieren.[31,35,36]

In Oxidationsreaktion mit CeO_2 als Katalysator wird das zu oxidierende Molekül mithilfe von Sauerstoffionen aus dem Gitter oxidiert. Es bildet sich eine Sauerstoffleerstelle an der Oberfläche. Diese wird anschließend durch Sauerstoff als Reaktand gefüllt, so dass die ursprüngliche Ce^{3+}-Umgebung zu Ce^{4+} reoxidiert wird (siehe Gleichung (2)).[23] Sauerstoff kann folglich im Material reversibel ein- und wiederausgebaut werden. Diese physikochemische Eigenschaft ist als Sauerstoffspeicherkapazität (engl. *oxygen storage capacity*, kurz: OSC) definiert.[7,30,37,38]

$$2\ \mathrm{CeO_2} \leftrightharpoons 2\ \mathrm{Ce'_{Ce}} + \mathrm{V_O^{\bullet\bullet}} + 3\ \mathrm{O_O} + 0.5\ \mathrm{O_2} \qquad (2)$$

In CeO_2 sind die Sauerstoffvakanzen $V_O^{\bullet\bullet}$ die Hauptpunktdefekte, so dass das Metalloxid meist als $CeO_{2-\delta}$ angeben wird mit δ als Maß für das Sauerstoffdefizit.[39] Während unter oxidierenden Bedingungen nur eine Sauerstoffionenleitfähigkeit über die Bildung von intrinsischen Anti-Frenkel Defektpaaren vorliegt[40], können unter reduzierenden Bedingungen (Erniedrigung des Sauerstoffpartialdruckes, Reduktionsmittel, etc…) Ce^{4+}-Ionen zu Ce^{3+}-Ionen reduziert werden, so dass eine gemischte ionische und elektronische n-typische Leitfähigkeit vorherrscht. Entscheidend ist hierbei, dass der Sauerstofftransport von der Anzahl der Leerstellen und Ce^{3+}/Ce^{4+}-Ionen in der Umgebung abhängt.

Die OSC wird durch qualitative oder quantitative Verfahren bestimmt, wobei letztere den Wert meist mit der Einheit µmol g^{-1} angeben. Eine große Problematik in der Bestimmung der OSC sind die zahlreichen Methoden sowie die unterschiedlich gewählten Reaktionstemperaturen, die einen Vergleich der Werte mit anderen Arbeitsgruppen erschweren.[7] Für eine qualitative Untersuchung werden in vielen Literaturstellen die Defektbanden von CeO_2 im Ramanspektrum auf die Hauptbande (F_{2g}) normiert und als Maß für die OSC formuliert.[41–45] Da allerdings nicht nur die Defekte, sondern auch die Mobilität der Sauerstoffionen eine wichtige Rolle in der OSC einnehmen, ist die mit der Ramanspektroskopie bestimmte Prognose allein nicht verlässlich.

Für die quantitative Bestimmung wird unter anderem die thermogravimetrische Analyse verwendet, bei der die Gewichtsänderung des zu untersuchenden CeO_2-Materials unter Sauerstoff- und CO/H_2-reicher Atmosphäre gemessen wird.[46–48] Eine weitere Option für die OSC bildet die *Temperature Programmed Reduction* (TPR) Methode.[37,49–51] Hier wird die Probe unter Wasserstoff- oder Kohlenstoffmonoxidatmosphäre (H_2-TPR bzw. CO-TPR) auf bis zu 1000 °C geheizt, wobei der austretende Sauerstoff aus CeO_2 über die thermische Leitfähigkeit oder über sein Signal im Massenspektrum detektiert wird. Die quantitative Analyse erfolgt über die Integration des Sauerstoffsignales bis hin zur gewünschten Temperatur, wobei bei CeO_2 meist zwei große Peaks zu beobachten sind.[52] Ersterer besitzt sein Maximum bei ca. 400 °C und wird dem Sauerstoff in Oberflächennähe zugeschrieben. Erst bei Temperaturen von über 700 °C kann auch der Sauerstoff aus dem *bulk*-Material entzogen werden, welcher durch die temperaturabhängige Diffusion an die Oberfläche der CeO_2-Probe transportiert werden kann.[53,54] In vielen Fällen wurde mit dieser Methodik der Einfluss von Nanostrukturierung und Fremdatomdotierung auf die Verschiebung der beiden Signalmaxima und der Sauerstoffspeicherkapazität untersucht.[32,53,55] Jedoch berücksichtigt das Verfahren nicht, dass bei der Reduktion von CeO_2 ein thermodynamisches Gleichgewicht vorliegen muss, um die komplette Sauerstoffspeicherkapazität bei einer bestimmten Temperatur zu ermitteln.

Eine Methode, die dies berücksichtigt, ist die *pulse injection method*[52,56], bei der die CeO_2-Probe mit hoher spezifischer Oberfläche bei definierter Temperatur über kurze Gaspulse von wenigen Sekunden mit CO oder H_2 reduziert und anschließend mit O_2-Pulsen

oxidiert wird. Die Gase können analog zum TPR-Verfahren über einen Wärmeleitfähigkeitsdetektor (engl. *Thermal Conductivity Detector*, kurz: TCD) ermittelt werden. Der gespeicherte Sauerstoff wird hierbei über O_2-Referenzpulse und die Integration der TCD-Signale bestimmt. Durch aufeinanderfolgende Reduktionspulse wird die Probe bis zum Maximum bei der gewählten Temperatur reduziert, so dass mittels sukzessiven Sauerstoffpulsen die komplette Sauerstoffspeicherkapazität bei der vorgegebenen Temperatur (*total* oder *complete* OSC, kurz: OSCc) berechnet wird. Bei der hier im Projekt verwendeten Temperatur von 430 °C, welche analog zur Reaktionstemperatur in der HCl-Oxidation gehalten ist, werden neben dem Oberflächensauerstoff auch die mobilen Sauerstoffspezies im Bulk berücksichtigt.[7,30,57] Um lediglich den reaktivsten Sauerstoff zu ermitteln, kann mit selbiger Methode, aber alternierenden CO/H_2- und O_2-Pulsen, die sogenannte dynamische OSC[38,47,58] bestimmt werden. Sie zeichnet sich dadurch aus, dass der am einfachsten verfügbare Sauerstoff aus dem Gitter ausgebaut wird.[59,60]

Sowohl die totale als auch die dynamische OSC können über zahlreiche Präparationsmethoden gesteuert werden. Die entscheidenden Faktoren sind die Sauerstoffleerstellenbildungsenthalpie und die Mobilität des Gittersauerstoffes.[7,31,32,61] Die Sauerstoffbildungsenthalpie hat einen Einfluss auf die Anzahl der intrinsischen Defekte bei gegebener Temperatur, während die Mobilität des Gittersauerstoff bzw. der Sauerstoffleerstellen durch die vorherrschende Anzahl der Leerstellen[39] und der Migrationsenthalpie[58,62] bedingt ist. Letztere beiden Parameter können einerseits durch Nanostrukturierung (Kapitel 2.1.2) gesteuert werden, um die Anzahl von strukturell bedingten Defekten zu erhöhen, und andererseits durch das Einbringen von aliovalenten Fremdatomen (Kapitel 2.1.3) manipuliert werden, die die Bildung extrinsischer Defekte begünstigt. In beiden Fällen wird analog zu den gebildeten Fehlstellen gemäß Gleichung (2) auch die Anzahl von Ce^{3+}-Ionen erhöht. Folglich ist das Verhältnis von Ce^{3+} zu Ce^{4+}- ein qualitatives Merkmal für die vorhandenen Defekte in CeO_2.

2.1.2 Nano- und Mesostrukturierung

Eine Nanostrukturierung von Katalysatoren erweist sich meist als vorteilhaft, da durch die Herstellung kleiner Nanopartikel oder –teilchen immer eine höhere spezifische Oberfläche und eine größere Anzahl von aktiven Plätzen resultiert. Dabei kann die Nanostrukturierung von Metalloxiden über verschiedene Wege erfolgen. So können neben sphärischen Partikeln[63,64] unterschiedlicher Größe auch Nanostrukturen synthetisiert werden, die an der Oberfläche nur über eine definierte Oberflächenterminierung verfügen. Im Bereich des CeO_2 wurden beispielsweise Nanowürfel (100), Nanostäbe (110) oder Nanooktaeder (111) mittels Hydrothermalverfahren hergestellt.[65–67] Dabei weisen die Netzebenen unterschiedliche Oberflächenenergien und Bildungsenthalpien für die Sauerstoffleerstellen auf. Für Ersteres ist die Reihenfolge (100) < (110) < (111), woraus entnommen wer-

den kann, dass die (111)-Oberfläche die thermodynamisch stabilste bzw. die (100)-Oberfläche die reaktivste Netzebene darstellt.[68–70] Mittels Computersimulationen wurde diese Rangfolge für die katalytische Reaktivität in Oxidationsreaktionen vorausgesagt.[68,71] Experimentell wurde dies zunächst von Zhou *et al.* mithilfe der CO-Oxidation und dem Vergleich zu undefinierten Nanopartikeln ähnlicher BET-Oberfläche bestätigt.[72] Weitere Studien folgten und ermittelten, dass Nanostäbe die höchste Aktivität normiert auf die BET-Oberfläche in der CO-Oxidation besitzen. Es konnte sich folglich die Reihenfolge (110) > (100) > (111) etablieren[73], welches die exakt umgekehrte Sequenz der Bildungsenthalpien für die Sauerstoffleerstellen ((110) < (100) < (111)) darstellt.[74] Ausgehend vom Mars-van Krevelen-Mechanismus wurde formuliert, dass eine Erhöhung der Sauerstoffvakanzbildung, eine höhere Aktivität in Oxidationsreaktionen zur Folge hatte.[71] Dieses Phänomen konnte auch für weitere Oxidationsreaktionen wie unter anderem der Rußoxidation (*soot oxidation*) bestätigt werden.[75] Im Falle der HCl-Oxidation konnten Li *et al.* diesen Trend weiterhin verifizieren.[67] Unter den harschen Bedingungen des Deacon-Prozesses zeigte sich analog zu den genannten Oxidationsreaktionen die höchste Reaktivität bei den Nanostäben, die zudem noch eine verbesserte Stabilität gegenüber der Bildung von $CeCl_3$ aufwiesen. Beide Parameter stimmen damit sehr gut mit dem Trend der gemessenen OSC-Werten überein.

Neben dem Einfluss der verschiedenen Oberflächenterminierungen auf die Sauerstoffspeicherkapazität und den katalytischen Eigenschaften spielt auch die Partikelgröße eine entscheidende Rolle für die Oberflächenchemie von CeO_2-Materialien. Tsunekawa *et al.* demonstrierten experimentell, dass die Gitterkonstante von 2 – 8 nm großen CeO_2-Partikeln immens ansteigt verglichen mit nicht-nanoskopischem CeO_2.[76,77] Neben Deshpande *et al.*[9] korrelieren auch Zhou und Huebner diesen Anstieg mit der erhöhten Konzentration von größeren Ce^{3+}-Ionen und der damit verbundenen höheren Anzahl von Sauerstoffleerstellen.[78] Letztere bestimmten diese Anzahl der Defekte über die Veränderung der Gitterkonstante mit der Größe der Partikel. Dabei lassen die Autoren außen vor, dass sich Defekte eher an der CeO_2-Oberfläche befinden als im Inneren des Partikels und so maßgeblich an dem Austausch mit Sauerstoff beteiligt sind.[79] Eine direkte Korrelation der Partikelgröße mit der OSC ist so nicht möglich. Erst Özkan *et al.* synthetisierten basierend auf einer angepassten Hydrothermalmethode mit einem tetravalenten Cerpräkursor ($(NH_4)_2Ce(NO_3)_6$) sphärische CeO_2-Partikel unterschiedlicher Größe, die über einen defektfreien Bulkzustand verfügen.[80] Unabhängig von Defekten und Gitterverspannungen konnte so der Einfluss der Partikelgröße im Bereich von 4 – 12 nm auf die OSC bestimmt werden. Anders als Sayle *et al.* postulierten, ergab sich die höchste OSCc für die größten Partikel (12 nm) bedingt durch die geringere Bildungsenthalpie bei wachsenden Partikeln.[81,82] Die Autoren weisen zudem daraufhin, dass es ein Optimum der Partikelgröße für die OSC gibt. Allerdings ist die Herstellung von Partikeln mit definierter Größe in den höheren Bereichen (> 15 nm) nur schwierig zu steuern. Unkontrollierte Agglomeration

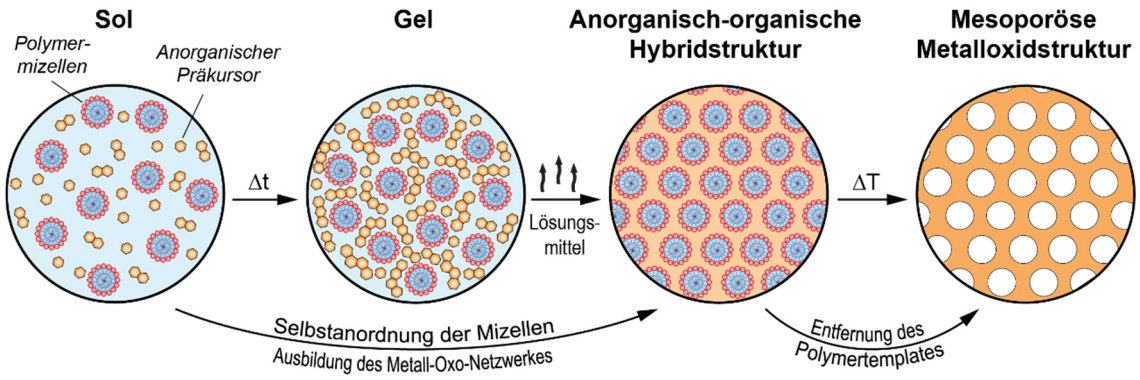

Abbildung 3: Schematische Darstellung der *soft templating* Methode über einen Sol-Gel-Ansatz zur Präparation geordneter Mesoporenstrukturen.

und Sinterprozesse führen zu undefinierten Partikelgrößen, so dass nicht die gesamte Oberfläche für katalytische Prozesse zugänglich ist.

Die Verwendung von mesoporösen Materialien ist hier vorteilhaft, da diese bei gleichhohen spezifischen Oberflächen eine bessere Zugänglichkeit für die Reaktanden bieten. Mögliche morphologische Veränderungen in Folge katalytischer Prozesse können zudem leicht anhand der Umorganisation bzw. Beschädigung der geordneten Mesoporen-Strukturen mit mikroskopischen Methoden verfolgt werden. Solche morphologischen Veränderungen ermöglichen einen direkten Bezug zur katalytischen Stabilität der Cerdioxid-Nanokomposite.

Geordnete Mesostrukturierung kann mithilfe des Templatverfahrens induziert werden, welche grob in drei Schritte eingeteilt ist: (i) Präparation des Templats, (ii) Synthese des Zielmaterials unter Einfluss des Templats und (iii) Templatentfernung. Des Weiteren wird zwischen *hard templating* und *soft templating* unterschieden.[83–86] Bei Ersterem bildet eine feste, starre Struktur wie u. a. vorgefertigte Polymerkugeln oder poröse Membranen aus SiO_2[87,88] oder Al_2O_3 [89,90] das strukturdirigierende Reagenz, welches anschließend nasschemisch imprägniert wird. Nachdem das gewünschte Material in die kristalline Form überführt wird, muss das Templat vorzugsweise mittels Tempern oder dem Einsatz von Natronlauge oder Flusssäure bei SiO_2-basierten Templaten[91] vollständig entfernt werden. Obwohl mit diesem Verfahren hochgeordnete poröse Strukturen hergestellt werden können, ist die Auswahl von geeigneten Templatmaterialien begrenzt und deren Beseitigung erfolgt meist unvollständig.[92] Die daraus resultierende Verunreinigung an der Oberfläche des Zielmaterials erschwert folglich eine systematische Untersuchung katalytisch aktiver Materialien wie beispielsweise CeO_2. Das *soft templating* hingegen basiert auf der Verwendung von ambiphilen Tensidmolekülen, welche sich parallel zu den Präkursoren des Zielmaterials in Lösung befinden und sich gemäß ihrer Hydrophilie zu Mizellverbänden organisieren (siehe Abbildung 3).[93,94] Die Wahl der Tenside entscheidet hier maßgeblich, welche Porendurchmesser – meist zwischen 2-30 nm – und -anordnung generiert werden.[95] Die Entfernung der Polymermizellen erfolgt zudem bereits bei niedrigeren Temperaturen vollständig und verzichtet auf den Einsatz stark ätzender Substanzen. Obwohl

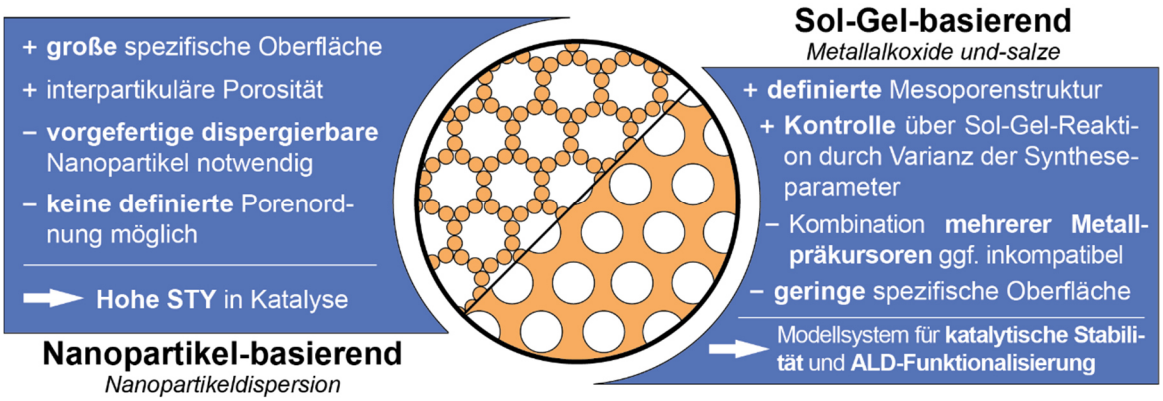

Abbildung 4: Vergleich zwischen auf Nanopartikeln und Sol-Gel-Synthese basierender mesoporöser CeO_2-Strukturen für den Einsatz als Modellkatalysatoren.

ein hohes Verständnis der physikochemischen Wechselwirkungen zwischen Mizelle und Präkursor notwendig ist, eignet sich das *soft templating* nicht zuletzt durch die hohe Anzahl von möglichen Templaten ideal, um die Poren- und Partikelgröße zu variieren und deren Einflüsse auf katalytische Eigenschaften zu studieren. Weiterhin lassen sich hiermit Substrate mit hoher spezifischer Oberfläche herstellen, welche für die Oberflächenfunktionalisierung mit aktiven Materialien dienen.

Ein Spezialfall des *soft templating* ist der sogenannten EISA-Prozess[96], mit welchem sowohl mesoporöse Dünnschichten also auch Pulver präpariert werden. EISA steht für *evaporation-induced self-assembly* und basiert auf der Selbstanordnung von Tensidmolekülen zu Mizellen beim Verdampfen des Lösungsmittels (meist Alkohole). Die Methode beruht im Generellen auf einem Sol-Gel-Ansatz, der zur Synthese von nanokristallinen Metalloxid-Schichten und -Pulvern verwendet werden kann.[97–99] Als Ausgangsmaterialien für das jeweilige Metalloxid werden die entsprechenden Metallalkoxide oder Metallsalze eingesetzt, welche durch Zugabe von Wasser hydrolysiert und sukzessiv kondensiert werden. Die Mesostrukturierung erfolgt dabei durch ambiphile Tenside mit polarer Kopfgruppe und unpolarem Schwanz, die im Sol Mizellen ausbilden.[100] Das mesoporöse Oxid entsteht durch anschließendes Entfernen des Polymertemplats bei höheren Temperaturen (ca. 300 – 500 °C), so dass im Sinne eines Replikationsprozesses jede Mizelle in eine entsprechende Mesopore umgewandelt wird. Die Porenwanddicke und die Porengröße können durch das eingesetzte Polymer variiert werden, während die Partikelgröße über die Dauer der Temperaturbehandlung gesteuert wird.[101,102]

Neben molekularen Präkursoren können auch vorgefertigte Nanopartikel verwendet werden. Die Herstellung über Sol-Gel-Synthesen eignet sich meist nur für Materialien, die über entsprechende Metallalkoxide oder –salze verfügen, deren Hydrolyse- und Kondensationsreaktion gesteuert werden können. Im Falle von CeO_2 wird hier meist $CeCl_3x7H_2O$ gewählt.[101,103,104] Allerdings verkompliziert sich der Prozess bei der Synthese von Multimaterialoxiden unter Einsatz mehrerer molekularer Präkursoren. Die entsprechenden Reaktionsschritte müssen kompatibel sein, um keine Nebenphasen oder Phasensegregation

zu erhalten. Somit eignen sich vorgefertigte Nanopartikel, die bereits die gewünschte Stöchiometrie besitzen und in kristalliner Form vorliegen, als Präkursoren für den Templatprozess.[64,105,106] Zudem erhöht sich die spezifische Oberfläche stark, da neben den induzierten Mesoporen durch das Templat auch interpartikuläre Zwischenräume die Porosität steigern. Jedoch sind bedingt durch die Wandstärke zwischen den Mesoporen definiert kleine Partikelgrößen mit enger Partikelgrößenverteilung notwendig, um die Mesoporen in das Material zu integrieren. Da es sich bei Nanopartikeln anders als bei den Sol-Gel-Präkursoren um sehr unflexible und starre Strukturen handelt, können meist keine hochgeordneten Mesostrukturen hergestellt werden (siehe Abbildung 4).[107,108]

Um die Mesostrukturierung besser zu kontrollieren, wurden Block-Copolymere entwickelt, die entsprechend ihrer Zusammensetzung größenspezifische Mesoporen generieren. Die bekanntesten Vertreter solcher Block-Copolymere sind die Polymerserien Pluronic® P-123 und F-127, welche aus alternierenden Blockeinheiten von hydrophilem Polyethylenoxid (PEO) und hydrophobem Polypropylenoxid (PPO) bestehen und je nach Konzentration sphärische oder zylindrische Mizellen ausbilden.[109–111] Mithilfe dieser strukturdirigierenden Reagenzien lassen sich entsprechend der Blockeinheiten- und folglich Mizellengröße Porendurchmesser von etwa 5 bzw. 8 nm herstellen. Während mit diesen Polymeren erfolgreich hochgeordnete Strukturen aus SiO_2 wie SBA-15[99,112] oder KIT-6[113,114] hergestellt werden können, erweist sich die Ausbildung geordneter Porenstruktur mit kristallinen Wänden bei Metalloxiden (wie TiO_2, ZrO_2, Al_2O_3, CeO_2, etc.)[103,115–118] als durchaus herausfordernd. Gründe hierfür sind unter anderem die erhöhte Hydrolyse- und Kondensationsgeschwindigkeit metalloxidischer Präkursoren sowie das Partikel- bzw. Kristallitwachstum der Metalloxide bei erhöhten Temperaturen. Die Kristallitgröße kann so die aus dem verwendeten Templat resultierende geringe Porenwanddicke von ca. 4 nm[110] übersteigen, wodurch die geordnete Porenstruktur gestört wird.

Alternative Blockpolymere wie Poly(ethylen-co-butylen)-*block*-Poly(ethylenoxid) (KLE)[103,119–124] oder Poly(isobuten)-*block*-Poly(ethylenoxid) (PIB-*b*-PEO)[102,108,125–127] beheben diese Nachteile und verfügen über eine erhöhte thermische Stabilität und bilden Wanddicken von ca. 11 nm aus. Die genannten Diblock-Copolymere besitzen zudem den Vorteil, dass sie sich bereits bei sehr geringen Konzentrationen zu kugelförmigen Mizellen anordnen und einen Durchmesser von ca. 20 – 30 nm besitzen. Da die verwendeten Diblock-Copolymere uniforme Mizellen mit identischer Größe bilden, können mesoporöse CeO_2-Materialien mit definierter Porengröße und Mesostruktur erhalten werden. Die Porenwanddicke und die Porengröße können durch das eingesetzte Polymer variiert werden, während die Partikelgröße über die Dauer der Temperaturbehandlung gesteuert wird.[102,128,129] Es lassen sich mit dem modifizierten EISA-Prozess Verfahren sowohl dünne Schichten als auch Pulver herstellen.

Die dünnen Schichten werden über das Verfahren der Tauchbeschichtung präpariert, bei der ein Substrat in eine Lösung eingetaucht und mit definierter Geschwindigkeit herausgezogen wird.[130] Alternativ können die Dünnfilme über die Rotationsbeschichtung hergestellt werden, bei der die gegebene Präkursorlösung auf ein Substrat mit eingestellter Rotationsgeschwindigkeit aufgebracht wird. In beiden Fällen verdampft das verwendete Lösungsmittel bereits während der Beschichtung, so dass sich eine dünne Schicht abhängig von der Rotation- bzw. Zuggeschwindigkeit und der Luftfeuchte ergibt.[131] Mit diesem Verfahren konnte eine Reihe von mesoporösen Metalloxiden als Dünnschichten präpariert werden.[98,123]

Dank der geordneten Ausrichtung der Mesoporen und der definierten Probengeometrie stellen mesoporöse Schichten perfekte Modellsysteme dar, um die Funktionalisierung der porösen Oberfläche zu dokumentieren (siehe Kapitel 2.2.). Zwar besitzen mesoporöse Dünnschichten und analog präparierte mesoporöse Pulver die gleiche spezifische Oberfläche in Quadratmeter pro Gramm, allerdings unterscheidet sich die verfügbare Masse und damit die Anzahl an aktiven Stellen. Aufgrund des daraus resultierenden erhöhten Signal-zu-Rausch-Verhältnis, können so an mesoporösen Pulvern die Sauerstoffspeicherkapazität und katalytischen Eigenschaften unter realen Bedingungen statistisch genauer und zuverlässiger erfasst werden.

Die Herstellung von mesoporösen Metalloxid-Pulvern basiert grundsätzlich auf der gleichen Ausgangslösung wie bei der Herstellung mesoporöser Dünnfilme. Ein grundsätzliches Problem bei der Präparation von Pulvern liegt im potentiell inhomogenen Verlauf der Kondensation in der Sol-Gel-Reaktion, da das Entfernen der Lösungsmittel als zentralem Schritt beim Templatierungsprozess an der Oberfläche schneller erfolgt als im Inneren der Probe. Die Mizellbildung der verwendeten PIB-*b*-PEO Block-Copolymere ist jedoch sehr robust gegenüber solchen Inhomogenitäten, so dass die Mesoporenstruktur ähnlich geordnet ausgebildet wird wie bei Dünnfilmen.

Dies wird durch eine kürzlich veröffentlichte Publikation von Eder *et al.* bestätigt, in der die Herstellung von WO_3-Pulver mit geordneter Porenstruktur im Hinblick auf photokatalytische Anwendungen beschrieben ist.[132] Die Synthese gelang hierbei über Polyisoprenblock-Polyethylenoxid (PI-*b*-PEO), welches weiterhin von Weller *et al.* verwendet wurde, um komplexe Oxide wie $CsTaWO_6$ herzustellen.[133]

Bisher existieren nur wenige Publikationen zur Herstellung von Cerdioxid-Pulvern mit geordneter Mesoporenstruktur, wobei die meisten Synthesen auf *hard templating* beruhen.[87,134–136] Sayle und Mitarbeiter konnten mithilfe von theoretischen Berechnungen demonstrieren, dass zwar die Größe der Mesoporengröße eine Rolle spielt, die Sauerstoffspeicherkapazität jedoch maßgeblich von der Wanddicke analog zu dem Einfluss von Partikelgrößen beeinflusst wird.[137] In den meisten Beispielen in der Literatur werden lediglich ungeordnete CeO_2-Strukturen verwendet, um hohe Oberflächen für die katalyti-

schen Messungen zu generieren. Jedoch verfügen diese Materialien nicht über eine definierte Wandstärke, um die theoretisch ermittelten Werte zu bestätigen. Folglich ist ein mesostrukturiertes CeO_2-Material wünschenswert, welches über definierte Porengrößen und Wanddicken verfügt. Während die Reaktanden durch die Mesoporen die gesamte Oberfläche des Materials erreichen können, kann die Wandstruktur über Dotierungen oder unterschiedliche Partikelgrößen variiert werden. Zudem stellt die Verteilung der Porengrößen vor und nach der HCl-Oxidation einen direkten Zusammenhang zu der Katalysatorstabilität her. Mesoporöse Pulver bilden somit ein neues, geeignetes Modellsystem für Einflussstudien obig genannter Parameter auf die OSC sowie der katalytischen Aktivität und Stabilität im Deacon-Prozess.

2.1.3 Dotierungen mit Seltenerdmetallen

Die Dotierung mit Fremdatomen erwies sich als eine vielversprechende Option das Ce^{3+}/Ce^{4+}-Verhältnis zu kontrollieren und damit die Bildung von Sauerstoffleerstellen zu begünstigen. Neben Untersuchungen zu tetravalenten Ionen konnte in der Literatur gezeigt werden, dass trivalente Kationen wie La^{3+}, Eu^{3+}, Gd^{3+} und Sm^{3+} die Konzentration an Sauerstoffleerstellen und damit die Ionenleitfähigkeit in CeO_2-basierten Materialien erhöhen.[138–140] Wenn ein aliovalentes Ion in das CeO_2-Gitter eingebaut wird, entsteht eine weitere Sauerstoffleerstelle zusammen mit der Reduktion eines benachbarten Ce^{4+}-Ion zu Ce^{3+}, um die Ladungsmissverhältnisse zu kompensieren (siehe Gleichung (3)).[7,141] Dadurch entstehen weitere extrinsische Sauerstoffvakanzen, die die Mobilität von Sauerstoff im Gitter erhöhen.

$$2\ \mathrm{Ce_{Ce}} + \mathrm{O_O} + \mathrm{M_2O_3} \rightarrow 2\ \mathrm{M'_{Ce}} + \mathrm{V_O^{\bullet\bullet}} + 2\ \mathrm{CeO_2} \qquad (3)$$

Des Weiteren werden bedingt durch das Größenverhältnis zwischen dem M^{3+}- und Ce^{4+}-Ion strukturelle Verspannungen im Gitter induziert, welche gemäß Gopal *et al.* bereits bei undotierem CeO_2 einen Einfluss auf die Speicherfähigkeiten besitzen.[142] Studien von Farra *et al.*[23] und Wang *et al.*[55] berichten allerdings, dass Gd-dotierte Cerdioxid-Partikel trotz der erhöhten Konzentration an Sauerstoffvakanzen eine geringere katalytische Aktivität in der HCl- sowie CO-Oxidation zeigen. Möller *et al.*[24] konnten bestätigen, dass der Einfluss der Sauerstoffspeicherkapazität bei der Dotierung von Cerdioxid mit trivalenten Ionen auf die Aktivität im Deacon-Prozess gering ist.

Zwar erhöhen Gd^{3+}- und Sm^{3+}-Dotierungen die Leerstellenkonzentration und damit die Ionenmobilität von CeO_2, allerdings lassen sich die induzierten Leerstellen aufgrund der fehlenden Redoxeigenschaft der trivalenten Ionen nicht mit atmosphärischem Sauerstoff füllen wie es beim Ce^{4+}/Ce^{3+}-Redoxpaar der Fall ist.[143] Eine Möglichkeit vermehrt katalytisch funktionelle Sauerstoffleerstellen zu implementieren, ist daher die Dotierung mit Elementen, die ähnliche Redoxeigenschaften wie Cer besitzen. Solche Elemente sind das Lanthanoid Terbium und das im Periodensystem benachbarte Praseodym. Genau wie Cer

können beide Materialien ihre Oxidationsstufe leicht von 3+ zu 4+ wechseln und besitzen dabei ähnlich interessante Redoxeigenschaften, um den einfachen Ein- und Ausbau von Sauerstoff zu gewährleisten.[34,144] Aufgrund ihrer interessanten Redoxchemie bieten sich Untersuchungen von Terbium- und Praseodym-dotiertem CeO_2 an, die die Sauerstoffspeicherkapazität und die katalytische Aktivität in der HCl-Oxidation verknüpfen. Mittels der H_2-TPR wurde bereits von Trovarelli *et al.*[32] demonstriert, dass das Dotieren mit Tb und Pr zu einer verbesserten Reduzierbarkeit bei niedrigen Temperaturen im Vergleich zum undotierten CeO_2 führt. Des Weiteren wurde von Farra *et al.*[23] berichtet, dass der prozentuale Anteil der Dotierung einen Einfluss auf die Sauerstoffspeicherkapazität besitzt, wobei ein merklicher Anstieg bei ca. 10 at.-% zu verzeichnen ist.

Um den Einfluss von tri-/tetravalenten Fremdatomen wie Tb und Pr auf die Sauerstoffspeicherkapazität zu ermitteln und auf die katalytischen Eigenschaften in der HCl-Oxidation anzuwenden, beschäftigt sich das Promotionsprojekt unter anderem mit der Herstellung von entsprechend dotierten mesoporösen CeO_2-Strukturen (siehe Kapitel 3.1). Dank ihrer hohen spezifischen Oberfläche und der geordneten Porosität eignen sich die Materialien ideal, um die Auswirkung der Dotierelemente auf die katalytische Stabilität unter korrosiven Bedingungen in der HCl-Oxidation mithilfe der Rasterelektronenmikroskopie und der Stickstoffphysisorption zu verfolgen. Als Vergleich wurde zudem noch ein Vertreter der trivalenten und tetravalenten Dotierungselemente berücksichtigt, um die Ergebnisse der mischvalenten Ionen einzuordnen.

2.1.4 Cer-Zirkonium-Mischoxide

Neben der Dotierung mit Seltenerdmetallen besitzt die feste Lösung aus CeO_2 und ZrO_2 ein großes Anwendungspotenzial in der Katalyse.[27,37,46,145–147] Als passiver Bestandteil für den Drei-Wege-Katalysator zeichnet es sich sowohl durch eine höhere OSC als auch eine erhöhte thermische Stabilität aus, welche bei Prozesstemperaturen von >1000 °C essentiell ist.[148–152] Die auftretenden Sinterprozesse sind im Vergleich zu reinem CeO_2 erniedrigt, so dass selbst bei hoher Expositionsdauer der erforderliche Kontakt mit der aktiven Edelmetallkomponente gewährleistet wird.

Die hohe Sauerstoffspeicherkapazität der CeO_2-ZrO_2 Materialien ergibt sich über die unterschiedlichen Ionenradien ($r(Zr^{4+})$ = 84 pm, $r(Ce^{4+})$ = 97 pm)[153], die mit steigendem Dotierungsgrad zu einer erhöhten Verspannung im Gitter führen.[154,155] Durch die Relaxation des Gitters diese Verspannungen abzubauen ist es energetisch eher möglich, den Sauerstoff von einem Oberflächenplatz zu entnehmen, wie kürzlich von Otero *et al.* mithilfe der Dichtefunktionaltheorie (DFT) berechnet wurde. Auf einer Zr-dotierten CeO_2(111)-Oberfläche wird die Bildung von Sauerstoffleerstellen von ursprünglichen 1,89 eV auf 1,16 eV gesenkt.[156] Anders als bei trivalenten Ionen wird folglich die Reduzierbarkeit des katalytischen Materials erhöht, ohne dass sich Sauerstoffleerstellen basierend auf dem La-

dungsausgleich der aliovanten Fremdionen bilden.[7] Während im reinen CeO_2 der Reduktionsgrad durch die Volumenvergrößerung der Einheitszelle limitiert ist - bedingt durch die Reduktion von Ce^{4+}- (97 pm) zu größeren Ce^{3+}-Ionen (114 pm) – erlaubt der Einbau von Zr^{4+} (84 pm) in das CeO_2-Gitter dieses Wachstum auszugleichen und folglich den Reduktionsgrad zu erhöhen.[155] Madier *et al.* nutzten $^{18}O/^{16}O$ Isotopenaustauschmessungen, um die höhere Mobilität durch das verspannte Mischgitter von CeO_2-ZrO_2 nachzuweisen.[147]

Durch ihre verbesserten physikochemischen Eigenschaften wurden die CeO_2-ZrO_2-Oxide in weiteren Bereichen der Katalyse als aktive Komponente in der Oxidation von flüchtigen organischen Komponenten[157–159], Dampfreformierung[160,161], Wassergas-Shift-Reaktion[162–166] oder Rußoxidation[30,167,168] getestet - in allen Fällen mit engem Bezug zu der Sauerstoffspeicherkapazität. Atribak *et al.* ermittelten die höchste OSC und katalytische Aktivität in der Rußoxidation bei einem stöchiometrischen Verhältnis von $Ce_{0.76}Zr_{0.24}O_2$, wobei hier die Materialien mit unterschiedlichen Kristallitgrößen und BET-Oberflächen hergestellt wurden.[168] Trotz der höheren thermischen Stabilität ist der Transfer dieser Ergebnisse auf die HCl-Oxidation nicht trivial. Kanzler *et al.* beschäftigten sich mit CeO_2-ZrO_2-Nanofasern, basierend auf einer Sol-Gel-Synthese in Kombination mit Elektrospinnen, um sie als Modellsysteme für die HCl-Oxidation zu verwenden und den Einfluss der Zr-Einbindung auf die Stabilität zu studieren.[28] Während sich bei reinen CeO_2-Fasern und höheren HCl/O_2-Verhältnissen (2.5:1) die spezifische Produktbildungsrate mit der Reaktionszeit immens verringerte, konnten bereits durch die Zugabe von 20 at.-% Zr katalytisch stabile CeO_2-ZrO_2-Nanofasern hergestellt werden. Des Weiteren konnten die Autoren demonstrieren, dass mindestens 20 at.-% Ce enthalten sein muss, um eine signifikant höhere Aktivität zu erhalten. Bei der Verwendung von Nanorods mit der aktivsten (110)-Kristallebene wurde beobachtet, dass der stabilisierende Effekt unter gleichen katalytischen Bedingungen bereits bei 5 at.-% Zr auftrat.[169] Dies wurde mithilfe thermodynamischer Modellberechnungen gestützt. Um das geeignetste CeO_2-ZrO_2-Verhältnis zu ermitteln, synthetisierte Sun *et al.* eine Vielzahl an unterschiedlichen Zusammensetzungen mit gleichbleibender BET-Oberfläche – jedoch unterschiedlichen Kalzinierungsprotokollen – um den Einfluss der BET-Oberfläche auf die katalytische Aktivität zu vernachlässigen.[57] Hierbei konnte ein direkter Zusammenhang zwischen der OSC und der katalytischen Ausbeute pro Zeit in der CO-Oxidation und der HCl-Oxidation für CeO_2-ZrO_2-Systeme ermittelt werden. Allerdings muss bei der vermehrten Inklusion von Zr und den aus Nanopartikeln zusammengesetzten Agglomeraten beachtet werden, dass sich auch die Kristallstruktur von kubisch zu Mischungen von tetragonal und monoklin veränderte. Die vorherrschende Kristallstruktur bedingt u. a. die OSC sowie die katalytischen Eigenschaften, wobei eine kubische Struktur bevorzugt ist.[51] Aus diesem Grund ist die optimale Zusammensetzung von CeO_2-ZrO_2 stets umstritten[7], da nicht zuletzt auch morphologische Faktoren einen Einfluss auf die vorliegende Kristallstruktur ausüben. Die Änderung der Kristallsysteme könnte eine mögliche Erklärung für die unterschiedlichen bestimmten CeO_2-ZrO_2-Optima

von Sun *et al.*[57] ($Ce_{0.8}Zr_{0.2}O_2$) und Fei *et al.*[17] ($Ce_{0.5}Zr_{0.5}O_2$) darstellen. Jedoch zeigen beide Publikationen, dass der Zr-Gehalt eine entscheidende Rolle für die katalytische Aktivität in der HCl-Oxidation einnimmt.

Möller *et al.* stellten Nanofasern aus CeO_2-Nanopartikeldispersionen her, die dank interpartikulärer Zwischenräume von wenigen Nanometern über eine höhere BET-Oberfläche von ca. 120 m^2 g^{-1} verfügten.[170] Nach den Reaktion in der HCl-Oxidation sank die BET-Oberfläche auf die Werte von unporösen Fasern[171] und mit ihr auch der katalytische Umsatz. Die Studie gibt jedoch preis, dass die Verwendung von kontrolliert agglomerierten Nanopartikeln eine praktikable Variante ist, um die BET-Oberfläche und mit ihr die zugänglichen aktiven Plätze für die katalytische Umsetzung zu erhöhen. Allerdings ist durch den Transfer von ca. 5 nm Partikeln in Nanofasern mit Durchmessern von 100 nm immer noch ein großer Teil beschränkt zugänglich, da in den interpartikulären Zwischenräumen von < 5 nm die erschwerte Knudsen-Diffusion vorliegt. Des Weiteren schlagen die Autoren vor, dass mit der chemischen Dotierung von Zr die mangelnde Stabilität ausgeglichen werden kann.

Mit der Herstellung von mesoporösen Strukturen mithilfe der PIB-*b*-PEO-Template und entsprechenden Nanopartikeldispersionen der CeO_2-ZrO_2-Reihe sollen so die Nachteile der Nanofasern ausgeglichen und hohe spezifische Oberflächen mit gleichmäßig erhöhter Oberflächenzugänglichkeit gewährt werden. Dabei werden die untemplatierten CeO_2-ZrO_2-Nanopartikel mit definierter Stöchiometrie zum Vergleich analog bzgl. der OSC und den katalytischen Eigenschaften getestet (siehe Kapitel 3.2.).

Erst vor kurzem zeigten Sun *et al.*[172], dass die Abscheidung von ultradünnen (1-2 nm) CeO_2-Schichten auf vorgefertigte ZrO_2-Nanopartikel eine aktive jedoch vor allem katalytisch stabile Komponente darstellt. Die verwendete nasschemische Methode erlaubt allerdings keine präzise Abscheidung von dünnen Schichten in der Form von Kern-Schale-Strukturen, um den Einfluss der CeO_2-Schichtdicke auf die katalytische Stabilität zu testen. Eine alternative Präparationsmethode liefert die im nächsten Kapitel vorgestellte Atomlagenabscheidung (ALD).

2.2 Präparation definierter Schichten in porösen Substraten

2.2.1 Atomlagenabscheidung (ALD)

Mithilfe der Atomlagenabscheidung (engl. *atomic layer deposition*, kurz: ALD) lassen sich Dünnschichten – meist Metalloxide – im Bereich von wenigen (Sub-)Monolagen herstellen.[173,174] Der zyklische Prozess der ALD basiert auf der selbstbegrenzenden Reaktion der Reaktanden in der Gasphase mit einer Festkörperoberfläche. Neben der Möglichkeit definierte Schichtdicken auf Substrate aufzudampfen, gewährleistet die ALD auch eine konforme Bedeckung von 3D-Strukturen.[175,176] Momentan liegt das Hauptfeld der ALD in der Herstellung von high-k-Dielektrika in der Mikroelektronik.[177] Die dünne Beschichtung von großen Oberflächen besitzt jedoch auch in den Anwendungsbereichen der Katalyse, Batterien, Superkondensatoren, Filtersystemen und Brennstoffzellen ein hohes Potenzial.[178–180] In diesen Gebieten werden häufig nanoporöse oder fibröse Materialien eingesetzt, die mithilfe der ALD funktional beschichtet werden können.[181–184]

Ähnlich zur chemischen Gasphasenabscheidung (engl. *chemical vapor deposition*, kurz: CVD) basiert die Schichtbildung der ALD auf einer chemischen Reaktion von zwei oder mehreren Ausgangsstoffen.[185] Allerdings werden die Reaktanden bei der ALD nacheinander in die Reaktionskammer geführt. Zwischen den einzelnen Zufuhrschritten wird die Kammer mit einem Inertgas wie z. B. Stickstoff oder Argon gespült, um die Teilreaktionen

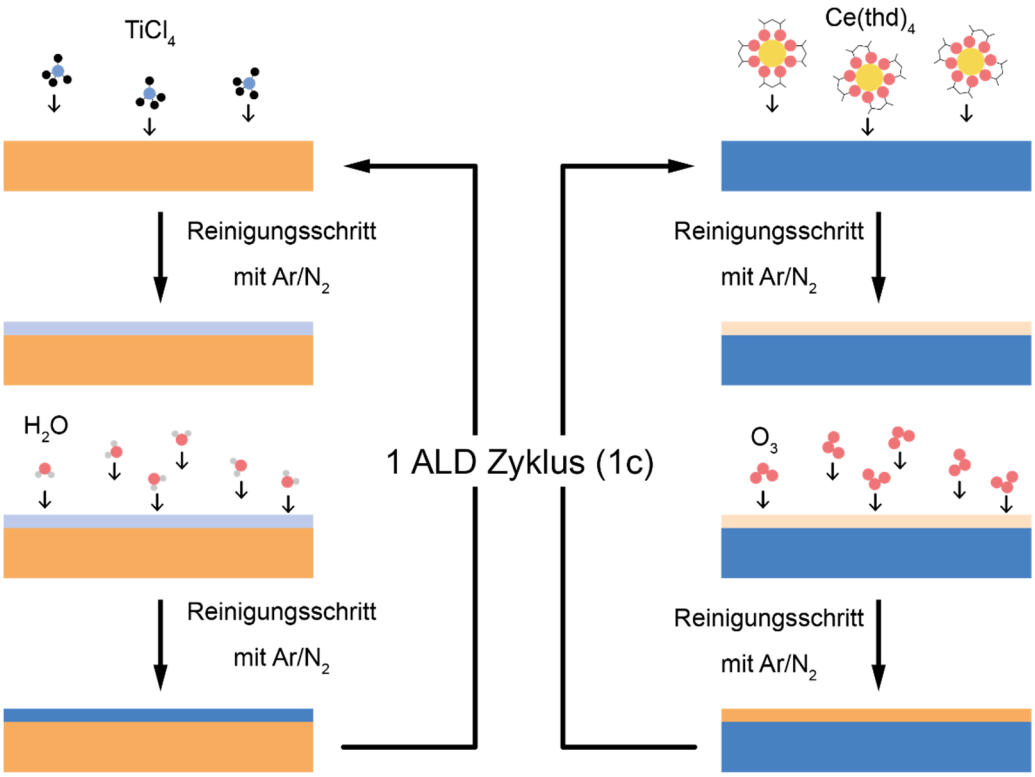

Abbildung 5: Abscheidungsprozess von Metalloxiden via ALD am Beispiel von Titan(IV)-chlorid ($TiCl_4$) mit H_2O sowie Tetrakis(2,2,6,6-tetramethyl-3,5-heptanedionato)-Cer(IV) $Ce(thd)_4$ und Ozon (O_3) (rechts). Der Prozess teilt sich jeweils in 4 zeitlich voneinander getrennte Reaktionschritte, bei denen die Reaktanden separat an die Oberfläche chemisorbieren und durch das Oxidationsmittel (H_2O / O_3) die erforderlichen OH-Gruppen regenerieren.

voneinander zu trennen. Dadurch kann die Reaktion auf die Oberfläche begrenzt werden. Durch die geeignete Wahl von meist leicht flüchtigen Präkursoren, welche gasförmig in den Reaktor geleitet werden und nicht mit sich selbst reagieren können, wird eine Teilreaktion bei beliebiger Gasmenge und Expositionsdauer auf maximal eine Monolage begrenzt.[177] Es lassen sich folglich definiert dünne Schichten im Bereich weniger Nanometer und konformer Bedeckung des Substrates abscheiden.[186,187]

Im Vergleich zu anderen Beschichtungsmethoden wie beispielsweise der chemischen und physikalischen Gasabscheidung[188,189] besitzt die ALD zahlreiche Vorteile. Die ALD erlaubt es Schichtdicken im Angströmbereich kontrolliert zu wachsen. Damit eignet sich das Verfahren speziell zur Herstellung von Ultradünnfilmen, die durch Schichtdicken unter 10 nm charakterisiert sind. Einen weiteren Vorteil bildet der industrielle Einsatz dieser Methode, da während eines Abscheidungsvorganges gleich mehrere Substrate simultan beschichtet werden können. Mittlerweile existieren Reaktoren, die mithilfe räumlich getrennter Zufuhr der Reaktanden durchgehend beschichten und die entsprechenden Dünnfilme produzieren.[179,190]

Die Abfolge von zwei Reaktions- und Reinigungsschritten wird als Zyklus bezeichnet (siehe Abbildung 5).[191] Dieser wird im Rahmen des Abscheidungsprozesses mehrfach wiederholt. Da pro Zyklus das Schichtwachstum theoretisch auf eine Monolage begrenzt ist, kann mittels der Zyklenanzahl die Schichtdicke definiert kontrolliert werden. In der Praxis kann jedoch nicht immer eine geschlossene Schicht erreicht werden. Ein wesentlicher Grund für dieses Phänomen ist die sterische Hinderung der adsorbierten Reaktanden, die Oberflächenstellen abschirmen und somit weitere Adsorptionen verhindern.[189,192,193] Der Ablauf von unvollständigen Teilreaktionen ist eine weitere Ursache, da diese die Reaktionsstellen an der Oberfläche reduzieren.[189] Daher wird in der Literatur neben den Instrumentparametern und den eingesetzten Reaktanden die Abscheiderate oder englisch

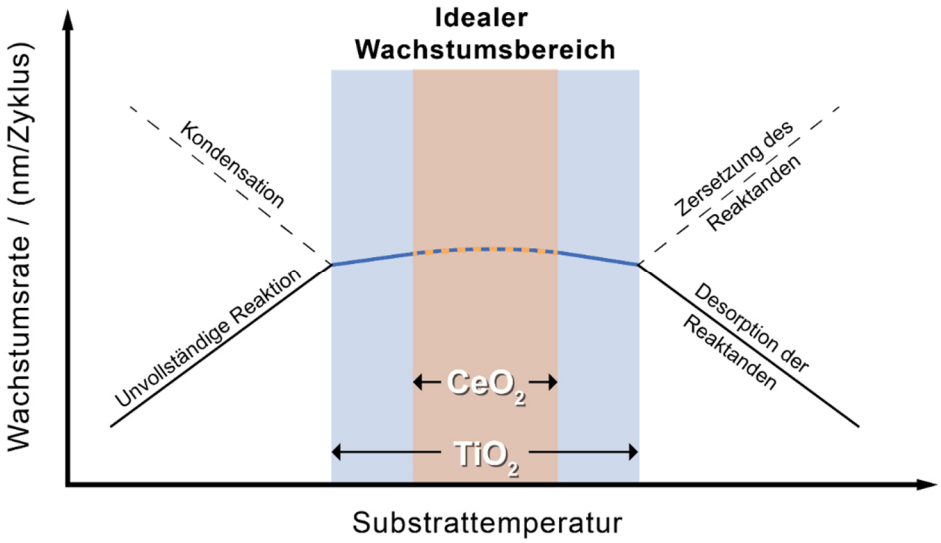

Abbildung 6: Qualitative Darstellung des idealen Wachstumsbereichs für die Abscheidung (*ALD window*) von CeO_2 und TiO_2-Schichten. Der Bereich kann mittels der eigensetzten Parameter und Präkursoren variieren und durch die Bestimmung der Wachstumrate ermittelt werden.

growth per cycle angegeben. Das aufzuwachsende Materialsystem und die gewählten instrumentellen Parameter sind hierbei entscheidende Größen für die Aufwachsrate (siehe Abbildung 6).[191,194]

2.2.2 ALD an porösen Substraten

Die Schwierigkeit bei der Beschichtung von porösen Substraten liegt in der Wahl der Reaktionsparameter. In den meisten Fällen werden glatte Substrate bedampft, so dass geringe Pulsraten ausreichen, um die Substratoberfläche mit dem Reaktandengas zu benetzen. Bei morphologisch anspruchsvollen Substraten wie beispielsweise einer durchgängigen Porenstruktur muss gewährleistet werden, dass die Reaktanden die gesamte Porenoberfläche erreichen und sich dort homogen als Metalloxide abscheiden können.[177] In der Literatur wurde bereits darüber berichtet, dass höhere Verweildauern der Reaktanden im Reaktor zu einer besseren Bedeckung der Poren führen.[183,195,196] Durch die höheren Kontaktzeiten kann der gasförmige Reaktand tiefer in das Porensystem eindringen und an die gesamte Substrat- bzw. Porenoberfläche adsorbieren (siehe Abbildung 7). Anschließende Physisorptionsuntersuchungen bewiesen, dass sich mit zunehmender ALD-Zyklenanzahl der Porendurchmesser verringert.[197] Mittlerweile existieren viele Fallstudien zur Beschichtung von anodisierten Alumiumoxidmembranen (AAO)[90,198], SiO_2-Gele[199,200], Kohlenstoffnanoröhren[201] oder Zeoliten[202], um den Einfluss der aufgewachsenen Komponente auf die physikochemischen Eigenschaften zu untersuchen. Im Sinne der Katalyse werden Pulvermaterialien gegenüber Dünnfilmen bevorzugt. Jedoch erweist sich die Abscheidung in porösen Pulvern mit nanometerweiten aber mikrometerlangen Poren und der daraus resultierenden hohen spezifischen Oberfläche als herausfordernd.[203] Die Beschichtung dieser großen Flächen wird folglich nicht nur von der Diffusion, sondern auch vom Angebot der Reaktanden kontrolliert.[199] Die meisten *conformality*-Studien wurden an porösen Systemen mit Porengrößen > 30 nm unter zur Hilfenahme bildgebender Methoden durchgeführt.[177] Für Materialien mit Porengrößen < 30 nm sind nur wenige Fallstudien bekannt. Viele davon beziehen sich aufgrund der geringen absoluten Oberfläche und der klar definierten Geometrie auf poröse Dünnfilme.[177,204]

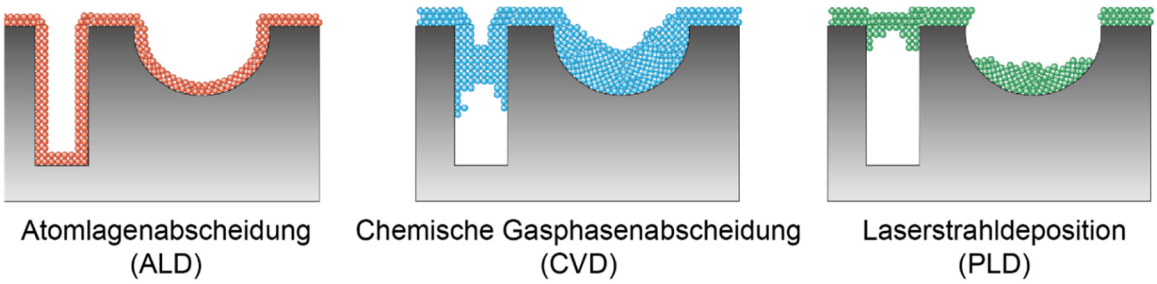

Abbildung 7: Abscheidungsprofil auf komplexen Substraten via ALD, CVD und PLD.

Cameron *et al.* berichteten die erfolgreiche Abscheidung von Al_2O_3, TiO_2 und SiO_2 in Al_2O_3 Membranen mit Porendurchmessern von ca. 5 nm, welche mithilfe von *in situ* N_2-Leitwertmessungen überprüft wurde.[205] Des Weiteren befassten sich Detavernier *et al.*[179] mit der Beschichtung von mesoporösen SiO_2-Dünnfilmen, die eine Porengröße von 4 nm besitzen. Die Mesoporen sind hierbei durch kleine Zwischenkanäle miteinander verbunden. Mit der ALD sollte anschließend TiO_2 in die Poren abgeschieden und mit einem analog beschichteten oxidierten Siliziumsubstrat als Referenz verglichen werden. Der Vorgang wurde mit einer *in situ* Röntgenfluoreszenzanalyse (XRF) untersucht. Die Autoren zeigten zum einen, dass die Aufwachsrate von TiO_2 auf die mesoporösen Substrate 2,5-mal größer ist als das Wachstum auf den SiO_2-Wafern. Zum anderen konnten Detavernier *et al.* anhand der unterschiedlichen Steigungen der XRF-Messungen verschiedene Stadien der TiO_2-Beschichtung beschreiben. So werden zunächst die 4 nm Poren an der Oberfläche beschichtet, um mit steigender ALD-Zyklenanzahl komplett gefüllt zu werden. Mit jedem weiteren Zyklus erfolgt die Abscheidung einer reinen TiO_2-Schicht auf der Oberfläche des zuvor mesoporösen SiO_2-Films. Dies konnte anschließend mit *in situ* Experimenten der Kleinwinkelröntgenstreuung mit streifendem Einfall (GI-SAXS)[196] und ellipsometrischer Porosimetrie (EP)[206] verifiziert werden, welche die Porosität der Materialien während des Beschichtungsprozesses untersuchen. Die Autoren konnten so ermitteln, dass die geringe Größe der Porenkanäle von < 5 nm zwischen zwei Mesoporenschichten das Schichtwachstum bei gleichbleibenden Präkursoren limitiert. Nach einer bestimmten Abscheidungsdicke verkleinern die Porengänge so weit, dass der molekulare Präkursor nicht mehr zu den nächsten Porenschichten gelangen kann.[179]

Allerdings verwendeten die Autoren keine Substrate mit einem geordneten Porensystem, sondern zylindrische Poren, welche mit kleinen Kanälen undefinierter Größe verbunden sind. Das System ist folglich nicht ideal, um die Abscheidung von dünnen Schichten auf porösen Metalloxidsubstraten mit der ALD und all ihren Einstellungsparametern (Pulszeit, Substrattemperatur, Verweildauer im Reaktor, etc…) systematisch zu studieren. Hierzu wäre ein Modellsystem notwendig, welches sowohl über eine definierte Porengröße und –form verfügt als auch über gleich große Zwischenkanäle verbunden ist. Unter der Verwendung der PIB-*b*-PEO-Template lassen sich entsprechende kubisch angeordnete Übergangsmetalloxide mit Porengrößen um etwa 14 nm herstellen, welche ähnlich einer Invers-Opal-Struktur untereinander verknüpft sind.[102,108] Dadurch bilden diese Dünnschichten ideale Modellsysteme, um die Abscheidung von Metalloxiden mittels ALD in poröse Substrate systematisch zu studieren. In einem ersten Schritt müssen jedoch sowohl die Synthese von geordneten mesoporösen Substraten als auch die instrumentellen Parameter für die ALD-Beschichtung optimiert werden, bevor die CeO_2-Abscheidung auf mesoporösen ZrO_2 bzw. TiO_2 behandelt und die Schichtdickenabhängigkeit auf die OSC analysiert werden kann.

Aus Vorarbeiten konnte bereits die Präparation von mesoporösen CeO_2-ZrO_2-Schichten optimiert werden[101], wobei hier die Dünnfilme vom $Ce_{0,5}Zr_{0,5}O_2$ die am meisten geordnete Mesoporenstruktur zeigten und am besten als Modellsystem für die ALD-Beschichtung geeignet sind. Da für die Überprüfung mittels REM, Laserellipsometrie, Flugzeit-Sekundärionen-Massenspektrometrie (ToF-SIMS) und Reflektometrie ein Kontrastelement förderlich ist, wurde anstelle von CeO_2 zunächst TiO_2 aufgewachsen. Des Weiteren ist die Beschichtung mit TiO_2 aufgrund des günstig verfügbaren Präkursors ($TiCl_4$) und des hohen Anwendungspotenzials u.a. als Farbstoffsolarzelle einer der meistuntersuchten ALD-Kandidaten in der Literatur.[186,195,196,207] Literarische Vergleiche mit den hier experimentell bestimmten Daten können folglich umfassend durchgeführt werden. Die Resultate sind in Kapitel **3.3** dargestellt.

Basierend auf den Resultaten von Granozzi *et al.*, die die Abhängigkeit des Ce^{3+}/Ce^{4+}-Verhältnisses von der Cerdioxid-Schichtdicke auf TiO_2-Substrate beobachteten[10] und Sun *et al.*, die mit ultradünnen (1-2 nm) CeO_2-Schichten auf vorgefertigten ZrO_2-Partikeln einen zukunftsweisenden aktiven und stabilen Katalysatoren für die HCl-Oxidation nachwiesen[11], wurde die Präparation von mesoporösen Dünnschichten aus ZrO_2 und TiO_2 optimiert. Hierzu wurden die mechanischen Eigenschaften der Filme, welche mithilfe von molekularen Präkursoren sowie Nanopartikeldispersionen hergestellt wurden, während ihres Kalzinierungsprotokolls untersucht, um den Einfluss der Präkursoren und des verwendeten PIB-*b*-PEO-Templates auf die Formation der Mesoporenstruktur zu bestimmen. Die Studie in Kapitel **3.4.** sollte zudem aufklären, bei welcher Temperatur die Porenordnung durch das Kristallitwachstum zerstört wird und welche Auswirkungen es auf die mechanischen Verspannungen im System hat.

Mit den bereits eingestellten instrumentellen Parametern der ALD für die Beschichtung von porösen Substraten aus Kapitel **3.3** und den optimierten sol-gel-basierten ZrO_2-Dünnfilmen aus Kapitel **3.4** sollte nun die Beschichtung von CeO_2 auf porösen ZrO_2-Schichten untersucht werden. Zusätzlich zu den bereits genannten Charakterisierungsoptionen soll mittels der Röntgenphotoelektronenspektroskopie (XPS) der Ce^{3+}-Gehalt mit steigender Schichtdicke berechnet werden. Da die Dünnfilme aufgrund ihrer geringen absoluten Oberfläche nicht in der Flusskatalyse oder in der OSC-Apparatur gemessen werden können, wurde mittels Impedanzspektroskopie[103,208] die Leitfähigkeit in Abhängigkeit der Schichtdicke bestimmt (siehe Kapitel **3.5**). Die gemessenen Werte sollen Aufschluss über die ionische Mobilität geben, die in enger Verbindung mit der Sauerstoffspeicherkapazität steht.

3. Publikationen und Projekte

3.1 The Impact of Alio-/Isovalent Ions (Gd, Zr, Pr and Tb) on the Catalytic Stability of Mesoporous Ceria in the HCl Oxidation Reaction

Accepted

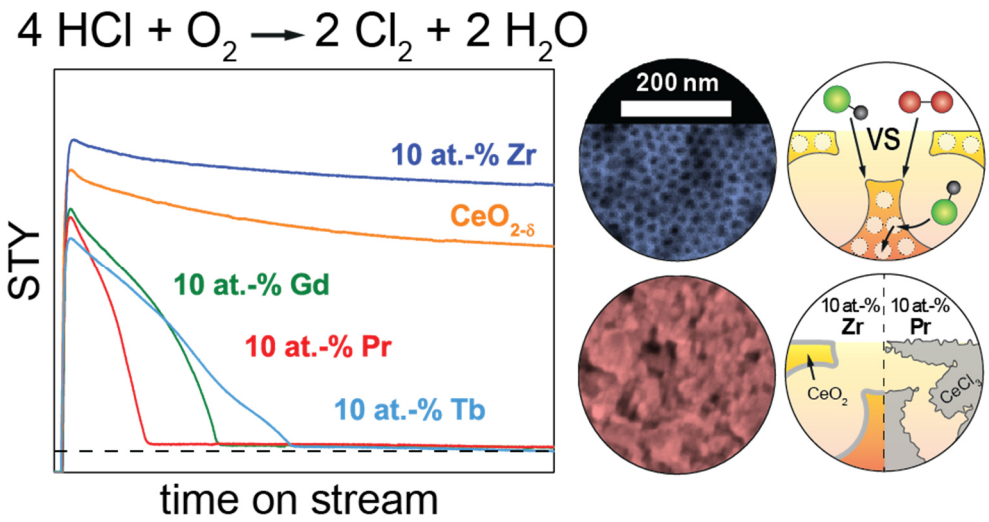

Reprinted with permission from

P. Cop, R. Maile, Y. Sun, I. Djerdj, O. Khalid, H. Over, B. M. Smarsly, The Impact of $M^{3+/4+}$-Doping of Mesoporous CeO_2 on the Catalytic Stability in the HCl Oxidation Reaction, *ACS Applied Nano Materials,* **2020**, *accepted.*

https://pubs.acs.org/doi/abs/10.1021/acsanm.0c00994

The Impact of Alio-/Isovalent Ions (Gd, Zr, Pr and Tb) on the Catalytic Stability of Mesoporous Ceria in the HCl Oxidation Reaction

Pascal Cop,[a,b] Ruben Maile,[a,b] Yu Sun,[a,c] Omeir Khalid,[a,b] Igor Djerdj,[d] Patrick Esch,[e] Sven Heiles,[e] Herbert Over,[a,b,] Bernd M. Smarsly[a,b,]**

a. Physikalisch-Chemisches Institut, Justus Liebig University, Heinrich-Buff-Ring 17, D-35392 Giessen, Germany

b. Center of Materials Research, Justus Liebig University, Heinrich-Buff-Ring 16, D-35392 Giessen, Germany.

c. Key Laboratory for Advanced Materials, Research Institute of Industrial Catalysis, School of Chemistry and Molecular Engineering, East China University of Science and Technology, Shanghai 200237, PR China.

d. Josip Juraj Strossmayer University of Osijek, Department of Chemistry, Cara Hadrijana 8/A, 31000 Osijek, Croatia

e. Institute of Inorganic and Analytical Chemistry, Justus Liebig University Giessen, 35392 Giessen, Germany

KEYWORDS: mesoporous, ceria, doped, praseodymium, stability, OSC, HCl oxidation

ABSTRACT

CeO_2 is a promising material in the catalytic retrieval of Cl_2 from HCl by oxidation with O_2 due to its beneficial redox properties (Ce^{3+}/Ce^{4+}) and accompanied oxygen storage capacity (OSC). Two options to tailor the OSC is the usage of dopants and nanostructuring. In this work, we report the synthesis of mesoporous doped $Ce_{0.9}M_{0.1}O_2$ (M = Zr, Gd, Pr and Tb) powders with identical mesopore size, shape and surface area (≈90 m^2 g^{-1}), in order to investigate the impact of alio- (Gd), iso- (Zr), alio-/isovalent (Pr, Tb) dopants on the OSC as well as on the catalytic activity/stability. The cubic arrangement of spherical 12 nm mesopores surrounded by a crystalline framework is obtained using a diblock copolymer as structure directing agent in the sol-gel based preparation approach, indicated by small X-ray scattering (SAXS) and scanning electron microscopy (SEM). Pr-doped CeO_2 revealed the highest oxygen storage capacity, but the lowest catalytic activity/stability in the HCl oxidation together with the Tb- and Gd-doped samples. By contrast, the Zr-doped mesoporous CeO_2 powders showed the highest catalytic performance and stability in the CO and HCl oxidation of all samples, but a lower OSC. These findings suggest that the OSC should therefore be treated with caution when relating the OSC to the catalytic performance in oxidation reactions. The differences in the stability are in agreement with recent studies of the HCl oxidation on model cerium oxide films with defined stoichiometry: the low stability of the aliovalent doped CeO_2 materials in the HCl oxidation reaction can be attributed to a large number of oxygen vacancies.

Introduction

CeO_2 is a promising catalyst material for diverse oxidation reactions, especially the catalytic gas-phase conversion of HCl into Cl_2, which is fundamental for the industrial-scale syntheses of e.g. PTFE, PVC or polyurethanes.[1,2] The catalytic oxidation process profits from the unique redox (Ce^{3+} / Ce^{4+}) behavior of CeO_2 being also utilized in oxygen sensors, fuel cells, biotechnology as well as catalytic and electrochromic thin film applications.[3–5] Furthermore, CeO_2 is an important component of the catalysts used for the elimination of toxic exhaust gases from automobiles. Its redox properties can be tailored, for instance, by nanostructuring[6,7] and doping with rare earth metal ions (gadolinium, praseodymium or terbium)[8–10], which affect the defect formation energy, the oxygen storage capacity (OSC) and also the transport of oxygen species. The oxygen vacancy-based defect chemistry was intensely studied in relation to the electrochemical properties, especially for nanomaterials.[7] A main feature of surface-dominated materials is the difference in the bulk and surface defect formation energies, which results in a high concentration of defects in the surface-near regions. Furthermore, the oxygen vacancy sites are related to the non-stoichiometry δ of $CeO_{2-\delta}$ and thereby alter its redox and transport properties,[11,12] and thus also the OSC. The exchanged amount of oxygen is quantified as dynamic OSC, when predominantly the surface oxygen vacancies are targeted, and total or complete OSC (OSCc), if surface as well as bulk oxygen vacancies are involved.

It is generally assumed that high values of the dynamic and total oxygen storage capacity promote a high catalytic activity of CeO_2 in oxidation reactions.[13–15] This relationship was especially described for Ce-Zr-oxides used in automotive catalysts in which the doping with Zr not only enhances the OSC and the thermal stability, but also the desired conversion rate in oxidation reactions.[12,16–18] Next to isovalent ions, also the doping with aliovalent ions (Gd^{3+}, Eu^{3+}, La^{3+},…) has been studied in regard to its effect on the ionic conductivity

and catalytic performance. For instance, Hernandez *et al.* revealed a higher performance of 10%-M^{3+}-doped ceria compared to pure ceria in the CO oxidation.[19] Trivalent ions enhance the ionic conductivity favoring the use of doped ceria as solid oxide fuel cell electrolytes (SOFC).[20] The latter is explained by the incorporation of additional oxygen vacancies compensating the local charge imbalance. In Kröger-Vink notation (see Equation (1)), the trivalent dopant M substitutes Ce^{4+} in the CeO_2 lattice which leads to the formation of one oxygen vacancy possessing a charge of +2 (depicted as two dots).

$$2\ Ce_{Ce}^{x} + O_{O}^{x} + M_2O_3 \rightarrow 2\ M_{Ce}' + V_{O}^{\bullet\bullet} + 2\ CeO_2 \qquad (1)$$

These extrinsic oxygen vacancies, often referred to as charge-compensating vacancies, facilitate the diffusion of oxygen ions through the vacancies themselves, thus lowering the activation enthalpy for oxygen migration[21] and thereby increasing the ionic conductivity. In case of incorporating isovalent ions such as Zr^{4+}, no extrinsic oxygen vacancies based on charge imbalance are formed. Due to the smaller ionic radius compared to Ce^{4+}, Zr^{4+}counterbalances the increase in unit cell volume when reducing Ce^{4+} to Ce^{3+}, lowering the oxygen vacancy formation energy,[22] and therefore allows for a higher degree of reduction than for undoped CeO_2. The combination of the oxygen vacancy formation and the migration dictates the ionic and electronic properties and hence, both types of dopants influence the OSC. Several oxidation reactions such as CO oxidation, water gas shift reaction, methanol oxidation or the soot combustion profit from a high OSC of the corresponding CeO_2 nanostructure[23,24], as the reaction mechanism involves the formation and refilling of an oxygen vacancy in the ceria lattice.

However, the relationship between the OSC and the HCl oxidation is still a matter of debate. Sun et al. showed an increase in the space-time-yield in the HCl oxidation reaction using CeO_2-ZrO_2 nanoparticles compared to CeO_2 particles, corresponding well to the OSC values.[13] Yet, Gd-doped CeO_2 nanofibers revealed the opposite trend[25] for the correlation

of HCl oxidation and OSC. Farra *et al.* studied the influence of different isovalent and aliovalent ions in the HCl oxidation combining experimental and computational methods.[26] These investigations showed an increase in the catalytic activity of Zr^{4+} and Hf^{4+}-doped CeO_2, while the trivalent dopants were found to be detrimental for the catalytic properties in the HCl oxidation. Their study raises the question, which effect redox-active dopants such as $Pr^{3+/4+}$ and $Tb^{3+/4+}$ exert on the OSC and HCl oxidation. Similar to cerium, both elements can change their oxidation state and can therefore enhance the ionic conductivity like trivalent and the reducibility as isovalent ions, respectively. In this study, the catalytic stability was mainly correlated to the decrease in the BET surface area.[24] In our previous work[27], electrospun CeO_2 nanofibers, synthesized from nanoparticle dispersions, were utilized as model catalyst to observe the morphological changes after used in the HCl oxidation.[27] However, a high-surface-area CeO_2-based material should also possess a defined particle morphology and size in the study of stability issues in the HCl oxidation reaction.

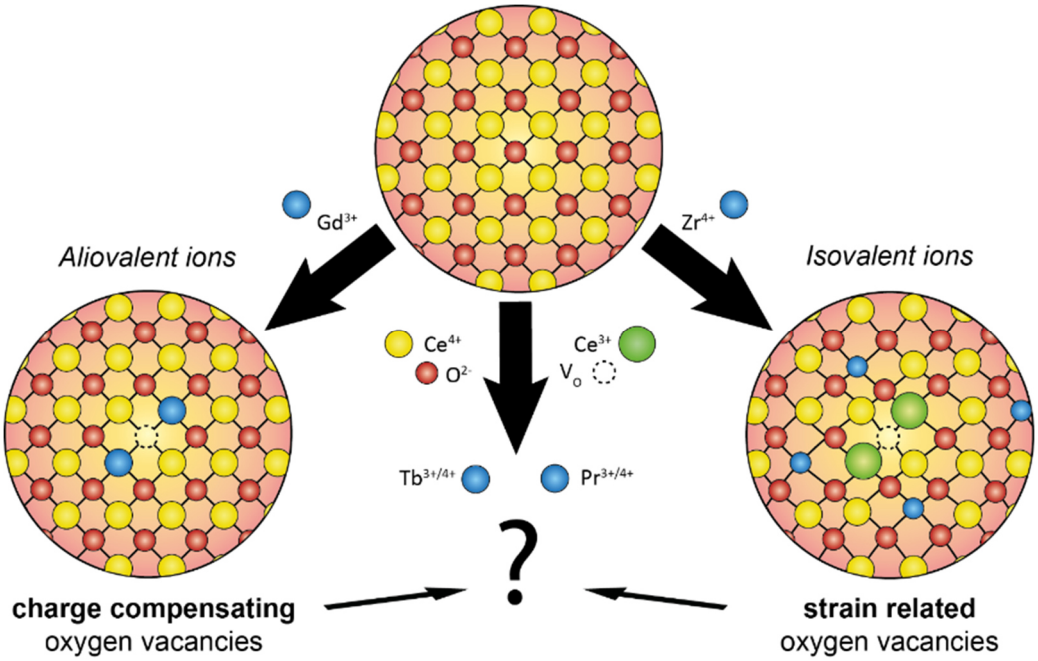

Scheme 1: Schematic overview of the introduced dopants and their effect on the formation of oxygen vacancies in the CeO_2 lattice.

In consequence, powders of defined nanoparticles of different composition might be regarded as suitable nanoscopic materials to study stability issues. However, agglomerates of isolated nanoparticles feature a random mutual arrangement, which consequently involves a very broad, and uncontrollable size distribution of micro- and mesopores, possibly containing small necks with hindered access. Hence, for such nanoparticulate materials the catalytic reaction might also be determined by diffusion-limitation, i.e. hindered access to the active sites. Another step further is the use of mesoporous CeO_2 catalysts possessing an ordered array of mesopores exhibiting unhindered diffusion of the gaseous reactants into the interior. In this spirit, in the present study, we synthesize CeO_2 materials featuring an ordered array of mesopores of uniform size for all the different compositions. Such materials provide identical accessibility for the gases throughout the sample, and facilitate to follow the deformation of the pore structure depending on the chosen conditions of the HCl oxidation.

The mesoporous CeO_2 materials were prepared using the diblock copolymer poly(isobutylene)-*block*-poly(ethylene) oxide referred to as PIB_{50}-*b*-PEO_{45} leading to a 3D network of spherical mesopores with a diameter of approx. 12 nm mesopores being connected by smaller channels.[28–31] While this sol-gel-based approach is mostly used for the fabrication of thin films, we adapted it to produce mesoporous powders of crystalline CeO_2 materials, also containing aliovalent and isovalent ions. Using rare earth metal chlorides as additives, Ce^{4+} ions are substituted by aliovalent (Gd), isovalent (Zr) and redox-active ions (Pr and Tb) (see Scheme 1) in order to reveal the influence of the dopants on the OSC and the catalytic properties in the HCl oxidation. Here, a concentration of 10 at.-% (10% $M^{3+/4+}$) was used for each substituting ion in the starting reaction mixture, as such content showed in previous studies already a significant impact on the catalytic properties and avoids the

occurrence of phase-separation and formation of the pure oxides of the dopants. The materials were subjected to a thorough characterization involving physisorption, electron microscopy, small-angle x-ray scattering, Raman spectroscopy, X-ray photoelectron spectroscopy and elemental analysis, before and after performing the catalytic reactions. Thereby, this study presents a conceptual methodology to assess catalytic stability in harsh reactions.

Experimental Section

Preparation of doped mesoporous CeO_2

Ordered mesoporous powders of doped (10 at.-% Zr, Gd, Pr, Tb) CeO_2 were prepared via an evaporation-induced self-assembly process (EISA) based on a combination of an approach by Weller et al.[32] and a previous published synthesis method of thin mesoporous CeO_2 thin films.[30] In this synthesis approach for 10 %-Zr CeO_2, 1.677 g [4.5 mmol] $CeCl_3 \cdot 7\ H_2O$ (98%, Sigma-Aldrich) and 0.089 g [0.5 mmol] $ZrOCl_2 \cdot 8\ H_2O$ (99.9%, Alfa Aesar) were added to 3.3 mL ethanol (99.8 %, Merck) and 3.3 mL 2-methoxy-ethanol (99%, Alfa Aesar). Another vessel was filled with 200 mg PIB_{50}-*b*-PEO_{45} (BASF, Ludwigshafen, Germany) dissolved in 3.3 mL ethanol and 1.7 ml acetic acid (> 99.85 %, Sigma-Aldrich). Both mixtures were treated in an ultrasonic bath for 30 min at 40 °C and 80 kHz. The solutions were cooled down to room temperature and mixed together. 100 µL dest. H_2O was added to the mixture which was then transferred to six 5 mL PTFE cups and covered with a glass dome on a heating stir plate. The solutions were heated up to 40 °C and kept at this

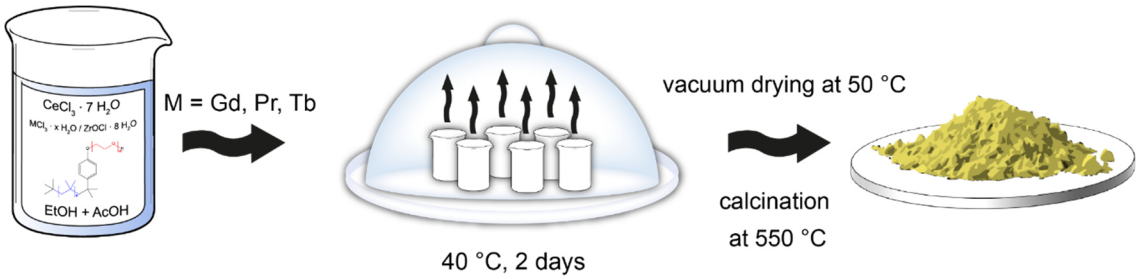

Figure 1: Schematic overview of the preparation of mesoporous doped ceria powders.

temperature under the glass dome for 2 days. The obtained powder was then dried in a vacuum oven at 50 °C overnight and afterwards annealed at 300 °C for 12 hours with a heating ramp of 0.75 K min^{-1}. In a last step, the powder was calcined at 550 °C for 10 min using a heating ramp of 10 K min^{-1} which led to the crystallization into the desired cubic crystal phase.

The same procedure was used for 10%-Gd, Pr and Tb doped mesoporous ceria by exchanging the zirconium precursor by the corresponding $MCl_3 \cdot 6\ H_2O$ (M = Gd, Pr, Tb) (>99%, Sigma Aldrich) (see Figure 1).

Characterization methods

Scanning electron microscopy (SEM) images were recorded using the model *Merlin* by *Zeiss* with an acceleration voltage of 2 keV and a current of 78 pA. In order to increase the conductivity of the samples, the films were sputtered with platinum for 10 s with an applied current of 40 mA. Energy dispersive X-ray spectroscopy (EDS) analyses were recorded by a *XMAX 50* detector from *Oxford Instruments* using a working distance of 5 mm and a current of 2 nA and an acceleration voltage of 10 keV. The crystalline phases quantification was determined by Rietveld analysis of X-ray powder diffractometry (XRD) acquired from a *PANalytical Empyrean* powder diffractometer using Cu-Kα radiation (λ = 1.541 Å). The crystallite sizes were calculated applying the Scherrer equation on the wide angle reflections. In addition, Raman spectroscopy measurements were recorded on *Senterra* by *Bruker* using a 532 nm laser. The obtained data was analyzed using the predicated software *OPUS*. Microwave plasma-atomic emission spectroscopy (MP-AES) measurements were recorded on a *4210 MP-AES* system by *Agilent Technologies*. Calibration solutions based on the metal chlorides were used to calculate the dopant concentration. The acid digestion of the samples was performed using aqua regia. Nitrogen physisorption experiments were carried

out using a *Quadrasorb* by *Quantachrome Instruments* at $T = 77$ K. Before each measurement, the samples were degassed at 120 °C for 30 h. By using the BET method, the surface area was calculated, while the pore size distributions were determined using a NLDFT approach using the adsorption branch of the isotherm assuming a spherical/cylindrical pore kernel for silica/nitrogen (77.4 K). X-ray photoelectron spectroscopy (XPS) measurements were recorded on a *PHI 5000 VersaProbe II* (Physical Electronics GmbH) using Al Kα line (1486.6 eV) as the X-ray source with a pressure of 10^{-6} Pa in the analysis chamber. The spectra of for all doped mesoporous CeO_2 materials were calibrated to a binding energy of 284.8 eV for the C 1s signal deriving from adventitious hydrocarbon. CasaXPS V2.3.17 was used to evaluate the obtained spectra. For the interpretation of the Ce3d spectra, three linear backgrounds were applied. Infrared (IR) were recorded on IR spectrometer Alpha II by Bruker Optik with an exchangeable DRIFT (diffuse reflectance infrared fourier transformation) module. The samples were investigated using 100 scans and a resolution of 4 cm^{-1}.

Catalytic studies

The determination of the oxygen storage capacity (OSC) was performed using a custom-made fixed-bed flow reactor already described in a previous article.[25] 30 mg of the doped ceria samples were placed in a stainless steel tube supported by quartz wool pads and transferred to a tube furnace. All of the OSC measurements were performed at 430 °C controlled by a thermocouple directly attached to the steel reactor. Using alternating pulses of 10 vol.-% carbon monoxide (CO) and oxygen (O_2) pulses with argon (Ar) as the carrier gas operated by a VICI multiposition valve stream selector with a total flow rate of 20 sccm, the ceria catalysts were reduced and oxidized, respectively. The flow rates were supervised by

MKS 1179B mass flow controllers, while the stream selector allows the time-resolved pulsing of the reducing and oxidizing agent. After passing the OSC reactor, the gas passes a stainless steel filter (2 µm pore size) and reaches the microvolume thermal conductivity detector VICI TCD2 operated with a filament temperature of 150 °C and a pure argon stream at 100 °C as the baseline. The custom-made setup allows to distinguish between the complete (OSCc) and the dynamic oxygen storage capacity (OSC). While the former is achieved by reducing the sample with consecutive 10s CO pulses and then oxidize the catalyst with 2s O_2 pulses, the dynamic OSC is studied by alternating CO (4s) and O_2 pulses (2s). The peak areas of the detected TCD signals for the oxygen pulses are used for calculating the amount of oxygen stored from the material at 430 °C and are normalized on oxygen reference pulses of the same pulse duration. As the mass of the weighed out catalyst is known, the values for OSC and OSCc are expressed as micromole oxygen per gram (µmol(O)/g).

The Deacon reaction measurements were conducted in a home-made fixed-bed flow reactor. The following gases were used in the reaction measurements: HCl 4.5, O_2, 5.0 and Ar 5.0 from AirLiquide, the flow rate of gases was controlled by digital mass flow controllers (MKS Instruments 1179B). Prior to feeding the gas mixture into the reactor, Ar was dried using a water absorption cartridge (ALPHAGAZ^{TM} purifier H_2O-free, AirLiquide). The Deacon reaction activity experiments were carried out under so-called "mild" condition where the argon-balanced reaction feeds contain 20 vol. % O_2 and 10 vol. % HCl. In constrast to the "mild conditions", the Deacon reaction stability experiments were carried out under "harsh" conditions where the argon-balanced reaction feeds contain 10 vol. % O_2 and 25 vol. % HCl. In both cases, the total volumetric flow rate was set to 15 cm^3 STP min^{-1} (sccm). Similar to the OSC measurements, 30 mg of catalyst was supported between two quartz wool wads in the reactor tube. Under the flowing reactant feed, the reactor was

heated to a reaction temperature of 430 °C with a linear rate of 10 K min^{-1}, held for 4 h (activity) and 24 h (stability) and then cooled down to the room temperature in pure argon atmosphere. Using a fiber-optic UV-Vis spectrometer (Ocean Optics USB4000 with a DH-2000-BAL light source) with a Z-shaped flow cell (Teflon®, 50 mm optical path length, FIAlab), the produced chlorine was monitored. The absorbance at a wavelength of λ_{max} = 329 nm (absorption maximum of chlorine) is proportional to the chlorine space time yield (STY) that was calibrated by standard iodometry.

The oxidation of CO experiments was carried out in another home-built fixed-bed flow reactor, which was described already in a previous publication.[13] The design includes a gas supply, the quartz tube reactor heated by a furnace, and analytics for the CO_2 quantification. A gas mixture of 1 vol.-% CO, 20 vol.-% O_2 and 79 vol.-% N_2 (CO Praxair, quality 4.7, O_2 Praxair, quality 5.0 and N_2, Linde) passes the reactor tube with flow rate of 36 cm^3 STP min^{-1} (sccm) controlled by digital mass flow controllers (SevenStar D07-19B). For the catalytic tests, 15 mg of catalyst was supported between two quartz wool wads. The furnace was heated to 430 °C (reaction temperature) with a rate of 20 K min^{-1} and kept till no changes in the conversion rate was observed. The gas composition was monitored online using the X-Stream-CO_2 analyzer (Rosement). The STY of CO_2 was calculated on the basis of the CO_2 concentration in the outlet gas stream.

Results & Discussion

Synthesis and Characterization of the Catalysts

The mesoporous doped CeO_2 powders studied in this work were synthesized using solutions of the corresponding metal salts and the structure directing agent PIB_{50}-*b*-PEO_{45} applying the so-called EISA-process.[33] The inorganic precursor and organic diblock copolymer are merged together in a mixture of ethanol and 2-methoxy-ethanol adding a small

amount of acetic acid lowering the pH value for tailoring the hydrolyzing rate as well as the solubility of the used template. Due to the glass dome, the evaporation of the solvents occurs in a saturated solvent vapor atmosphere. By annealing the obtained powders to 300 °C with a low heating ramp of 0.75 K min^{-1}, the template PIB_{50}-*b*-PEO_{45} decomposes completely as previously demonstrated by thermogravimetric analysis (TGA).[31] In the final heating step at 550 °C, the amorphous oxide was transferred into the desired crystalline phase, while simultaneously the mesoporosity is generated by template removal. The usage of this particular template in combination with the controlled evaporation and annealing steps enables the formation of an ordered 3D array of spherical mesoporous interconnected similarly to inverse-opal structures.

For all the synthesized compounds (CeO_2, 10 at.-% Zr, 10 at.-% Gd, 10 at.-% Pr, 10 at.-% Tb), mesopores of well-defined spherical shape and short-range order are observed in SEM analyses (Figure 2), with pore diameters of 11-12 nm. The slightly smaller apparent mesopore size compared to physisorption analysis and previous studies on mesoporous thin films is ascribed to the determination method using the SEM recordings.[29,31,34–36] Compared to thin films, the powders possess a higher roughness, which makes the mesopores appear

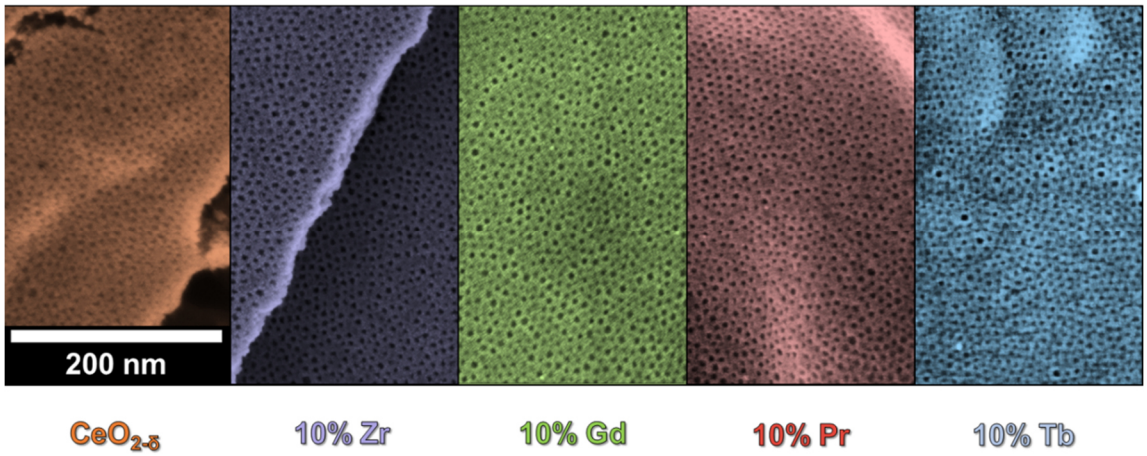

Figure 2: SEM images of the doped mesoporous powders. All of the samples show spherical pores with sizes around 11-12 nm.

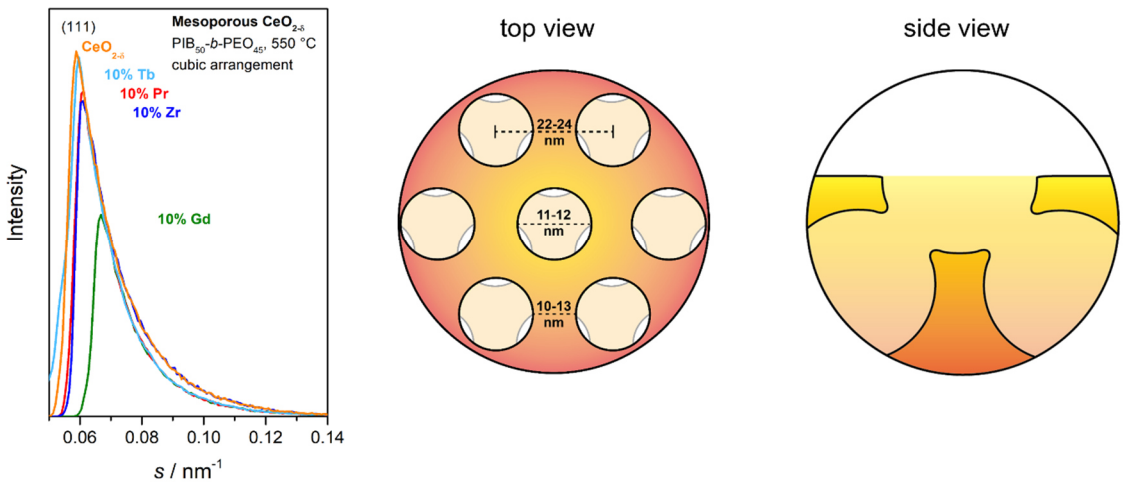

Figure 3: SAXS recordings of the doped mesoporous powders indicating a cubic arrangement of mesopores with a pore-to-pore distance between 22-24 nm (left). In addition, a scheme explaining the correlation between pore size, pore-to-pore distance and pore wall thickness is shown (right).

slightly smaller than the actual pore size. In addition, the pores slightly decrease in size due to the sputter process with platinum. In order to study the atomic ratio of the dopants and Ce, EDX investigations were performed yielding 11 at.-% Zr, 9 at.-% Gd, 12 at.-% Pr as well as 11 at.-% Tb for the corresponding samples.

The mesoporous powder samples were also analyzed using small-angle X-ray scattering (SAXS) (see Figure 3) revealing a broad maximum for all samples. While a direct structure validation is, of course, not possible based on one single SAXS Bragg reflection, this type of SAXS pattern is typical of mesoporous powders being templated by PIB-*b*-PEO-based block copolymers. Based on various previous studies on such mesoporous metal oxides, we interpret the signal as the strong (111) reflection of a cubic arrangement of spherical mesopores. Assuming a cubic arrangement and interpreting the maxima as the (111) Bragg

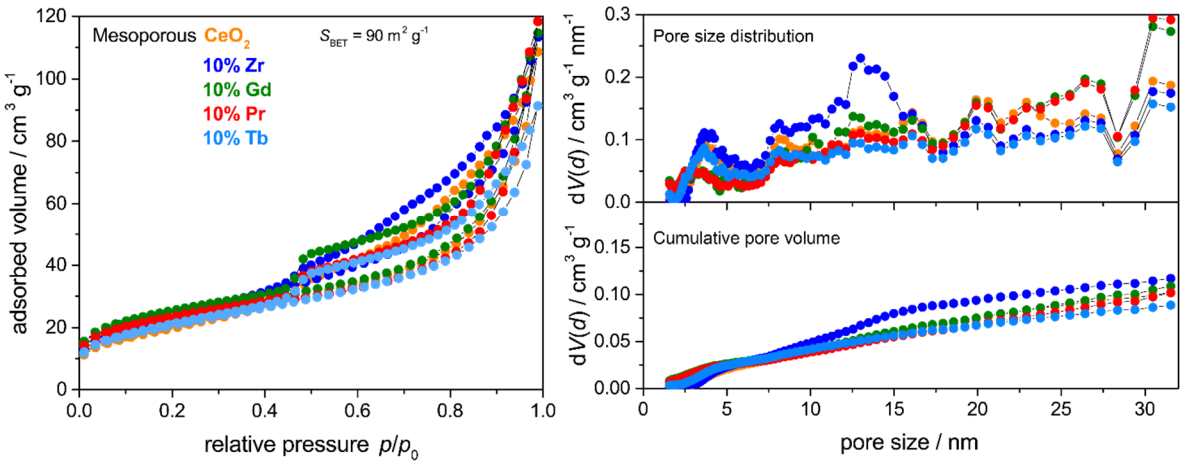

Figure 4: Nitrogen physisorption isotherms (left), the pore size distributions (top right) and cumulative pore volumes (bottom right) of the as-prepared mesoporous doped CeO_2 catalysts.

reflection, the pore-to-pore distance was obtained. Considering the pore diameters being 11-12 nm (SEM) and the pore-to-pore distance determined from SAXS (22-24 nm) yields a wall thicknesses of 10-13 nm (see Figure 3).

The physisorption isotherms are similar for all samples (Figure 4 left), revealing a mesopore volume of ca. 0.1 mL/g, a BET surface area of ca. 90 m^2/g for all materials and an average pore size of approx. 15 nm assuming a spherical pore geometry. The isotherms and the porosity parameters are in agreement with a 3D arrangement of connected spherical mesopores, as typically observed for such kind of block copolymers of the PIB-*b*-PEO-type in previous studies and as supported by the SEM analysis. The isotherms and the pore size distributions do not possess a defined shape as reported for other metal oxide materials in previous studies, which we attribute to two factors. First, in contrast to other studies[37] the mesopore space does not consist of larger spherical mesopores being connected through small meso- or micropores, but the spherical mesopores are better described as a 3D-connected array similar to inverse opals (see Figure 3). This view is supported by the pore size

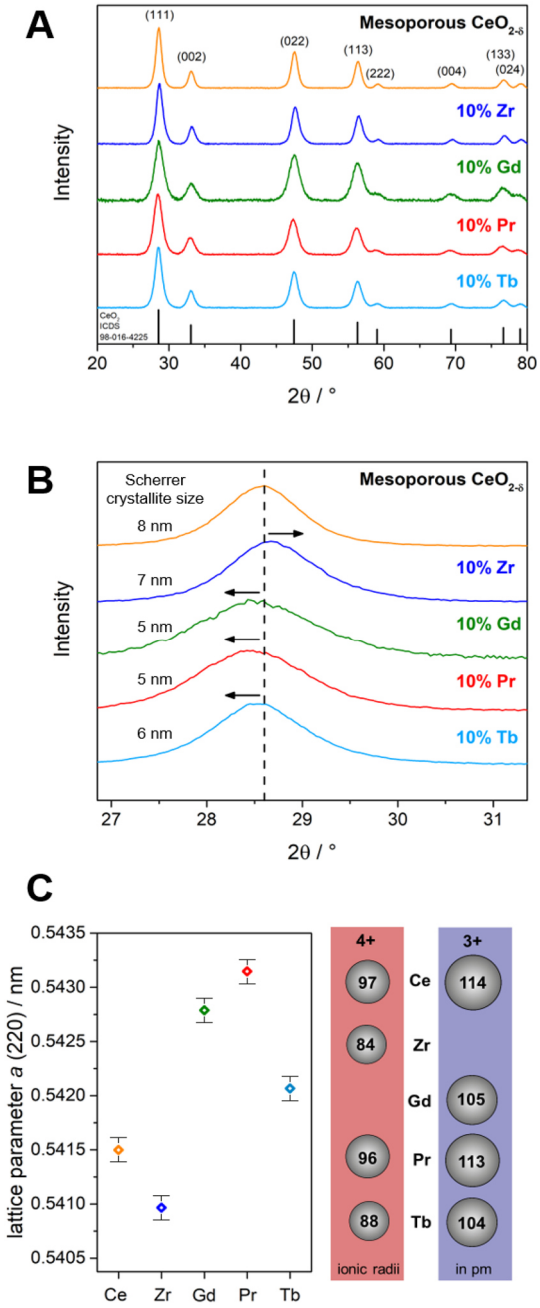

Figure 5: X-ray diffraction patterns of the mesoporous doped CeO_2 materials proving the existing of the cubic structure of CeO_2 (A) but feature a slight 2θ shift (B). By using NaCl as a reference material, the actual lattice parameters of the (220) were calculated (C). All of the ionic radii were taken from Shannon *et al.*[39] assuming that all of the ions are surrounded by of 8 oxygen ions in the CeO_2 crystal lattice. In addition, the obtained crystallite size is displayed in (B) determined by the Scherrer equation.

distributions, which do not show any indication of micropores or small mesopores in larger

amounts. Second, in contrast to SiO_2 the mesopores' shape differ, because the walls consist of crystalline nanoparticles of variable shape. Furthermore, the isotherms are almost identical in shape, which itself speaks for a defined templating and, hence, defined mesopore shape and arrangement. The physisorption and SAXS data are in agreement with each other in that the pore-to-pore distance determined by SAXS (22- 24 nm) fits well to the mesopore size (10 – 20 nm) and the crystallite sizes (wall thickness) of 5 nm – 8 nm. All in all, the different characterization methods are in conformity with a 3D-connected array of spherical mesopores in the as-prepared materials.

The crystal structure of the samples was studied by X-ray diffractometry (Figure 5). All samples exhibit the *Fm*-3*m* cubic structure of CeO_2 with slight 2θ shifts of all reflections, which are assigned to changing lattice constants, indicating the presence of a solid solution and excluding significant phase separation. Using the Scherrer equation[38], the crystallite sizes of the doped materials were calculated (Figure 5B). Despite the identical annealing step, the pure CeO_2 powders have an average crystallite size of 8 nm, while the Gd- and Pr-doped possess crystallites of 5 nm in size. In order to evaluate the shifts and neglect instrumental causes, the doped mesoporous powders were mixed with small amounts of NaCl serving as reference. By normalizing the acquired diffractograms to the (220)-reflection of CeO_2 the exact position of the reflections of doped CeO_2 were determined, in regard to pure CeO_2. It is found (Figure 5B) that for 10 at.-%-Zr CeO_2 the (220) reflection moves to a higher 2θ angle, while in case of 10 at.-%-Gd CeO_2, 10 at.-%-Pr CeO_2 and 10 at.-%-Tb CeO_2 a shift to lower 2θ angles is observed. The reason lies in the different ionic radii of the doped ions, which shrinks the lattice constant when replacing the Ce^{4+} ions (97 pm) by smaller ions such as Zr^{4+} (84 pm).[39] Concomitantly, the lattice constant enlarges when using larger ions such as Gd^{3+} (105 pm). In the case of praseodymium and terbium, both ion species M^{3+} or M^{4+} may be present. In case of Pr and Tb, the observed shifts of the

reflections to smaller 2θ angles point to the presence of Pr^{3+} (113 pm) and Tb^{3+} (104 pm), as the trivalent ions are larger than Ce^{4+} (see Figure 5 C). For praseodymium and terbium, the 3+ oxidation state is surprising, as the Pr^{4+} ion (95 pm) possesses a similar diameter as Ce^{4+} (97 pm) and could thus replace Ce^{4+}. The 3+ oxidation state leads to the formation of oxygen vacancies in order to compensate the charge imbalance. It is well established that the Pr^{4+} ion is not as stable as the Ce^{4+} ion eventuating in the reduction of mixed CePr-oxides when the oxygen partial pressure is below that in ambient air.[40] As our synthesis protocol uses a vacuum furnace to evaporate the remaining solvent, the prevailing reduced pressure induces the formation of Pr^{3+} ions, and similarly the incorporation of Tb^{3+} instead of Tb^{4+} can be explained. Thus, although the mesoporous powders are annealed up to 550 °C in the last step of the synthesis, Tb^{3+} and Pr^{3+} are not oxidized. This contradicts the findings of Li *et al.*[41] who prepared $Ce_{0.8}Pr_{0.2}O_{2-\delta}$ via a citric acid assisted sol-gel method and showed that the lattice constant only differed slightly from pure ceria concluding the presence of Pr^{4+} instead of Pr^{3+}. However, the difference between their and our samples lies in the porous structure and the different annealing temperatures (550 °C vs. 1000 °C). The latter may allow Pr^{3+} to completely reoxidize to Pr^{4+} ions, but our study uses a significantly lower temperature. Furthermore, Trovarelli *et al.* also experimentally confirmed the existence of Tb^{3+} and Pr^{3+} in doped CeO_2 samples based on the value of the fourth ionization potential dictating the ranking of stability of the +4 oxidation state (Ce > Pr > Tb).[14]

The mesoporous samples were investigated using Raman spectroscopy to elucidate the defects and determine the presence of possible phase-separated compounds (Pr_2O_3) (see Figure 5). The F_{2g} vibrational mode at around 465 cm^{-1}, which is typical for the cubic CeO_2 structure, was observed for every doped CeO_2 sample, thus being in agreement with the XRD analysis. The band shows a red shift indicating that a solid solution of the dopant with

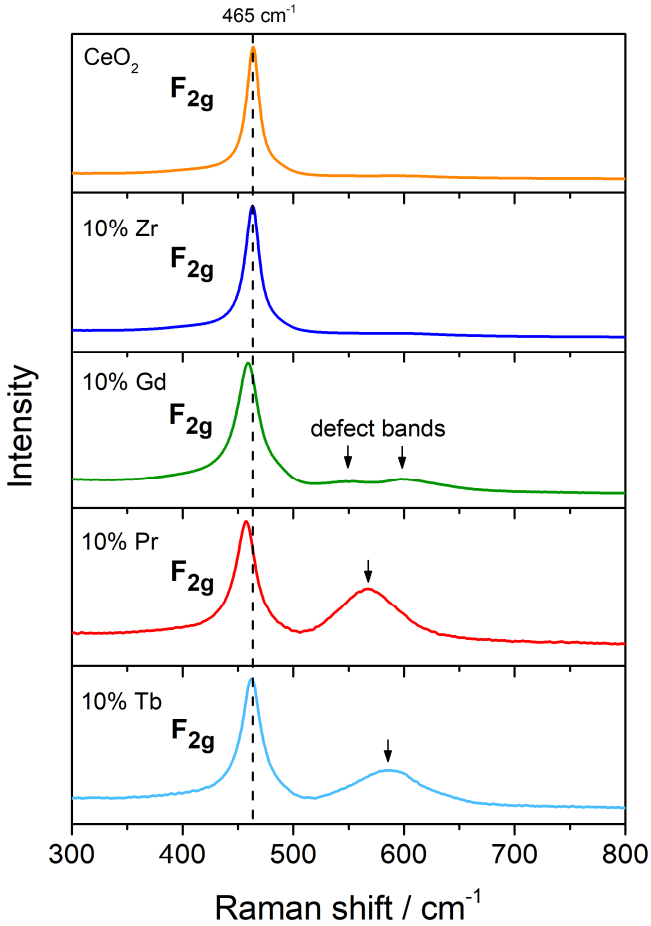

Figure 6: Raman spectra of the doped mesoporous CeO_2 powders. In all cases the vibrational F_{2g} mode is observed with a slight red shift. Additionally, for the Gd-, Pr- and Tb-doped samples, defect bands are detected.

the ceria is formed. Additionally, the Raman spectra of the Gd-, Pr- and Tb-doped ceria feature defect bands between 560 and 600 cm^{-1}. As explained by Guo *et al.*[42], the band at 580 cm^{-1} for Tb-doped ceria derives from the different oxidation state of the doped ion and is therefore directly related to the oxygen vacancy formation. This interpretation can also be applied to the defect mode at 560 cm^{-1} of the Pr-doped ceria. In the case of the Gd-doped samples, two defect bands are observed at 540 and 595 cm^{-1}. While the latter follows the same explanation as for the Pr- and Tb-doped samples, the former is explained to be a

second-order Raman mode of oxygen vacancies also observed by incorporating other trivalent ions such as Sm^{3+} or Eu^{3+}.[43] In order to determine the intrinsic defect sites, literature[41,44] suggests to compare the relative intensity of the defect D band at around 560 cm^{-1} with the F_{2G} band. In our case (see Figure S2), Pr-CeO_2 shows the highest amount of intrinsic defect sites and thus, oxygen vacancies, followed by Tb-, Gd-, Zr- and undoped CeO_2. However, the so-gained data has to be taken carefully, as this approach assumes that the defect band solely is effected by defect sites in the form of oxygen vacancies. Next to defect bands caused by the presence of oxygen vacancies, the M+-O band also exists near this area as observed for the Gd-doped sample. When comparing the same dopant with different concentration, the relative ratio of the two peaks is easily correlated to the dopant concentration, but the interpretation is impeded when comparing samples containing different dopant species. Here, the results correspond well to the XRD data indicating the presence of Pr and Tb in its 3+ oxidation state introducing charge compensating oxygen vacancies in the ceria lattice.

Next to the Raman spectroscopy, the CeO_2 samples were additionally investigated by FT-IR (see Figure S2), which show the absence of C-O and C-H vibrational modes indicating the complete decomposition of the used polymeric template for all samples. In all cases, the Ce-O vibrational mode[45] was present in the region between 850 – 500 cm^{-1} with no significant differences between each other. Only the intensity of the bands at around 3000 cm^{-1} and 1640 cm^{-1} differ in their intensity, which is assigned to the amount of water adsorbed on the surface due to the storage of the samples under ambient conditions.

Lastly, the dopant concentration as well as the Ce^{3+}/Ce^{4+} ratio was determined by using XPS (see Figure S1). The survey spectra feature the spectral band of Ce, O, C and Zr, Gd, Pr and Tb, respectively. The carbon signal most likely originates from contamination of the nanostructures while exposed to ambient air. In order to quantify the doped samples, the

Ce4d spectra were integrated and compared to the integral area of Zr4d, Gd4d and Tb4d while incorporating the relative sensitivity factors (RSF) for each compound into the calculations. These bands were picked as suitable as they are detected at similar low binding energies (120 – 200 eV) neglecting effects like loss of kinetic energy due to a higher penetration depth (see Figure S1). Hence, the observed signals derive from a similar depth of the nanostructure. In the case of Pr4d and Ce4d, the bands interfere with each other and are not separated properly. For this reason, we chose the Pr3d band at around 940 eV and collate it to Ce3d at 900 eV. The results are shown together with the EDS analyses in Table 1. The obtained values are nearly identical despite the fact that XPS only possess a penetration depth of around 5 nm and EDS covers more than 100 nm. The MP-AES results are based on the decomposition of the structure in solution using aqua regia and thus, includes the total dopant concentration in the CeO_2 sample, which is not limited to a local spot (EDS) or the surface (XPS). The data from the MP-AES differ slightly from the EDS and XPS data beside the Zr-doped sample and speak for the enrichment of the dopants in the bulk and not the surface. For the catalytic investigations, the present concentration of Zr, Gd, Pr and Tb on the surface is decisive as the dopants are directly involved in the oxidation reaction with the gaseous reactants.

Table 1: Comparison of the dopant amount in atomic percentage of the doped mesoporous CeO_2 samples measured by MP-AES, calculated by XPS, and detected by EDS.

Sample	**10%-Zr**	**10%-Gd**	**10%-Pr**	**10%-Tb**
MP-AES: M^{x+} / at.-%	10±1	15±1	13±1	13±1
XPS: M^{x+} / at.-%	10±1	9±1	11±1	12±1
EDS: M^{x+} / at.-%	11±2	9±3	12±2	11±3

The Ce^{3+} concentration is calculated by using the Ce3d line.[46–48] There are many published articles proposing strategies to distinguish between the contribution of CeO_2 and the

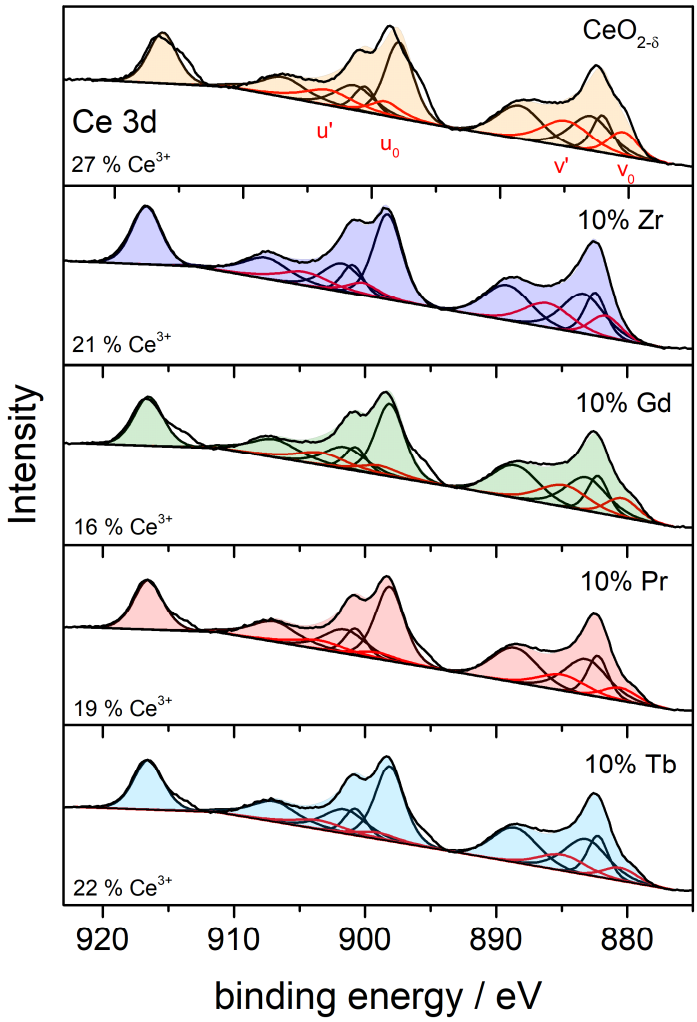

Figure 7: XPS Ce3d spectra of the doped mesoporous CeO_2 powders to calculate the ratio of Ce^{3+} and Ce^{4+}. The corresponding bands for Ce^{3+} are depicted in red.

reduced form (Ce_2O_3) involving the use of linear combination of reference spectra of pure CeO_2 and Ce_2O_3 which we obtained for ultra-thin films on Ru(0001) single crystal.[49] Hence, we fitted the bands of the Ce3d utilizing these reference spectra and differentiated the pure CeO_2 doublet signals (u, u'', u''' and v, v'', v''') and two Ce_2O_3 doublets (u_0, u' and v_0, v') (see Figure 7). The high number of signals derives from the interaction of CeO_2 upon radiation, which was intensively described by Romeo et al..[50] The 10 lines are composed of five spin-orbit split pairs with a splitting of 18.5 eV between the corresponding u and v denoted peak. The $3d_{5/2}$ lines are labeled as v_0, v, v', v'', and v''', and the spin-orbit split of the $3d_{3/2}$ lines as u_0, u, u', u'', and u'''. As every sample was investigated under the

same experimental conditions, the undoped and doped CeO_2 materials are assumed to experience the same degree of reduction upon radiation. We also considered the approach by Skála *et al.*[51], describing the asymmetric shape of u and v by modelling it using two symmetric peaks. By applying this model, we calculated the highest Ce^{3+} concentration with 27 % for the pure CeO_2 samples followed by the Tb-doped (22 %) and Zr-doped (21 %) mesoporous powders. However, one has to consider that the condition of the XPS analyses does not correctly reflect the condition in the following catalytic investigations. The visible shoulders in the Ce3d spectra derive from the usage of a stainless steel holder resulting into charge effects and shifting the peaks around 2-3 eV. They were not considered in the calculations of the Ce^{3+} concentration.

To conclude, the thorough characterization of mesoporous doped CeO_2 powders enables to study the influence of the dopants on the dynamic and complete oxygen storage capacity (OSC/OSCc) as well as the catalytic behavior in the HCl oxidation.

Dynamic and Total Oxygen Storage Capacity (OSC, OSCc)

The OSC of a ceria material is often related to the catalytic activity in oxidations reactions. Here, we investigated the OSC by using CO as the reducing and oxygen as the oxidizing agent. In the following, we distinguish between the total (OSCc) and the dynamic oxygen storage capacity (OSC), which were both performed at 430 °C being the same temperature as used for the HCl and CO oxidation. The OSCc is obtained by applying 10 vol.-%-CO pulses to the material until a maximum of reduction is achieved. Afterwards, 10

vol.-%-O_2 pulses reoxidize the sample giving the amount of oxygen which is needed for maximum oxidation the sample from the reduced state (Figure 8). Furthermore, using the

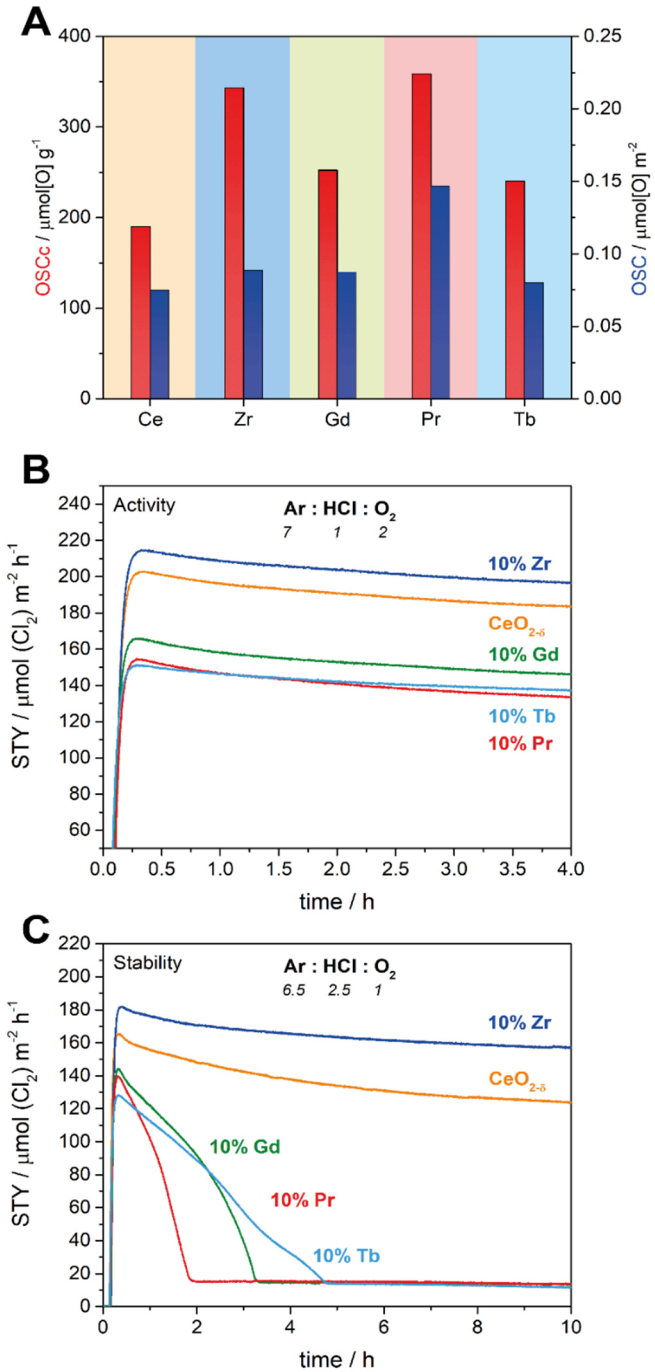

Figure 8: Results of the doped ceria mesoporous powders in regards to the total and dynamic oxygen storage capacity (A) and the HCl oxidation with mild (B) and harsh conditions (C) at 430 °C as a function of the time on stream.

same setup, the sample is reduced and oxidized alternately by pulsing CO and O_2. The so-

obtained dynamic OSC may have more relevance for the actual catalytic reaction, as the sample never reaches a completely reduced state and only includes the most reactive oxygen species in the ceria lattice. The usage of well-defined, ordered mesoporous materials for such studies and comparison is advantageous, because the mesopore size is large and the pore network so extended that it is justified to assume unhindered transport of the involved gases through the pore space, i.e. the diffusion through the pore space can be excluded as rate-limiting factor.

In Figure 8, the measured OSC(c) data for the doped mesoporous ceria samples are compiled. All of the measurements were performed two times for each type of material, to validate the reproducibility of the OSC(c) measurements. It is observed that each dopant enhances the total as well as the dynamic oxygen storage capacity, but to a quite different extent. The integration of only 10 at.-%-Zr leads to a higher complete (OSCc) as well as dynamic OSC, which is in agreement with previous studies.[13,18,52,53] The incorporation of Gd^{3+} increases both, the OSC and OSCc. The moderate increase in the OSC by only ca. 10% compared to the analogue mesoporous cerium oxide sample confirms our previous study on doped electrospun nanofibers.[25] However, these results on Gd-doped CeO_2 nanomaterials are generally surprising, as Gd^{3+} is not redox-active and substitutes redox-active Ce^{4+} in the ceria lattice, which, at first glance, should decrease the oxygen storage capacity compared to pure CeO_2, especially the OSCc value. This enhancement in the OSC and OSCc in Gd-doped CeO_2 cannot be explained by possibly different surfaces areas, as the BET surfaces are practically identical for all materials. We believe these findings are attributed to the experimental conditions in our OSC measurements. The chosen analysis temperature of 430 °C is not high enough to substantially reduce bulk oxygen which usually starts above 600 °C.[54–56] Thus, the here measured OSCc values – similar to the OSC – rather correspond to the surface and bulk mobile oxygen vacancies at the given temperature.

The values of the OSC(c) are influenced by several different factors. In the case of the total OSC, the measured uptake of oxygen by the catalyst is determined by the available surface oxygen and the mobile oxygen bulk species at a given temperature (here 430 °C).[12] Thus, the OSC value is controlled by the oxygen vacancy formation and the oxygen migration activation energy dictating the mobility of bulk oxygen migrating to the ceria surface. In addition, morphological factors such as the particle size[57] and the BET surface area influence the OSC value. In a recent study, we showed that with increasing particle size in the range from 5 – 12 nm an enhancement of the OSCc at 430 °C occurred, which was explained by the lowered oxygen vacancy formation energy with rising particle size.[57] However, in the present case the surface areas and the particle sizes are quite similar, excluding a significant impact of these particles.

In the case of trivalent ions like Gd^{3+}, the transport of oxygen to the particle surface is increased by an increasing number of oxygen vacancies.[58] In essence, the incorporation of Gd into mesoporous CeO_2 results in an increase in the OSC(c) at the given temperature of 430 °C, which can be attributed to the enhanced mobility of oxygen species, allowing to reduce and oxidize a greater part of the ceria material. This interpretation is supported by Anirban *et al.*[59] having calculated an activation energy of 0.86 eV for the transport/conductivity in nanocrystalline 20 at.-% Gd-doped CeO_2 which is significantly lower than the one of pure CeO_2 (1.0 eV).[60] Thus, their results confirm the enhanced mobility of oxygen of ceria containing a trivalent ion. In addition, our experimental findings are in good agreement with those of Veranitisagul *et al.*[61] and Guo *et al.*.[54] The latter reported the doping of CeO_2 with Nd facilitating the diffusion of bulk oxygen to the surface and therefore increasing also the OSCc value. While the same is applicable for Gd^{3+}, increasing the reaction temperature above 600 °C, at which the reduction of bulk oxygen takes place, would most likely lead to a smaller OSCc value compared to pure CeO_2.

By contrast, the incorporation of isovalent Zr^{4+} ions reduces the oxygen vacancy formation energy given by the reported increased strain-related reducibility, being a thermodynamic parameter, which however also affects the ionic transport.[11,62] The OSC(c) values of the Tb-doped are quite similar to the Gd-doped ones, while the OSCc is larger than pure CeO_2. Although Tb can – in contrast to Gd – potentially switch between its 3+ and 4+ oxidation state, the similarity in the OSC(c) values suggests Tb^{4+} is not present in our materials and occurs only in the 3+ state. This finding is in good agreement with the XRD results (see Figure 5) showing a larger lattice parameter for the Tb-doped CeO_2 mesoporous material due to the presence of Tb^{3+} ions being larger than Ce^{4+} ions. This also pertains to the existence of more oxygen vacancies than in the undoped CeO_2 system fitting to the results obtained from Raman spectra and the observed defect bands (see Figure 6).

Lastly, Pr-doped mesoporous CeO_2 reveals the highest OSC(c) among the doped samples. Not only does the incorporation of Pr raise the OSCc value, but also the dynamic OSC by the double amount of oxygen stored per square meter. In contrast to the Tb-doped sample, Pr changes its oxidation state between 3+ and 4+ during the redox cycle increasing the amount of stored and released oxygen. These results show that the amount of reversible oxygen vacancies in Pr-doped CeO_2 is increased in comparison with the other doped CeO_2 samples, consistent with the Raman findings (see Figure 6). Furthermore, the results are in good agreement with other studies

investigating redox properties of Pr-doped CeO_2. Ahn *et al.*[63] showed by H_2 temperature-programmed reduction experiments that the incorporation of Pr in the ceria lattice promotes the bulk reduction of the materials even at lower temperatures. The authors explain this phenomenon by the increased oxygen vacancy concentration as well as by the formation of an ordered arrangement of the existing vacancies facilitating the oxygen mobility. In addition, our findings also match the results of Trovarelli[64] revealing the bulk reduction of Pr-

and Tb-doped CeO_2 to occur at lower temperatures compared to undoped CeO_2. In combination with our experimental findings, the usage of multivalent ion such as Pr tailors both the amount of oxygen vacancies and the oxygen mobility in the system and thus enhances the total oxygen storage capacity at the given temperature.

Catalytic Performance Tests

HCl oxidation reactions were carried out on mesoporous powders in order to elucidate the relationship between the catalytic performance, stability and OSC/OSCc (Figure 8). Such experiments were performed under mild ($HCl:O_2$ = 1:2, Fig. 7 B) and harsh ($HCl:O_2$ = 2.5:1, Fig. 7 C) conditions. Substantial differences are observed in the STY between these two reaction conditions, as a function of the time on stream and normalized on the specific surface area (see Table 2). For the mild conditions, all of the samples exhibit a moderate, but continuous decay in the STY. In case of the doped ceria samples the HCl oxidation performed under harsh conditions (Figure 8 C) shows significantly more drastic changes in the STY over time, dropping to almost zero for the Pr-, Gd- and Tb-doped sample within a few hours. Moreover, the conversion rate of HCl to Cl_2 decreases fastest for Pr-doped ceria followed by the Gd- and Tb-doped sample, whereas the pure ceria sample and the Zr-doped catalyst remain stable even beyond a 10 hours' exposure time.

First, these comparative results demonstrate that a relatively high OSC(c) value, as for the Pr-containing material, does not necessarily correlate to a high activity in an oxidation reaction, if compared with the other materials of identical morphology. Second, the marked decay in the STY of the Pr-, Gd- and Tb-doped sample indicates pronounced chemical alterations, which were addressed by XRD analysis on the used materials. After applying the harsh HCl oxidation several additional XRD reflections (see Figure 9) are observed for the Gd-, Pr- and Tb-doped ceria materials which are assigned to $CeCl_3$ x H_2O in all cases.

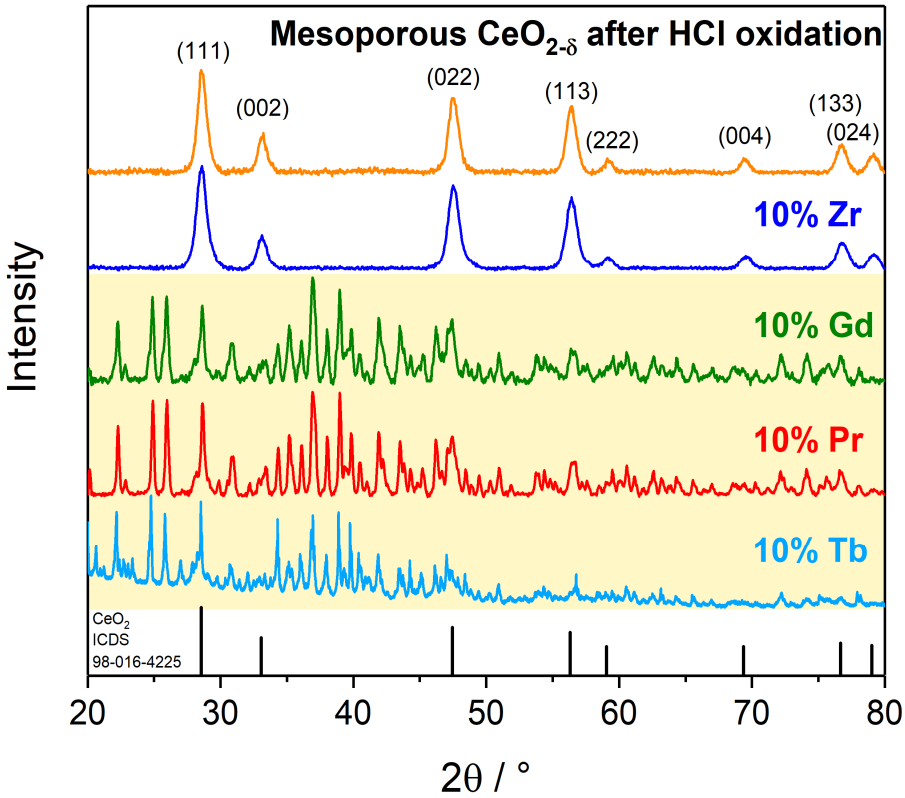

Figure 9: X-ray diffraction patterns of the mesoporous doped CeO_2 materials upon the harsh HCl oxidation. Additionally, the reference pattern of cubic CeO_2 (ICDS 98-016-4225) is displayed.

According to the results of Rietveld refinement (see Figure S5), no other crystalline metal chloride ($GdCl_3$, $PrCl_3$ or $TbCl_3$) is present. The content of $CeCl_3$ is 87 wt.-% and 91 wt.-% for the Pr-doped and Tb-doped sample, respectively, and the rest of the material consists of pure CeO_2.

In order to study the impact of oxidative catalytic reactions on the mesoscopic structure, the doped samples were investigated after the HCl (harsh and mild) oxidation reactions (Figure 9). The defined mesopores were clearly visible using SEM before the catalytic

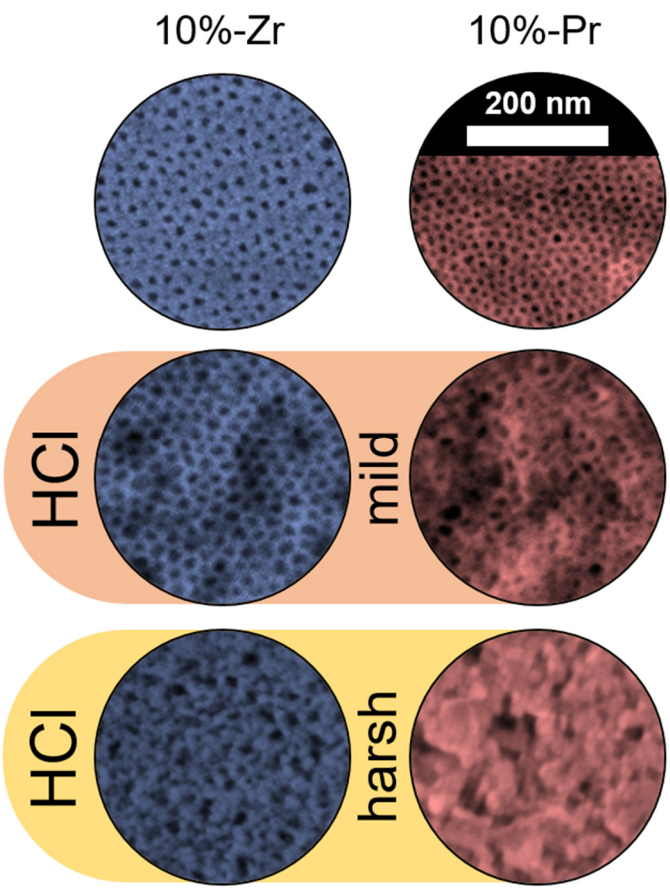

Figure 10: SEM images of the Zr- and Pr-doped mesoporous CeO_2 before (first row) and after and HCl oxidation. The latter was performed using mild (second row) and harsh conditions (third row).

studies. While the Zr-doped mesoporous material still depicts the defined shape and arrangement of 13 nm-sized-mesopores, the Pr-doped mesoporous powder exhibits a pronounced deformation of the porous structure even after applying the mild reaction condition. Upon harsh reaction conditions, the ordered mesoporous structure degrades to bigger agglomerated particles being consistent with $CeCl_3$ x H_2O observed in the XRD pattern (see Figure 9).

Although the SEM images taken after mild and harsh treatment in the HCl oxidation imply that these catalytic conditions affect the porous structures negatively, these alterations might also partially be due to the heat treatment itself. To disentangle the impact of

the catalytic reaction from the heat treatment all of the doped materials were used in a CO oxidation reaction at 430 °C which thus resembles the OSC(c) measurements. SEM reveals an unchanged mesoporous structures for all materials (see Figure S7). Hence, the changes visible in SEM after the HCl oxidation solely originate from chemical corrosion by HCl and Cl_2.

These results are supported by nitrogen physisorption. As shown in Table 2, the high specific surface area of the pristine Pr- and Tb-doped ceria samples shrinks to 15 and 8 m^2 g^{-1}, respectively, while the chlorinated Gd-doped catalyst indicated a surface area of less than 1 m^2 g^{-1}. However, the decrease in the BET-surface area and the accompanied decrease in pore volume are also observed for the pure ceria and 10%-Zr doped sample, despite the absence of $CeCl_3$ formation (XRD analysis). These observations primarily indicate the disruption of the mesopore space for the Gd-, Pr- and Tb-doped materials. The mesoscopic alterations observed by SEM and physisorption correlate to the transformation of the CeO_2 materials into $CeCl_3xH_2O$ and even in-depth chlorination as observed by XRD. $CeCl_3$ x H_2O grows unhindered into large crystals, and in particular the entire CeO_2-based framework (pore walls) is involved, indicated by the sharp $CeCl_3$ x H_2O XRD reflections. By contrast, in case of the Zr- and undoped CeO_2 sample the ordered mesostructure is persistent. The preservation of the porous structure via SEM combined with the changes in pore volume by nitrogen physisorption measurements indicate that only a fraction of the material, e.g. the mesopore surface, surface gets chlorinated reducing the accessible surface area during the Deacon process, yet without affecting the catalytic performance. In addition, Table 2 reveals the highest structural stability against HCl/Cl_2 for the Zr-doped samples, as the pore volume decreases least of all and the mesopores maintained, still possessing an average diameter of around 14 nm in diameter (see Figure S6)), while a certain

deformation is certainly present (see Figure 10). This structural persistence correlates well with the stability of the STY in the HCl oxidation.

Table 2: N_2-physisorption investigations of the mesoporous doped ceria including the BET-surface area and the porous volume before and after the harsh HCl oxidation.

Sample	**$CeO_{2-\delta}$**	**10%-Zr**	**10%-Gd**	**10%-Pr**	**10%-Tb**
BET, as-prepared / $m^2\ g^{-1}$	90±5	92±5	88±5	91±5	86±5
BET, after HCl oxidation / $m^2\ g^{-1}$	28±5	32±5	---	14±5	8±5
Pore volume, as-prepared / $cm^3\ g^{-1}$	0.10	0.16	0.10	0.10	0.10
Pore volume, after HCl oxidation / $cm^3\ g^{-1}$	0.04	0.1	---	0.03	0.01
Pore volume loss	65%	39%	---	70%	89%

In order to interpret the quite different impact of the dopants on the catalytic and, concomitantly, the structural stability, the differences on the level of the oxygen vacancies need to be discussed. Our results clearly show that for Gd-, Pr- and Tb-doped ceria catalysts the decay in both types of stability is most pronounced, and in these materials the ions exist in the 3+ oxidation state, which imposes the presence of a correspondingly large concentration of oxygen vacancies. Hence, the pronounced chloride formation is related to the O- and Cl-species entering oxygen vacancies at the surface.[65] As these vacancies are required in the HCl oxidation for producing the final product Cl_2, the occupancy of chlorine atoms in these vacancies is an important process occurring at the surface, to occasionate the desorption of Cl_2. If, however, chlorine species diffuse into sublayers, mediated by a pronounced number of oxygen vacancies, irreversible formation and growth of $CeCl_3$ occurs. Our experiments cannot clarify if the crystallization of $CeCl_3$ proceeds as nucleation/growth process at the surface or if indeed the entire particles are transformed. The interpretation that the oxygen

vacancies are a decisive parameter is supported by our experiments showing that this process occurs for the Gd-, Pr- and Tb-doped ceria catalyst, but was prevented when using Zr as the dopant (see Figure 11). As doping ceria with Zr reduces the oxygen vacancies formation energy, but does not provide oxygen vacancies directly, the chlorination of the bulk is prohibited. In the other cases, the higher amount of extrinsic oxygen vacancies induced by trivalent ions promotes a higher oxygen diffusion, but also allows the chlorine species to reach the bulk and subsequently lead to the formation of $CeCl_3$, which is inactive in the catalytic reaction.

Lastly, Pr-doped CeO_2 provides both, high ionic mobility and high amount of oxygen

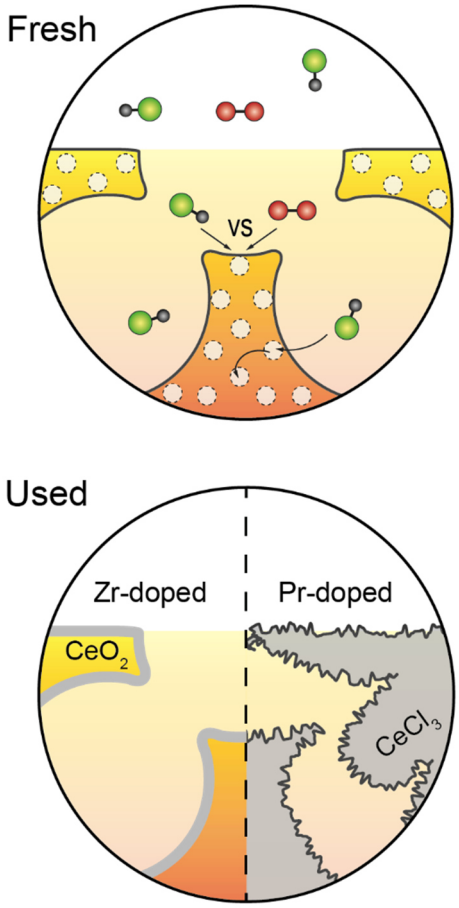

Figure 41: Schematic illustration of the $CeCl_3$ formation in the Zr- and Pr-doped mesoporous CeO_2 during the harsh conditions of the HCl oxidation.

vacancies as reflected by the high OSC values. The comparably fast degradation of the

catalytic activity in the HCl oxidation compared to the other tested doped materials can thus be qualitatively correlated to the larger number of oxygen vacancies as observed by large OSC(c) values. In good agreement with the explanation for the higher OSC(c), the material replenishes quickly the oxygen vacancies on the surface, and also shows enhanced transport oxygen ions compared to CeO_2 and Zr-doped CeO_2. We speculate that this also seems to apply for chlorine thus spurring the chlorination process of the material thus, showing the lowest stability of the investigated materials. Therefore, we can conclude that a higher amount of irreversible extrinsic oxygen vacancies is detrimental for keeping stable activity in the HCl oxidation and thus, tailoring the oxygen vacancy formation energy is decisive for preparing the most stable and active model catalyst in the Deacon process.

Conclusions

This study was devoted to shed more light into the relationship between the oxygen storage capacity, catalytic performance in an oxidation reaction and the stability under harsh conditions as in the Deacon reaction (HCl oxidation). Many catalytic investigations in the literature assign the catalytic properties of ceria-based materials to the oxygen storage capacity. By choosing an appropriate model system in the form of mesoporous CeO_2 powders with a 3D network of defined mesopores, we tailored the type and amount of oxygen vacancies by incorporating Gd^{3+}, Zr^{4+}, $Pr^{3+/4+}$ and $Tb^{3+/4+}$ dopants. All mesoporous samples feature an identical, 3D network of ordered mesopore of uniform size and shape, which provides the central conceptual methodology of this study. In particular, the size of the mesopores (ca. 13 – 15 nm) and the absence of a significant amount of micropores assure that the transport hindrance of educt molecules to active sites can be neglected when comparing the reactivities of the differently doped materials. Hence, these mesoporous powders allow for a reliable and meaningful relation of composition, and hence the impact of oxygen

vacancies, with the stability and activity in the HCl oxidation reaction. We find the relationship between the dynamic and total OSC and the catalytic stability depends strongly on the induced type of oxygen vacancies (see Zr^{4+} vs. Pr^{3+}, Tb^{3+}) as well as on the mechanism of the investigated reaction, in this case the HCl oxidation reaction. In general, the OSC/OSCc depends on the oxygen vacancy formation energy as well as the amount of oxygen vacancies and oxygen migration to the surface. These parameters were enhanced by the addition of trivalent ions. While Pr and Tb exist in the 3+ oxidation state as shown by XRD, in-depth chlorination was observed. Hence, despite the high OSC(c) of the Pr-doped sample, a high accessible amount of oxygen vacancies for chlorine results in inactivation of the catalyst, and hence the space-time yield drops to almost zero within a few hours on stream. By contrast, mesoporous CeO_2 without any additional dopant is quite stable in the Deacon reaction, probably because the concentration of oxygen vacancies is comparably small. A recent study on thin cerium oxide films showed that Cl species can occupy oxygen vacancies on the surface, which is possibly decisive for the formation of $CeCl_3$ and thus the deactivation of the catalyst.[47] A study using Prompt Gamma Activation Analysis (PGAA) on CeO_2 powder revealed that chlorine can enter the bulk structure under oxidizing conditions occupying the O-vacancy positions, without the formation of crystalline hydrated $CeCl_3$.[26,66] Li *et al.* found surprisingly high concentration of chlorine within CeO_2 nanorods upon HCl oxidation without affecting the stability of the rods.[67] Our study is in line with these previous works, but furthermore suggests that the Cl species can occupy oxygen vacancies at least on the surface. We speculate that a high concentration of oxygen vacancies may even allow Cl to diffuse at least into sub-surface parts of the materials, perhaps even into the bulk material leading to the formation of $CeCl_3$ thereby deactivating the catalyst. Further studies are needed to clarify how deep chlorine is able to penetrate into

CeO_2 and thus to determine the crystallization mechanism of hydrated $CeCl_3$ in the Deacon reaction.

All in all, our study confirms that increasing the stability of CeO_2 can be achieved by the usage of Zr^{4+} as the dopant, providing a better reducibility of ceria without introducing charge-compensating and oxygen vacancies increasing the mobility for the Cl species in the bulk. As our model system based on mesoporous powders with defined 3D-connected spherical pores allowed to study the morphology changes efficiently after the harsh condition of the HCl oxidation using SEM and nitrogen physisorption, further research will be conducted on $Ce_xZr_{1-x}O_2$ mesoporous structures in order to further address the interplay between composition, reactivity and stability for one dopant.

ASSOCIATED CONTENT

Supporting Information

The following files are available free of charge.

X-ray photoelectron spectroscopy of the as-prepared doped mesoporous CeO_2 powders; X-ray diffraction (XRD) patterns of the mesoporous CeO_2 samples after the HCl oxidation under mild conditions; Rietveld refinement of the mesoporous CeO_2 samples after the HCl oxidation under harsh conditions; nitrogen physisorption measurements of the as-prepared doped CeO_2 samples and after the harsh conditions of the HCl oxidation; DRIFT measurement of the doped CeO_2 samples; Analyses of the D/F_{2G}-ratio based on the Raman spectra;

AUTHOR INFORMATION

Corresponding Author

*(B.S.) E-mail: bernd.smarsly@phys.chemie.uni-giessen.de

*(H.O.) E-mail: herbert.over@phys.chemie.uni-giessen.de

Author Contributions

The manuscript was written through contributions of all authors. All authors have given approval to the final version of the manuscript.

Notes

The authors declare no competing financial interest.

ACKNOWLEDGMENT

The authors thank Tim Weber for the XPS measurements and Christian Sack for the help on the XPS analyses. The authors would also like to thank Sebastian Werner, Kevin Turke and Felix Badaczewski for the nitrogen physisorption measurements. The authors thank Bernhard Spengler for the ability to perform MP-AES measurements. I. Dj. acknowledges the support by the Croatian Science Foundation under the project number PZS-2019-02 2467.

REFERENCES

(1) Amrute, A. P.; Mondelli, C.; Moser, M.; Novell-Leruth, G.; López, N.; Rosenthal, D.; Farra, R.; Schuster, M. E.; Teschner, D.; Schmidt, T.; Pérez-Ramírez, J. Performance, Structure, and Mechanism of CeO_2 in HCl Oxidation to Cl_2. *J. Catal.* **2012**, *286*, 287–297.

(2) Moser, M.; Mondelli, C.; Amrute, A. P.; Tazawa, A.; Teschner, D.; Schuster, M. E.; Klein-Hoffman, A.; López, N.; Schmidt, T.; Pérez-Ramírez, J. HCl Oxidation on IrO_2-Based Catalysts: From Fundamentals to Scale-Up. *ACS Catal.* **2013**, *3* (12), 2813–2822.

(3) Capdevila-Cortada, M.; Vilé, G.; Teschner, D.; Pérez-Ramírez, J.; López, N. Reactivity Descriptors for Ceria in Catalysis. *Appl. Catal. B Environ.* **2015**, *197*, 299–312.

(4) Trovarelli, A.; de Leitenburg, C.; Boaro, M.; Dolcetti, G. The Utilization of Ceria in Industrial Catalysis. *Catal. Today* **1999**, *50* (2), 353–367.

(5) Filtschew, A.; Hofmann, K.; Hess, C. Ceria and Its Defect Structure: New Insights from a Combined Spectroscopic Approach. *J. Phys. Chem. C* **2016**, *120* (12), 6694–6703.

(6) Trovarelli, A.; Llorca, J. Ceria Catalysts at Nanoscale: How Do Crystal Shapes Shape Catalysis? *ACS Catalysis*, **2017**, *7* (7), 4716–4735.

(7) Sun, C.; Li, H.; Chen, L. Nanostructured Ceria-Based Materials: Synthesis, Properties, and Applications. *Energy Environ. Sci.* **2012**, *5* (9), 8475-8505.

(8) Coduri, M.; Scavini, M.; Brunelli, M.; Pedrazzin, E.; Masala, P. Structural Characterization of Tb- and Pr-Doped Ceria. *Solid State Ionics* **2014**, *268* (Part A), 150–155.

(9) Mendiuk, O.; Nawrocki, M.; Kepinski, L. The Synthesis of $Ce_{1-x}Ln_xO_{2-y}$ (Ln=Pr, Sm, Gd, Tb) Nanocubes by Hydrothermal Methods. *Ceram. Int.* **2016**, *42* (1), 1998–2012.

(10) Yang, N.; Orgiani, P.; Di Bartolomeo, E.; Foglietti, V.; Torelli, P.; Ievlev, A. V.; Rossi, G.; Licoccia, S.; Balestrino, G.; Kalinin, S. V.; Aruta, C. Effects of Dopant Ionic Radius on Cerium Reduction in Epitaxial Cerium Oxide Thin Films. *J. Phys. Chem. C* **2017**, *121* (16), 8841–8849.

(11) Wang, H.-F.; Li, H.-Y.; Gong, X.-Q.; Guo, Y.-L.; Lu, G.-Z.; Hu, P. Oxygen Vacancy Formation in CeO_2 and $Ce_{1-x}Zr_xO_2$ Solid Solutions: Electron Localization, Electrostatic Potential and Structural Relaxation. *Phys. Chem. Chem. Phys.* **2012**, *14* (48), 16521–16535.

(12) Li, P.; Chen, X.; Li, Y.; Schwank, J. W. A Review on Oxygen Storage Capacity of CeO_2 -Based Materials: Influence Factors, Measurement Techniques, and Applications in Reactions Related to Catalytic Automotive Emissions Control. *Catal. Today* **2019**, *327*, 90–115.

(13) Sun, Y.; Li, C.; Djerdj, I.; Khalid, O.; Cop, P.; Sann, J.; Weber, T.; Werner, S.; Turke, K.; Guo, Y.; Smarsly, B. M.; Over, H. Oxygen Storage Capacity versus Catalytic Activity of Ceria-Zirconia Solid Solutions in CO and HCl Oxidation. *Catal. Sci. Technol.* **2019**, *9* (9), 2163–2172.

(14) Trovarelli, A.; De Leitenburg, C.; Dolcetti, G. Design Better Cerium-Based Oxidation Catalysts. *Chemtech* **1997**, *27* (6), 32.

(15) Amrute, A. P.; Mondelli, C.; Moser, M.; Novell-Leruth, G.; López, N.; Rosenthal, D.; Farra, R.; Schuster, M. E.; Teschner, D.; Schmidt, T.; et al. Performance, Structure, and Mechanism of CeO_2 in HCl Oxidation to Cl_2. *J. Catal.* **2012**, *286*, 287–297.

(16) Aneggi, E.; Boaro, M.; De Leitenburg, C.; Dolcetti, G.; Trovarelli, A. Insights into the Redox Properties of Ceria-Based Oxides and Their Implications in Catalysis. *J. Alloys Compd.* **2006**, *408–412*, 1096–1102.

(17) Neto, R. C. R.; Schmal, M. Synthesis of CeO_2 and $CeZrO_2$ Mixed Oxide Nanostructured Catalysts for the Iso-Syntheses Reaction. *Appl. Catal. A Gen.* **2013**, *450*, 131–142.

(18) Sugiura, M. Oxygen Storage Materials for Automotive Catalysts: Ceria-Zirconia Solid Solutions. *Catal. Surv. from Asia* **2003**, *7* (1), 77–87.

(19) Hernández, W. Y.; Laguna, O. H.; Centeno, M. A.; Odriozola, J. A. Structural and Catalytic Properties of Lanthanide (La, Eu, Gd) Doped Ceria. *J. Solid State Chem.* **2011**, *184* (11), 3014–3020.

(20) Lucid, A. K.; Keating, P. R. L.; Allen, J. P.; Watson, G. W. Structure and Reducibility of CeO_2 Doped with Trivalent Cations. *J. Phys. Chem. C* **2016**, *120* (41), 23430–23440.

(21) Tilley, R. J. D. *Defects in Solids*, 1st Ed.; John Wiley & Sons Inc.: Hoboken, New Jersey, **2008**.

(22) Vinodkumar, T.; Rao, B. G.; Reddy, B. M. Influence of Isovalent and Aliovalent Dopants on the Reactivity of Cerium Oxide for Catalytic Applications. *Catal. Today* **2015**, *253*, 57–64.

(23) Wang, Z.; Wang, Q.; Liao, Y.; Shen, G.; Gong, X.; Han, N.; Liu, H.; Chen, Y. Comparative Study of CeO_2 and Doped CeO_2 with Tailored Oxygen Vacancies for CO Oxidation. *ChemPhysChem* **2011**, *12* (15), 2763–2770.

(24) Fan, L.; Xi, K.; Zhou, Y.; Zhu, Q.; Chen, Y.; Lu, H. Design Structure for CePr Mixed Oxide Catalysts in Soot Combustion. *RSC Adv.* **2017**, *7* (33), 20309–20319.

(25) Möller, M.; Urban, S.; Cop, P.; Weller, T.; Ellinghaus, R.; Kleine-Boymann, M.; Fiedler, C.; Sann, J.; Janek, J.; Chen, L.; Klar, P. J.; Hofmann, D. M.; Philipps, J.; Dolcet, P.; Gross, S.; Over, H.; Smarsly, B. M. Synthesis and Physicochemical Characterization of $Ce_{1-x}Gd_xO_{2-\delta}$: A Case Study on the Impact of the Oxygen Storage Capacity on the HCl Oxidation Reaction. *ChemCatChem* **2015**, *7* (22), 3738–3747.

(26) Farra, R.; Garcia-Melchor, M.; Eichelbaum, M.; Hashagen, M.; Frandsen, W.; Allan, J.; Girgsdies, F.; Szentmiklosi, L.; Lopez, N.; Teschner, D. Promoted Ceria: A Structural, Catalytic, and Computational Study. *ACS Catal.* **2013**, *3* (10), 2256–2268.

(27) Möller, M.; Over, H.; Smarsly, B.; Tarabanko, N.; Urban, S. Electrospun Ceria-Based Nanofibers for the Facile Assessment of Catalyst Morphological Stability under Harsh HCl Oxidation Reaction Conditions. *Catal. Today* **2015**, *253*, 207–218.

(28) Sallard, S.; Schröder, M.; Boissière, C.; Dunkel, C.; Etienne, M.; Walcarius, A.; Oekermann, T.; Wark, M.; Smarsly, B. M. Bimodal Mesoporous Titanium Dioxide Anatase Films Templated by a Block Polymer and an Ionic Liquid: Influence of the Porosity on the Permeability. *Nanoscale* **2013**, *5* (24), 12316–12329.

(29) Graberg, T. Von; Hartmann, P.; Rein, A.; Gross, S.; Seelandt, B.; Röger, C.; Zieba, R.; Traut, A.; Wark, M.; Janek, J.; Smarsly, B. M. Mesoporous Tin-Doped Indium Oxide Thin Films: Effect of Mesostructure on Electrical Conductivity. *Sci. Technol. Adv. Mater.* **2011**, *12* (2), 025005.

(30) Cop, P.; Göttlicher, M.; Schörmann, J.; Boissiere, C.; Beyer, A.; Becker, C.; Volz, K.; Over, H.; Smarsly, B. M. Atomic Layer Deposition of Titania in Ordered Mesoporous Cerium Zirconium Oxide Thin Films: A Case Study. *J. Phys. Chem. C* **2019**, *123*, 12851–12861.

(31) Cop, P.; Kitano, S.; Niinuma, K.; Smarsly, B.; Kozuka, H. In-Plane Stress Development in Mesoporous Thin Films. *Nanoscale* **2018**, *10*, 7002–7015.

(32) Weller, T.; Deilmann, L.; Timm, J.; Dörr, T. S.; Beaucage, P. A.; Cherevan, A. S.; Wiesner, U. B.; Eder, D.; Marschall, R. A Crystalline and 3D Periodically Ordered Mesoporous Quaternary Semiconductor for Photocatalytic Hydrogen Generation. *Nanoscale* **2018**, *10*, 3225–3234.

(33) Grosso, D.; Cagnol, F.; Soler-Illia, G. J. d. A. A.; Crepaldi, E. L.; Amenitsch, H.; Brunet-Bruneau, A.; Bourgeois, A.; Sanchez, C. Fundamentals of Mesostructuring through Evaporation-Induced Self-Assembly. *Adv. Funct. Mater.* **2004**, *14* (4), 309–322.

(34) Hartmann, P.; Lee, D.; Smarsly, B. M.; Janek, J. Mesoporous TiO_2: Comparison of Splitting Reaction. *ACS Nano* **2010**, *4* (6), 3147–3154.

(35) Reitz, C.; Suchomski, C.; Haetge, J.; Leichtweiss, T.; Jagličić, Z.; Djerdj, I.; Brezesinski, T. Soft-Templating Synthesis of Mesoporous Magnetic $CuFe_2O_4$ Thin Films with Ordered 3D Honeycomb Structure and Partially Inverted Nanocrystalline Spinel Domains. *Chem. Commun.* **2012**, *48* (37), 4471–4473.

(36) Weidmann, C.; Brezesinski, K.; Suchomski, C.; Tropp, K.; Grosser, N.; Haetge, J.; Smarsly, B. M.; Brezesinski, T. Morphology-Controlled Synthesis of Nanocrystalline η-Al_2O_3 Thin Films, Powders, Microbeads, and Nanofibers with Tunable Pore Sizes from Preformed Oligomeric Oxo-Hydroxo Building Blocks. *Chem. Mater.* **2012**, *24* (3), 486–494.

(37) Thommes, M.; Smarsly, B.; Groenewolt, M.; Ravikovitch, P. I.; Neimark, A. V. Adsorption Hysteresis of Nitrogen and Argon in Pore Networks and Characterization of Novel Micro- and Mesoporous Silicas. *Langmuir* **2006**, *22* (2), 756–764.

(38) Patterson, A. L. The Scherrer Formula for X-Ray Particle Size Determination. *Phys. Rev.* **1939**, *56* (10), 978–982.

(39) Shannon, R. D. Revised Effective Ionic Radii and Systematic Studies of Interatomic Distances in Halides and Chalcogenides. *Acta Cryst* **1976**, *A32*, 751–767.

(40) Michel, K.; Eufinger, J.-P.; Elm, M. T.; Ulbrich, G.; Lerch, M.; Janek, J. Combining Two Redox Active Rare Earth Elements for Oxygen Storage - Electrical Properties and Defect Chemistry of Ceria-Praseodymia Single Crystals. *Phys. Chem. Chem. Phys.* **2017**, *19*, 17661–17669.

(41) Li, L.; Chen, F.; Lu, J. Q.; Luo, M. F. Study of Defect Sites in $Ce_{1-x}M_xO_{2-\delta}$ (x = 0.2) Solid Solutions Using Raman Spectroscopy. *J. Phys. Chem. A* **2011**, *115* (27), 7972–7977.

(42) Guo, M.; Lu, J.; Bi, Q.; Luo, M. Effect of Optical Absorbance on the Raman Spectra of $Ce_{0.9}Tb_{0.1}O_{2-\delta}$ Solid Solution. *ChemPhysChem* **2010**, *11* (8), 1693–1699.

(43) McBride, J. R.; Hass, K. C.; Poindexter, B. D.; Weber, W. H. Raman and X-Ray Studies of $Ce_{1-x}RE_xO_{2-y}$, Where RE=La, Pr, Nd, Eu, Gd, and Tb. *J. Appl. Phys.* **1994**, *76* (4), 2435–2441.

(44) Wu, Z.; Li, M.; Howe, J.; Meyer, H. M.; Overbury, S. H. Probing Defect Sites on CeO_2 Nanocrystals with Well-Defined Surface Planes by Raman Spectroscopy and O_2 Adsorption. *Langmuir* **2010**, *26* (21), 16595–16606.

(45) Lara-López, Y.; García-Rosales, G.; Jiménez-Becerril, J. Synthesis and Characterization of TiO_2, CeO_2, and TiO_2-CeO_2 Particles for Application in the Treatment of Phenol. *J. Ceram. Process. Res.* **2019**, *20* (1), 24–29.

(46) Mullins, D. R. The Surface Chemistry of Cerium Oxide. *Surf. Sci. Rep.* **2015**, *70* (1), 42–85.

(47) Mullins, D. R.; Overbury, S. H.; Huntley, D. R. Electron Spectroscopy of Single Crystal and Polycrystalline Cerium Oxide Surfaces. *Surf. Sci.* **1998**, *409* (2), 307–319.

(48) Schierbaum, K. D. Ordered Ultra-Thin Cerium Oxide Overlayers on Pt (111) Single Crystal Surfaces Studied by LEED and XPS. *Surf. Sci.* **1998**, *399* (1), 29–38.

(49) Sack, C.; Lustemberg, P.; Koller, V.; Ganduglia-Pirovano, M. V.; Over, H. Interaction of HCl with a CeO_2(111) Layer Supported on Ru(0001): A Theory and Experiment Combined Study. *J. Phys. Chem. C* **2018**, *122* (34), 19584–19592.

(50) Romeo, M.; Bak, K.; El Fallah, J.; Le Normand, F.; Hilaire, L. XPS Study of the Reduction of Cerium Dioxide. *Surf. Interface Anal.* **1993**, *20* (6), 508–512.

(51) Skála, T.; Šutara, F.; Prince, K. C.; Matolín, V. Cerium Oxide Stoichiometry Alteration via Sn Deposition: Influence of Temperature. *J. Electron Spectros. Relat. Phenomena* **2009**, *169* (1), 20–25.

(52) Dutta, G.; Waghmare, U. V.; Baidya, T.; Hegde, M. S.; Priolkar, K. R.; Sarode, P. R. Reducibility of $Ce_{1-x}Zr_xO_2$: Origin of Enhanced Oxygen Storage Capacity. *Catal. Letters* **2006**, *108* (3–4), 165–172.

(53) Boaro, M.; Giordano, F.; Recchia, S.; Santo, V. D.; Giona, M.; Trovarelli, A. On the Mechanism of Fast Oxygen Storage and Release in Ceria-Zirconia Model Catalysts. *Appl. Catal. B Environ.* **2004**, *52* (3), 225–237.

(54) Guo, J.; Shi, Z.; Wu, D.; Yin, H.; Gong, M.; Chen, Y. Effects of Nd on the Properties of CeO_2-ZrO_2 and Catalytic Activities of Three-Way Catalysts with Low Pt and Rh. *J. Alloys Compd.* **2015**, *621*, 104–115.

(55) Teng, M.; Luo, L.; Yang, X. Synthesis of Mesoporous $Ce_{1-x}Zr_xO_2$ (x = 0.2-0.5) and Catalytic Properties of CuO Based Catalysts. *Microporous Mesoporous Mater.* **2009**, *119* (1–3), 158–164.

(56) Zhu, H.; Qin, Z.; Shan, W.; Shen, W.; Wang, J. Pd/CeO_2-TiO_2 Catalyst for CO Oxidation at Low Temperature: A TPR Study with H_2 and CO as Reducing Agents. *J. Catal.* **2004**, *225* (2), 267–277.

(57) Özkan, E.; Cop, P.; Benfer, F.; Hofmann, A.; Votsmeier, M.; Guerra, J. M.; Giar, M.; Heiliger, C.; Over, H.; Smarsly, B. M. Rational Synthesis Concept for Cerium Oxide Nanoparticles: On the Impact of Particle Size on the Oxygen Storage Capacity. *J. Phys. Chem. C* **2020**, *124* (16), 8736–8748.

(58) Dholabhai, P. P.; Adams, J. B.; Crozier, P.; Sharma, R. A Density Functional Study of Defect Migration in Gadolinium Doped Ceria. *Phys. Chem. Chem. Phys.* **2010**, *12* (28), 7904–7910.

(59) Anirban, S.; Dutta, A. Structural and Ionic Transport Mechanism of Rare Earth Doped Cerium Oxide Nanomaterials: Effect of Ionic Radius of Dopant Cations. *Solid State Ionics* **2017**, *309*, 137–145.

(60) Mansilla, C.; Holgado, J. P.; Espinós, J. P.; González-Elipe, A. R.; Yubero, F. Microstructure and Transport Properties of Ceria and Samaria Doped Ceria Thin Films Prepared by EBE-IBAD. *Surf. Coatings Technol.* **2007**, *202* (4–7), 1256–1261.

(61) Veranitisagul, C.; Koonsaeng, N.; Laosiripojana, N.; Laobuthee, A. Preparation of Gadolinia Doped Ceria via Metal Complex Decomposition Method: Its Application as Catalyst for the Steam Reforming of Ethane. *J. Ind. Eng. Chem.* **2012**, *18* (3), 898–903.

(62) Nagai, Y.; Nonaka, T.; Suda, A.; Sugiura, M. Structure Analysis of CeO_2-ZrO_2 Mixed Oxides as Oxygen Storage Promoters in Automotive Catalysts. *R&D Rev. Toyota CRDL* **2002**, *37* (4), 20–27.

(63) Ahn, K.; Yoo, D. S.; Prasad, D. H.; Lee, H. W.; Chung, Y. C.; Lee, J. H. Role of Multivalent Pr in the Formation and Migration of Oxygen Vacancy in Pr-Doped Ceria: Experimental and First-Principles Investigations. *Chem. Mater.* **2012**, *24* (21), 4261–4267.

(64) Trovarelli, A. Structural and Oxygen Storage/Release Properties of CeO_2-Based Solid Solutions. *Comments Inorg. Chem.* **1999**, *20* (4–6), 263–284.

(65) Sack, C. C. CeO_x(111)/Ru(0001) Als Modellkatalysator Für Die HCl-Oxidation, PhD Thesis, Institute of Physical Chemistry, Justus-Liebig-University Giessen, **2019**. http://geb.uni-giessen.de/geb/volltexte/2019/14841/

(66) Farra, R.; Wrabetz, S.; Schuster, M. E.; Stotz, E.; Hamilton, N. G.; Amrute, A. P.; Pérez-Ramírez, J.; López, N.; Teschner, D. Understanding CeO_2 as a Deacon Catalyst by

Probe Molecule Adsorption and in Situ Infrared Characterisations. *Phys. Chem. Chem. Phys.* **2013**, *15* (10), 3454–3465.

(67) Li, C.; Sun, Y.; Djerdj, I.; Voepel, P.; Sack, C.-C.; Weller, T.; Ellinghaus, R.; Sann, J.; Guo, Y.; Smarsly, B. M.; Over, H. Shape-Controlled CeO_2 Nanoparticles: Stability and Activity in the Catalyzed HCl Oxidation Reaction. *ACS Catal.* **2017**, *7*, 6453–6463.

3.2 Connectivity Matters: Comparison of Nanoparticle vs. Nanoparticle-Derived Mesoporous Ceria-Zirconia Structures in the HCl Oxidation Reaction

to be submitted

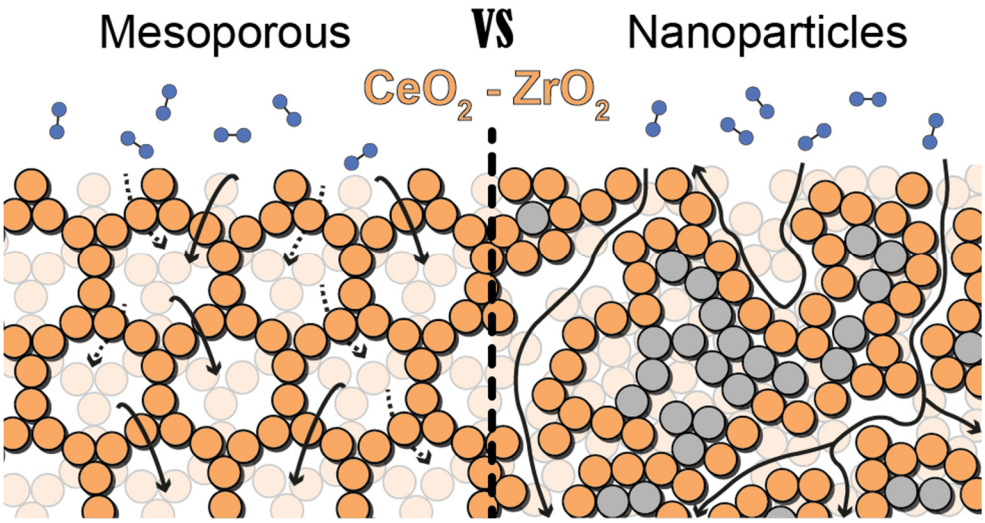

P. Cop, R. Maile, Y. Sun, F. Badaczewski, E. Özkan, C. C. Sack, H. Over, B. M. Smarsly, Connectivity Matters: Comparison of Nanoparticle vs. Nanoparticle-Derived Mesoporous Ceria-Zirconia Structures in the HCl Oxidation Reaction, *Chemistry of Materials,* **2020**, *to be submitted.*

Connectivity Matters: Comparison of Nanoparticle vs. Nanoparticle-Derived Mesoporous Ceria-Zirconia Structures in the HCl Oxidation Reaction

Pascal Cop,[a,b] *Ruben Maile,*[a,b] *Yu Sun,*[c] *Felix Badaczewski,*[a,b] *Elifkübra Özkan,*[a,b] *Carl-Christian Sack,*[a,b] *Tim Weber,*[a,b] *Herbert Over,* [a,b] *Bernd M. Smarsly* [a,b] *

a. Physikalisch-Chemisches Institut, Justus-Liebig-University, Heinrich-Buff-Ring 17, D-35392 Giessen, Germany.

b. Center of Materials Research, Justus-Liebig-University, Heinrich-Buff-Ring 16, D-35392 Giessen, Germany.

c. Key Laboratory for Advanced Materials, Research Institute of Industrial Catalysis, School of Chemistry and Molecular Engineering, East China University of Science and Technology, Shanghai 200237, PR China.

KEYWORDS: mesoporous, nanoparticle, ceria, zirconia, OSC, HCl oxidation

ABSTRACT

We synthesized CeO_2-ZrO_2 nanoparticles as building blocks for preparing mesoporous powders based on nanoparticle dispersion and achieve surface areas up to 180 m^2 g^{-1}, while maintaining the accessibility to the surface due to the combination of templated mesopores and interstitial porosity of the particles. Oxygen storage measurements and the catalytic conversion of hydrogen chloride into chlorine (Deacon Process) were used as model reaction to address the impact of a defined mesopore morphology on the catalytic performance. Our study reveals that the dynamic oxygen storage capacity of the CeO_2-ZrO_2 nanoparticles themselves is overall lower in comparison with the mesoporous powders generated thereof. A similar result is obtained in regards to the catalytic properties in the Deacon process indicating that the highly distributed mesopores in the CeO_2-ZrO_2 matrix enhance the access to the catalytically active sites for the gaseous reactants resulting in an improved chlorine conversion. Furthermore, the mesostructured CeO_2-ZrO_2 powders showed an increased stability against chlorination compared to the nanoparticles due to the absence of possible agglomerates transforming to $CeCl_3$ as observed for CeO_2 nanoparticles. For agglomerated nanoparticles the diffusion to the surface is a surprisingly relevant rate-determining parameter and might not be suitable for studying the intrinsic catalytic properties.

Introduction

The research on heterogeneous catalysts based on CeO_2 materials has grown more strongly in the recent years, as they developed to promising candidates in industrial redox reactions. Owned to their unique redox properties (Ce^{3+} / Ce^{4+})[1], CeO_2 catalysts are suitable to be used in a variety of oxidation[2,3] as well as hydrogenation processes[4], participating passively as an oxygen supplier or as the active phase like in the Deacon process, i.e. the catalytic conversion of hydrogen chloride into chlorine.[2,5] While RuO_2/TiO_2-based catalysts[6] are currently used in the industry, CeO_2-based materials are recommended as promising alternatives in the catalyzed HCl oxidation due to their high oxygen storage capacity (OSC) and the non-volatile chloride species formed at higher temperatures.[7–9] However, the harsh conditions on the CeO_2 catalysts owing to the corrosive gas mixture of HCl/Cl_2 and the elevated temperatures often lead to a degradation of the catalytic activity in a long-term run. Hence, there needs to be emphasized research on the catalytic stability of CeO_2 materials in the HCl oxidation.

In recent studies, investigation of shape-controlled CeO_2 nanoparticles revealed the highest stability of rod-like particles with distinctive (110)-orientation[10], whereas another study demonstrates enhancing the stability in the Deacon process under the presence of water.[11] A further option takes advantage of the addition of different metal oxides such as Al_2O_3 or ZrO_2 for stabilizing CeO_2 against the occurring in-depth chlorination[12] as well as sintering[13,14] during the reaction process. We could verify this effect in recent studies[15], in which we used electrospun $Ce_xZr_{1-x}O_2$ nanofibers of 100 – 200 nm in diameter to visualize the corrosive reaction impact on the fiber morphology using scanning electron microscopy (SEM). The obtained results indicated a better performance and hence, better stability, of the mixed oxides compared to the pure CeO_2 nanofibers suffering from alterations of the

fiber structure. In a further study[16], we used pre-synthesized and dispersible nanoparticles as precursors for inducing a mesoporous structure due to interparticular gaps between the particles and thus, increasing the BET surface area of the nanofibers. They showed a better performance in the Deacon process, but indicated the loss of the fiber structure after the harsh condition of the HCl oxidation reaction. One approach to overcome these stability issues is the incorporation of Zr in the CeO_2 lattice.[17] As our study prepared the nanofibers with high BET surface area using CeO_2-nanoparticles, synthesizing corresponding dispersible CeO_2–ZrO_2 nanoparticles as precursors is required. While the nanofibers are suitable morphologies for tracing changes with straightforward scanning electron microscopy on the micrometer scale, structural rearrangements are hard to detect because of the disordered mesostructure. Hence, a suitable material system for studying the catalytic stability should possess a regular arrangement on the nanometer scale, facilitating the detection of structural alterations. Furthermore, in an ideal model system, every particle should be equally accessible to react with the gaseous molecules and participate in the reaction. In many catalytic studies the accessibility of the catalyst is primarily addressed in the form of packing the material in the catalyst bed, i.e. on a macroscopic scale. However, the nanoscopic arrangement of catalyst material is equally crucial with respect to accessibility, for instance, if the porosity is in the micropore dimension creating diffusion limitations.[18] A step in this direction are porous materials possessing similar specific surface areas like nanoparticles, but provide in contrast to the particles an improved accessibility of the surface due to interconnected pores. Recently, Lu et al. revealed an enhanced OSC of CeO_2, which they assigned to the interconnected 3D framework of their material.[19] Nanoparticles embedded in a controlled porous surrounding provide complete access to the active sites of the particle and are thus, superior model systems for studying the catalytic properties.

The model catalysts of our choice in this study are therefore ordered mesoporous powders with pores of defined shape below 25 nm in diameter to ensure high surface area, a large number of active sites and facilitated gaseous diffusion at the same time. Such materials were used to examine the changes in pore volume and pore sizes before and after the catalyzed corrosive reaction using physisorption techniques, providing inside into possible transformation reactions in the HCl oxidation reaction. In addition, we report the synthesis of $Ce_xZr_{1-x}O_2$ (x = 0, 0.2, 0.4, 0.6, 0.8 and 1) nanoparticle dispersions functioning as the precursor source. As they will be needed in the templating process, the particle must not exceed a particle size of more than 10 nm limited by the expected pore wall thickness to be used successfully as building blocks.[20] Although the preparation of nanoparticles of CeO_2 was investigated in detail in numerous publications[21–23], tailoring the CeO_2-ZrO_2-ratio of uniform particles without the risk of agglomeration or coagulation for several days represented a challenge by itself.

Then, the mesostructure was established by using the diblock copolymer poly(isobutylene)-*block*-poly(ethylene) oxide referred to as PIB_{50}-*b*-PEO_{45} leading to a cubic network of around 14 nm mesopores connected by smaller channels.[24,25] Our approach constitutes a combination of Weller et al.[26] and previous sol-gel-based studies on the impact of such structure-directing agent on the fabrication of thin mesoporous films.[27,28] The latter work also demonstrated the successful transfer of the given preparation of mesoporous thin films, using molecular precursors to a process using nanoparticle dispersions.[29]

Within this study, we would also like to show the influence of the utilized solvent on the pore size distribution determined by nitrogen physisorption as well as Small Angle X-Ray Scattering (SAXS) to ensure a well-characterized porous system. Morphologically analyzed by Scanning (SEM) and Transmission Electron Microscopy (TEM), the mesoporous

powders as well as the nanoparticles are studied by X-Ray Diffraction (XRD) and Raman spectroscopy to validate the existing crystal structure and by X-Ray Photoelectron Spectroscopy (XPS) to determine the Ce^{3+} content of the samples. The samples were utilized for catalytic tests under diffusion-controlled conditions to study the influence of randomly connected nanoparticle and controlled agglomerated nanoparticle-derived mesoporous $Ce_xZr_{1-x}O_2$ structures on the catalytic performance.

Hence, the dynamic and total oxygen storage capacity (OSCc) were measured to relate the effect of ZrO_2 doping of CeO_2 on the with the activity in the CO and HCl oxidation.[30] Furthermore, Sayle *et al.* showed that the catalytic activity of CeO_2 materials is further dependent on the kind of nanostructure (particle, rods, mesostructured) accompanied by a change in the defect concentration and the level of oxygen depletion.[31] We will use our comparison between the nanoparticles and mesoporous powders to show the impact of the mesostructure on the OSC and the relation to the catalytic activity in the HCl oxidation. Also, the catalytic stability is subjected to the harsh condition of the Deacon process, comparing the randomly connected and mesoscopically ordered CeO_2-ZrO_2 nanoparticles with respect to the relevance of the interconnection of the nanoscopic pore space.[13,32]

Experimental Section

Preparation of sol-gel-derived mesoporous $Ce_xZr_{1-x}O_2$ powders

Ordered mesoporous powders of $Ce_xZr_{1-x}O_2$ (x=0, 0.2, 0.4, 0.6, 0.8 and 1) were prepared via an evaporation-induced self-assembly process (EISA) based on a combination of an approach by Weller et al..[26] For a total metal precursor amount of 5 mmol, the associated quantities of $CeCl_3 \cdot 7\ H_2O$ (98%, Sigma-Aldrich) and $ZrOCl_2 \cdot 8\ H_2O$ (99.9%, Alfa Aesar) were added to 3.3 mL ethanol (99.8 %, Merck) and 3.3 mL 2-methoxy-ethanol (99%, Alfa Aesar). 200 mg PIB_{50}-*b*-PEO_{45} (BASF, Ludwigshafen, Germany) were dissolved in 6.6 mL ethanol and 1.7 ml acetic acid (> 99.85 %, Sigma-Aldrich). Both mixtures were treated in an ultrasonic bath for 30 min at 40 °C and 80 kHz. After cooling down to room temperature, both solutions were mixed together and 100 µL dest. H_2O was added to the mixture. The final solution was transferred to six 5 mL PTFE cups and covered with a glass dome on a heating stir plate. The solutions were heated up to 40 °C and covered at this temperature with a glass dome for 2 days. The obtained powder was then dried in a vacuum oven at 50 °C overnight and subsequently annealed at 300 °C for 12 hours with a low heating ramp of 0.75 K min^{-1}. In a final step, the obtained powders were calcined at 550 °C for 10 min using a heating ramp of 4.5 K min^{-1} which led to the crystallization into the desired crystal structure.

Preparation of the nanoparticle dispersions

$Ce_xZr_{1-x}O_2$ nanoparticles (x=0, 0.2, 0.4, 0.6, 0.8 and 1) were synthesized via a sol-gel-route.[33] For a total metal precursor amount of 5 mmol the appropriate amounts of $(NH_4)_2Ce(NO_3)_6$ (99 %, *Acros Organics*) and $ZrOCl_2 \cdot 8\ H_2O$ (>98 %, *Alfa Aesar)* were dissolved in 40 mL distilled water. Precipitation of the metal hydroxides was achieved by adding 1.5 mL of a 25% aqueous NH_3 (Roth) solution to raise pH above 10 which was subsequently neutralized by washing the precipitation repeatedly with distilled water. A total of 5 mL distilled water and 65% HNO_3 (Roth) was added to the washed precipitate.

The ratio of HNO_3 – metal content was varied systematically from 1:1 for a pure CeO_2 sample to 1.5:1 for a pure ZrO_2 sample. By sonicating the resultant suspension for 60 min, a transparent sol was obtained. The sols were dialyzed against distilled water (MWCO: 6000-8000) over 2 days with repeatedly water exchange. For the investigation of the OSC and the catalytic performance, the $Ce_xZr_{1-x}O_2$ nanoparticles were annealed at 550 °C for 10 min with a heating ramp of 4.5 K min^{-1}.

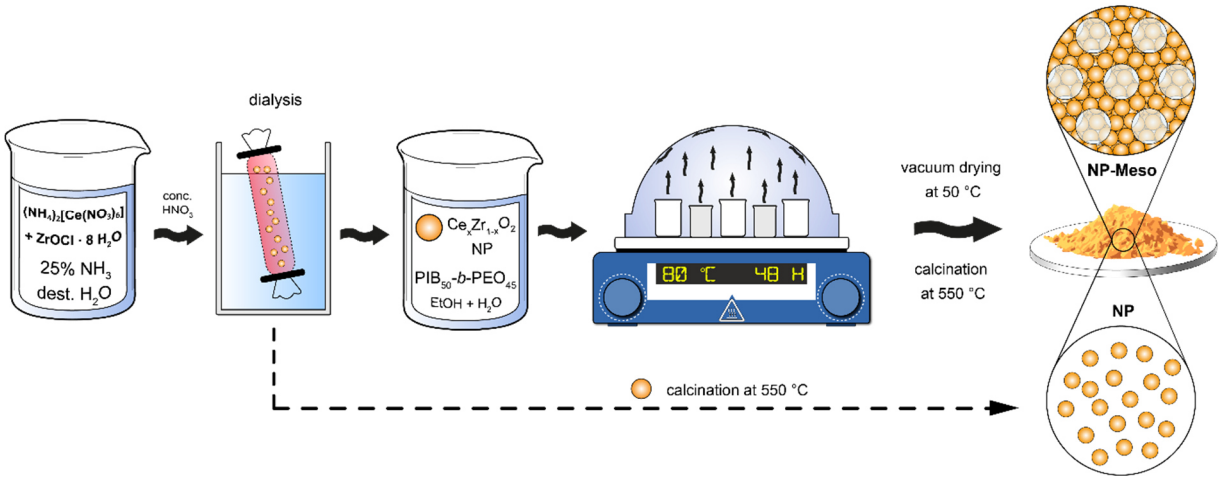

Figure 5: Schematic overview of the preparation of nanoparticle-derived mesoporous doped ceria powders.

Preparation of the nanoparticle-derived mesoporous structure

Similar to the sol-gel-approach, 200 mg PIB_{50}-*b*-PEO_{45} (*BASF*) were dissolved in 7.5 mL distilled water and added to the nanoparticle dispersion. After stirring for 10 min the solution was transferred into 5 mL PTFE cups. For solvent evaporation, the dispersions were heated for 3 days at 60 °C under a glass dome. All the following steps were performed as mentioned in the preparation of sol-gel-derived mesoporous $Ce_xZr_{1-x}O_2$ powders with an annealing temperature at 550 °C for 10 min with a heating ramp of 4.5 K min^{-1}. The preparation is summarized in Figure 1.

Characterization methods

Scanning electron microscopy (SEM) images were recorded using the model *Merlin* by *Zeiss* with an acceleration voltage of 2 keV and a current of 78 pA. In order to increase the conductivity of the samples, the films were sputtered with platinum for 10 s with an applied current of 40 mA. Energy dispersive X-ray spectroscopy (EDS) analyses were recorded by a *XMAX 50* detector from *Oxford Instruments* using a working distance of 5 mm and a current of 2 nA and an acceleration voltage of 10 keV. Nitrogen physisorptions experiments were carried out using a *Quadrasorb* by *Quantachrome Instruments* at T = 77 K. Before each measurement, the samples were degassed at 120 °C for 30 h. By using the BET method, the surface area was calculated, while the pore size distributions were determined using a NLDFT approach using the adsorption branch of the isotherm assuming a spherical/cylindrical pore kernel for silica/nitrogen (77.4 K). The crystalline phases of the materials were studied by X-ray diffraction (XRD) acquired from a *PANalytical Empyrean* powder diffractometer using Cu-Kα radiation (λ = 1.541 Å) at 40 kV and 40 mA. The crystallite sizes were calculated applying the Scherrer equation on the wide angle reflections. In addition, Raman spectroscopy measurements were recorded on *Senterra* by *Bruker* using a 532 nm laser. The obtained data was analyzed using the predicated software *OPUS*. X-ray photoelectron spectroscopy (XPS) measurements were recorded on a *PHI 5000 VersaProbe II* (Physical Electronics GmbH). The spectra of for all doped mesoporous CeO_2 materials were calibrated to a binding energy of 284.8 eV for the C 1s deriving from adventitious hydrocarbon and 916.7 eV for Ce 3d u’’’ signal from the ceria species. Next to the six signals deriving from CeO_2 (v, v’’, v’’’ and u, u’’, u’’’), we also take the four additional signals from Ce_2O_3 (v0, v’ and u0, u’) into account. Based on the findings of

Skala et al.[34] we used a combination of two signals to fit the observed asymmetry of *u* and *v* resulting in better fit conditions. CasaXPS V2.3.17 was used to evaluate the obtained spectra. Transmission electron microscopy (TEM) were recorded on a *CM30* instrument by *Philipps*, which was operated at 300 kV, using copper mesh grids for the sample preparation. SAXS experiments were performed on the Austrian beamline at the Elettra Synchrotron in Trieste. A wavelength λ of 0.154 nm, a Pilatus3 1M detector and a sample-detector distance of 1.2 m were used for data collection. A scattering vector s (=2sin(θ)/λ) range from ca. 0.01 nm^{-1} to 0.6 nm^{-1} was achieved. The powder samples were placed on adhesive tapes for the measurements. Beforehand the empty tapes were measured for background corrections. The SAXS curves were normalized to absolute intensities by using Wavemetrics IGOR Pro. The raw data were radially averaged and corrected for sample transmission and normalized to the primary beam intensity.

Catalytic studies

The determination of the oxygen storage capacity (OSC) was performed using a custom-made fixed-bed flow reactor already described in a previous article.[32] 30 mg of the CeO_2-ZrO_2 structures were placed in a stainless steel tube supported by quartz wool pads and transferred to a tube furnace. All of the OSC measurements were performed at 430 °C controlled by a thermocouple directly next to the steel reactor. In order to reduce and oxidize the ceria catalysts 10 vol.-% carbon monoxide (CO) and oxygen (O_2) pulses with argon (Ar) as the carrier gas were used, which were operated by a *VICI* multiposition valve stream selector, with a total flow rate of 20 sccm. The stream selector allows the time-resolved pulsing of the reducing and oxidizing agent which flow rate were supervised by *MKS 1179B* mass flow controllers. After traversing the OSC reactor, the gas passes a stainless

steel filter (2 µm pore size) and reaching the microvolume thermal conductivity detector VICI TCD2 operated with a pure argon stream at 100 °C as the baseline and a filament temperature of 150 °C. The setup allows to distinguish between the complete (OSCc) and the dynamic oxygen storage capacity (OSC). While the former is achieved by reducing the sample with consecutive 10 s CO pulses and then oxidize the catalyst with 2 s O_2 pulses, the dynamic OSC is studied by alternating CO (4s) and O_2 pulses (2s). The resulting TCD peak areas of the oxygen pulses are fundamental for the calculation of the amount of oxygen stored from the material at 430 °C and are normalized on oxygen reference pulses of the same pulse duration. By knowing the mass of the weighed out catalyst, the values for OSC and OSCc are expressed as micromole oxygen per gram (µmol(O)/g).

The Deacon reaction measurements were conducted in a home-made fixed-bed flow reactor.[13] The reactor comprises the gas supply, the quartz tube reactor, heated by furnace, and UV/vis analytics for chlorine quantification. The following gases were used in the reaction measurements: HCl 4.5, O_2, 5.0 and Ar 5.0 from AirLiquide, the flow rate of gases was controlled by digital mass flow controllers (MKS Instruments 1179B). Prior to feeding the gas mixture into the reactor, Ar was dried using a water absorption cartridge (ALPHAGAZ™ purifier H_2O-free, AirLiquide). The Deacon reaction activity experiments were carried out under so-called "mild" condition where the argon-balanced reaction feeds contain 20 vol. % O_2 and 10 vol. % HCl. The Deacon reaction stability experiments were carried out under condition where the argon-balanced reaction feeds contain 10 vol. % O_2 and 25 vol. % HCl. The total volumetric flow rate was set to 15 $cm^3STPmin^{-1}$ (sccm). Typically, 30 mg of catalyst was supported between two quartz wool wads in the reactor tube. Under the flowing reactant feed, the reactor was heated to a reaction temperature of 430 °C with a linear rate (computer controlled) of $10K \cdot min^{-1}$, held for 4h and 24h (reaction time), then

cooled down to the room temperature in pure argon atmosphere. The product analysis was accomplished by a fiber-optic UV-Vis spectrometer (Ocean Optics USB4000 with a DH-2000-BAL light source) with a Z-shaped flow cell (Teflon®, 50 mm optical path length, FIAlab). The absorbance at a wavelength of λ_{max} = 329 nm (absorption maximum of chlorine) is proportional to the chlorine space time yield (STY) that was calibrated by standard iodometry.

Results and Discussion

In preliminary studies, the synthesis of solely sol-gel-derived mesoporous CeO_2-ZrO_2 was investigated without the need of preformed buildings blocks. Here, the approach was similar to the proposed one in the experimental section for the nanoparticle-derived ones with the exception that the metal salts $CeCl_3 \cdot 7\ H_2O$ and $ZrOCl_2 \cdot x\ 8\ H_2O$ were used together with the diblock copolymer. The attempt was based on a combination of the method by Weller et al.[26] and our previous published syntheses of equivalent mesoporous CeO_2-ZrO_2 thin films[27,28] utilized the same template PIB_{50}-*b*-PEO_{45}. The structural studies using SEM and nitrogen physisorption reveal the presence of a cubic arrangement of 12-15 nm mesopores with BET surface areas ranging from 50-70 $m^2\ g^{-1}$. However, XRD studies demonstrated for the mixtures around 50:50 the existence of Ce-lean and Ce-rich phases. This could be further proven by EDS analyses, displaying a high deviation of the Ce-content of the as-prepared samples. As these samples are not suitable for investigating the impact of the Zr-dopant content on the OSC(c), preformed nanoparticles with defined CeO_2-ZrO_2-ratio were synthesized in order to avoid phase separation and even further increase the specific surface area of the samples while maintaining an interconnected porous network.

Characterization of the nanoparticles

The nanoparticles were synthesized by sol-gel-driven mechanism based on the work of Deshpande *et al.*[33] and yield nearly monodisperse yet crystalline nanoparticles. By adjusting the amount of the given precursors $(NH_4)_2Ce(NO_3)_6$ and $ZrOCl_2 \cdot\ 8\ H_2O$, the composition of $Ce_xZr_{1-x}O_2$ (x = 0 – 1) of the nanoparticle can be tailored precisely. A hydrolysis step at basic conditions (pH > 10) due to the addition of aqueous NH_3 solution lead to the

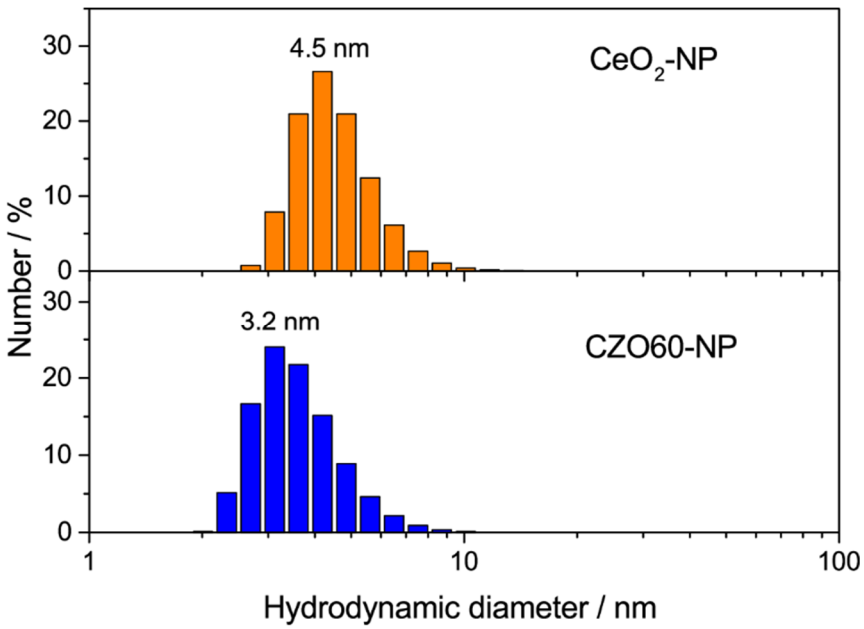

Figure 6: (Top) DLS results of the CeO_2 and CZO60 nanoparticle dispersions being used as-prepared for the synthesized mesoporous powders. (Bottom) TEM images of the same nanoparticles after annealing at 550 °C with the corresponding SAED investigation.

formation of $Ce(OH)_4$ which growth is controlled by subsequently decreasing the pH using nitric acid. In this low pH range, the smaller formed hydroxide particles dissolve easily while the already bigger $Ce(OH)_4$ particles grow only slowly. The particle sol is then transferred slowly to a higher pH value of around 5 by dialysis. For further details on this approach, please refer to the work of Deshpande *et al.*.[33]

The as-prepared nanoparticles dispersions were investigated by DLS resulting in 3-5 nm in hydrodynamic diameter (see Figure 2). The sols were dispersed in H_2O, while also other solvents such as ethanol, ethanol:2-methoxyethanol-mixture, tetrahydrofuran or methanol were used. However, the only eligible dispersion medium was H_2O forming a stable nanoparticle sol lasting at least 2 weeks, while the others lead to the precipitation of the nanoparticles. In order to prepare the mesoporous structure with a well-defined mesoporous structure using a nanoparticle sol, the size of the nanoparticles need to be smaller than the thickness of the pore walls. These do not exceed 15 nm, when using the here added template

PIB_{50}-*b*-PEO_{45}[24,27,35]. Hence, the obtained particle dispersions are suitable as building blocks to prepare mesoporous powders.

Morphological characterization of the nanoparticle-derived mesoporous $Ce_xZr_{1-x}O_2$

The preparation of the nanoparticle-derived mesoporous structures follows a so-called evaporation-induced self-assembly (short: EISA-process)[36] using the nanoparticles as precursors and a diblock copolymer PIB_{50}-*b*-PEO_{45} as the structure-directing agent. During the heating of the solution at 80 °C for 2 days under a glass dome, the water evaporates slowly in a saturated solvent vapor atmosphere and the inorganic particles attach on the outer shell of the polymeric micelles assembling into an ordered cubic structure. Although the template already decomposes at around 300 °C using a long holding time, which was proven by thermogravimetric measurements in a previous work[28], an annealing step at 550 °C was chosen to increase the crystallite size of the compound and to ensure no structural changes during the catalytic and OSC studies at 430 °C. The same procedure was applied to the nanoparticles after dialysis to ensure comparability for the catalytic investigations.

Figure 3A+B show TEM images of the prepared nanoparticles after an annealing temperature at 550 °C possessing sizes of 6±1 nm for pure CeO_2 and 7±2 nm for CZO60 nanoparticles. SAED (Figure 3C) proves the cubic structure for the CeO_2 particles. However, the displayed rings are too broad, owned to the small crystallite size, to detect a shift of the circles to smaller interatomic distances *d* indicating the incorporation of smaller Zr^{4+} ions in the CeO_2 lattice. The prepared nanoparticle-derived porous structures show a high distribution of mesopores on the surface of the powder with 12-17 nm in diameter proven by SEM (Figure 3E). Owned to the roughness and the low conductivity of the CeO_2-ZrO_2

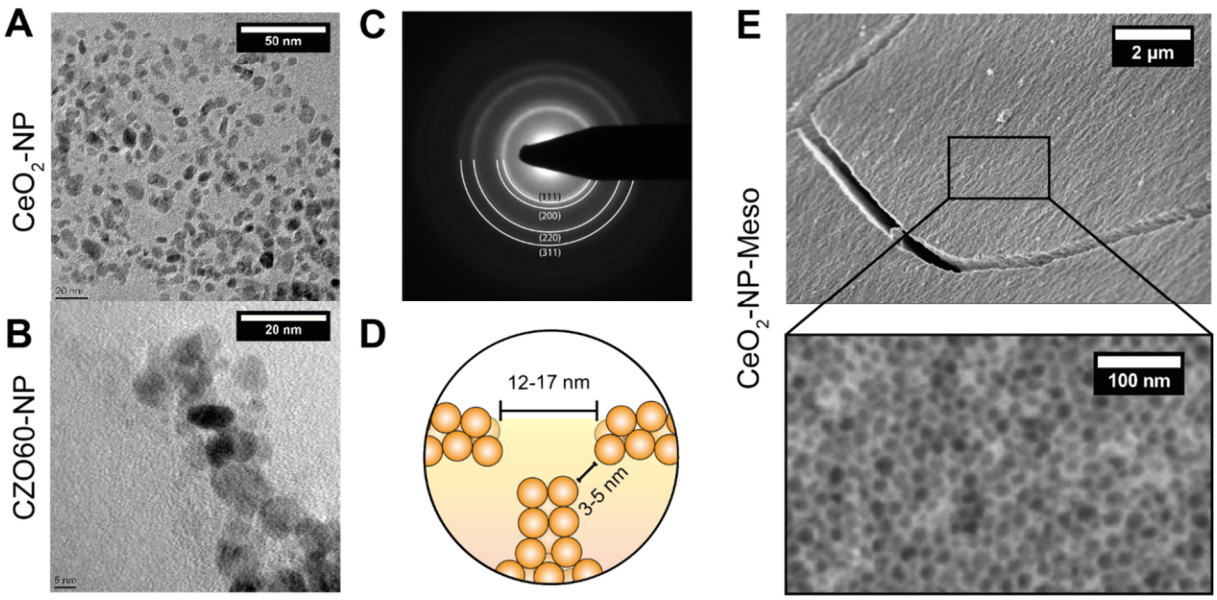

Figure 7: TEM images of the CeO_2-NP (A) and CZO60-NP (B) after annealing the particles at 550 °C including the SAED investigation of the CeO_2- NP (C). Additionally, a schematic side view (D) and SEM recordings of the nanoparticle-derived mesoporous CeO_2 powders after 300 °C in different magnifications (E) are depicted.

powders, visualizing the mesopores of the powders emerged to be quite challenging (see Figure S2). In addition, the orientation of the powder and the pores complicated the measurement of the pore size to get a representative diameter for the investigated sample. However, in order to validate the pores in the depth of the synthesized compounds nitrogen physisorption measurement were carried out (see Figure 4) and compared to the non-templated nanoparticles. The latter show the presence of pores smaller than 5 nm, which is assigned to the interparticular gaps between the nanoparticles. The same pore maximum is also registered for the mesoporous powders. Although H_2O was required for the nanoparticles to form a stable dispersion, the template PIB_{50}-*b*-PEO_{45} was solved either in ethanol or H_2O changing the micelle diameter of the ambiphilic polymer and hence, the resulting

pore size maximum shifts from 8 nm (ethanol/water) to 14 nm (only water) (see Figure

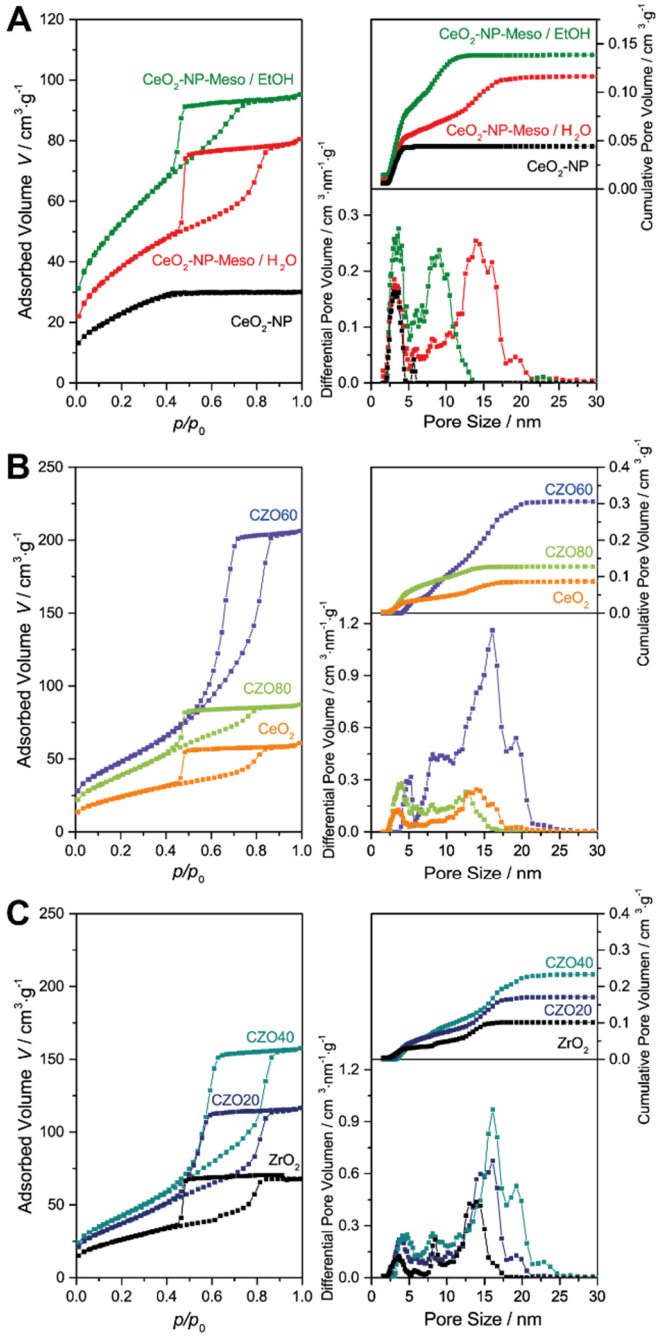

Figure 8: Nitrogen physisorption isotherms and pore size distribution including the cumulative and differential pore volume of the prepared CeO_2-NP in comparison with CeO_2-NP-Meso using different solvents after the decomposition of the polymer at 300 °C (A), using H_2O as the solvent for CeO_2, CZO80, CZO60 (B) and CZO40, CZO20 and ZrO_2 after an annealing temperature of 550 °C (C).

4A). Water acts as a swelling agent for the micelles allowing them to enlarge to a certain degree. Therefore, the synthesis attempts using nanoparticles is further beneficial in comparison with the sol-derived porous powders as it enables a precise control of the pore sizes by simply changing the amount of H_2O in the system. As higher mesopores sizes are favorable for the upcoming catalytic studies as it reduces possible side effects based on limited gaseous diffusion, the further study will concentrate on the nanoparticle-derived mesoporous $Ce_xZr_{1-x}O_2$ (x=0, 0.2, 0.4, 0.6, 0.8 and 1) synthesized by using only H_2O as the solvent. The corresponding nitrogen isotherms are shown in Figure 4B and 4C. While all of the samples possess the aforementioned two pore maxima, the intensity of the bigger mesopores changes significantly. One of the reason could lie in the different sintering process of the nanoparticles during the annealing step at 550 °C. It was presented before[30], that CeO_2-ZrO_2 particles show a different sintering and growing behavior revealing the smallest particle sizes for the equivalent mixtures, while the pure oxides possess the highest. This is in good agreement with our results in which CZO60 show the highest adsorbed volume at a specific pore size and the pure oxides the lowest resembling a similar volcano plot like the growth of CeO_2-ZrO_2 particles. Another reason is a possible segregation between templated and non-templated particles. Thus, the CeO_2 and ZrO_2 samples consists not completely of particles assembled to around the mesopores but also areas, in which the particles agglomerate randomly explaining the smaller cumulative pore volume compared to the one of CZO60 and the differences in the ratio of pores <5 nm and pores >10 nm (see Figure 4). As the size of the nanoparticles during the templating process is similar according to the DLS measurements (see Figure 2), the interaction between the nanoparticles and the diblock copolymer during the alignment of the particles around the micelles seem decisive for the formation of the mesostructured. Further studies need to be performed to evaluate the cause of the pore volume variations.

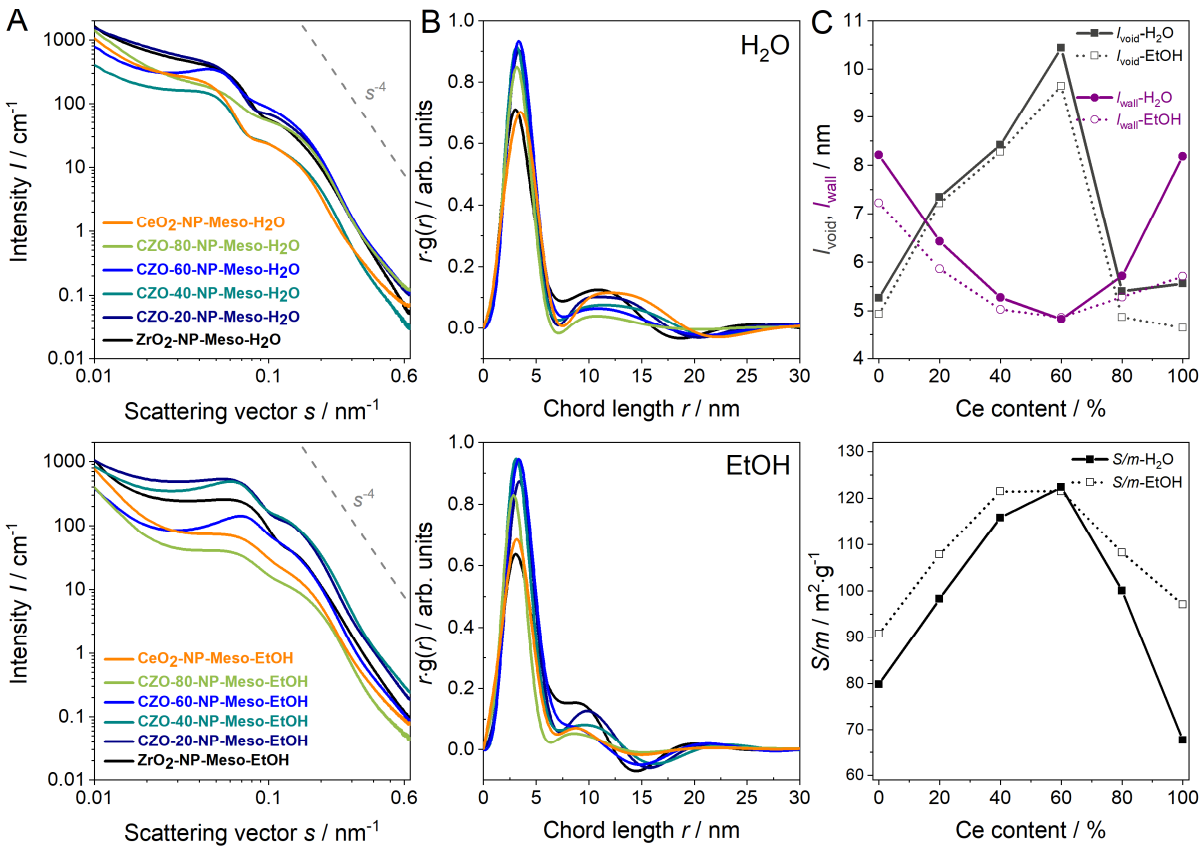

Figure 9: SAXS data (A) and chord-length distributions (B) of the water (top) and water/ethanol (bottom) treated mesoporous mixed oxides. Structural parameters derived from the CLDs (C): void size l_{void}, wall size l_{wall} (top) and surface area S/m (bottom)

In order to validate the order of the porous structures, the prepared powders annealed at 300 °C and 550 °C were investigated using SAXS. Figure 5A shows the normalized SAXS curves of the nanoparticle-derived mesoporous CeO_2-ZrO_2 oxides. The presence of two pronounced peaks indicates a highly ordered pore structure. At large *s* values the data follows Porods-asymptote (s^4), demonstrating an ideal two-phase system with sharp interfaces on the nanometer scale. The well-established chord length distribution (CLD) method, which is capable to quantify a two-phase system, was chosen for an in-depth data evaluation. A CLD curve g(*r*) corresponds to a statistical distribution of distances between phase

boundaries (oxide - pore). One major benefit of this approach is that no assumptions concerning pore geometries are needed. Further information and detailed evaluations can be found in references.[37–39]

The CLDs r·g(r) of the nanoparticle-derived mesoporous powders in Figure 5B depict a strong maximum at 3 nm for both solvents, water (top) and ethanol/water (bottom). In the case of the only water-treated samples a broader second peak from 7 nm to 20 nm is observable, whereas for the ethanol-treated samples the second peak is much narrower, expanding from 7 nm to 15 nm. This finding fits very well with the pore size distributions of the physisorption analysis in Figure 4 and shows the significant influence of the solvent on the pore structure. The minima, e.g. negative values, in the CLDs corresponds to pore-pore distances. These distances are lower for the ethanol-treated samples, 15 nm compared to 20 nm.

The void size l_{void}, wall size l_w (Figure 5 C, top) and the surface area S/m (bottom) were derived following earlier studies.[40,41] The average void size l_{void} is with 5 nm the lowest for the two pure oxides showing that small micropores are dominant in the pore system. CZO60 shows a nearly doubled size with ~10 nm. The wall size l_w, e.g. the oxide phase between two voids, shows an opposite trend. Here, the pure oxides exhibit the largest walls sizes with 8 nm and CZO60 the smallest with 5 nm.

The surface areas S/m follow the same trend as the BET surfaces. CZO40 and CZO60 have the highest surface areas and the pure oxide the lowest. The ethanol-treated samples show overall higher surface areas due to a higher microporosity and smaller mesopores compared to the water-treated samples.

Overall, the SAXS analysis shows the significant impact of the solvent and the doping on the pore structure and oxide phase. This analysis is in good agreement with the results obtained by physisorption, SEM and – in the following – XRD.

Next to the morphological studies of the prepared compounds, the crystal structure of the nanoparticle-derived mesoporous $Ce_xZr_{1-x}O_2$ (x=0, 0.2, 0.4, 0.6, 0.8 and 1) were studied using XRD as well as Raman spectroscopy (see Figure 6). The former reveals the Fm3m cubic structure for CeO_2 which signals shifts to higher 2θ angles with larger Zr-content suggesting the formation of solid solutions as the incorporation of smaller Zr^{4+} ions decreases the lattice constant of the compound. The resulting shift can be evaluated by Vegard's law[42,43] handling the lattice parameter for ZrO_2 and CeO_2 in a linear approach to estimate the solid solution's atomic content, which is in good agreement with the expected content further verified by XPS and EDS studies (see Figure S8). In addition, the XRD indicates the present of pure tetragonal ZrO_2 instead of an often received monoclinic and tetragonal mixture.[30,44] The average crystallize sizes calculated using Scherrer's equation[45] show as expected[30] the highest values for both the pure oxides, while the nearly 50:50 CeO_2-ZrO_2 mixtures possess the smallest sizes explaining its cumulative pore volume (Figure 4) and BET surface area (Table 1). These results suggest, in good agreement with the SAXS data, the pore walls consist of 1-2 particles and/or crystallites. When comparing the XRD patterns from the nanoparticles with their mesoporous counterpart, they indicate no significant change. The same applies to the results of the Raman spectroscopy in Figure 6C, which further allows to study the transfer of the cubic into the tetragonal structure. Figure 6C depicts the cubic crystal structure with the prominent F_{2g} and 2TO band until CZO20, at which the Raman active A_{1g}, B_{1g} and E_g modes become dominant indicating the tetragonal structure.[46,47] The blue-shift of the F_{2g} band is explained similar to the 2θ shift to higher angles by the incorporation of the smaller Zr^{4+} ion in the CeO_2 lattice and the resulting decreasing lattice constant.[46] Furthermore, the shift indicates that a solid solution

is formed instead of an undesired byphase. Lastly, the small increase of the 2TO band from CeO_2 to CZO60 is explained by the higher amount of defect sites due to the existing lattice mismatch between Zr^{4+} and Ce^{4+}. The corresponding defect bands vanish slightly until the tetragonal phase is formed at the CZO20 sample with the dominant B_{1g}- and E_g- band in a similar Raman shift range. Both, the XRD and Raman spectroscopy, show no physico-chemical differences between the nanoparticle and nanoparticle-derived mesoporous structures.

As the Ce^{3+}-concentration is tailored by nanostructuring, XPS investigations (see Figure S5+S6) resulted in a remarkably higher Ce^{3+}-content of the nanoparticle-derived mesoporous structure than for the nanoparticle itself (see Table 1). These were calculated by using the Ce3d line[48–50], while distinguishing between the contribution of CeO_2 and its reduced form Ce_2O_3 using linear combinations of reference spectra of pure CeO_2 and Ce_2O_3 obtained for ultra-thin films on Ru(0001) single crystals.[51] One of the reasons might be the higher surface area of the structure in which the nanoparticles are connected in a controlled

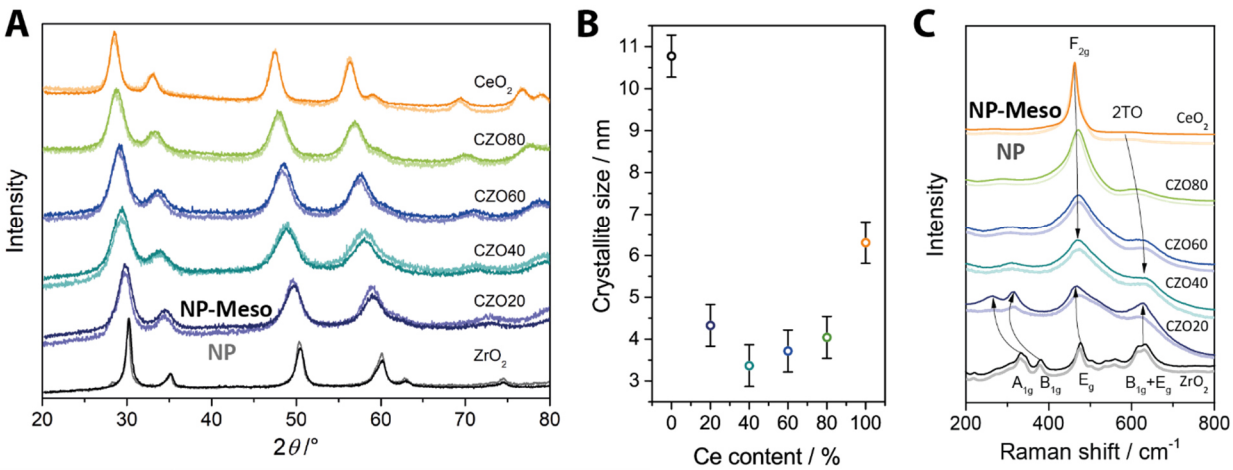

Figure 10: (A) XRD of the CZO nanoparticles (bright) and nanoparticle-derived mesoporous powders as well as the crystallize sizes using the Scherrer equation (B). (C) Raman spectra of the CZO-NP-Meso structures with the assigned bands.

way leading to a higher excess of accessible surface enriched with Ce^{3+}.[52,53] Another explanation could be the higher stress and strain in the CeO_2 particles forced into the mesoporous structure than for the sole particles. The impact of strain on CeO_2 ultrathin films were investigated by Gopal *et al.* connecting the non-stochiometry and hence, the amount of defects and concentration of Ce^{3+} ions with the uniaxial strain.[54] As the Ce^{3+}/Ce^{4+}-ration in every composition of the nanoparticle-derived mesoporous powders is always significantly improved, this increase has to be related to the formation of the porous structure and need to be address in more detail in a future study.

Table 1: Summary of performed on the morphological and structural analyses on the nanoparticle and nanoparticle-derived mesoporous $Ce_xZr_{1-x}O_2$ compounds.

		CeO_2	CZO80	CZO60	CZO40	CZO20	ZrO_2
XPS Ce^{3+} / %	NP	9	13	15	18	17	0
	NP-Meso	27	25	24	23	31	0
BET surface area / $m^2\ g^{-1}$	NP	80	120	120	120	90	70
	NP-Meso	90	150	180	160	140	100

Oxygen storage capacity

When using CeO_2 materials in catalytic oxidation processes, the activity is often compared to the OSC. Here, we differentiate between the total (OSCc) and the dynamic oxygen storage capacity (OSC), which are both measured at 430 °C using CO as the reductant and oxygen as the oxidizing agents. The chosen operational temperature is the same temperature, at which the HCl oxidation is performed. The OSCc is obtained by pulsing CO pulses

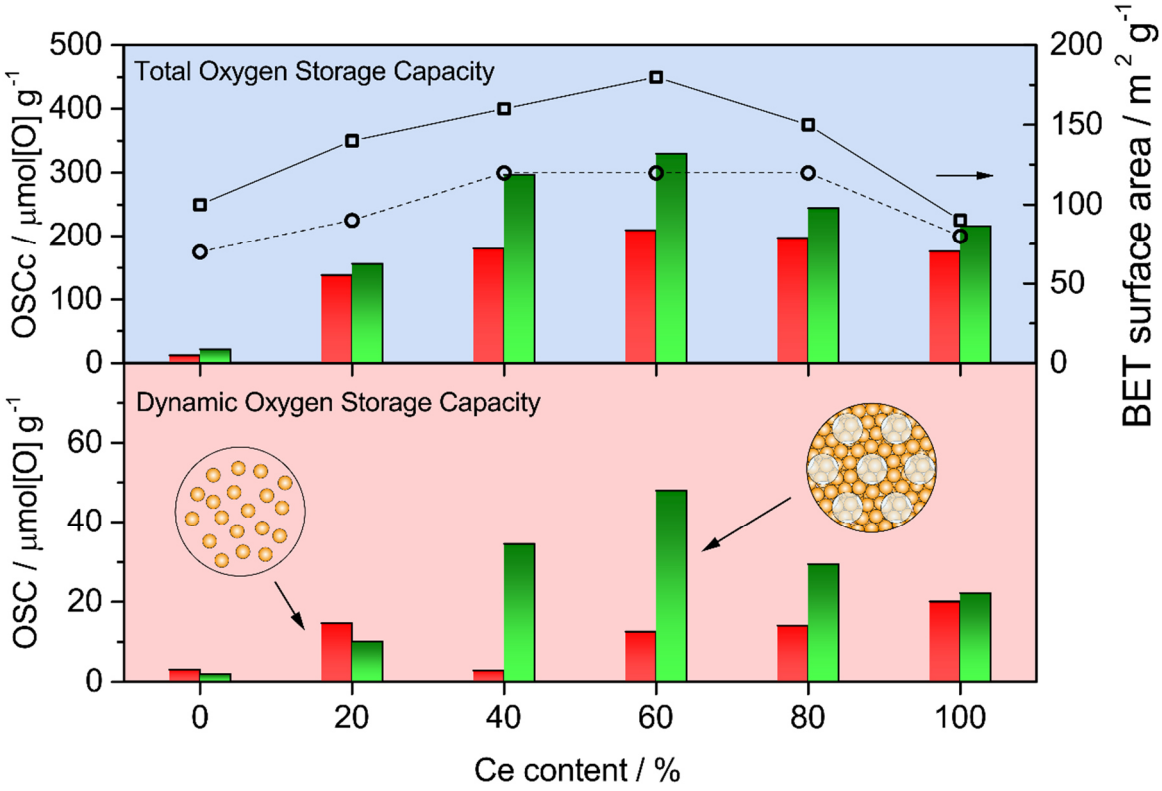

Figure 11: Comparison of the total (top) and dynamic oxygen storage capacity (bottom) of the CZO nanoparticles (red) and the mesoporous structures made of nanoparticles (green) in dependence of the Zr-content.

to the CeO_2 catalyst until the sample is reduced completely and then reoxidized entirely by using O_2-pulses. By using the same setup, the sample is also partially reduced and oxidized again by pulsing CO and O_2 alternatingly, which is referred as dynamic oxygen storage capacity (OSC). The OSC may have more relevance in the catalytic reaction as the sample never reaches a complete reduced state at the given temperature. Both, the measured OSCc and OSC values, are shown in Figure 7 for the nanoparticles as well as the nanoparticle-derived mesoporous powders dependent on the composition.

On the one hand, the obtained data proves a well-known relation: The OSCc increases with doping Zr-ions in the ceria lattice. The maximum value in this study is determined for the CZO60 composition, which is in good agreement with the observed OSC data in some publication demonstrating this mixture to possess the highest total OSC.[55–58] In other cases,

the highest OSC was calculated at CZO80.[59] The differences may derive from different setups and operational conditions. Compared to our previous study[30], the variance derives from the different existing crystal structure at the same Ce/Zr-ratio. In our case, we still have the cubic phase dominant, while it was a transformation to the tetragonal phase in Yu *et al.*[30] which is most likely related to the different size of the obtained particles and a consequence of the nanostructuring.

On the other hand, the OSCc results reveal that the nanoparticle-derived structures have remarkably higher OSCc values than the nanoparticles, despite their similarities in crystallize and particle size. These higher OSCc values corresponds well to the elevated BET surface area for the nanoparticle-derived mesoporous system. The OSCc considers the surface oxygen and the mobile oxygen species from the bulk at the given temperature of 430 °C but does not reduce the bulk completely. The bulk reduction begins at temperatures above 700 °C proven by *temperature programmed reduction* (TPR) investigations[60], which can be decreased by among others the addition of rare earth metal ions or zirconium ions in the ceria lattice.[61] In our study, the amount of available surface oxygen is raised for the mesostructured samples and hence, results in an increased OSCc value per gram catalyst.

In the case of the dynamic OSC, the most active surface oxygen is determined. By applying low total flow rates (here: 20 sccm), the interaction of the gaseous reactants with the catalyst surface is controlled by the diffusion process to the actives sites for the material. Thus, the dynamic OSC value corresponds to the accessibility of the oxygen vacancies and the surface oxygen, respectively. As shown in Figure 7, the nanoparticle-derived mesoporous CeO_2-ZrO_2 powders possess improved OSC values. During the alternating short CO and O_2 pulses, a larger area of the catalyst is reduced and reoxidized than for the nanoparticles.

This indicates further that the connectivity of the particles within the pore walls of the mesostructured sample benefits its storage capacities.

HCl Oxidation

As the connectivity plays already an important role for the OSC and these values for CeO_2-ZrO_2 structures show a relation to its catalytic properties[30], we carried out HCl oxidation experiments under harsh conditions in order to focus on the performance of the synthesized compounds with the best performance in the OSC measurements (CZO60) as well as pure CeO_2 as reference. In both cases, the nanoparticles and nanoparticle-derived mesoporous powders equivalent were chosen. The catalytic studies are shown in Figure 8A and were performed under low total flow rates to ensure a diffusion controlled process. In this way, the accessibility of the catalytically active surface is decisive for the specific chlorine production rate per gram catalyst (space-time yield [STY]).

At first sight, both the NP-Meso samples have a higher STY in comparison with the corresponding nanoparticles. In good agreement with the OSC results, the enhanced accessibility for the gaseous reactants due to the mesoporous structure is decisive for the production of chlorine over time. When comparing the catalytic performance of the pure CeO_2 samples with similar surface areas of 80 $m^2\ g^{-1}$ for the non-templated and 90 $m^2\ g^{-1}$ for the mesostructured nanoparticles, the STY of CeO_2-NP-Meso is doubled after 24 hours in comparison with the sole nanoparticles.

In addition, we can conclude a positive effect of the Zr-doping on its catalytic properties as the CZO60 samples experiences higher STY values than their counterpart. In agreement with the dynamic OSC values, the high accessibility of the most readily available oxygen

species combined with the improved reducibility due the incorporation of Zr in the CeO_2 lattice, lead to the highest STY values in our study.

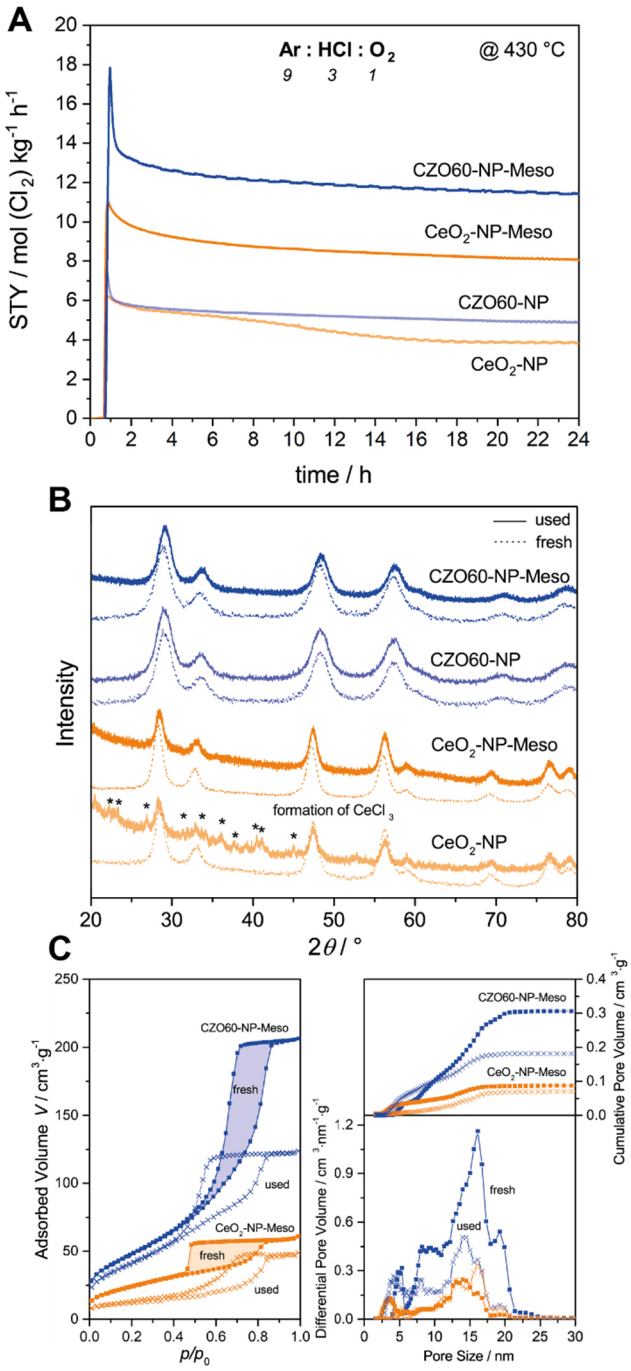

Figure 8: (A) Stability measurements under harsh condition of the HCl oxidation at 430 °C, (B) XRD measurements and nitrogen physisorption studies (C) after the catalytic tests of the CeO_2 and CZO60 nanoparticles and the corresponding nanoparticle-derived mesoporous powders.

In the case of the nanoparticles, the pure CeO_2 sample even show a drastic decline of the STY after 6 hours, while the others samples display a less strongly decrease slope. The formation of $CeCl_3 \cdot H_2O$ for the CeO_2 nanoparticles determined by XRD measurements after the HCl oxidation (see Figure 8B) indicates the formation of $CeCl_3$, which is irreversible at the operational conditions of the HCl oxidation and leads to the decay in chlorine production. The randomly agglomerated nanoparticles favor the formation of undesired $CeCl_3$, clogging the interparticular gaps (see Figure S7) and lead to the decreased STY. Even after the agglomerates are made inactive for the catalytic conversion of HCl to Cl_2, other parts of the CeO_2, which are still accessible for the gaseous reactants are continuing the production of Cl_2.The proposed explanation of decay process is quite difficult to investigate systematically, as the nanoparticles align themselves randomly in the catalyst bed and post-catalytic characterization method such as TEM only reveal chosen parts of the nanoparticles. The XRD studies reveal though, that alongside chlorinated species still a large amount of cubic CeO_2 is present. Contrary to the sole nanoparticles, the induced mesostructure allows to neglect the random agglomeration of the particles and ensures equal conditions for all the present nanoparticles in the pore walls.

While the XRD studies provide insight of the crystal structure changes of the system, the nanoparticle-derived mesoporous CeO_2 and CZO60 powders were further investigated by nitrogen physisorption (see Figure 8C + Figure S7). Both samples show reduced pore volume after the Deacon process and the BET surface area shrinks from 90 to 40 $m^2\ g^{-1}$ for the CeO_2 NP-Meso and from 180 to 150 $m^2\ g^{-1}$ for the CZO60 NP-Meso sample. However, in both cases, there is still a large number of the former pores left between 12-17 nm as seen in SEM recordings (see Figure S9). A difference can be observed in the range of the small pores below 5 nm which are not considered in detail by the applied NLDFT model for determining the pore size distribution. In the case of the CeO_2 samples, these small

pores assigned to the interparticular gaps observed in the fresh samples seem to vanish indicating the sintering process based on the formation of $CeCl_3$ in the near-surface region. This phenomenon is a good agreement with the CeO_2 nanoparticles, but is not witnessed for the CZO60-NP-Meso sample, which is accredited to the higher stability of Zr-doped CeO_2 materials preventing in-depth chlorination.[13,17] This was verified in this study, for both the nanoparticle and the nanoparticle-derived mesoporous powders as the CZO60-NP show a higher long-term stability in the Deacon process compared to the CeO_2-NP.

In previous studies[16,32], we demonstrated that pure CeO_2 nanoparticles are rendered quite stable even under the harsh conditions of the HCl oxidation. We also showed that the incorporation of these nanoparticles in a nanostructure such as nanofibers is favorable in terms of its catalytic properties. While the nanofibers consisted of several particles in diameter, the mesoporous structure is composed of 1-2 particles according to the Scherrer crystallite size and the observed particle size based on TEM images of the nanoparticles (see Figure 3A+B). Taking these findings into account, the improvement of the catalytic properties in the Deacon process of nanoparticle-derived systems may be explained by the enhanced accessibility of and facilitated diffusion to the surface sites of the NP-Meso compared to the NP. In addition, the amount of ceria in the pore wall with its particles is too low in order to fully transfer from the active CeO_2 to the deactivated $CeCl_3$. The chlorination near the surface is performed decreasing the interstitial porosity of the particles as observed in the nitrogen physisorption measurements (Figure 8A), but only remains near-surface. Due to the low pore wall thickness and the number of particles per wall, small diffusion path exists, which allows to access the interior of the pore wall as well as the particles and to recover the oxide easily: every particle has the same condition to participate in the catalytic reaction and randomly agglomerated particles with non-accessible material

do not exist. The incorporation of Zr enhances withstanding the chlorination process[62] by containing a higher reducibility and better accessible oxygen vacancies than pure CeO_2 with CZO60-NP-Meso possessing the smallest pore walls according to the SAXS results (see Figure 5).

Conclusions

In this study, we demonstrated a suitable preparation method of mesoporous $Ce_xZr_{1-x}O_2$ powders using the corresponding nanoparticles sols as precursors. These solid solutions were investigated widely using XRD and Raman for validating the crystal structure as well as SEM, TEM, SAXS and nitrogen physisorption for characterizing the existing cubic pore structure of 12-17 nm mesopores. The mesoporous powders and the corresponding sole nanoparticles – annealed and characterized under the same operational parameters – were tested in two model reactions, namely OSC and HCl oxidation, to evaluate the nanoscopic connectivity between the particles and the accessibility of the samples with gaseous reactants.

Total and dynamic OSC measurements showed a maximum for the CZO60 sample but more importantly, also remarkably higher dynamic OSC values for the nanoparticle-derived structures in comparison with the non-templated particles. As the OSC(c) is often handled as descriptor for ceria materials regarding its catalytic properties, the relationship was verified with our findings of their performance in the Deacon process. The nanoparticle-derived mesoporous structure achieved an increased STY, while also revealing an improved catalytic stability against the chlorination process during the catalytic conversion of HCl to Cl_2. Based on our findings, we conclude that for future studies not only the size and composition of the particles need to be accounted, but also the connectivity of the catalytically active CeO_2 particles. This proposed relation needs to be addressed further by creating CeO_2 porous model systems with different pore wall thicknesses and particle sizes in order to find its best combination for a nanostructured catalyst in the HCl oxidation.

ASSOCIATED CONTENT

The following files are available free of charge.

Characterization overview of sol-gel-derived mesoporous $Ce_xZr_{1-x}O_2$ powders including SEM, nitrogen physisorption experiments, XRD and EDS results; SEM images of the nanoparticle-derived mesoporous $Ce_xZr_{1-x}O_2$ powders using ethanol and H_2O; nitrogen physisorption measurements for the $Ce_xZr_{1-x}O_2$ nanoparticles; Comparison of pore volume and porosity phase of the nanoparticle-derived mesoporous $Ce_xZr_{1-x}O_2$ powders; Ce3d and Zr3d XPS spectra of the nanoparticles and nanoparticle-derived mesoporous $Ce_xZr_{1-x}O_2$ powders; comparison of the nitrogen physisorption results of pure CeO_2 nanoparticles and the mesoporous powder after the the HCl oxidation reaction; Summary of the composition anylses applying EDS, XPS and the Vegard's law on the XRD data of the nanoparticle-derived mesoporous $Ce_xZr_{1-x}O_2$ powders; SEM images of the nanoparticle-derived mesoporous CeO_2 and CZO60 samples after the HCl oxidation.

AUTHOR INFORMATION

Corresponding Author

*(B.S.) E-mail: bernd.smarsly@phys.chemie.uni-giessen.de

*(H.O.) E-mail: herbert.over@phys.chemie.uni-giessen.de

Author Contributions

The manuscript was written through contributions of all authors. All authors have given approval to the final version of the manuscript.

Notes

The authors declare no competing financial interest.

ACKNOWLEDGMENT

The authors thank Lysander Wagner for the TEM sample preparation. In addition, the authors thank Sebastian Werner and Kevin Turke for nitrogen physisorption experiments.

This project was supported by the Center for Materials Research (LaMa) of the Justus-Liebig-University Giessen, Germany.

REFERENCES

(1) Trovarelli, A. Catalytic Properties of Ceria and CeO_2-Containing Materials. *Catal. Rev.* **1996**, *38* (4), 439–520.

(2) Amrute, A. P.; Mondelli, C.; Moser, M.; Novell-Leruth, G.; López, N.; Rosenthal, D.; Farra, R.; Schuster, M. E.; Teschner, D.; Schmidt, T.; et al. Performance, Structure, and Mechanism of CeO_2 in HCl Oxidation to Cl_2. *J. Catal.* **2012**, *286*, 287–297.

(3) Capdevila-Cortada, M.; Vilé, G.; Teschner, D.; Pérez-Ramírez, J.; López, N. Reactivity Descriptors for Ceria in Catalysis. *Appl. Catal. B Environ.* **2015**, *197*, 299–312.

(4) Vilé, G.; Bridier, B.; Wichert, J.; Pérez-Ramírez, J. Ceria in Hydrogenation Catalysis: High Selectivity in the Conversion of Alkynes to Olefins. *Angew. Chemie - Int. Ed.* **2012**, *51* (34), 8620–8623.

(5) Moser, M.; Mondelli, C.; Amrute, A. P.; Tazawa, A.; Teschner, D.; Schuster, M. E.; Klein-Hoffman, A.; López, N.; Schmidt, T.; Pérez-Ramírez, J. HCl Oxidation on IrO_2-Based Catalysts: From Fundamentals to Scale-Up. *ACS Catal.* **2013**, *3* (12), 2813–2822.

(6) Seki, K. Development of RuO_2/Rutile-TiO_2 Catalyst for Industrial HCl Oxidation Process. *Catal. Surv. from Asia* **2010**, *14* (3), 168–175.

(7) Moser, M.; Mondelli, C.; Schmidt, T.; Girgsdies, F.; Schuster, M. E.; Farra, R.; Szentmiklósi, L.; Teschner, D.; Pérez-Ramírezz J. Supported CeO_2 Catalysts in Technical Form for Sustainable Chlorine Production. *Appl. Catal. B Environ.* **2013**, *132–133*, 123–131.

(8) Over, H.; Schomäcker, R. What Makes a Good Catalyst for the Deacon Process? *ACS Catal.* **2013**, *3* (5), 1034–1046.

(9) Pérez-Ramírez, J.; Mondelli, C.; Schmidt, T.; Schlüter, O. F. K.; Wolf, A.; Mleczko, L.; Dreier, T. Sustainable Chlorine Recycling via Catalysed HCl Oxidation: From Fundamentals to Implementation. *Energy Environ. Sci.* **2011**, *4* (12), 4786–4799.

(10) Li, C.; Sun, Y.; Djerdj, I.; Voepel, P.; Sack, C. C.; Weller, T.; Ellinghaus, R.; Sann, J.; Guo, Y.; Smarsly, B. M.; et al. Shape-Controlled CeO_2 Nanoparticles: Stability and Activity in the Catalyzed HCl Oxidation Reaction. *ACS Catal.* **2017**, *7* (10), 6453–6463.

(11) Li, C.; Hess, F.; Djerdj, I.; Chai, G.; Sun, Y.; Guo, Y.; Smarsly, B. M.; Over, H. The Stabilizing Effect of Water and High Reaction Temperatures on the CeO_2-Catalyst in the Harsh HCl Oxidation Reaction. *J. Catal.* **2018**, *357*, 257–262.

(12) Li, C.; Sun, Y.; Hess, F.; Djerdj, I.; Sann, J.; Voepel, P.; Cop, P.; Guo, Y.; Smarsly, B. M.; Over, H. Catalytic HCl Oxidation Reaction: Stabilizing Effect of Zr-Doping on CeO2 Nano-Rods. *Appl. Catal. B Environ.* **2018**, *239*, 628–635.

(13) Kanzler, C. H.; Urban, S.; Zalewska-Wierzbicka, K.; Hess, F.; Rohrlack, S. F.; Wessel, C.; Ostermann, R.; Hofmann, J. P.; Smarsly, B. M.; Over, H. Electrospun Metal Oxide Nanofibres for the Assessment of Catalyst Morphological Stability under Harsh Reaction

Conditions. *ChemCatChem* **2013**, *5* (9), 2621–2626.

(14) Trovarelli, A. *Catalysis by Ceria and Related Materials*; Trovarelli, A., Ed.; Imperial College Press: London, **2002**; Vol. 2.

(15) Möller, M.; Over, H.; Smarsly, B.; Tarabanko, N.; Urban, S. Electrospun Ceria-Based Nanofibers for the Facile Assessment of Catalyst Morphological Stability under Harsh HCl Oxidation Reaction Conditions. *Catal. Today* **2014**, *253*, 207–218.

(16) Möller, M.; Tarabanko, N.; Wessel, C.; Ellinghaus, R.; Over, H.; Smarsly, B. M. Electrospinning of CeO_2 Nanoparticle Dispersions into Mesoporous Fibers: On the Interplay of Stability and Activity in the HCl Oxidation Reaction. *RSC Adv.* **2018**, *8* (1), 132–144.

(17) Urban, S.; Tarabanko, N.; Kanzler, C. H.; Zalewska-Wierzbicka, K.; Ellinghaus, R.; Rohrlack, S. F.; Chen, L.; Klar, P. J.; Smarsly, B. M.; Over, H. Stable and Active Mixed Zr-Ce Oxides for Catalyzing the Gas Phase Oxidation of HCl. *Catal. Letters* **2013**, *143* (12), 1362–1367.

(18) Mitchell, S.; Pinar, A. B.; Kenvin, J.; Crivelli, P.; Kärger, J.; Pérez-Ramírez, J. Structural Analysis of Hierarchically Organized Zeolites. *Nat. Commun.* **2015**, *6*, 8633

(19) Lu, J.; Asahina, S.; Takami, S.; Yoko, A.; Seong, G.; Tomai, T.; Adschiri, T. Interconnected 3D Framework of CeO_2 with High Oxygen Storage Capacity: High-Resolution Scanning Electron Microscopic Observation. *ACS Appl. Nano Mater.* **2020**, *3*, 2346-2353.

(20) Szeifert, J. M.; Fattakhova-Rohlfing, D.; Georgiadou, D.; Kalousek, V.; Rathouský, J.; Kuang, D.; Wenger, S.; Zakeeraddin, S. M.; Grätzel, M.; Bein, T. Brick and Mortar Strategy for the Formation of Highly Crystalline Mesoporous Titania Films from Nanocrystalline Building Blocks. *Chem. Mater.* **2009**, *21* (7), 1260–1265.

(21) Bumajdad, A.; Eastoe, J.; Mathew, A. Cerium Oxide Nanoparticles Prepared in Self-Assembled Systems. *Adv. Colloid Interface Sci.* **2009**, *147–148* (C), 56–66.

(22) Dhall, A.; Self, W. Cerium Oxide Nanoparticles: A Brief Review of Their Synthesis Methods and Biomedical Applications. *Antioxidants* **2018**, *7* (8), 1–13.

(23) Yu, Y.; Zhong, L.; Zhong, Q.; Cai, W. Controllable Synthesis of CeO_2 Nanoparticles with Different Sizes and Shapes and Their Application in NO Oxidation. *RSC Adv.* **2016**, *6* (56), 50680–50687.

(24) Graberg, T. Von; Hartmann, P.; Rein, A.; Gross, S.; Seelandt, B.; Röger, C.; Zieba, R.; Traut, A.; Wark, M.; Janek, J.; et al. Mesoporous Tin-Doped Indium Oxide Thin Films: Effect of Mesostructure on Electrical Conductivity. *Sci. Technol. Adv. Mater.* **2011**, *12* (2), 025005.

(25) Hartmann, P.; Lee, D.; Smarsly, B. M.; Janek, J. Mesoporous TiO_2 : Comparison of

Splitting Reaction. *ACS Nano* **2010**, *4* (6), 3147–3154.

(26) Weller, T.; Deilmann, L.; Timm, J.; Dörr, T. S.; Beaucage, P. A.; Cherevan, A. S.; Wiesner, U. B.; Eder, D.; Marschall, R. A Crystalline and 3D Periodically Ordered Mesoporous Quaternary Semiconductor for Photocatalytic Hydrogen Generation. *Nanoscale* **2018**, *10*, 3225–3234.

(27) Cop, P.; Göttlicher, M.; Schörmann, J.; Boissiere, C.; Beyer, A.; Becker, C.; Volz, K.; Over, H.; Smarsly, B. M. Atomic Layer Deposition of Titania in Ordered Mesoporous Cerium Zirconium Oxide Thin Films: A Case Study. *J. Phys. Chem. C* **2019**, *123*, 12851–12861.

(28) Cop, P.; Kitano, S.; Niinuma, K.; Smarsly, B.; Kozuka, H. In-Plane Stress Development in Mesoporous Thin Films. *Nanoscale* **2018**, *10*, 7002–7015.

(29) Cop, P.; Hess, K.; Werner, S.; Meinusch, R.; Smarsly, B. M.; Kozuka, H. Comparison of In-Plane Stress Development in Sol-Gel- And Nanoparticle-Derived Mesoporous Metal Oxide Thin Films. *Langmuir* **2019**, *35* (50), 16427–16437.

(30) Sun, Y.; Li, C.; Djerdj, I.; Khalid, O.; Cop, P.; Sann, J.; Weber, T.; Werner, S.; Turke, K.; Guo, Y.; et al. Oxygen Storage Capacity versus Catalytic Activity of Ceria–Zirconia Solid Solutions in CO and HCl Oxidation. *Catal. Sci. Technol.* **2019**, *9*, 2163–2172.

(31) Sayle, T. X. T.; Caddeo, F.; Zhang, X.; Sakthivel, T.; Das, S.; Seal, S.; Ptasinska, S.; Sayle, D. C. Structure − Activity Map of Ceria Nanoparticles, Nanocubes, and Mesoporous Architectures. **2016**, *28*, 7287–7295.

(32) Möller, M.; Urban, S.; Cop, P.; Weller, T.; Ellinghaus, R.; Kleine-Boymann, M.; Fiedler, C.; Sann, J.; Janek, J.; Chen, L.; et al. Synthesis and Physicochemical Characterization of $Ce_{1-x}Gd_xO_{2-\delta}$: A Case Study on the Impact of the Oxygen Storage Capacity on the HCl Oxidation Reaction. *ChemCatChem* **2015**, *7* (22), 3738–3747.

(33) Deshpande, A. S.; Pinna, N.; Beato, P.; Antonietti, M.; Niederberger, M. Synthesis and Characterization of Stable and Crystalline $Ce_{1-x}Zr_xO_2$ Nanoparticle Sols. *Chem. Mater.* **2004**, *16*, 2599–2604.

(34) Skála, T.; Šutara, F.; Prince, K. C.; Matolín, V. Cerium Oxide Stoichiometry Alteration via Sn Deposition: Influence of Temperature. *J. Electron Spectros. Relat. Phenomena* **2009**, *169* (1), 20–25.

(35) Weidmann, C.; Brezesinski, K.; Suchomski, C.; Tropp, K.; Grosser, N.; Haetge, J.; Smarsly, B. M.; Brezesinski, T. Morphology-Controlled Synthesis of Nanocrystalline η-Al_2O_3 Thin Films, Powders, Microbeads, and Nanofibers with Tunable Pore Sizes from Preformed Oligomeric Oxo-Hydroxo Building Blocks. *Chem. Mater.* **2012**, *24* (3), 486–494.

(36) Brinker, C. J.; Lu, Y.; Sellinger, A.; Fan, H. Evaporation-Induced Self-Assembly: Nanostructures Made Easy. *Adv. Mater.* **1999**, *11* (7), 579–585.

(37) Smarsly, B.; Antonietti, M.; Wolff, T. Evaluation of the Small-Angle X-Ray Scattering of

Carbons Using Parametrization Methods. *J. Chem. Phys.* **2002**, *116* (6), 2618–2627.

(38) Smarsly, B.; Göltner, C.; Antonietti, M.; Ruland, W.; Hoinkis, E. SANS Investigation of Nitrogen Sorption in Porous Silica. *J. Phys. Chem. B* **2001**, *105* (4), 831–840.

(39) Badaczewski, F.; Loeh, M. O.; Pfaff, T.; Dobrotka, S.; Wallacher, D.; Clemens, D.; Metz, J.; Smarsly, B. M. Peering into the Structural Evolution of Glass-like Carbons Derived from Phenolic Resin by Combining Small-Angle Neutron Scattering with an Advanced Evaluation Method for Wide-Angle X-Ray Scattering. *Carbon* **2019**, *141*, 169–181.

(40) Stoeckel, D.; Wallacher, D.; Zickler, G. A.; Perlich, J.; Tallarek, U.; Smarsly, B. M. Coherent Analysis of Disordered Mesoporous Adsorbents Using Small Angle X-Ray Scattering and Physisorption Experiments. *Phys. Chem. Chem. Phys.* **2014**, *16* (14), 6583–6592.

(41) Stoeckel, D.; Wallacher, D.; Zickler, G. A.; Thommes, M.; Smarsly, B. M. Elucidating the Sorption Mechanism of Dibromomethane in Disordered Mesoporous Silica Adsorbents. *Langmuir* **2015**, *31* (23), 6332–6342.

(42) Vegard, L. Die Konstitution Der Mischkrstalle Und Die Raumfüllung Der Atome. *Zeitschrift für Phys.* **1921**, *5* (1), 17–26.

(43) Denton, A. R.; Ashcroft, N. W. Vegard's Law. *Phys. Rev. A* **1991**, *43*, 3161–3164.

(44) Cheema, T. A.; Garnweitner, G. Phase-Controlled Synthesis of ZrO_2 Nanoparticles for Highly Transparent Dielectric Thin Films. *Crystengcomm* **2014**, *16* (16), 3366–3375.

(45) Patterson, A. L. The Scherrer Formula for X-Ray Particle Size Determination. *Phys. Rev.* **1939**, *56* (10), 978–982.

(46) Schilling, C.; Hofmann, A.; Hess, C.; Ganduglia-Pirovano, M. V. Raman Spectra of Polycrystalline CeO_2 : A Density Functional Theory Study. *J. Phys. Chem. C* **2017**, *121* (38), 20834–20849.

(47) Sobol, A. A.; Voronko, Y. K. Stress-Induced Cubic-Tetragonal Transformation in Partially Stabilized ZrO_2: Raman Spectroscopy Study. *J. Phys. Chem. Solids* **2004**, *65* (6), 1103–1112.

(48) Mullins, D. R.; Overbury, S. H.; Huntley, D. R. Electron Spectroscopy of Single Crystal and Polycrystalline Cerium Oxide Surfaces. *Surf. Sci.* **1998**, *409* (2), 307–319.

(49) Mullins, D. R. The Surface Chemistry of Cerium Oxide. *Surf. Sci. Rep.* **2015**, *70* (1), 42–85.

(50) Schierbaum, K. D. Ordered Ultra-Thin Cerium Oxide Overlayers on Pt (111) Single Crystal Surfaces Studied by LEED and XPS. *Surf. Sci.* **1998**, *399* (1), 29–38.

(51) Sack, C.; Lustemberg, P.; Koller, V.; Ganduglia-Pirovano, M. V.; Over, H. Interaction of

HCl with a CeO_2(111) Layer Supported on Ru(0001): A Theory and Experiment Combined Study. *J. Phys. Chem. C* **2018**, *122* (34), 19584–19592.

(52) Deshpande, S.; Patil, S.; Kuchibhatla, S. V. N. T.; Seal, S.; Deshpande, S.; Patil, S.; Kuchibhatla, S. V. N. T.; Seal, S. Size Dependency Variation in Lattice Parameter and Valency States in Nanocrystalline Cerium Oxide Size Dependency Variation in Lattice Parameter and Valency States in Nanocrystalline Cerium Oxide. *Aplplied Phys. Lett.* **2005**, *87*, 133113.

(53) Loschen, C.; Bromley, S. T.; Neyman, K. M.; Illas, F. Understanding Ceria Nanoparticles from First-Principles Calculations. *J. Phys. Chem. C* **2007**, *111* (28), 10142–10145.

(54) Balaji Gopal, C.; García-Melchor, M.; Lee, S. C.; Shi, Y.; Shavorskiy, A.; Monti, M.; Guan, Z.; Sinclair, R.; Bluhm, H.; Vojvodic, A.; et al. Equilibrium Oxygen Storage Capacity of Ultrathin $CeO_{2-\delta}$ Depends Non-Monotonically on Large Biaxial Strain. *Nat. Commun.* **2017**, *8* (May), 15360.

(55) Suda, A.; Ukyo, Y.; Sobukawa, H.; Sugiura, M. Improvement of Oxygen Storage Capacity of CeO_2-ZrO_2 Solid Solution by Heat Treatment in Reducing Atmosphere. *J. Ceram. Soc. Japan* **2002**, *110* (2), 126–130.

(56) Nagai, Y.; Nonaka, T.; Suda, A.; Sugiura, M. Structure Analysis of CeO_2-ZrO_2 Mixed Oxides as Oxygen Storage Promoters in Automotive Catalysts. *R&D Rev. Toyota CRDL* **2002**, *37* (4), 20–27.

(57) Madier, Y.; Descorme, C.; Le Govic, a M.; Duprez, D. Oxygen Mobility in CeO_2 and $Ce_xZr_{(1-x)}O_2$ Compounds: Study by CO Transient Oxidation and $^{18}O/^{16}O$ Isotopic Exchange. *J. Phys. Chem. B* **1999**, *103* (50), 10999–11006.

(58) Li, P.; Chen, X.; Li, Y.; Schwank, J. W. A Review on Oxygen Storage Capacity of CeO_2-Based Materials: Influence Factors, Measurement Techniques, and Applications in Reactions Related to Catalytic Automotive Emissions Control. *Catal. Today* **2019**, *327*, 90–115.

(59) Trovarelli, A.; Zamar, F.; Llorca, J.; De Leitenburg, C.; Dolcetti, G.; Kiss, J. T. Nanophase Fluorite-Structured CeO_2-ZrO_2 Catalysts Prepared by High-Energy Mechanical Milling: Analysis of Low-Temperature Redox Activity and Oxygen Storage Capacity. *J. Catal.* **1997**, *169* (2), 490–502.

(60) López, J. M.; Gilbank, A. L.; García, T.; Solsona, B.; Agouram, S.; Torrente-Murciano, L. The Prevalence of Surface Oxygen Vacancies over the Mobility of Bulk Oxygen in Nanostructured Ceria for the Total Toluene Oxidation. *Appl. Catal. B Environ.* **2015**, *174–175*, 403–412.

(61) Trovarelli, A. Structural and Oxygen Storage/Release Properties of CeO_2-Based Solid Solutions. *Comments Inorg. Chem.* **1999**, *20* (4–6), 263–284.

(62) Urban, S.; Tarabanko, N.; Kanzler, C. H.; Zalewska-Wierzbicka, K.; Ellinghaus, R.; Rohrlack, S. F.; Chen, L.; Klar, P. J.; Smarsly, B. M.; Over, H. Stable and Active Mixed Zr-Ce Oxides for Catalyzing the Gas Phase Oxidation of HCl. *Catal. Letters* **2013**, *143*

(12), 1362–1367.

3.3 Atomic Layer Deposition of Titania in Ordered Mesoporous Cerium Zirconium Oxide Thin Films: A Case Study

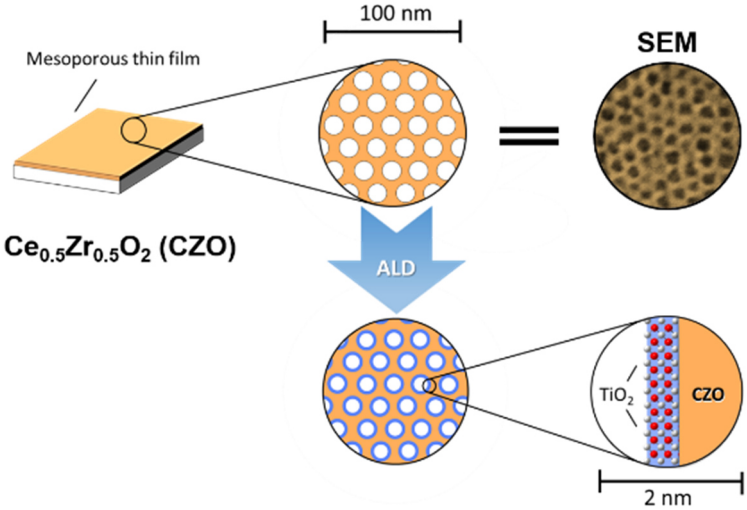

Reprinted with permission from

P. Cop, M. Göttlicher, J. Schörmann, C. Boissiere, A. Beyer, C. Becker, K. Volz, H. Over, B. M. Smarsly, Atomic Layer Deposition of Titania in Ordered Mesoporous Cerium Zirconium Oxide Thin Films: A Case Study, *J. Phys. Chem. C* **2019**, *123*, 12851–12861.

https://pubs.acs.org/doi/full/10.1021/acs.jpcc.9b02069

THE JOURNAL OF PHYSICAL CHEMISTRY C

Article

Cite This: J. Phys. Chem. C 2019, 123, 12851−12861

pubs.acs.org/JPCC

Atomic Layer Deposition of Titania in Ordered Mesoporous Cerium Zirconium Oxide Thin Films: A Case Study

P. Cop,[†,‡] M. Göttlicher,[†,§] J. Schörmann,[‡,§] C. Boissiere,[∥] A. Beyer,[⊥] C. Becker,[⊥] K. Volz,[⊥] H. Over,[*,†,‡] and B. M. Smarsly[*,†,‡]

[†]Physikalisch-Chemisches Institut, Justus-Liebig-Universität, Heinrich-Buff-Ring 17, D-35392 Giessen, Germany

[‡]Center for Materials Research and [§]I. Physikalisches Institut, Justus-Liebig-Universität, Heinrich-Buff-Ring 16, D-35392 Giessen, Germany

[∥]Laboratoire Chimie de la Matière Condensée de Paris Collège de France, 11 Place, Marcelin Berthelot, 75005 Paris, France

[⊥]Department of Physics and Materials Science Center, Philipps-Universität Marburg, Hans-Meerwein-Straße 6, D-35032 Marburg, Germany

Supporting Information

ABSTRACT: A strategy is presented to deposit defined layers of TiO_2 onto the pore surface within ordered mesoporous, crystalline CeO_2-ZrO_2 thin films using atomic layer deposition (ALD). As structure-directing agent, a special diblock copolymer, poly(isobutylene)-*block*-poly(ethylene oxide), was used, resulting in a three-dimensional arrangement of spherical pores with diameter around 13 nm. High resolution transmission electron microscopy investigations evidence the presence of anatase TiO_2 coatings within the mesopores, while ellipsometric porosimetry studies together with time-of-flight secondary-ion mass spectrometry depth profiles indicate the deposition inside the mesopores up to 50 ALD cycles. Afterward, the interconnecting channels between the mesopores are filled completely prohibiting further transport of the gaseous TiO_2 precursor into the ordered structure of mesopores and hence, limit the layer growth on the surfaces of the pores. Therefore, the size of the mesopores and their connections are decisive when growing transition-metal oxide layers on the surface of porous substrates and need to be considered for future depositions using ALD. The hybrid TiO_2/CeO_2-ZrO_2 materials are studied by several complementary analytical techniques, to validate the deposition process and also the applicability of these techniques for such materials in general.

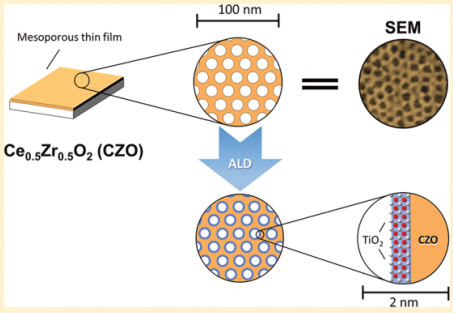

INTRODUCTION

Recent advances in the preparation of nanostructured materials revealed particular interests in metal/oxide and oxide/oxide nanostructures. Merging the unique characteristics of two materials into one system can be favorable, especially for metal oxides. The combination of two different metal oxides can enhance the overall material properties, for instance, in gas sensing, electrochemical energy storage, medical treatment, and (photo/electro) catalysis[1−9] due to synergetic effects. Such effects are related to the interface between the two materials affecting the formation of oxygen vacancies, stabilizing desired ion species, or, in general, enhancing the catalytic activity and stability.[10−17] In addition, by tailoring the layer thickness of the active metal oxide species, the properties of thin layers of the oxide(s) may differ from the bulk counterpart. Core−shell nanostructures are one important example using the benefits of two metal oxides by maximizing the interfacial surface area between the core and shell metal oxides. For instance, a ZnO shell on SnO_2 nanorods enhances the selectivity in H_2 gas sensing.[18] Single-crystalline ZnO nanorods covered with a porous MnO_2 shell possess improved supercapacitor performance.[19] Dumesic and co-workers deposited Nb_2O_5 layers into the pores of mesoporous silica (SBA-15) and studied this hybrid catalyst in the gas-phase dehydration of 2-propanol confirming the superiority of their catalyst in activity and stability compared to commercial Nb_2O_5.[20] By changing the thickness of the γ-Fe_2O_3 shell layers on a Fe_3O_4 core, the magnetic properties depending on the temperature were modified for its usage in magnetic hyperthermia treatments.[21] Artiglia et al. demonstrated the preparation of CeO_2/TiO_2 core/shell structure stabilizing the Ce^{3+} species on the TiO_2 surface.[10] In that study, by changing the thickness of the coating layer with a wet impregnation method, the ratio of Ce^{3+}/Ce^{4+} was tailored. However, this kind of deposition method is difficult to control and does not provide a homogeneous and conformal coating of the core material, because the nanoparticles are attached to each other in an uncontrollable fashion and also might move during deposition,

Received: March 4, 2019
Revised: April 23, 2019
Published: April 29, 2019

DOI: 10.1021/acs.jpcc.9b02069
J. Phys. Chem. C 2019, 123, 12851−12861

resulting in an inhomogeneous coating with the second metal oxide. By contrast, in mesoporous thin films, the crystalline metal oxide structure is stabilized and completely accessible. The impregnation of a continuous mesoporous metal oxide framework is therefore fundamentally more suitable in comparison to corresponding nanoparticles.

Besides the usage of impregnation methods such as co-condensation,[22] grafting,[23,24] and wet impregnation,[25,26] atomic layer deposition (ALD) is a promising alternative for the deposition of defined layers with nanometer-sized thickness. While physical and chemical vapor deposition techniques are able to deposit a variety of metal oxides on planar substrates, ALD allows the coating of conformal layers even on complex substrate morphologies by separating the gas−solid reactions with purging steps and therefore building up the film layer by layer.[27−31] This self-limiting nature of the ALD enables the atomic-level control of the formed layer in the interior of a nanopore according to the desired physicochemical effects.

While the deposition in porous structures with pore sizes above 50 nm is easily confirmed by using electron microscopy techniques, the difficulty of validating thin conformal coatings arises with decreasing pore sizes. In the last years, various complex porous substrates such as SBA-15,[20] aluminum oxide membranes,[32−34] carbon,[35] and zeolites[36] were coated with active species using ALD to study the effect of the deposition layers on the specific material properties. Kraffert et al. demonstrate the shift of the crystallization temperature of ferrihydrite films to higher temperatures using coatings of alumina and silica on the mesopore surface.[37] Detavernier et al. presented the possibilities to prove the conformal coating of mesoporous thin films with pore size less than 10 nm in a tutorial review.[38] They presented in situ X-ray fluorescence and ellipsometric porosimetry (EP) investigations not only on the validation of the deposition in the interior pore layers, but also on the formation of metal oxide layers on top of the substrate. In continuous studies, Detavernier's group used the in situ EP technique to investigate the ALD growth of TiO_2 in mesoporous silica films and HfO_2 in TiO_2 films with ink-bottle mesopores.[39,40] The latter revealed that the limit of tuning the pore size in these mesoporous materials is determined by the diameter of the smallest pores connecting the bigger pore layers and hence, literally being the "bottleneck" of the ALD. This was additionally proven by the same group using in situ synchrotron-based grazing-incidence small-angle X-ray scattering (SAXS) on Pluronic F127-templated titania thin films.[41]

However, the mesoporous thin films templated by the block copolymer Pluronic F127 only yielded a nonordered structure of mesopores with small pore sizes below 8 nm and connecting channels of nonuniform sizes and shapes. Hence, transition-metal oxides with well-ordered mesopore arrangements as well as larger mesopore diameters (i.e., >10 nm) are desirable, to study size effects of crystalline metal oxide coating layers on the pore surface. Consequently, with defined pore shape, connection, and size, the details of the ALD-based deposition can be studied more accurately and systematically than for nonordered porous films because changes in the pore size and accessibility can be detected and quantified more reliably and can thus be related to deposition parameters. By using specific block copolymers, our group has achieved mesoporous structures with pore sizes between 12 and 25 nm forming a three-dimensional (3D) network of spherical mesopores connected by smaller channels.[41−45] The cubic ordered structures with pore sizes around 14 nm were synthesized using the diblock copolymer poly(isobutylene)-*block*-poly(ethylene) oxide referred to as PIB_{50}-*b*-PEO_{45}. The template was already used to prepare various metal oxides, e.g., TiO_2,[42,43] indium tin oxide,[44] Al_2O_3,[45] and $Ce_xZr_{1-x}O_2$,[46] which showed a favorable ordered structure in its 1:1 mixture $Ce_{0.5}Zr_{0.5}O_2$ (CZO), making it a good model system to study the incorporation of TiO_2 into the mesoporous structure using ALD. Furthermore, we have chosen CZO and TiO_2 as model case, as TiO_2/CeO_2 material systems have been proven to be promising catalysts for various reactions, for instance, in the selective catalytic oxidation of NH_3 to N_2[47] and catalytic reduction of NH_3 to NO[48] (SCR). Spectroscopic studies of the interfacial sites of these binary oxides were investigated by Fang et al.,[49] revealing an enrichment of anatase on the interfacial sites as the Ti^{4+} substitutes Ce^{4+} in the cubic CeO_2 lattice. Huang et al.[50] successfully prepared CeO_2@TiO_2 core−shell nanostructures with an enhanced catalytic activity, stability, and superior tolerance against SO_2 and H_2O for low-temperature SCR of NO_x using NH_3. The reason for selecting TiO_2/CeO_2 is ascribed to the high mobility of lattice oxygen inside the catalyst and thus the increased oxygen storage capacity, which can be further raised by incorporating zirconium ions in the ceria lattice.[51] Since the CZO-TiO_2 interface thus endows these two oxides with beneficial properties, we chose mesoporous CZO thin films as substrate with defined layers of TiO_2, which are deposited using ALD. Taking TiO_2 as the oxide to be deposited by ALD is favorable, as its growth using $TiCl_4$ and H_2O is widely studied[52−54] and shows sufficiently different properties compared to the CZO mesoporous film, allowing for its detection within the final hybrid films.

As the main goal, in this work, ordered mesoporous CZO thin films are prepared and infiltrated with TiO_2 using the ALD technique, to study the incorporation process inside the mesopores (see Figure 1). The study also addresses the

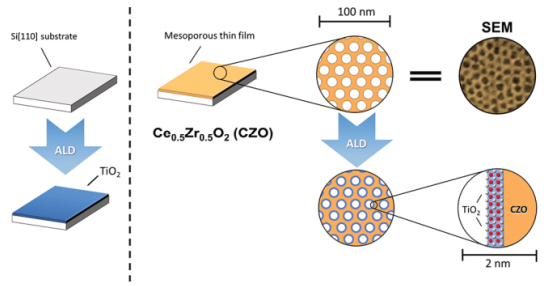

Figure 1. Schematic overview of the strategy for studying the atomic layer deposition (ALD) of thin layers of TiO_2 in the mesoporous matrix of $Ce_{0.5}Zr_{0.5}O_2$ thin films with pore sizes of 13 nm verified by top-view scanning electron microscopy (SEM) recordings. In addition, pure silicon [110] substrates were coated with TiO_2 to verify the growth rate.

question whether the bigger, spherical mesopores (ca. 15−20 nm in diameter) can be impregnated, even though the smaller channels between the spherical mesopores may limit the amount of deposited oxide on the pore surface. The films are analyzed by several state-of-the-art methods, using scanning electron microscopy (SEM) and high-resolution (scanning)

DOI: 10.1021/acs.jpcc.9b02069
J. Phys. Chem. C 2019, 123, 12851−12861

transmission electron microscopy (HR(S)TEM) to visualize the mesoporous structure, while laser ellipsometry, X-ray reflectometry (XRR), and time-of-flight secondary-ion (SI) mass spectrometry (ToF-SIMS) investigations give information about the TiO_2 content inside the porous network. Finally, X-ray diffraction (XRD), selected area electron diffraction (SAED), and the evaluation of the atomic planes in the HRTEM images are used to determine the crystal structure. Ellipsometric porosimetry was used to study the filling of mesopores upon consecutive ALD within the mesoporous films. This study is thus intended to demonstrate if and how typical laboratory characterization techniques can be used ex situ to study and validate the ALD within the interior pore structure, providing a guide to ALD-based growth of different transition-metal oxides on crystalline mesoporous substrates in general. In particular, special emphasis is put on validating the analysis of the growth/deposition of TiO_2 by using complementary techniques, each of them providing a different type of information. Furthermore, in the future, the presented mesoporous systems will allow investigating the influence of the ALD layer thickness on the physicochemical and catalytic properties, such as the catalytic performance in the SCR of NO_x using NH_3.

■ EXPERIMENTAL SECTION

Preparation of the Mesoporous Thin Films. The fabrication of mesoporous CZO thin films[46] using an evaporation-induced self-assembly (EISA) approach was based on a precursor solution, $CeCl_3{\cdot}7H_2O/ZrOCl_2{\bullet}8H_2O/PIB_{50}$-*b*-$PEO_{45}/H_2O$/2-methoxy-ethanol/ethanol, mole ratio 0.5:0.5:0.005:18:10:35. PIB_{50}-*b*-PEO_{45} (50 mg; BASF, Ludwigshafen, Germany) was added to 1 mL of ethanol (99.8%, Merck), while 110 mg of $CeCl_3{\bullet}7H_2O$ (98%, Sigma-Aldrich) and 92 mg of $ZrOCl_2{\bullet}8H_2O$ (99.9%, Alfa Aesar) were dissolved in 0.5 mL of ethanol and 0.5 mL of 2-methoxy-ethanol (99%, Alfa Aesar) in both cases at room temperature. Both mixtures were treated in an ultrasonic bath for 30 min at 35 °C and 80 kHz. The solutions were cooled down to room temperature and mixed together. After 5 min stirring, 0.1 mL of distilled H_2O was added to the solution to start the hydrolysis process.

After a stirring time of 90 min, the solution was freed from agglomerates using 0.2 μm syringe filters. A small amount (100 μL) of this solution was taken and deposited on a partially oxidized 2 in. Si[110] wafer rotating at 1000 rpm for 60 s using a spin Coater Kit SCK-200P from Instras Scientific. The relative humidity inside the chamber was kept constant at 20%, utilizing a custom-made glass enclosure. The films were treated at such low relative humidity for additional 3 min and then transferred to a preheated furnace at 130 °C to force the solvent to evaporate. Afterward, the films were aged at 300°C in air for 12 h to remove the structure-directing agent. In the final step, the coated substrates were annealed to 600 °C in air to obtain crystalline CZO thin films and cut into 1 × 1 cm^2 pieces for the ALD procedure.

ALD. Si[110] wafers and the mesoporous CZO thin films were coated with TiO_2 using a PicoSun R200 ALD reactor. The deposition was performed using a reactor temperature of 200 °C with an intermediate space flow between the reactor and the vacuum pump of 150 sccm nitrogen, while 80 sccm nitrogen was carried through the precursor lines. A typical ALD cycle consisted of a 0.1 s $TiCl_4$ pulse followed by a 35 s purging step with nitrogen. Afterward, H_2O was pulsed for 0.1 s into the reaction chamber. A last purging step of 35 s using nitrogen completed the cycle (see Figure 2). To achieve a higher dwell time of the precursor in the reaction chamber allowing the precursor to reach every pore in the complex oxide, the PICOFLOW diffusion enhancer was applied. Within 1.5 s, the flow rate of the carrier gas was throttled to 40 sccm and the valve at the end of the reaction chamber was closed. After 1.3 s, the precursor pulse of 0.1 s was initiated. In the next 30 s, the gaseous precursors are able to chemisorb on the substrate surface and the nonadsorbed precursor and possible byproducts were flushed out of the chamber. The thin films were coated using 0, 5, 10, 25, 50, 100, 150, and 200 cycles, which are labeled as 0c, 5c, ..., 200c in the following work.

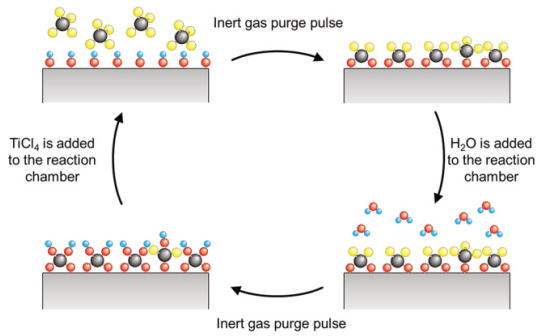

Figure 2. Schematic overview of the ALD process for preparing thin films of TiO_2. The precursors are $TiCl_4$ and H_2O, while nitrogen was used as the inert gas.

Characterization of the Coated and Noncoated Mesoporous Thin Films. Scanning electron microscopy (SEM) images were recorded using the model Merlin by Zeiss with an acceleration voltage of 2 keV and a current of 50 pA. To increase the conductivity of the samples, the films were sputtered with platinum for 10 s with an applied current of 40 mA. The acquired mesopores were sized by using the program Fiji.app. For every determined pore size, the diameters of 100 mesopores were measured. The crystalline phases of the thin films were studied by grazing-incidence X-ray diffraction (GI-XRD) acquired from a PANalytical X'Pert[3] MRD diffractometer. An incidence angle of ω = 0.25° was set at which the samples were scanned in the 2θ range of 20−70° with a scan speed of 0.6° min^{-1} and a step size of 0.01° using 2θ mode. The crystallite sizes were calculated applying the Scherrer equation[55] on the wide-angle reflections. The X-ray reflectivity measurements were performed on a PANalytical X'Per[3] MRD diffractometer. Here, the films were investigated using $2\theta/\omega$ mode in the incident angle scan range of 0.1−2°. The data analysis was performed utilizing the corresponding software X'Pert Reflectivity. All of the X-ray experiments were done using Cu Kα radiation. The thicknesses of the films were determined using a SE400adv laser ellipsometry by Sentech, which is equipped with a HeNe laser (633 nm). The samples were measured at the specific angle of 70° assuming a two-model system consisting of the CZO film and the Si[110] substrate. For the time-of-flight secondary-ion mass spectrometry (ToF-SIMS), a ToF-SIMS 5-100 model by IonTOF GmbH was used with an acceleration voltage of 25 keV for the Bi(I) primary-ion source. The depth profiles were recorded using Cs ions at 500 eV and a current of 50 nA. Only 50 × 50

DOI: 10.1021/acs.jpcc.9b02069
J. Phys. Chem. C 2019, 123, 12851−12861

μm^2 of the generated 100 × 100 μm^2 crater was analyzed with a resolution of 256 × 256 pixels^2. The measurements were carried out under charged compensation.

TEM samples were prepared by conventional mechanical grinding followed by argon ion milling until electron transparency in a GATAN precision ion polishing system. The STEM measurements were carried out in a CS-corrected JEOL JEM 2200FS operating at 200 kV. The high-angle annular dark-field signal was utilized for the imaging. This signal provides *z*-contrast, which allows to differentiate between the different materials in the samples.[56]

For the ellipsometric porosimetry, the refractive index as well as the thickness of films were measured using a variable-angle spectroscopic ellipsometer (VASE) M2000DI from Woollam. The data were recorded with an incident angle of 70°, and the thickness and refractive index were obtained at 700 nm by using a Cauchy model[57] for fitting ellipsometric data between 450 and 1000 nm wavelengths. The films were exposed to different relative pressures of ethanol achieved by mixing ethanol and dry air in different ratios using two mass flow controllers. While increasing the relative pressure of ethanol from 0 to 100% in 20 min, the isotherm points were recorded every 20 s. The calculation of the pore volume was then determined by a previously reported procedure.[58]

■ RESULTS AND DISCUSSION

The mesoporous CZO thin films acting as the model system for the atomic layer deposition were prepared using solutions of the corresponding metal salts ($CeCl_3 \cdot 7H_2O$ and $ZrOCl_2 \bullet 8H_2O$) and the structure-directing block copolymer PIB_{50}-*b*-PEO_{45}.

In this so-called EISA approach,[59] the inorganic precursor and the organic template were put together in a mixture of ethanol and 2-methoxy-ethanol. Via spin coating, the solution was deposited on a partially oxidized Si[110] substrate to produce thin films with initial thicknesses of around 100 nm. A following annealing step decomposed the polymeric template and induced the crystallization eventuating in the desired mesoporous CZO thin film with a cubic arrangement of the mesopores, which was proven by SAXS measurements and SEM recordings in previous works.[46,60] The obtained mesoporous structure depends on the used block copolymer. In this work, 14 nm mesopores were obtained, which is common for PIB_{50}-*b*-PEO_{45}.[42,44,45] Furthermore, interconnecting channels between two mesopore layers perpendicular to the substrate are present (see the SEM image in Figure 1) allowing a gaseous precursor used in the ALD to reach the entire surface of the mesopore network.

To calculate the growth rate of TiO_2, Si[110] wafers were coated with TiO_2 by ALD using the same deposition parameters as using the mesoporous samples. The growth rate of TiO_2 can be determined using laser ellipsometry by measuring the thickness after different numbers of applied ALD cycles (Figure 3). However, as the thicknesses after 5, 10, 25, and 50 cycles are below the detection limit of the ellipsometric analyses, only 100, 150, and 200 cycles are taken into account for the calculation of growth rate. The resulting growth rate for TiO_2 using the diffusion-enhancer function of our ALD setup is 0.067 nm per cycle, i.e., it is linear. However, the deposition rate for low number of cycles was reported to follow a nonlinear trend.[61] In the beginning, the deposition is supposed to be aggravated, as the precursor has to attach to the hydroxyl group on the surface of the silicon substrate, while

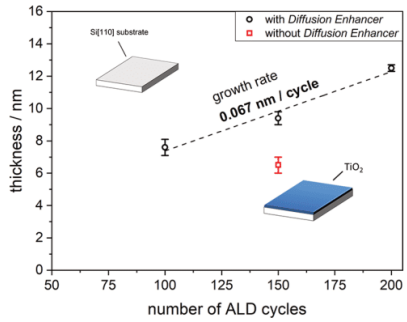

Figure 3. Thickness of the TiO_2-deposited Si[110] substrates depending on the number of ALD cycles. The dashed line illustrates the assumption concerning the growth rate. Additionally, the obtained thickness after 150 cycles with (black) and without using the diffusion-enhancer function (red) is shown.

after one complete cycle, the precursor reacts with Ti−OH groups. This assumption is, of course, only the case under the supposition that $TiCl_4$ chemisorbs on the substrate surface as a perfect monolayer entirely. The diffusion-enhancer function increases the dwell time of the titanium precursor $TiCl_4$ and H_2O in the ALD reactor and, hence, the contact with the substrates. It allows the precursor to chemisorb on more active spots than without using the function and therefore covering more area of the substrate and leading to a higher surface saturation per cycle. Hence, the growth rate is increased. Especially with complex substrates like mesoporous thin films, this higher resting time facilitates the diffusion in the porous network and allows coating even the lowermost pore layer. However, when transferring the growth rate obtained by coating the Si wafers to the deposition on mesoporous thin films, one has to take into account that a different roughness of the substrate influences the growth rate as shown by Langner et al.[62]

Using different numbers of ALD cycles, TiO_2 was then deposited on the mesoporous CZO thin films. The changes of thickness and refractive indices depending on the number of ALD cycles were investigated using laser ellipsometry (see Figure 4). While the thickness of the CZO films after 5 and 10 cycles remains constant at 92 nm, the refractive index of these films increases. After 25 cycles, the film slightly raises in thickness and refractive index, which is continued even for 50 cycles. For 100, 150, and 200 cycles, the thickness increases faster eventuating in a 13 nm coating on top of the mesoporous film. Although a direct differentiation of the original film and the added layer is not possible, the results indicate a TiO_x layer forming especially with higher cycle counts. Moreover, the alteration of the refractive index depending on the cycle number shows a saturation, and no significant change of the refractive index is observed after 50 cycles. Even with a growing TiO_2 layer on top, the refractive index remains constant. The resulting refractive index of around 2.14 between 50 and 200 cycles is still lower than the one of dense CZO[63] and anatase determined by the ellipsometric studies of the coated silicon substrates suggesting a mixture of CZO and TiO_2 for the measured films. The rising refractive index for the films after 5, 10, and 25 cycles reveals a possible deposition in the mesopores, as no significant thickness rise was detected. A decrease in the pore size and therefore in porosity due to TiO_2 attaching to the pore surface

DOI: 10.1021/acs.jpcc.9b02069
J. Phys. Chem. C 2019, 123, 12851−12861

The Journal of Physical Chemistry C Article

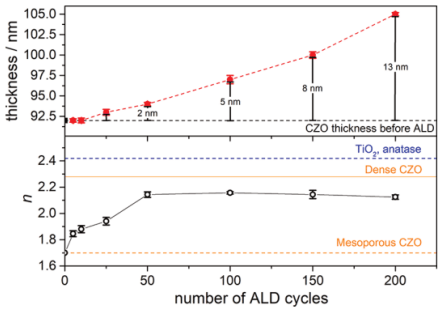

Figure 4. Thickness (top) and refractive index (bottom) of the mesoporous CZO film before and after applying a certain number of ALD cycles, determined by laser ellipsometry performed using λ = 633 nm. The difference in size between the sample before and after the deposition via ALD is also displayed as well as the refractive index of anatase (blue), dense (solid line), and mesoporous (dashed line) CZO (orange). The former is based on ellipsometric studies of the deposited TiO_x film on Si[110] substrates.

raises the refractive index above the initial index of refraction of the mesoporous CZO films.

To prove the existence of TiO_2 inside the mesopores, depth profile analyses of the films using ToF-SIMS were carried out. Secondary ions like CeO^-, ZrO^-, TiO^-, as well as Si^- anions were detected and help to clarify the location of these species inside the film. By using Cs ions as the sputter source, the film was skimmed and the subjacent layer was analyzed concerning these ions. Following this procedure, depth profiles were recorded and are shown exemplarily in Figure 5 for the films after 5, 25, and 150 cycles. Additionally, the untreated CZO film was sputtered as long as the silicon was reached. An investigation by a surface profilometer revealed a thickness of 92 nm, which is in good agreement with the results of the ellipsometric studies. As seen in Figure 5, the signals of CeO^- and ZrO^- proceed parallel to each other, indicating the equal distribution of these species in the film. The different intensity derives from the ion-specific ionization energy of the analyzed anions. The homogeneity of the TiO_x species inside the film is proven by considering the TiO^- count slope, which is also parallel with the CZO species CeO^- and ZrO^- slope. Moreover, all of the three secondary ions decrease equally when reaching the silicon substrate pointed out by the Si^- signal. With higher number of ALD cycles, the TiO^- counts increase, revealing a higher amount of Ti in the film. It is also observed that after 150 cycles, there is a thin layer of TiO_x present on top of the CZO film, which is in good agreement with the laser ellipsometric studies. Furthermore, the depth profiles show that the ablation rate differs by ionic species. While the film after five ALD cycles needs only 120 s of sputter time to be completely removed, the sample after 150 cycles requires already 230 s. As all samples were analyzed using the same instrumental parameters, a semiquantitative analysis of the TiO_x content is possible. Hence, the signal ratio of TiO^- to ZrO^- depending on the number of ALD cycles is in relation to the TiO_x amount in the film and was calculated after a sputter time of 50 s for every sample (Figure 5). Here, the saturation curve for the TiO^-/ZrO^- ratio is similar to the dependence of the refractive index as a function of the number of ALD cycles. While the TiO_x content raises within the first 50 cycles inside the mesoporous films, it remains nearly constant within the films for the following cycles. This finding indicates that the mesopores seem to be either completely filled or coated in a way that diffusion to lower pore layers is impossible.

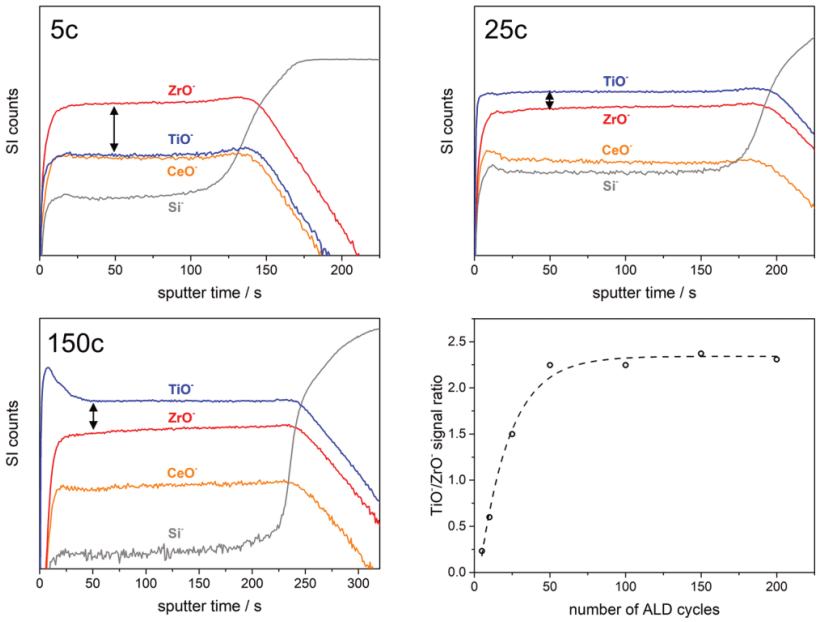

Figure 5. ToF-SIMS depth profiles of the mesoporous CZO film after 5, 25, and 150 ALD cycles. Next to the ions derived from the thin film (TiO^-, ZrO^-, and CeO^-), the signal from the utilized silicon substrate (Si^-) is depicted by plotting the secondary-ion (SI) counts logarithmic dependent on the sputter time. In addition, the signal ratio of TiO^- to ZrO^- at 50 s of sputtering in relation to the ALD cycles is shown.

DOI: 10.1021/acs.jpcc.9b02069
J. Phys. Chem. C 2019, 123, 12851−12861

Further deposition cycles at the given ALD conditions only add TiO_x layers on the top of the film, implied by the TiO^- signal maximum before reaching the mesoporous CZO network for the film after 150 cycles. As after every sputter step an area of $50 \times 50\ \mu m^2$ was investigated, 3D topographical images were calculated as shown in Figure 6 for the uncoated

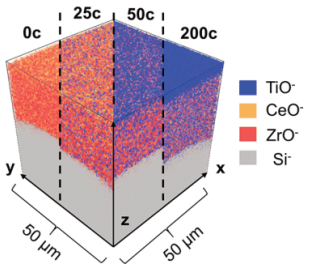

Figure 6. Three-dimensional (3D) topographic images based on the ToF-SIMS depth profiles for the untreated mesoporous CZO films, as well as after 25, 50, and 200 ALD cycles. The *z* axis corresponds to the sputter time.

CZO film, as well as after 25, 50, and 200 cycles of the atomic layer deposition. Here, the layer on top of the CZO film is even more evident, while the content of TiO_x inside the film stays nearly constant between the samples after 50 and 200 ALD cycles. This observation indicates again that the pores in the sublayers are not accessed by the gaseous ALD precursors and only a top layer on the CZO is growing, which differs slightly from the obtained thickness on silicon substrates. The disparity occurs as the mesoporous CZO and Si substrates are quite different concerning their roughness, material properties, as well as the specific surface area. The latter gives diffusion processes a higher impact on the growth rate.

To verify the pore arrangement and the TiO_2 deposition on the topmost pore layer, the films were analyzed using SEM (see Figure 7). The uncoated sample reveals an ordered array

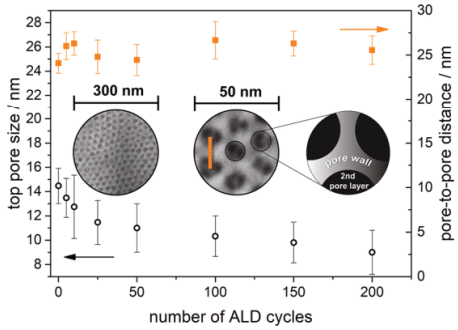

Figure 7. Pore size (black circles) and pore-to-pore distances (orange rectangles) based on the SEM images for the uncoated and coated mesoporous CZO using different numbers of ALD cycles.

of mesopores with ca. 14 nm diameter (top view), which shrink with increasing number of ALD cycles. As the same procedure for a Pt overcoat was used to increase the conductivity of the analyzed samples, the determined pore size may be a bit smaller than the actual one without an overcoat. Similar to the ToF-SIMS and ellipsometry results, the mesopore size drops significantly until 50 cycles and then slowly decreases down to 9 nm in diameter after 200 ALD cycles (see Figure 8), whereas the pore-to-pore distance remains almost constant for every sample at 25 nm. By considering the shrinkage of the mesopore size, the width of pore walls enlarges with the increasing number of ALD cycles.

However, in contrast to the assumption based on the ToF-SIMS conclusion that the pores are possibly filled, mesopores are still visible according to the SEM images. In general, SEM analysis reveals only the film from a top view (see Figure 8). While the second pore layer is visible in the uncoated CZO films even up to 10 cycles, it is not detectable from 25 cycles onward. This observation implies that the interconnecting channels between the pore layers are filled preventing the access of the gaseous ALD precursors to the inner pore surfaces. As the ToF-SIMS and ellipsometric studies suggest a TiO_x layer thickness of around 13 nm after 200 cycles, we assume the layer was deposited as pillars around the existing mesopores. Hence, in a top view, the mesopores are still visible, but are decreased only slightly in their lateral diameter as the pillars coalesce slowly.

The thin films were also investigated using X-ray reflectivity (see Figure 9). Due to the present ordered cubic arrangement of the mesopores, the (111) Bragg signal is visible next to the critical angle and the common fringes. The critical angle shifts to higher *s*-values or incident angles for higher ALD cycles. As the critical angle is directly related to the density of the materials, a density increase from 1.9 to 3.1 g cm^{-3} indicates the filling of the mesopores, while these values are much lower than the crystallographic densities of pure CeO_2 (7.3 g cm^{-3}), tetragonal ZrO_2 (6.1 g cm^{-3}), or TiO_2-anatase (3.89 g cm^{-3}). Obviously, these low density values are due to the significant mesoporosity of the CZO films as well as in the presence of small crystallites with a few nanometers in diameter decreasing the density in comparison to the bulk equivalent. However, the enhancement in the density being stronger up to 50 cycles than for 100, 150, and 200 cycles implies the impregnation of the inner mesopores until 50 cycles. Hence, the mesoporosity decreases and the density increases accordingly, which is in good agreement with the refractive index results based on the ellipsometric measurements (Figure 4). Furthermore, the visible Bragg maximum related to the cubic pore arrangement perpendicular to the substrate plane broadens after 5, 10, and 25 ALD cycles and vanishes after undergoing 50 growth cycles. As the maximum originates from electron density differences and its width corresponds to the variation of these difference values, the original mesopores surrounded by pure CZO are coated with a different material, e.g., TiO_2, on the pore surface. After 50 cycles, the interconnecting channels are filled and the gaseous ALD precursors can only reach the topmost pore layers. The recurring electron density disparity necessary for the Bragg signal to be detected disappears and hence the signal vanishes, as seen in Figure 9. As the Bragg signal derives from the cubic arrangement of the mesopores, the visible signal corresponds to the (111) reflection. By multiplying the reciprocal *s* value of the slope maximum of the different samples by the square root of 3, the XRR data reveal a pore-to-pore distance in the *z*-direction of around 18 nm. Due to the heat treatment of the film during its preparation, the mesopores undergo an ellipsoidal deformation and overall shrinkage in the direction perpendicular to the substrate level, resulting in a smaller pore-to-pore distance in comparison to the obtained values in the *x*- and *y*-directions, respectively, as

DOI: 10.1021/acs.jpcc.9b02069
J. Phys. Chem. C 2019, 123, 12851−12861

The Journal of Physical Chemistry C Article

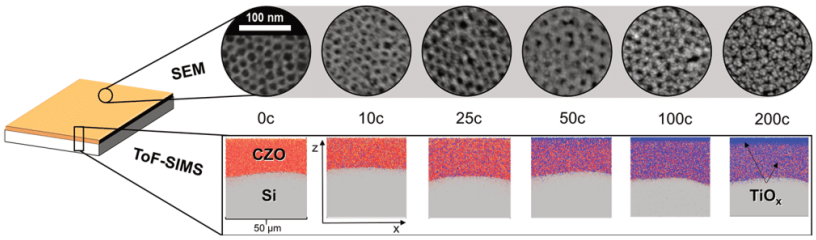

Figure 8. Differentiation of the SEM and ToF-SIMS investigations for the uncoated and coated mesoporous CZO films. The SEM images reveal morphological changes of the porous structure from a top view of the film (top), while the ToF-SIMS depth profile shows the secondary-ion distribution inside the whole film (bottom).

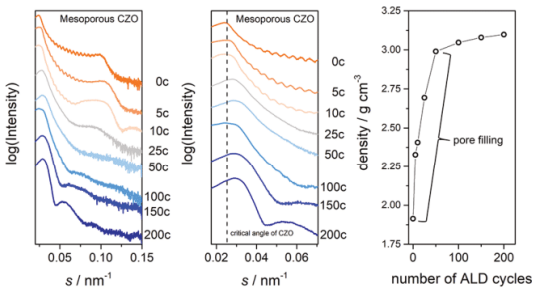

Figure 9. XRR data of the CZO mesoporous thin films before and after depositing TiO_2 via ALD using different numbers of growth cycles, and the calculation of the average density based on the position of the critical angle.

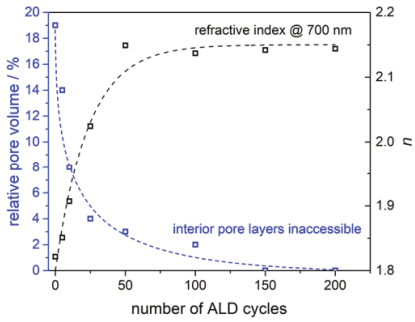

Figure 10. Refractive index n at 700 nm and relative pore volume determined by ellipsometric porosimetry (EP) dependent on the number of ALD cycles. The dotted lines serve as a guide to the eye to illustrate the curve slope.

presented in Figure 7, based on the SEM investigations (around 25 nm). Finally, the second maximum observed for the sample after 200 ALD cycles is a fringe and was used together with the third maximum/second fringe to determine the thickness of the TiO_x top layer to be 12 nm, which is in accordance with the ellipsometric result providing 13 nm.

To analyze the mesoporosity, nitrogen physisorption measurements were performed on a 500 nm film prepared by repetitive coatings (see Figure S1). The investigation reveals a pore size distribution with an average size of around 13 nm, with a second maximum of around 5−6 nm. The latter can be assigned to the interconnecting channels and seem to be the limiting factor for the ALD, which is in good agreement with the work of Dendooven et al.[40] However, after five growth cycles via ALD, the adsorbed volume already shrinks down to 50% in comparison to the uncoated film. After 10 cycles, the pore volume remains constant implying the filling of the interconnecting channels, preventing further deposition inside the mesopores. This contradicts the observation made via ToF-SIMS and laser ellipsometry. A possible reason for this result is a stacking mismatch of the various mesoporous CZO layers caused by the repetitive coating resulting in a different model system compared to the single-coated CZO films. Unfortunately, using the given method without multilayer coating, only thicknesses around 100 nm are achieved, which is too thin for the nitrogen physisorption measurements.

To determine the relative pore volume defined as the volume fraction of pores in an otherwise presumed dense film, environmental ellipsometric porosimetry (EEP) analyses were performed on the coated thin films. The results are shown next to the measured refractive index at 700 nm in Figure 10. As expected, the relative pore volume quickly decreases from around 20% for the uncoated sample with increasing number of ALD cycles and reaches less than 4% (±2%) above 50 cycles. This is in good agreement with the findings of the laser ellipsometry and ToF-SIMS studies as after 50 cycles the pores are not accessible anymore for the gaseous ALD precursor as well the solvent used in the EEP measurement. The interconnecting channels are filled and prohibit the access to the pores in the depth. While the mesopore volume can be determined with reasonable precision, the evaluation of the pore size distribution was associated with quite high fundamental uncertainty: the pore-size-dependent condensation of the used fluid (ethanol) within the mesopores is substantially superimposed by the wetting of the oxidic surface by ethanol. Since the wettability in general considerably affects the calculation of pore sizes (see, e.g., the Kelvin equation) and since the wetting behavior is unknown in this particular case, no pore size distribution is shown based on EEP (see EEP data in Figure S2).

While all of these analyses suggest an impregnation of the mesopores, GI-XRD measurements were performed on the sample to study the presence of crystalline TiO_2. The results are shown in Figure 11 for the uncoated films as well as the films after the ALD procedure. The cubic structure of $Ce_{0.5}Zr_{0.5}O_2$ based on the reference pattern is observed for every sample, while the sharp reflections can be assigned to the Si[110] substrate. Using the Scherrer equation, the average crystallite size for CZO is 7 nm. However, there is no evidence of a TiO_2 crystal phase. When annealing the sample after the deposition procedure to 600 °C for 10 min and cooling down to room temperature, the (011) reflection of anatase is visible for the coated film after 200 cycles but not after 25 cycles. This

DOI: 10.1021/acs.jpcc.9b02069
J. Phys. Chem. C 2019, 123, 12851−12861

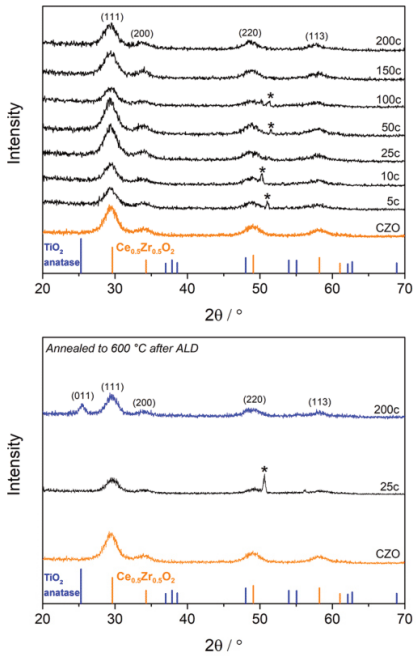

Figure 11. (Top) X-ray diffraction pattern of the mesoporous CZO thin film before and after the ALD using different amount of cycles. (Bottom) X-ray diffraction pattern of the mesoporous thin film after 0, 25, and 200 ALD growth cycles, followed by an annealing step to 600 °C. In both cases, the reference pattern for the cubic lattice of $Ce_{0.5}Zr_{0.5}O_2$ (ICDS 98-016-1650; orange) and anatase (ICDS 98-015-4604) are shown. The reflections marked with an asterisk derive from the Si[110] substrate.

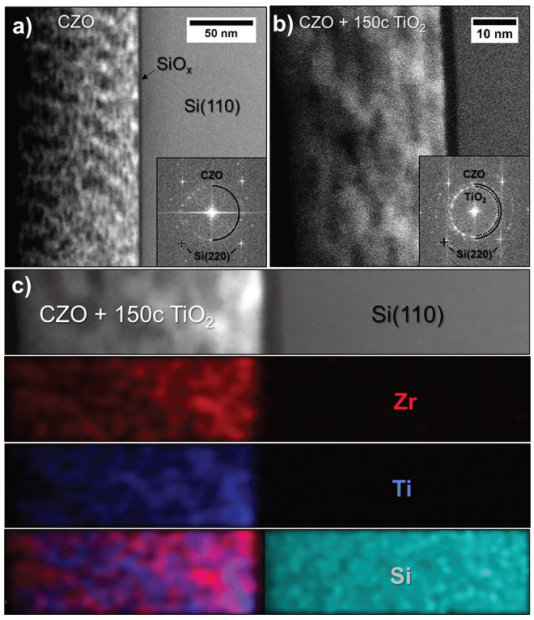

Figure 12. High-resolution STEM images of the untreated mesoporous CZO thin film before (a) and after 150 TiO_2-ALD cycles (b). Moreover, the FFT calculations based on the atomic lattices are displayed within the STEM images (a) and (b). EDX measurements of the film after 150 cycles are additionally presented for Zr, Ti, and Si (c).

observation can be explained in two ways: On the one hand, the amount of presumably amorphous TiO_x in the pores crystallizing into anatase is insufficient for the XRD investigations to be detected. On the other hand, only the 13 nm TiO_x layer on top of the film shown by ToF-SIMS and laser ellipsometry can crystallize, forming anatase after the postdeposition heating step.

Finally, the films were analyzed using transmission electron microscopy (TEM, Figure S3) and high-resolution STEM (HRSTEM) to visualize the TiO_x coating of the mesoporous CZO network. The results are presented in Figures S4 and 12a–c. The brightness in these images derives from the *z*-contrast, meaning that compounds with a higher atomic number appear brighter. As shown in Figure 12a, the film consists of distributed bright and dark spots, in which the latter can be assigned to the mesopores. In this cross-sectional view of the mesoporous film, the thickness is determined as 94 nm, with a 2.7 nm thick SiO_2 layer on top of the silicon substrate. By comparing the HRSTEM images of the films before and after 150 ALD cycles, the latter appears to have a reduced contrast implying the filling of the mesopores. To distinguish between TiO_x and CZO, local energy-dispersive X-ray (EDX) measurements were performed. The results shown in Figure 12c illustrate the distribution of the elements Ti, Zr (representative for the CZO film), and Si. The overlay of the Ti and Zr signals demonstrates the complementary distribution of these elements inside the film, giving direct evidence that the pores are indeed coated with Ti or TiO_x, respectively. Although these images do not provide information on the interconnecting channels, the occurring crystal phases can be determined by considering the present atomic planes and determining the interplanar spacing d of the samples using a fast Fourier transformation (FFT) calculation. The latter is shown for both analyzed films in Figure 12a,b. These FFT patterns reveal the presence of $Ce_{0.5}Zr_{0.5}O_2$, as the brightest circle has an interplanar spacing d of 0.305 nm, which can be assigned to the (111) reflection of the tetragonal crystal structure. Furthermore, the sample exposed to 150 ALD cycles features an additional diffraction ring, which was measured to possess an interplanar spacing d = 0.350 nm, which corresponds to the (011) reflection of anatase.

According to the ToF-SIMS results, there is no further impregnation of the pores after 50 cycles (see Figure 5). Therefore, we conclude that for the samples after 50 ALD cycles, the existent TiO_x inside the mesopores is indeed crystalline TiO_2 in the anatase crystal structure.

■ CONCLUSIONS

This work summarizes different characterization methods to identify and characterize the infiltration of TiO_2 into an ordered mesoporous $Ce_{0.5}Zr_{0.5}O_2$ structure using ALD. It was verified by ToF-SIMS and ellipsometric investigations that TiO_2 was deposited into the mesopores up to 50 ALD cycles, followed by the formation of a top layer of TiO_2 for subsequent cycles, still maintaining observable pore sizes of around 10 nm detectable in SEM images. While XRD does not clarify the existing crystal structure of TiO_2 inside the pores, the FFT of HRSTEM images proves the deposited anatase

DOI: 10.1021/acs.jpcc.9b02069
J. Phys. Chem. C 2019, 123, 12851−12861

The Journal of Physical Chemistry C Article

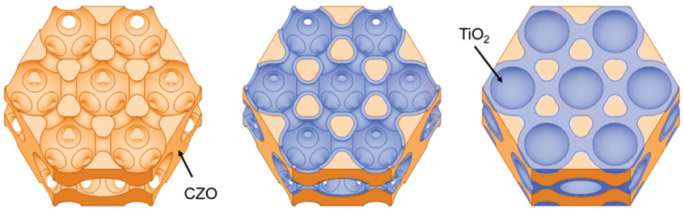

Figure 13. Schematic model of the TiO_2 deposition in the mesoporous CZO film using ALD. TiO_2 covers the surface of the 13 nm mesopores as well as the smaller interconnecting channel leading to a decrease in the average pore size. At a certain number of ALD cycles, the channels are completely filled, preventing the gaseous precursor to reach the inner pore layers while still retaining pores in the topmost pore layer.

structure. EDX measurements of the mesoporous film verified additionally the complementary distribution of CZO and TiO_2. The complete procedure is schematized in Figure 13. The catalytic performance of the herein prepared CZO/TiO_2 mesoporous thin films depending on the TiO_2 layer thickness will be addressed in upcoming studies.

All in all, this case study shows the successful deposition of an active species inside a mesoporous network by using ex situ characterization techniques and serves therefore as a guideline for future atomic layer depositions for different metal oxides into complex, porous substrates.

■ ASSOCIATED CONTENT

Supporting Information

The Supporting Information is available free of charge on the ACS Publications website at DOI: 10.1021/acs.jpcc.9b02069.

> Nitrogen physisorption measurements of repetitive coated mesoporous thin films before and after the ALD process; EEP isotherms; transmission electron microscopy (TEM) images; and selected area electron diffraction (SAED) measurements of the coated and uncoated films (PDF)

■ AUTHOR INFORMATION

Corresponding Authors

*E-mail: over@uni-giessen.de (H.O.).
*E-mail: bernd.smarsly@phys.chemie.uni-giessen.de (B.M.S.).

ORCID

C. Boissiere: 0000-0003-1212-6850
H. Over: 0000-0001-7689-7385
B. M. Smarsly: 0000-0001-8452-2663

Author Contributions

The manuscript was written through contributions of all authors. All authors have given approval to the final version of the manuscript.

Notes

The authors declare no competing financial interest.

■ ACKNOWLEDGMENTS

The authors thank Philip Klement for the guidance to deposit TiO_2 with the atomic layer deposition, and Adrian Schürmann for the schematic 3D model. The authors also thank Sebastian Werner, Kevin Turke, and Felix Badaczewski for the nitrogen physisorption measurements, as well as Kristin Kirchberg for the TEM and SAED recordings. This project was supported by the Center for Materials Research (LaMa) of the Justus-Liebig-University Giessen, Germany.

■ REFERENCES

(1) Miller, D. R.; Akbar, S. A.; Morris, P. A. Nanoscale Metal Oxide-Based Heterojunctions for Gas Sensing: A Review. *Sens. Actuators, B* **2014**, *204*, 250−272.
(2) Quackenbush, N. F.; Paik, H.; Woicik, J. C.; Arena, D. A.; Schlom, D. G.; Piper, L. F. J. X-Ray Spectroscopy of Ultra-Thin Oxide/Oxide Heteroepitaxial Films: A Case Study of Single-Nanometer VO_2/TiO_2. *Materials* **2015**, *8*, 5452−5466.
(3) Morgan, P. E. D.; Marshall, D. B. Functional Interfaces for Oxide/Oxide Composites. *Mater. Sci. Eng., A* **1993**, *162*, 15−25.
(4) Shi, J. On the Synergetic Catalytic Effect in Heterogeneous Nanocomposite Catalysts. *Chem. Rev.* **2013**, *113*, 2139−2181.
(5) Xu, Z.; Yu, L.; Xu, X.; Miao, J.; Jiang, Y. Effect of Oxide/Oxide Interface on Polarity Dependent Resistive Switching Behavior in ZnO/ZrO_2 Heterostructures. *Appl. Phys. Lett.* **2014**, *104*, No. 192903.
(6) Jiang, R.; Tung, S. o.; Tang, Z.; Li, L.; Ding, L.; Xi, X.; Liu, Y.; Zhang, L.; Zhang, J. A Review of Core-Shell Nanostructured Electrocatalysts for Oxygen Reduction Reaction. *Energy Storage Mater.* **2018**, *12*, 260−276.
(7) Trovarelli, A.; de Leitenburg, C.; Boaro, M.; Dolcetti, G. The Utilization of Ceria in Industrial Catalysis. *Catal. Today* **1999**, *50*, 353−367.
(8) Ahn, S. H.; Lee, N.; Choi, C.; Shin, S. W.; Han, Y.; Park, H. C. Feasibility Study of Fe_3O_4 /TaO_x Nanoparticles as a Radiosensitizer for Proton Therapy. *Phys. Med. Biol.* **2018**, *63*, No. 114001.
(9) Zhong, C. J.; Maye, M. M. Core-Shell Assembled Nanoparticles as Catalysts. *Adv. Mater.* **2001**, *13*, 1507−1511.
(10) Artiglia, L.; Agnoli, S.; Paganini, M. C.; Cattelan, M.; Granozzi, G. Core-Shell Nanoparticles as Artificial Enzymes with Peroxidase-Like Activity. *ACS Appl. Mater. Interfaces* **2014**, *6*, 20130−20136.
(11) Agnoli, S.; Reeder, A. E.; Senanayake, S. D.; Hrbek, J.; Rodriguez, J. A. Structure and Special Chemical Reactivity of Interface-Stabilized Cerium Oxide Nanolayers on TiO_2(110). *Nanoscale* **2014**, *6*, 800−810.
(12) Bai, J.; Sun, X.; Han, G.; Diao, G. Double-Shell CeO_2@TiO_2 Hollow Spheres Composites with Enhanced Light Harvesting and Electron Transfer in Dye-Sensitized Solar Cells. *J. Alloys Compd.* **2017**, *722*, 864−871.
(13) Saqer, S. M.; Kondarides, D. I.; Verykios, X. E. Catalytic Oxidation of Toluene over Binary Mixtures of Copper, Manganese and Cerium Oxides Supported on γ-Al_2O_3. *Appl. Catal., B* **2011**, *103*, 275−286.
(14) Saqer, S. M.; Kondarides, D. I.; Verykios, X. E. Catalytic Activity of Supported Platinum and Metal Oxide Catalysts for Toluene Oxidation. *Top. Catal.* **2009**, *52*, 517−527.
(15) Liu, R.; Duay, J.; Lee, S. B. Heterogeneous Nanostructured Electrode Materials for Electrochemical Energy Storage. *Chem. Commun.* **2011**, *47*, 1384−1404.
(16) Nong, H. N.; Oh, H. S.; Reier, T.; Willinger, E.; Willinger, M. G.; Petkov, V.; Teschner, D.; Strasser, P. Oxide-Supported $IrNiO_x$ Core-Shell Particles as Efficient, Cost-Effective, and Stable Catalysts for Electrochemical Water Splitting. *Angew. Chem., Int. Ed.* **2015**, *54*, 2975−2979.
(17) Moser, M.; Mondelli, C.; Schmidt, T.; Girgsdies, F.; Schuster, M. E.; Farra, R.; Szentmiklósi, L.; Teschner, D.; Pérez-Ramírez, J.

Supported CeO_2 catalysts in Technical Form for Sustainable Chlorine Production. *Appl. Catal., B* **2013**, *132–133*, 123–131.
(18) Huang, H.; Gong, H.; Chow, C. L.; Guo, J.; White, T. J.; Tse, M. S.; Tan, O. K. Low-Temperature Growth of SnO_2 Nanorod Arrays and Tunable n-p-n Sensing Response of a ZnO/SnO_2 heterojunction for Exclusive Hydrogen Sensors. *Adv. Funct. Mater.* **2011**, *21*, 2680–2686.
(19) He, Y. B.; Li, G. R.; Wang, Z. L.; Su, C. Y.; Tong, Y. X. Single-Crystal ZnO Nanorod/Amorphous and Nanoporous Metal Oxide Shell Composites: Controllable Electrochemical Synthesis and Enhanced Supercapacitor Performances. *Energy Environ. Sci.* **2011**, *4*, 1288–1292.
(20) Pagán-Torres, Y. J.; Gallo, J. M. R.; Wang, D.; Pham, H. N.; Libera, J. A.; Marshall, C. L.; Elam, J. W.; Datye, A. K.; Dumesic, J. A. Synthesis of Highly Ordered Hydrothermally Stable Mesoporous Niobia Catalysts by Atomic Layer Deposition. *ACS Catal.* **2011**, *1*, 1234–1245.
(21) Obaidat, I. M.; Nayek, C.; Manna, K. Investigating the Role of Shell Thickness and Field Cooling on Saturation Magnetization and Its Temperature Dependence in Fe_3O_4/γ-Fe_2O_3 Core/Shell Nanoparticles. *Appl. Sci.* **2017**, *7*, 1269.
(22) Burkett, S. L.; Sims, S. D.; Mann, S. Synthesis of Hybrid Inorganic-Organic Mesoporous Silica by Co-Condensation of Siloxane and Organosiloxane Precursors. *Chem. Commun.* **1996**, 1367–1368.
(23) Aronson, B. J.; Blanford, C. F.; Stein, A. Solution-Phase Grafting of Titanium Dioxide onto the Pore Surface of Mesoporous Silicates: Synthesis and Structural Characterization. *Chem. Mater.* **1997**, *9*, 2842–2851.
(24) Maschmeyer, T.; Rey, F.; Sankar, G.; Thomas, J. M. Heterogeneous Catalysts Obtained by Grafting Metallocene Complexes onto Mesoporous Silica. *Nature* **1995**, *378*, 159–162.
(25) Jiang, S. P. A Review of Wet Impregnation - an Alternative Method for the Fabrication of High Performance and Nano-Structured Electrodes of Solid Oxide Fuel Cells. *Mater. Sci. Eng., A* **2006**, *418*, 199–210.
(26) González Vargas, O. A.; De Los Reyes Heredia, J. A.; Montesinos Castellanos, A.; Chen, L. F.; Wang, J. A. Cerium Incorporating into MCM-41 Mesoporous Materials for CO Oxidation. *Mater. Chem. Phys.* **2013**, *139*, 125–133.
(27) O'Neill, B. J.; Jackson, D. H. K.; Lee, J.; Canlas, C.; Stair, P. C.; Marshall, C. L.; Elam, J. W.; Kuech, T. F.; Dumesic, J. A.; Huber, G. W. Catalyst Design with Atomic Layer Deposition. *ACS Catal.* **2015**, *5*, 1804–1825.
(28) Mahurin, S.; Bao, L.; Yan, W.; Liang, C.; Dai, S. Atomic Layer Deposition of TiO_2 on Mesoporous Silica. *J. Non-Cryst. Solids* **2006**, *352*, 3280–3284.
(29) Alibabaei, L.; Farnum, B. H.; Kalanyan, B.; Brennaman, M. K.; Losego, M. D.; Parsons, G. N.; Meyer, T. J. Atomic Layer Deposition of TiO_2 on Mesoporous NanoITO: Conductive Core–Shell Photoanodes for Dye-Sensitized Solar Cells. *Nano Lett.* **2014**, *14*, 3255–3261.
(30) Marizy, A.; Roussel, P.; Ringuedé, A.; Cassir, M. Atomic Layer Deposition of Epitaxial CeO_2 Thin Layers for Faster Surface Hydrogen Oxidation and Faster Bulk Ceria Reduction/Reoxidation. *J. Mater. Chem. A* **2015**, *3*, 10498–10503.
(31) George, S. M. Atomic Layer Deposition: An Overview. *Chem. Rev.* **2010**, *110*, 111–131.
(32) Berland, B. S.; Gartland, I. P.; Ott, A. W.; George, S. M. In Situ Monitoring of Atomic Layer Controlled Pore Reduction in Alumina Tubular Membranes Using Sequential Surface Reactions. *Chem. Mater.* **1998**, *10*, 3941–3950.
(33) Cameron, M. A.; Gartland, I. P.; Smith, J. A.; Diaz, S. F.; George, S. M. Atomic Layer Deposition of SiO_2 and TiO_2 in Alumina Tubular Membranes: Pore Reduction and Effect of Surface Species on Gas Transport. *Langmuir* **2000**, *16*, 7435–7444.
(34) Pellin, M. J.; Stair, P. C.; Xiong, G.; Elam, J. W.; Birrell, J.; Curtiss, L.; George, S. M.; Han, C. Y.; Iton, L.; Kung, H.; et al. Mesoporous Catalytic Membranes: Synthetic Control of Pore Size and Wall Composition. *Catal. Lett.* **2005**, *102*, 127–130.
(35) Reitz, C.; Breitung, B.; Schneider, A.; Wang, D.; Von Der Lehr, M.; Leichtweiss, T.; Janek, J.; Hahn, H.; Brezesinski, T. Hierarchical Carbon with High Nitrogen Doping Level: A Versatile Anode and Cathode Host Material for Long-Life Lithium-Ion and Lithium-Sulfur Batteries. *ACS Appl. Mater. Interfaces* **2016**, *8*, 10274–10282.
(36) Sree, S. P.; Dendooven, J.; Korányi, T. I.; Vanbutsele, G.; Houthoofd, K.; Deduytsche, D.; Detavernier, C.; Martens, J. A. Aluminium Atomic Layer Deposition Applied to Mesoporous Zeolites for Acid Catalytic Activity Enhancement. *Catal. Sci. Technol.* **2011**, *1*, 218–221.
(37) Kraffert, K.; Karg, M.; Schmack, R.; Clavel, G.; Boissiere, C.; Wirth, T.; Pinna, N.; Kraehnert, R. Stabilization of Mesoporous Iron Oxide Films against Sintering and Phase Transformations via Atomic Layer Deposition of Alumina and Silica. *Adv. Mater. Interfaces* **2018**, No. 1800360.
(38) Detavernier, C.; Dendooven, J.; Sree, S. P.; Ludwig, K. F.; Martens, J. A. Tailoring Nanoporous Materials by Atomic Layer Deposition. *Chem. Soc. Rev.* **2011**, *40*, 5242–5253.
(39) Dendooven, J.; Devloo-Casier, K.; Levrau, E.; Van Hove, R.; Pulinthanathu Sree, S.; Baklanov, M. R.; Martens, J. A.; Detavernier, C. In Situ Monitoring of Atomic Layer Deposition in Nanoporous Thin Films Using Ellipsometric Porosimetry. *Langmuir* **2012**, *28*, 3852–3859.
(40) Dendooven, J.; Goris, B.; Devloo-Casier, K.; Levrau, E.; Biermans, E.; Baklanov, M. R.; Ludwig, K. F.; Van Der Voort, P.; Bals, S.; Detavernier, C. Tuning the Pore Size of Ink-Bottle Mesopores by Atomic Layer Deposition. *Chem. Mater.* **2012**, *24*, 1992–1994.
(41) Dendooven, J.; Devloo-Casier, K.; Ide, M.; Grandfield, K.; Ludwig, K. F.; Van Der Voort, P.; Bals, S.; Detavernier, C. In *In Situ Characterization of ALD in Mesoporous Thin Films by Grazing Incidence Small Angle X-Ray Scattering*, 12th International Conference on Atomic Layer Deposition (ALD 2012), 2012; p 6605.
(42) Hartmann, P.; Lee, D.; Smarsly, B. M.; Janek, J. Mesoporous TiO_2: Comparison of Splitting Reaction. *ACS Nano* **2010**, *4*, 3147–3154.
(43) Sallard, S.; Schröder, M.; Boissière, C.; Dunkel, C.; Etienne, M.; Walcarius, A.; Oekermann, T.; Wark, M.; Smarsly, B. M. Bimodal Mesoporous Titanium Dioxide Anatase Films Templated by a Block Polymer and an Ionic Liquid: Influence of the Porosity on the Permeability. *Nanoscale* **2013**, *5*, 12316–12329.
(44) Von Graberg, T.; Hartmann, P.; Rein, A.; Gross, S.; Seelandt, B.; Röger, C.; Zieba, R.; Traut, A.; Wark, M.; Janek, J.; et al. Mesoporous Tin-Doped Indium Oxide Thin Films: Effect of Mesostructure on Electrical Conductivity. *Sci. Technol. Adv. Mater.* **2011**, *12*, No. 025005.
(45) Weidmann, C.; Brezesinski, K.; Suchomski, C.; Tropp, K.; Grosser, N.; Haetge, J.; Smarsly, B. M.; Brezesinski, T. Morphology-Controlled Synthesis of Nanocrystalline η-Al_2O_3 Thin Films, Powders, Microbeads, and Nanofibers with Tunable Pore Sizes from Preformed Oligomeric Oxo-Hydroxo Building Blocks. *Chem. Mater.* **2012**, *24*, 486–494.
(46) Cop, P.; Kitano, S.; Niinuma, K.; Smarsly, B.; Kozuka, H. In-Plane Stress Development in Mesoporous Thin Films. *Nanoscale* **2018**, *10*, 7002–7015.
(47) Lee, S. M.; Lee, H. H.; Hong, S. C. Influence of Calcination Temperature on Ce/TiO_2 catalysis of Selective Catalytic Oxidation of NH_3 to N_2. *Appl. Ca.tal., A* **2014**, *470*, 189–198.
(48) Shen, Y.; Zheng, D.; Yang, B.; Ni, S.; Zhu, S. Synergetic Catalysis of Ceria and Titania for Selective Reduction of NO. *J. Rare Earths* **2012**, *30*, 431–436.
(49) Fang, J.; Bi, X.; Si, D.; Jiang, Z.; Huang, W. Spectroscopic Studies of Interfacial Structures of CeO_2-TiO_2 Mixed Oxides. *Appl. Surf. Sci.* **2007**, *253*, 8952–8961.
(50) Huang, B.; Yu, D.; Sheng, Z.; Yang, L. Novel CeO_2@TiO_2 Core–shell Nanostructure Catalyst for Selective Catalytic Reduction of NO_x with NH_3. *J. Environ. Sci.* **2017**, *55*, 129–136.

DOI: 10.1021/acs.jpcc.9b02069
J. Phys. Chem. C 2019, 123, 12851–12861

(51) Wang, H.-F.; Li, H.-Y.; Gong, X.-Q.; Guo, Y.-L.; Lu, G.-Z.; Hu, P. Oxygen Vacancy Formation in CeO_2 and $Ce_{1-x}Zr_xO_2$ Solid Solutions: Electron Localization, Electrostatic Potential and Structural Relaxation. *Phys. Chem. Chem. Phys.* **2012**, *14*, 16521−16535.
(52) King, D. M.; Liang, X.; Zhou, Y.; Carney, C. S.; Hakim, L. F.; Li, P.; Weimer, A. W. Atomic Layer Deposition of TiO_2 Films on Particles in a Fluidized Bed Reactor. *Powder Technol.* **2008**, *183*, 356−363.
(53) Reiners, M.; Xu, K.; Aslam, N.; Devi, A.; Waser, R.; Hoffmann-Eifert, S. Growth and Crystallization of TiO_2 Thin Films by Atomic Layer Deposition Using a Novel Amido Guanidinate Titanium Source and Tetrakis-Dimethylamido-Titanium. *Chem. Mater.* **2013**, *25*, 2934−2943.
(54) Aarik, J.; Aidla, A.; Uustare, T.; Kukli, K.; Sammelselg, V.; Ritala, M.; Leskelä, M. Atomic Layer Deposition of TiO_2 Thin Films from TiI_4 and H_2O. *Appl. Surf. Sci.* **2002**, *193*, 277−286.
(55) Patterson, A. L. The Scherrer Formula for X-Ray Particle Size Determination. *Phys. Rev.* **1939**, *56*, 978−982.
(56) Pennycook, S. J.; Jesson, D. E. High-Resolution Z-Contrast Imaging of Crystals. *Ultramicroscopy* **1991**, *37*, 14−38.
(57) Fujiwara, H. *Spectroscopic Ellipsometry: Principles and Applications*, 1st ed.; John Wiley & Sons Inc.: Hoboken, New Jersey, 2007.
(58) Boissiere, C.; Grosso, D.; Lepoutre, S.; Nicole, L.; Bruneau, A. B.; Sanchez, C. Porosity and Mechanical Properties of Mesoporous Thin Films Assessed by Environmental Ellipsometric Porosimetry. *Langmuir* **2005**, *21*, 12362−12371.
(59) Brinker, C. J.; Lu, Y.; Sellinger, A.; Fan, H. Evaporation-Induced Self-Assembly: Nanostructures Made Easy. *Adv. Mater.* **1999**, *11*, 579−585.
(60) Brezesinski, T.; Antonietti, M.; Groenewolt, M.; Pinna, N.; Smarsly, B. The Generation of Mesostructured Crystalline CeO_2, ZrO_2 and CeO_2-ZrO_2 Films Using Evaporation-Induced Self-Assembly. *New J. Chem.* **2005**, *29*, 237−242.
(61) Aarik, J.; Aidla, A.; Mändar, H.; Uustare, T. Atomic Layer Deposition of Titanium Dioxide from $TiCl_4$ and H_2O: Investigation of Growth Mechanism. *Appl. Surf. Sci.* **2001**, *172*, 148−158.
(62) Langner, A.; Knez, M.; Müller, F.; Gösele, U. TiO_2 Microstructures by Inversion of Macroporous Silicon Using Atomic Layer Deposition. *Appl. Phys. A Mater. Sci. Process.* **2008**, *93*, 399−403.
(63) Peña-Rodríguez, O.; Sánchez-Valdés, C. F.; Garriga, M.; Alonso, M. I.; Obradors, X.; Puig, T. Optical Properties of Ceria-Zirconia Epitaxial Films Grown from Chemical Solutions. *Mater. Chem. Phys.* **2013**, *138*, 462−467.

DOI: 10.1021/acs.jpcc.9b02069
J. Phys. Chem. C 2019, 123, 12851−12861

3.4 Comparison of In-Plane Stress Development in Sol-Gel- and Nanoparticle-Derived Mesoporous Metal Oxide Thin Films

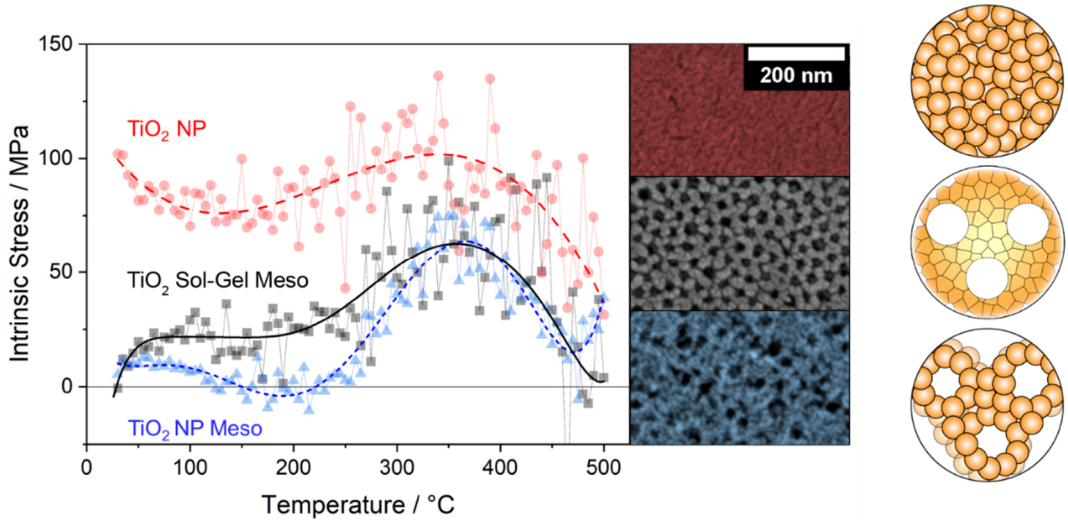

Reprinted with permission from

P. Cop, K. Hess, S. Werner, R. Meinusch, B. M. Smarsly, H. Kozuka, Comparison of In-Plane Stress Development in Sol-Gel- and Nanoparticle-Derived Mesoporous Metal Oxide Thin Films, *Langmuir,* **2019**, *35* (50)*, 16427-16437.*

https://pubs.acs.org/doi/full/10.1021/acs.langmuir.9b02455

LANGMUIR Article
Cite This: *Langmuir* 2019, 35, 16427−16437
pubs.acs.org/Langmuir

Comparison of In-Plane Stress Development in Sol−Gel- and Nanoparticle-Derived Mesoporous Metal Oxide Thin Films

Pascal Cop,[†,‡] Kevin Hess,[†,‡,§] Sebastian Werner,[†,‡] Rafael Meinusch,[†,‡] Bernd M. Smarsly,*[,†,‡] and Hiromitsu Kozuka*[,§]

[†]Physikalisch-Chemisches Institut, Justus Liebig University, Heinrich-Buff-Ring 17, 35392 Giessen, Germany
[‡]Center of Materials Research, Justus Liebig University, Heinrich-Buff-Ring 16, 35392 Giessen, Germany
[§]Department of Chemistry and Materials Engineering, Kansai University, 3-3-35 Yamate-cho, Suita, Osaka 564-8680, Japan

Supporting Information

ABSTRACT: By using an evaporation-induced self-assembly (EISA) process, mesoporous metal oxide thin films are prepared via molecular precursors undergoing a sol−gel transition or by using nanoparticle dispersions as the starting materials. Both methods are employed together with PIB_{50}-*b*-PEO_{45} as the structure-directing agent to produce porous TiO_2 and ZrO_2 thin films with spherical mesopores of around 14 nm in diameter. These nanoparticle- and sol−gel-derived films were investigated in terms of the intrinsic in-plane stress development during the heat treatment up to 500 °C to evaluate the impact of solvent evaporation, template decomposition and crystallization on the mechanical state of the film. The investigation revealed the lowest intrinsic stress for the nanoparticle-derived mesoporous film, which is assigned to the combination of the relaxing effects of the utilized diblock copolymer and the interparticular gaps between the precrystalline nanoparticles. Furthermore, the residual in-plane stress was studied after annealing steps ranging from 300 to 1000 °C and cooling down to room temperature. Here, TiO_2 nanoparticle-derived mesoporous films possess a lower residual stress than the sol−gel-derived mesoporous films, while in the case of ZrO_2 films, sol−gel-derived coatings reveal the smallest residual stress. The latter is based on the lower thermal expansion coefficient of the dominant monoclinic crystal phase compared to that of the silicon substrate. Hence, the present crystal structure has a strong influence on the mechanical state. The observation in this study helps to further understand the stress-related mechanical properties and the formation of mesoporous metal oxides.

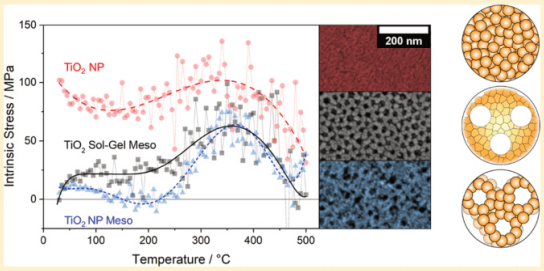

INTRODUCTION

Recent advances in the thin film technology enabled the tailor-made preparation of metal and oxide films for various applications such as (photo)catalysis, sensors, optics, and electronics.[1,2] The rising number of application fields has also affected different preparation methods to fabricate thin films with the required properties. Within these synthesis approaches there are physical methods such as the physical (PVD) or chemical vapor deposition (CVD), which can be divided even further into methods such as the atomic layer deposition (ALD) allowing the fabrication of ultrathin layers on complex substrates.[3−5] While these physical methods aim for the preparation of dense thin films, mesoporous thin films are mostly prepared wet-chemically using sol−gel-based approaches known as the evaporation-induced self-assembly process (EISA).[6,7] It permits to control the porosity as well as the size of the pores by using metal precursors in combination with different structure-directing agents in the form of surfactants or block copolymers such as poly(isobutylene)-*block*-poly(ethylene oxide) referred to as PIB_x-*b*-PEO_y[8−11] and poly(styrene)-*b*-poly(4-vinylpyridine) (PS-*b*-P4VP)[12] or the commercially available Pluronic F-127[13−15] and P-123.[16,17] With these approaches, a variety of mesoporous metal oxide thin films can be prepared including HfO_2, MgO, CeO_2, ZrO_2, TiO_2, Al_2O_3,[10,18−25] and more complex oxides such as PZT[26] or (Ca, Zn)Fe_2O_4[27,28] with a diversity of applications.[29] Next to exchanging the template, the precursor system can be substituted as well. In recent papers, nanoparticle dispersions were used instead of metal alkoxides or chlorides benefiting from a lower annealing temperature as the introduced nanoparticles are already crystalline before the deposition procedure.[19,30] Decreasing the annealing temperature also prohibits a possible disruption of the mesostructure due to the missing temperature-induced crystallization.

Benkstein and Semancik prepared nanoparticle-derived mesoporous thin films of anatase as conductometric gas sensors showing an improved gas sensitivity in comparison to dense TiO_2 thin films.[31] One possible reason for this

Received: August 8, 2019
Revised: September 30, 2019
Published: November 20, 2019

DOI: 10.1021/acs.langmuir.9b02455
Langmuir 2019, 35, 16427−16437

improvement is the higher internal surface area of the nanoparticle-derived films possessing interparticle pores in the range of 1−5 nm. Yue et al. prepared mesoporous thin films using Nb-doped TiO_2 nanoparticle dispersions with different dopant concentrations and PIB_{50}-*b*-PEO_{45} as the structure-directing agent.[32] They revealed that the open mesopore structure provides a suitable morphology for investigating the interfacial charge storage. In addition, Brezesinski et al. compared self-organized mesoporous TiO_2 using nanocrystals showing high impact on the capacitive charge storage and insertion capacities, which is ascribed to the high accessibility due to the mesoporous network.[33] Lastly, Hartmann et al. presented a study of the photoelectrochemical water splitting reaction of TiO_2 mesoporous thin films derived from a nanoparticle dispersion in comparison to a metal chloride solution.[30] In contrast to the previous studies, the nanoparticle-derived mesoporous thin film showed a weaker performance, here in the water splitting reaction, than the sol−gel-derived film, addressing the question how the choice of the metal oxide precursor affects the physicochemical properties of the final mesoporous film via fundamental structure-related characteristics.

However, when preparing dense or mesoporous films above 1 μm in thickness by a single coating step, using nanoparticle dispersions or sol−gel precursor solutions, the films are prone to crack during the firing step.[34] The cracking originates most prominently from the in-plane tensile stress development during the annealing, referred to as the intrinsic in-plane stress, which includes solvent evaporation and densification processes shrinking the films to 70% of their initial thickness.[35] During the cooling procedure to room temperature, the difference in the thermal expansion coefficients between the substrate and the film either raises or lowers the in-plane stress observed at room temperature labeled as the residual in-plane stress.[34]

For the successful preparation of thicker films without repetitive deposition, the in-plane stress must be kept low, which can be obtained by introducing additives, for example, polymers or chelating agents to the precursor solutions.[36]

In a previous study, we were able to demonstrate the in-plane stress development of sol−gel-derived mesoporous titania and ceria-zirconia thin films revealing the impact of the used structure-directing agent and different sol−gel precursors such as metal alkoxides and chlorides on the in-plane stress during the heat treatment until 500 °C.[37] Such heat treatment is commonly applied in the synthesis of mesoporous metal oxides to remove the organic template and to spur crystallization of the initially amorphous metal oxide. As stated earlier, nanoparticle dispersions are a promising alternative for preparing mesoporous thin films, but the mechanical behavior of such films during the preparation is still not fully understood. Yet, structural reorganization on the nanometer scale as a consequence of stress build-up or release can possibly impact properties such as the conductivity and so forth. In this work, we take a closer look at the in-plane stress development of nanoparticle-derived ordered mesoporous and dense thin films and compare the results with ordered mesoporous films prepared from molecular precursors ("sol−gel-derived films") to study the influence of the precursor system on mechanical properties. We focus on the investigation of intrinsic stress experienced directly after the deposition via spin-coating and during the subsequent heat treatment up to 500 °C as well as on the residual stress after cooling down to room temperature after several annealing temperatures ranging from 300 to 1000 °C. Here, we concentrate on the investigation of TiO_2 and ZrO_2 thin films templated with PIB_{50}-*b*-PEO_{45} (Figure 1) as both materials are widely used and studied in various application fields using dense films as well as the mesoporous counterpart. In addition, our previously published work revealed that the intrinsic in-plane stress development showed quite a distinction between these materials deriving from the different precursor sources (alkoxide for TiO_2 and oxychloride for ZrO_2). This study reports the as-prepared nanoparticle-derived mesoporous equivalents with pore sizes around 14 nm and intends to clarify the impact of the metal oxide precursors contributing to further understandings of the in-plane stress development in porous thin films.

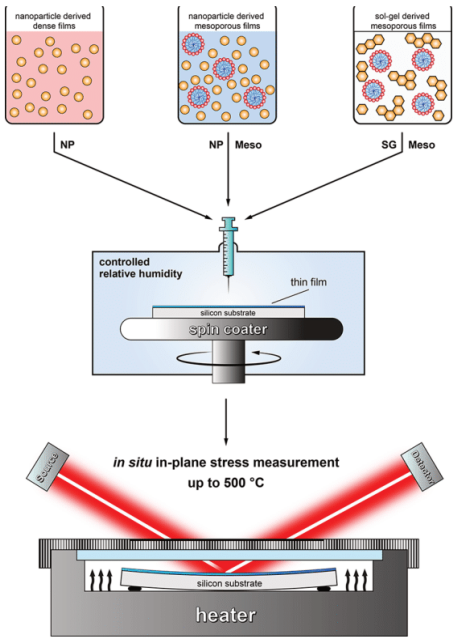

Figure 1. Schematic overview of the conceptual methodology of the study of intrinsic in-plane stress. Nanoparticle dispersions are used as precursor sources to prepare dense (NP) and mesoporous TiO_2 and ZrO_2 thin films (NP meso) and are compared to mesostructured films fabricated by a sol−gel precursor solution (SG meso). The films are deposited via spin-coating and subsequently transferred to the in-plane stress measurement apparatus to measure the curvature in situ and calculate the intrinsic stress during heating up to 500 °C.

■ EXPERIMENTAL SECTION

Synthesis of the TiO_2 and ZrO_2 Nanoparticles (NPs). TiO_2 NPs were synthesized with a benzyl alcohol synthesis based on Hartmann et al.[30] 1 mL of $TiCl_4$ (99.0%, Wako Pure Chemical) was first dissolved in 5 g of ethanol (99.5%, Wako Pure Chemical) before adding 20 g of benzyl alcohol (99.0%, Wako Pure Chemical) and 230 mL of 1,3-propanediol (98.0%, Tokyo Chemical Industry) to the solution. After 8 h of stirring at 80 °C, the mixture was added to 200 mL of diethyl ether (99.5%, Wako Pure Chemical), resulting in the formation of a white precipitate, which afterwards was separated and washed two times with diethyl ether through centrifuging. During the sol−gel process, the Ti−Cl bonds undergo alcoholysis and directly condensate with a chloride substitute or a OR group leading to the

DOI: 10.1021/acs.langmuir.9b02455
Langmuir 2019, 35, 16427−16437

metal-oxo network. Subsequently, the gathered NPs were dried at room temperature for 1 h, 90 mg of NPs were dispersed into a provided solution of 1.5 mL ethanol, 0.2 mL distilled water, and 0.5 mL 2-methoxyethanol (99.0%, Wako Pure Chemical). For the mesoporous thin films, only 0.5 mL of ethanol was used for the dispersion and mixed with 50 mg of PIB_{50}-*b*-PEO_{45} (BASF) dissolved in 1 mL of ethanol.

ZrO_2 NPs were synthesized using a microwave-assisted approach[19] with a microwave synthesis reactor Monowave 300 by Anton Paar. In a 30 mL microwave vessel, 624.5 mg of $ZrCl_4$ (>99.5%, Alfa Aesar) was dissolved in 2.5 mL of ethanol (99.8%, Thermo Fisher Scientific) by heating the solution to 120 °C for 1 min controlled by an integrated infrared thermometer. Afterward, 627.1 mg of $Zr(O^iPr)_4$ in 1-propanol (70%, Alfa Aesar) was added to the reaction tube and heated to 150 °C for 3 min. After the addition of 6 mL of 1-hexanol (99%, Grüssing GmbH), the solution was once again heated to 150 °C for 1 min, which was followed by mixing 6 mL of benzyl alcohol (99%, Grüssing GmbH) to the microwave vessel. The solution was then heated in a final step to 200 °C for 3 min. All temperature steps have been performed under microwave irradiation and a constant stirring rate of 350 rpm. After each temperature step, the reaction tube was cooled to 70 °C. Finally, the nanoparticles were precipitated in 70 mL of *n*-pentane (>99%, Tokyo Chemical Industry), obtained by centrifugation and washed two times using 60 mL of diethyl ether.

By adding benzyl alcohol, benzyloxy groups are formed together with the Zr precursors leading to Zr−O−Zr bonds at elevated temperatures, which is a prerequisite in forming crystalline ZrO_2 nanoparticles at comparable low annealing temperatures (<200 °C), while the 1-hexanol reduces the reaction rate during the condensation process and enables the steric stabilization in water and short-chain alcohols such as ethanol. Analogous to the TiO_2 NPs, 90 mg of the obtained ZrO_2 NPs were dispersed into a mixture of ethanol, distilled water, and 2-methoxyethanol used as the spin-coating solution for preparing the thin films.

Preparation of the Nanoparticle-Derived Mesoporous and Dense Thin Films. All spin-coating procedures were performed using a Spincoater 1H-D7 by Mikasa, while Si[100] wafers were utilized as the film substrates. The substrates were cleaned using an ultrasonic-assisted treatment and their surface was oxidized at 700 °C for 10 min.

The nanoparticle-derived thin films were achieved by depositing the crystalline TiO_2 precursor sol, which was priorly freed from agglomerates using a PTFE 0.2 μm syringe filter, at approximately 80% relative humidity by spin-coating at 1000 rpm for 60 s and altering for 2−3 min. Afterward, the films were transferred to the in-plane stress measurement apparatus and heated up to 500 °C (5 K min^{-1}) for intrinsic in-plane stress studies.

Preparation of the Sol−Gel-Derived Mesoporous Thin Films. The preparation of the sol−gel-derived mesoporous thin films was already reported in a previous study.[37] The same preparation conditions during spin-coating and the annealing steps were used to ensure a comparison between the sol−gel- and nanoparticle-derived mesoporous thin films.

The precursor solution was prepared with a mole ratio of $Ti(OC_3H_7^i)_4$ (TTIP)/PIB_{50}-*b*-PEO_{45}/H_2O/HCl/C_2H_5OH (EtOH) of 1:0.008:1:11:40 for the TiO_2 films and $ZrOCl_2{\cdot}8H_2O$/PIB_{50}-*b*-PEO_{45}/H_2O/$CH_3OC_2H_4OH$ (2-methoxy-EtOH)/EtOH of 1:0.005:18:10:35 for the ZrO_2 films. Hydrochloric acid (37%) was used as the source of HCl and the mole ratio for H_2O does not include that from the hydrochloric acid or from $ZrOCl_2{\cdot}8H_2O$. In this approach, 1.78 g of TTIP or 1.23 g of $ZrOCl_2{\cdot}8H_2O$ was dissolved in 7 mL of ethanol or 3.5 mL of ethanol and 3.5 mL of 2-methoxy-EtOH, respectively. In another vessel, 220 mg (TiO_2) or 350 mg (ZrO_2) of the diblock copolymer PIB_{50}-*b*-PEO_{45} was added in 7 mL of ethanol for both cases. After treating the template solution in an ultrasonic bath for approximately 30 min at 35 °C, the mixture was cooled down to room temperature at which the polymer and precursor solution were mixed together. Distilled water (0.1 mL) was added to the resulting solution, which was stirred afterward for 90 min. In the case of the TiO_2, 2 mL of hydrochloric acid (37%, Wako Pure Chemical) was added to tailor the pH value and start the hydrolysis step.

Analogous to the nanoparticle-derived thin films, the solutions were freed from agglomerates using a syringe filter and then deposited on silicon wafers at a relative humidity of 20%.

In-Plane Stress Measurements. The details of the in-plane stress measurement are explained in a previous article.[37]

The in-plane stress measurements were recorded using a thin film stress instrument with an incorporated furnace detecting the substrate deflection during the heat treatment up to 500 °C. To calculate the in-plane stress, Stoney's equation (see eq 1) was considered combining the curvature of the bare and coated substrates, R_s and R_f, respectively, with the in-plane stress σ

$$\sigma = \frac{E_s t_s^2}{6(1-\nu_s)t_f} \times \frac{1}{\Delta R} \tag{1}$$

in which $E_s/(1-\nu_s)$ stands for the biaxial elastic modulus of the Si[100] substrate, 1.805×10^{11} Pa.[38,39] While the thickness of the substrate (t_s = 525 μm) is given by the manufacture company, the film thickness t_f is recorded by a spectroscopic ellipsometer. The in-plane stress investigation was performed on 4 in. Si[100] wafers, which were analyzed before the deposition to determine the curvature R_s of the bare substrate. The residual stress was recorded at room temperature, while the intrinsic stress was detected using a simultaneous heating with a rate of 5 °C min^{-1} to 500 °C. All the measurements were carried out under ambient air.

For the intrinsic and residual stress investigation, an FLX-2320-S thin film stress measurement system by Toho Technology was utilized to measure the substrate curvature.

Intrinsic In-Plane Stress Analysis. For the intrinsic stress investigation two 4 in. Si[100] wafers were coated via spin-coating. After deposition, the coated substrates were transferred into the in-plane stress measurement apparatus for the in situ investigation. The other film was fabricated under the same deposition conditions and cut afterward into 11 small pieces. For the stress analysis, a heating ramp of 5 °C min^{-1} until 500 °C was employed. Every 5 °C, the substrate curvature was determined during the heating and cooling processes. By means of the determination of the curvature difference ΔR, the corresponding stress σ_{int} in dependence of the specific temperature was calculated via Stoney's formula. The film thickness was obtained by investigating the smaller coated Si substrates at specific temperatures of 25, 50, 100, 150, 200, ..., 500 °C and fitted to evaluate the thickness of the film every 5 °C copying the in situ stress measurement interval.

Residual In-Plane Stress Analysis. For the residual stress investigation, thin film samples were prepared also on two 4 inch Si[100] wafers using spin-coating. In contrast to the intrinsic stress measurement, after the deposition, the films were transferred into a preheated furnace at 130 °C to evaporate the remaining solvent and aged at 300 °C for 12 h to remove the template. The film thickness of the coated wafers and the changing curvature were recorded to determine the corresponding residual stress σ_{res}. This procedure was repeated for 400, 500, ..., 900 and 1000 °C, whereby the heat treatment started at room temperature with a heating ramp of 10 °C min^{-1} up to 1000 °C. For each temperature step, the holding time was 10 min. The intrinsic and residual stress analyses were carried out identically for the sol−gel- and nanoparticle-derived mesoporous thin films and dense TiO_2 and ZrO_2 thin films.

Characterization Methods. Scanning electron microscopy images were obtained using a JEOL Ltd. JSM-6330 FII microscope at acceleration voltages of 11−15 kV and applied currents of 11−13 nA. Before the analyses, the thin films were coated with osmium using a Neo Osmium Coater from Meiwafosis Co., Ltd. All of the investigated films were sputtered for 10 s with an applied current of 10 mA. The crystalline phases of the thin films were identified by grazing incidence X-ray diffraction (GI-XRD) patterns recorded on a Rigaku Corp. Ultima III diffractometer utilizing Cu Kα radiation in a 2θ scan mode with an incidence angle of ω = 1°. All investigated materials were scanned in the range of 20 until 65° with a scan speed

DOI: 10.1021/acs.langmuir.9b02455
Langmuir 2019, 35, 16427−16437

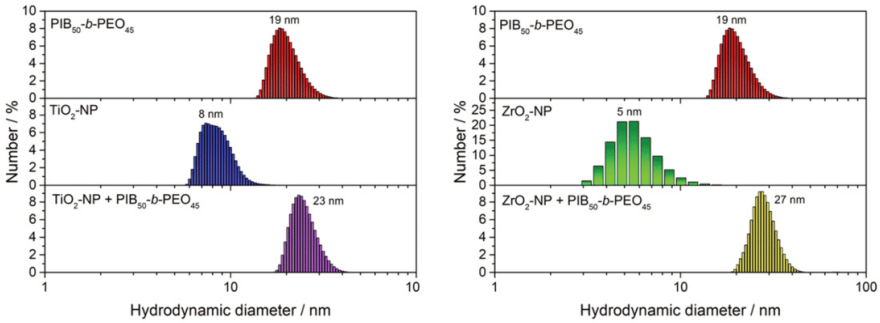

Figure 2. Dynamic light scattering (DLS) results of the utilized diblock copolymer PIB_{50}-*b*-PEO_{45}, as-prepared TiO_2 and ZrO_2 nanoparticles, and mixture of the nanostructures and the template.

4° min^{-1} in 0.02° steps. The calculations of the crystallite sizes *d* were performed using the Scherrer equation by applying a pseudo-Voigt plot to fit the wide angle reflections. Spectroscopic ellipsometric investigations were recorded on an M2000 V-Kk instrument from J.A. Woollam Co., Inc. using the included data analysis software Complete Ease for employing the model fits. All samples were measured at the specific angles of 65, 70, and 75° in a wavelength range of 370.9 until 998.5 nm, while the acquisition time was always 5 s. When the samples were fired above 700 °C, formation of SiO_2 on the Si wafer was taken into account. The thermogravimetric analyses were recorded under air using a thermal analyzer Thermo Plus TG 8120 by Rigaku Corp. Approximately 15.9 mg of the diblock copolymer PIB_{50}-*b*-PEO_{45} was investigated at a heating ramp of 5 °C min^{-1} simulating the same conditions as the thin film stress analysis. Dynamic light scattering (DLS) for particle size as well as zeta potential measurements were performed on a Zetasizer NanoZS from Malvern instruments. Transmission electron microscopy (TEM) images were recorded on a CM30 instrument by Philips, which was operated at 300 kV using copper mesh grids for the sample preparation.

■ RESULTS AND DISCUSSION

Characterization of the Nanoparticles. To prepare mesoporous thin films using a nanoparticle dispersion and a structure-directing agent, the size of the nanoparticles is required to be smaller than the pore wall thickness to obtain a well-defined mesoporous structure. Based on the utilized diblock copolymer PIB_{50}-*b*-PEO_{45} exhibiting spherical micelles, the pore walls do not exceed a thickness of around 15 nm.[8−10] Hence, as the nanoparticles are supposed to be used as building blocks in a typical brick-and-mortar approach, a particle size less than 10 nm is favorable.

The TiO_2 nanoparticles were synthesized based on a nonaqueous sol−gel route using benzyl alcohol as the solvent and oxygen donor.[40−42] In short, a solution of benzyl alcohol and 1,3-propanediol acting as a stabilizing agent is added to anhydrous $TiCl_4$ dissolved in ethanol. By stirring the solution for 8 h at 80 °C, titanium-oxo-hydroxo species are formed and will precipitate in nonpolar organic solvents such as diethyl ether. After drying the remaining precipitate, the obtained powder can readily be redispersed in ethanol and water.

The ZrO_2 nanoparticles were prepared by a microwave-assisted and solvent-controlled sol−gel approach using zirconium(IV) propoxide and zirconium(IV) chloride as zirconium precursors, which are dissolved in benzyl alcohol and 1-hexanol. While the synthesis is facile to perform, the reaction mechanism involves several steps including ligand exchange, alcoholysis, and alkyl halide elimination, which is described in detail by Suchomski et al.[19]

DLS measurements (Figure 2) were performed to obtain the hydrodynamic diameter of the metal oxide nanoparticles, which show an average size of 8 nm for TiO_2 and 5 nm for ZrO_2 with a positive zeta potential for both of them. Next, for the determination of the nanoparticle size, also micelles of PIB_{50}-*b*-PEO_{45} were investigated using DLS, both with and without the presence of metal oxide nanoparticles. Here, an average hydrodynamic diameter of 19 nm for the polymeric micelles is observed, which increases to 23 or 27 nm when the TiO_2 and ZrO_2 particles are added, respectively. These results demonstrate that the particles and the template do not exist separately as one would receive two size distributions in the DLS analyses. The presence of only one narrow size distribution confirms the absence of particle agglomerates by settling or clumping. Instead, the increase in the hydrodynamic radius suggests that a certain number of nanoparticles adsorbs on the micellar corona, which is favorable in terms of the templating process and explains the enhanced overall micellar diameter. Additionally, TEM investigations of the prepared TiO_2 nanoparticles reveal spherical particles with a 5.4 ± 1.0 nm diameter (see Figure S1). The TEM analyses of ZrO_2 nanostructures were shown in a previous work,[19] proving the existence of particles with a size of 2.5 ± 0.8 nm. The difference in the determined particle sizes via TEM and DLS derives from the solvation shell, which increases the hydrodynamic diameter measured by DLS.

Hence, the synthesized nanoparticles of TiO_2 and ZrO_2 are suitable building blocks for mesoporous thin films.

Intrinsic Stress Development in the Mesoporous TiO_2 Thin Films. The mesoporous TiO_2 thin films were prepared using a mixture of the nanoparticle dispersion and the block copolymer PIB_{50}-*b*-PEO_{45} in ethanol. The precursor solution was deposited on partially oxidized Si[100] substrates by a spin-coating approach allowing to fabricate thin films on 4 inch wafers with a thickness of around 100 nm. By varying the structure-directing agent, the porosity of the film can be tailored. In this case, PIB_{50}-*b*-PEO_{45} results in 13 nm mesopores, which aligned in a cubic array when using a sol−gel approach proven by SEM images. However, the as-prepared mesoporous thin films using the nanoparticle dispersion do not show a highly ordered mesoporous structure. In contrast to the metal-oxo units in the sol−gel-derived films, the building blocks or nanoparticles have a higher density and are thus less mobile in the nanoparticle-derived films. The

DOI: 10.1021/acs.langmuir.9b02455
Langmuir 2019, 35, 16427−16437

assembly of the nanoparticles around the micelles is therefore aggravated, hindering the formation of an ordered mesoporous structure after decomposition of the template.

As seen in Figure 3, mesopores of around 13 nm are observable. In addition, Suchomski et al. showed the presence of smaller pores of around 2−5 nm proven by nitrogen physisorption measurements of the nanoparticle-derived mesoporous thin films.[19] These derive from the interparticular space between the nanoparticles or their agglomerates. Therefore, the nanoparticle-derived thin films are often referred to as bimodal porous nanostructures.

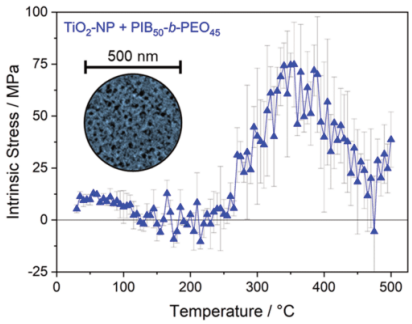

Figure 3. In-plane intrinsic stress of the nanoparticle-derived mesoporous TiO_2 thin films templated by PIB_{50}-*b*-PEO_{45} during the heating up to 500 °C. The heating ramp was 5 °C min^{-1}, while the curvature of the coated film was measured every 5 °C. The depicted data are the average of three recordings. The morphology of the film at 500 °C and after natural cooling is also shown using SEM.

The nanoparticle-derived mesoporous thin films were investigated regarding the in-plane stress development by transferring the freshly coated film directly in the in-plane stress measurement apparatus determining the curvature of the sample while heating the film up to 500 °C with a heating ramp of 5 °C min^{-1} and a measurement interval of 5 °C. In this in situ experiment, the impact of the solvent evaporation, polymeric micelles, and densification processes on the intrinsic stress within the film is studied. The Stoney's equation (eq 1) contains next to the thickness of the substrate t_s also the thickness of the coated layer t_f, which will change during the annealing procedure upon solvent evaporation and polymer decomposition. Analogously prepared TiO_2 thin films were analyzed via spectroscopic ellipsometry at specific annealing temperatures (25, 50, 100, ..., 500 °C) providing the corresponding thickness at the given temperatures.

To obtain the temperature every 5 °C similar to the curvature measurement during the in situ investigation, the thickness data were fitted with a linear regression (see Figure S2). The thus obtained intrinsic in-plane stress of nanoparticle-derived mesoporous TiO_2 thin films in dependence of the heating temperature is depicted in Figure 3. The investigation was performed three times with analogously prepared solutions and the same deposition parameters. The shown stress data in Figure 3 were calculated as the average of these three investigations (see Figure S3). The in-plane stress at room temperature is tensile at first and decreases slightly from 10 MPa to zero. This recession starts slightly around 75 °C, which is in good agreement with the boiling temperature of ethanol (ϑ_{bp} = 78.37 °C) and drops stronger around 100 °C corresponding to the evaporation of H_2O. Afterward, the intrinsic stress remains averagely constant until 250 °C. This phenomenon, as described in our previous article, can be assigned to the polymeric micelles being highly distributed in the film. The template contains ether and hydroxyl groups as part of the ethylene oxide unit (PEO), which may form hydrogen bridge bonds with the Ti−OH groups on the particle surface. The viscoelastic properties of the micelles also provide a buffer between each particle, leading to only small areas of contact. As the particles are spherical, an arrangement similar to a close-packing will cause gaps between the particles. This interparticular porosity in the range of a few nanometers also contributes to an overall low stress during this temperature segment.

After 250 °C, a significant rise in the intrinsic stress is observable until 350 °C, which is ascribed to the decomposition of the template and its decompressing effect of the system. The template removal was verified by thermogravimetric analysis (TGA) shown in Figure S4.

Beyond 350 °C, the intrinsic stress decreases and almost vanishes at about 475 °C. Such a maximum is typically observed for TiO_2 mesoporous and dense films.[36,37] Due to the high temperature, atomic diffusion in the TiO_2 particles is activated, leading to structural and stress relaxation. Above 475 °C, the stress increases slightly. By our knowledge, the crystallites grow in size leading to a less amount of grain boundaries in the particle. As the atomic diffusion coefficient is typically larger along the grain boundaries than within the grain, larger crystallites result in a reduced atomic diffusion. Hence, the tensile stress of the nanoparticle-derived mesoporous thin film increases after 475 °C.

To validate these assumptions and get a further understanding of the intrinsic stress development, nanoparticle-derived thin films without the addition of the template as well as sol−gel-derived mesoporous thin films were investigated analogously (Figure 4).

Figure 4 reveals that the dense nanoparticle-derived thin film (TiO_2 NP) experiences the highest intrinsic in-plane stress until 500 °C. At a temperature of 100 °C, the intrinsic stress is 4 times higher for the sol−gel-derived (TiO_2 SG meso) and nearly 8 times higher for the nanoparticle-derived (TiO_2 NP

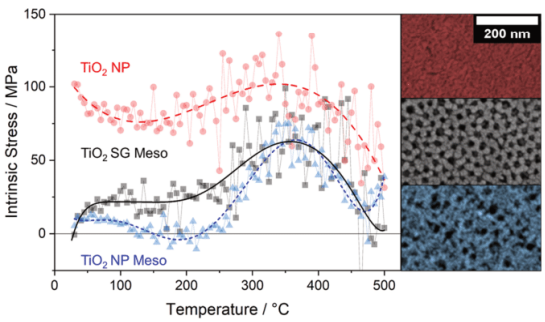

Figure 4. Comparison of the intrinsic in-plane stress of the mesoporous TiO_2 films prepared with PIB_{50}-*b*-PEO_{45} using a sol−gel precursor solution (black) or TiO_2 nanoparticle dispersion (blue) and without the addition of the diblock copolymer (red) during the heating process up to 500 °C. The SEM images correspond to the respective films treated at 500 °C. The curvature of the films was determined every 5 °C. The dashed and straight lines serve as guides for the eye.

DOI: 10.1021/acs.langmuir.9b02455
Langmuir 2019, 35, 16427−16437

meso) mesoporous thin films. Although the absolute stress values seem quite large for the dense thin films made of TiO_2 nanoparticles with a maximum of 120 MPa (Figure 4), sol–gel-derived dense TiO_2 films show even higher intrinsic in-plane stress up to 250 MPa.[36] This difference derives from the presence of the interparticular porosity due to the assembly of the around 7 nm nanoparticles compensating the stress build-up.

From 100 until 200 °C, the detected stress remains nearly constant for the mesoporous thin films, which can be attributed to the presence of micelles whose viscoelastic properties allow the system to relax. Another proof is provided by the following polymer decomposition seen by TGA (see Figure S4), which occurs in two steps at 200 and 270 °C. It is completed around 350 °C, which is the stress maximum for both types of mesoporous thin films. The sol–gel-derived mesoporous structure is still in an amorphous state, but the metal-oxo network has expanded itself around the subsequently removed micelles. Although the nanoparticle-derived dense film also reveals its stress maximum around 350 °C, the preceding stress uptake is significantly smaller than that for the mesoporous films.

From 350 to 500 °C, the stress decreases and reaches nearly zero for the sol–gel-derived film, which is assigned to the temperature-induced atomic diffusion leading to the crystallization into the anatase crystal phase confirmed by GI-XRD (Figure 5). In the case of the films made of nanoparticle

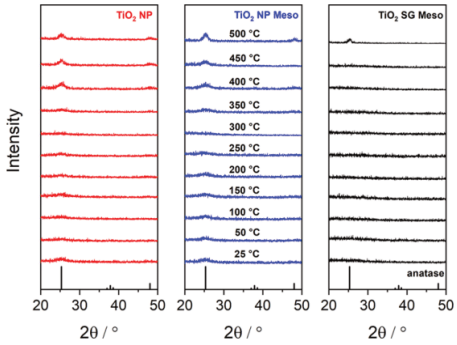

Figure 5. X-ray diffraction patterns of the dense (red) and mesoporous thin films using a TiO_2 nanoparticle dispersion (blue) and sol–gel precursor solution (black) after different annealing temperatures ranging from room temperature to 500 °C. In addition, the anatase reference pattern (ICDS 98-015-4604) is shown.

dispersion, GI-XRD reveals the presence of anatase even at room temperature. Above 350 °C, the (100) reflection of anatase intensifies and sharpens until 500 °C. By fitting the reflections with a pseudo-Voigt plot and using the Scherrer equation,[43] the average crystallite size was determined. It increases from around 3 nm at 350 °C up to 6 nm at 500 °C for the nanoparticle-derived films. In contrast, 9 nm crystallites are observed at 500 °C for the TiO_2 film based on a sol–gel precursor solution, that is, no gradual growth occurs. As mentioned above, the crystallite growth of the nanoparticle-derived thin films eventuates in fewer grain boundaries in the particles, leading to a lower atomic diffusion and hence to a higher in-plane stress build-up compared to the sol–gel-derived films.

Figure 6 shows a possible schematic overview describing the difference between the two types of mesoporous thin films. By

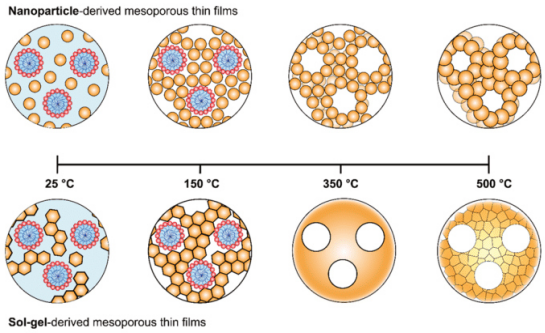

Figure 6. Schematic overview of the structural behavior inside the mesoporous thin film prepared using a nanoparticle dispersion (top) and a sol–gel precursor solution (bottom). The spheres represent the nanoparticles, while the hexagons signify units of the metal-oxo-network in the sol–gel process.

continuous condensation, the metal-oxo network becomes more rigid than the film composed of crystalline nanoparticles and interparticular pores. When the stress-relaxing polymeric micelles are removed, further cross-linking by polycondensation reactions is not inhibited anymore by ether or hydroxyl groups of the micelles coordinating to the Ti atoms in the precursor-derived films, leading to an increase in stress at 200–350 °C. In the case of the nanoparticle-derived mesoporous film, the nanoparticles continue to sinter, which raises the stress at the same temperature range. At higher temperatures, the crystallites grow in size leading to a less atomic diffusion inside the particle due to a less amount of grain boundaries. The densification process will therefore lead to the atomic diffusion-induced stress relaxation resulting in a small stress increase at 500 °C for the nanoparticle-derived mesoporous thin films.

Intrinsic Stress Development in the Mesoporous ZrO_2 Thin Films. Next to the TiO_2 thin films, also ZrO_2 coatings were investigated regarding the intrinsic in-plane stress development during the heating stage up to 500 °C. Analogous to the TiO_2 thin films, ZrO_2 ones were prepared using ZrO_2 nanoparticle dispersions or a precursor solution based on $ZrOCl_2 \cdot 8H_2O$ instead of an alkoxide. In our previous paper, we demonstrated that the utilized precursor forms a tetrametric structure of $[Zr_4(OH)_8]^{8+}$ consisting of two hydroxyl groups connected to a Zr^{4+} center, which facilely condensates around the PEO units of the used diblock copolymer PIB_{50}-*b*-PEO_{45} and hence compensates the stress uptake.

Figure 7 depicts the intrinsic in-plane stress development of the mesoporous ZrO_2 thin films. In good agreement with the stress study of the TiO_2 films, the nanoparticle-derived mesoporous thin films show a lower overall in-plane stress than the sol–gel-derived ones and a significant increase in the in-plane stress at around 270 °C caused by the template decomposition. This finding verifies most of the above mentioned assumptions. The crystalline nanoparticles and their interparticular porosity lower the stress as the interfacial contact area between the particles is generally lower than the rigid metal-oxo network of the sol–gel-derived thin films. At

DOI: 10.1021/acs.langmuir.9b02455
Langmuir 2019, 35, 16427–16437

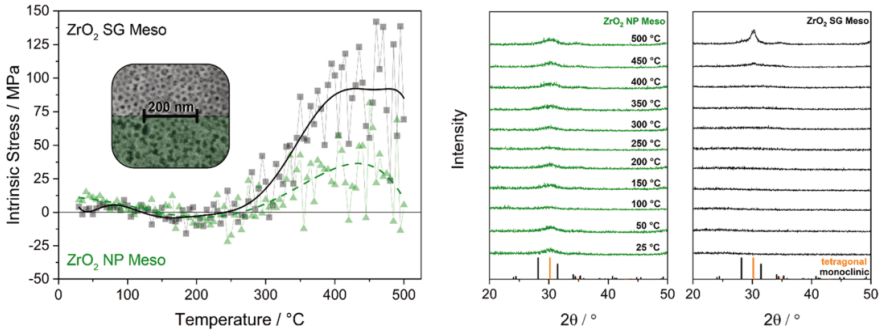

Figure 7. (left) In-plane intrinsic stress of the nanoparticle (green) and sol−gel-derived (black) mesoporous ZrO_2 thin films templated by PIB_{50}-*b*-PEO_{45} during the annealing step up to 500 °C. (right) GI-XRD investigation of analogously prepared thin films at different firing temperatures. The reference patterns for the tetragonal (ICSD 98-065-5671, orange) and monoclinic ZrO_2 (ICSD 98-008-0046, black) are also displayed.

500 °C, we do not observe a stress increase for the nanoparticle-derived films, which may be related to the absence of crystallite growth determined by GI-XRD (Figure 7) for the nanoparticle-based mesoporous film. The XRD results show the tetragonal phase for the nanoparticle-derived and a mixture of the tetragonal and monoclinic structure for the sol−gel-derived thin films at 500 °C, while only the latter shows a growth in the crystallite size based on the Scherrer equation. This phenomenon is in good agreement with the findings of Suchomski et al.[19] showing the beginning of the crystallite growth at annealing temperatures above 550 °C accompanied by the formation of the monoclinic phase. In addition, the used small nanoparticles possess a high specific surface area favoring the formation of the tetragonal instead of the monoclinic phase even at higher temperature based on the thermodynamic investigations by Navrotsky on the polymorphism of ZrO_2.[44]

Residual Stress of the TiO_2 and ZrO_2 Thin Films. Besides the intrinsic in-plane stress development during the heating up to 500 °C, also the residual stress using annealing temperatures of 300, 400, ..., 1000 °C and subsequent cooling down to room temperature was studied for the TiO_2 and ZrO_2 mesoporous thin films. With this approach, the influence of pore collapsing and particle growth on the stress was studied. The results for the TiO_2 and ZrO_2 thin films are shown in Figure 8 together with the corresponding SEM recordings.

When referring to the residual stress, the difference in the thermal expansion coefficient of the substrate and the film has to be taken into account in greater detail. While the investigation of the intrinsic stress only considers temperatures up to 500 °C during the heating procedure, the residual stress analyses of the films are performed at elevated annealing temperatures of 1000 °C and the subsequent cooling step back to room temperature. During the cooling process, the used silicon substrate and the coated metal oxide will not shrink identically and hence leading to an increased in-plane stress. If the thermal expansion coefficient is higher than the one from silicon (α_{Si} = 2.5 × 10^{-6} K^{-1}),[45] further tensile stress is expected after cooling down to room temperature. This difference in stress from the heated state and at room temperature is known as thermal stress and is directly related to the Young's Modulus *E* of the material.

In the case of TiO_2, the thermal expansion coefficient of bulk titania is $\alpha_{anatase}$ = 10.2 × 10^{-6} K^{-1}.[46] In a porous material, the thermal expansion is expected to be slightly lower[18] compared

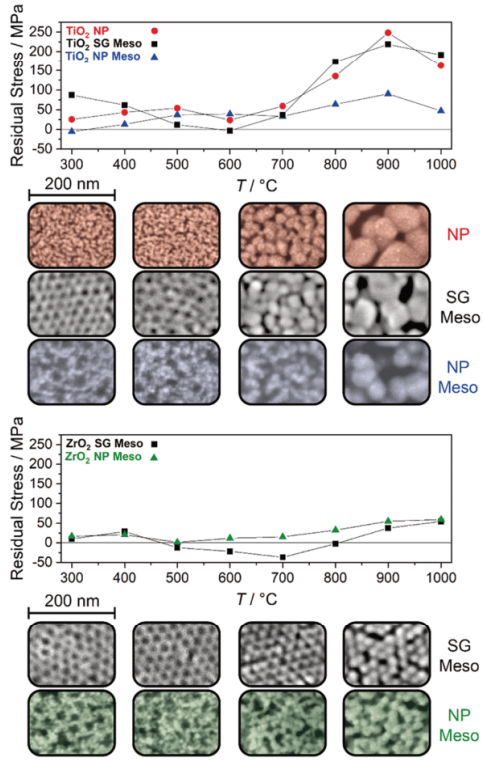

Figure 8. Residual in-plane stress development from 300 until 1000 °C of the mesoporous TiO_2 and ZrO_2 thin films prepared using a nanoparticle dispersion (NP meso) and a sol−gel precursor solution (SG meso). In addition to a comparison with nanoparticle-derived thin dense films (NP), also the SEM images at 300, 500, 700, and 900 °C are depicted.

to the one for bulk anatase but still higher than the one from the silicon substrate. Therefore, a tensile stress is anticipated, which we could verify for the TiO_2 thin films.

At first sight, the nanoparticle-derived mesoporous TiO_2 film experiences the least residual in-plane stress compared to its other TiO_2 counterparts. In the beginning from 300 until 400 °C, the sol−gel-derived thin films are confronted with higher

DOI: 10.1021/acs.langmuir.9b02455
Langmuir 2019, 35, 16427−16437

in-plane stress than the other films. They are amorphous, which was verified by GI-XRD (Figure 9A), in contrast to the nanoparticle-derived films. Hence, the stress decrease of the precursor solution-derived thin film is assigned to the temperature-induced atomic diffusion and the consequential crystallization in the anatase structure. The similar stress behavior of the nanoparticle-derived films in comparison with the amorphous sol−gel-derived film indicates that the crystallization process in the sol−gel-derived film has a direct impact to lower the stress in the system.

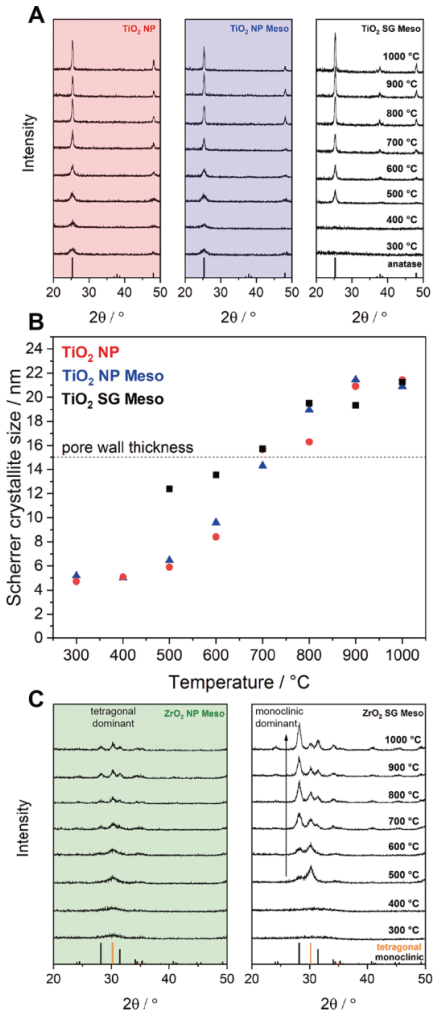

Figure 9. (A) X-ray diffraction patterns of the dense (red) and mesoporous thin films using a TiO_2 nanoparticle dispersion (blue) and sol−gel precursor solution (black) after different annealing temperatures ranging from 300 to 1000 °C. In addition, the anatase reference pattern (ICDS 98-015-4604) is shown. (B) Comparison of the calculated crystallite size using the Scherrer equation for the TiO_2 films in dependence of the annealing temperature. The dashed line shows the pore wall thickness determined for the sol−gel-derived mesoporous thin film at 300, 400, and 500 °C. (C) GI-XRD investigation of analogously prepared thin films at different annealing temperatures from 300 until 1000 °C. The reference patterns for the tetragonal (ICSD 98-065-5671, orange) and monoclinic ZrO_2 (ICSD 98-008-0046, black) are also displayed.

From 500 until 700 °C, the residual stress does not differ much among the investigated TiO_2 thin films as the mesopores as well as the interparticular pores compensate a possible stress build-up. For temperatures higher than 700 °C, the residual stress of all films increased significantly. The SEM images of the sol−gel-derived mesoporous thin films reveal the collapsing of the pores. In addition, the nanoparticle-derived films show a growth of the visible particles (SEM) and the crystallites using GI-XRD (Figure 9B). At 700 °C, the crystallite size exceeds the pore wall thickness determined by SEM, leading to the deformation of the pores. In addition, the higher crystallite size equals to a less amount of grain boundaries between the particles, leading to a higher elastic constant and a larger thermal stress generated during the cooling process. Hence, the combination of crystallite growth and the consequential pore collapse increases the stress. The detected crystal phase of the TiO_2 films remains anatase although the thermodynamically more stable rutile phase may be usually observed above 700 °C. Similar to the ZrO_2 nanoparticles and the tetragonal phase, this phenomenon is based on the small particle size of TiO_2. Zhang and Banfield[47] demonstrated with the help of the surface free energy that anatase is the dominant crystal phase that transforms to rutile after reaching a greater crystallite size, which in regard to our results is not acquired even after 1000 °C.

While the residual in-plane stress rises significantly up to 4 times in value at 900 °C compared to 700 °C for the sol-gel-derived mesoporous and nanoparticle-derived dense TiO_2 film, the nanoparticle-derived mesoporous TiO_2 only increases to twice its former value. This phenomenon is explained by taking the porosity of the films into account. Although the SEM images give a local impression of the pores, the average porosity can be calculated using the refractive index $n_{\text{thin film}}$ determined via spectroscopic ellipsometry. With the following eq 2[48] and the assumption that the film consists of dense anatase with a refractive index $n_{\text{anatase}} = 2.52$[46] and air as pores ($n_{\text{air}}$), the porosity of the films in dependence of the annealing temperature is computed.

$$\sigma = \frac{n_{\text{anatase}} - n_{\text{thin film}}}{n_{\text{anatase}} - n_{\text{air}}} \times 100\% \quad (2)$$

The results are shown in Figure 10. The calculated porosities for the nanoparticle-derived "dense" and mesoporous films are quite different due to the incorporation of mesopores. While the sol−gel-derived films owe their porosity solely to the mesopores, the nanoparticle-derived dense films' porosity develops from the gaps between the nanoparticles. The combination of both types of porosity is observed for the nanoparticle-derived mesoporous films eventuating in the highest detected porosity among the investigated films. Figure 10 also reveals the similarity between the nanoparticle films as the porosity slope decreases parallel when reaching an annealing temperature of 500 or 600 °C. Additionally, the porosities of the nanoparticle dense and the sol−gel-derived mesoporous TiO_2 thin films are in the same range and lower than those of the nanoparticle-derived mesoporous film. The dependence of the porosities resembles the residual stress between 700 and 1000 °C for the nanoparticle-derived films. Hence, this comparison explains the observation that both the intrinsic and residual stresses are the lowest for the nanoparticle-derived mesoporous film possessing the highest

DOI: 10.1021/acs.langmuir.9b02455
Langmuir 2019, 35, 16427−16437

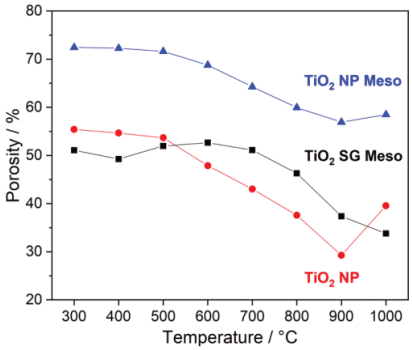

Figure 10. Porosity of the TiO_2 thin films with and without the addition of the diblock copolymer in dependence of the heating temperature. The porosity was calculated via eq 2.

porosity. In the end, all the investigated films turn into dense TiO_2 at elevated temperatures resulting in a higher thermal expansion coefficient than the porous films and greater difference compared to the silicon substrate. The higher disparity of the thermal expansion coefficient between the silicon substrate and the TiO_2 film eventually leads to an increased thermal stress eventuating in an overall higher tensile stress observed in Figure 8 at higher temperatures.

To transfer this assumption to metal oxide films in general, also ZrO_2 mesoporous thin films were investigated regarding the residual in-plane stress (see Figure 8). In contrast to the TiO_2 thin films, the overall detected residual stress is lower and even compressive (<0 MPa) for the sol−gel-derived ZrO_2 film at 500 °C at which the material crystallizes in the tetragonal phase (Figure 9C). The detected compressive stress is derived from the lower thermal expansion coefficient of the present ZrO_2 crystal phase in comparison with the one from the silicon substrate. However, analogously to the TiO_2 films, the determined residual stress slopes also indicate for the nanoparticle-derived mesoporous ZrO_2 film that the porous structure has indeed a compensating effect for the stress build-up as the residual in-plane stress increases significantly after 700 °C at which the SEM recordings still verify the mesoporous structure.

A major difference in the residual stress development compared to the TiO_2 films is the higher stress for the nanoparticle-based ZrO_2 films in comparison with the sol−gel-derived ZrO_2 thin films. To explain this finding, we need to take again the thermal expansion coefficients into account. In the case of ZrO_2, two different crystal structures are detected via GI-XRD (Figure 9C): the monoclinic and tetragonal phases. The GI-XRD data show that with higher temperatures, the sol−gel-derived mesoporous ZrO_2 thin films exhibit the tetragonal phase and switch then at around 700 °C to the monoclinic structure, becoming more and more dominant for higher temperatures, while the nanoparticle film remains mainly in the tetragonal phase. However, the different crystal structures possess different thermal expansion coefficients, namely, $\alpha_{monoclinic} = 7 \times 10^{-6}$ K^{-1} and $\alpha_{tetragonal} = 12 \times 10^{-6}$ K^{-1}.[49] As the difference in the thermal expansion coefficients between the silicon substrate ($\alpha_{Si} = 2.5 \times 10^{-6}$ K^{-1}) is larger for the tetragonal than for the monoclinic phase, a higher thermal stress and therefore a higher tensile residual stress for the nanoparticle-based ZrO_2 films are detected.

■ CONCLUSIONS

Our study shows subsequent analyses of the intrinsic (in situ up to 500 °C) and residual in-plane stress after different annealing temperatures and quenching to room temperature of mesoporous TiO_2 and ZrO_2 thin films using sol−gel and nanoparticle dispersions as start solutions. With this approach, the effects of the mesoporous structure and the pore collapse on the in-plane stress development were evaluated.

The investigations of the intrinsic in-plane stress revealed the lowest stress values for the nanoparticle-derived mesoporous system, which is ascribed to the combination of the relaxing effects of the utilized diblock copolymer PIB_{50}-*b*-PEO_{45} and the interparticular gaps between the precrystalline nanoparticles.

Regarding the residual in-plane stress development, the results for the TiO_2 films confirm the lowest stress values for the nanoparticle-derived mesoporous films, which is assigned to the higher porosity verified by spectroscopic ellipsometry and SEM investigations, leading to a stress-decompressing effect. ZrO_2 films showed an opposite behavior of the nanoparticle films having a higher overall stress than the sol−gel-derived ones. Here, the different detected crystal phases via GI-XRD and the consequently different thermal expansion coefficients lead to the result that the dominant crystal structure has a high influence on the experienced in-plane stress.

This work shows that due to the low intrinsic and residual in-plane stress development, mesoporous thin films prepared by using nanoparticle dispersion are preferred when desiring thicker films as the risk of possible cracking and the interrelated loss of specific material properties are the lowest of the investigated films here. Our study is another step to further understand the mechanical properties of mesoporous structures and how to tailor them for future applications.

■ ASSOCIATED CONTENT

Supporting Information

The Supporting Information is available free of charge at https://pubs.acs.org/doi/10.1021/acs.langmuir.9b02455.

> Thickness determination of the dense and mesoporous TiO_2 thin films; thermogravimetric analysis of the utilized diblock copolymer PIB_{50}-*b*-PEO_{45} in combination with the intrinsic stress data; and repetitive in-plane intrinsic stress measurements for the TiO_2 films (PDF)

■ AUTHOR INFORMATION

Corresponding Authors

*E-mail: bernd.smarsly@phys.chemie.uni-giessen.de (B.M.S.).
*E-mail: kozuka@kansai-u.ac.jp (H.K.).

ORCID

Bernd M. Smarsly: 0000-0001-8452-2663
Hiromitsu Kozuka: 0000-0002-3385-215X

Author Contributions

The manuscript was written through contributions of all authors. All authors have given approval to the final version of the manuscript.

Notes

The authors declare no competing financial interest.

DOI: 10.1021/acs.langmuir.9b02455
Langmuir 2019, 35, 16427−16437

ACKNOWLEDGMENTS

The authors thank Christian Suchomski for discussing and helping with the nanoparticle syntheses and Elifkübra Özkan for the TEM sample preparation. K.H. acknowledges DAAD for the financial support throughout his stay at the Kansai University, Osaka, Japan. This project was supported by the Center for Materials Research (LaMa) of the Justus-Liebig-University Giessen, Germany. This work is also supported by JSPS KAKENHI Grant Number JP19K22070.

REFERENCES

(1) Fortunato, E.; Barquinha, P.; Martins, R. Oxide Semiconductor Thin-Film Transistors: A Review of Recent Advances. *Adv. Mater.* **2012**, *24*, 2945−2986.

(2) Aegerter, M. A.; Almeida, R.; Soutar, A.; Tadanaga, K.; Yang, H.; Watanabe, T. Coatings Made by Sol-Gel and Chemical Nanotechnology. *J. Sol-Gel Sci. Technol.* **2008**, *47*, 203−236.

(3) Spende, A.; Sobel, N.; Lukas, M.; Zierold, R.; Riedl, J. C.; Gura, L.; Schubert, I.; Moreno, J. M. M.; Nielsch, K.; Stühn, B.; et al. TiO_2, SiO_2, and Al_2O_3 Coated Nanopores and Nanotubes Produced by ALD in Etched Ion-Track Membranes for Transport Measurements. *Nanotechnology* **2015**, *26*, 335301.

(4) O'Neill, B. J.; Jackson, D. H. K.; Lee, J.; Canlas, C.; Stair, P. C.; Marshall, C. L.; Elam, J. W.; Kuech, T. F.; Dumesic, J. A.; Huber, G. W. Catalyst Design with Atomic Layer Deposition. *ACS Catal.* **2015**, *5*, 1804−1825.

(5) Levrau, E.; Devloo-Casier, K.; Dendooven, J.; Ludwig, K. F.; Verdonck, P.; Meersschaut, J.; Baklanov, M. R.; Detavernier, C. Atomic Layer Deposition of TiO_2 on Surface Modified Nanoporous Low-k Films. *Langmuir* **2013**, *29*, 12284−12289.

(6) Grosso, D.; Cagnol, F.; Soler-Illia, G. J. D. A. A.; Crepaldi, E. L.; Amenitsch, H.; Brunet-Bruneau, A.; Bourgeois, A.; Sanchez, C. Fundamentals of Mesostructuring through Evaporation-Induced Self-Assembly. *Adv. Funct. Mater.* **2004**, *14*, 309−322.

(7) Brinker, C. J.; Lu, Y.; Sellinger, A.; Fan, H. Evaporation-Induced Self-Assembly : Nanostructures Made Easy. *Adv. Mater.* **1999**, *11*, 579−585.

(8) Cop, P.; Göttlicher, M.; Schörmann, J.; Boissiere, C.; Beyer, A.; Becker, C.; Volz, K.; Over, H.; Smarsly, B. M. Atomic Layer Deposition of Titania in Ordered Mesoporous Cerium Zirconium Oxide Thin Films: A Case Study. *J. Phys. Chem. C* **2019**, *123*, 12851−12861.

(9) von Graberg, T.; Hartmann, P.; Rein, A.; Gross, S.; Seelandt, B.; Röger, C.; Zieba, R.; Traut, A.; Wark, M.; Janek, J.; Smarsly, B. M. Mesoporous Tin-Doped Indium Oxide Thin Films: Effect of Mesostructure on Electrical Conductivity. *Sci. Technol. Adv. Mater.* **2011**, *12*, No. 025005.

(10) Weidmann, C.; Brezesinski, K.; Suchomski, C.; Tropp, K.; Grosser, N.; Haetge, J.; Smarsly, B. M.; Brezesinski, T. Morphology-Controlled Synthesis of Nanocrystalline η-Al_2O_3 Thin Films, Powders, Microbeads, and Nanofibers with Tunable Pore Sizes from Preformed Oligomeric Oxo-Hydroxo Building Blocks. *Chem. Mater.* **2012**, *24*, 486−494.

(11) Sallard, S.; Schröder, M.; Boissière, C.; Dunkel, C.; Etienne, M.; Walcarius, A.; Oekermann, T.; Wark, M.; Smarsly, B. M. Bimodal Mesoporous Titanium Dioxide Anatase Films Templated by a Block Polymer and an Ionic Liquid: Influence of the Porosity on the Permeability. *Nanoscale* **2013**, *5*, 12316−12329.

(12) Ren, Y.; Yang, X.; Zhou, X.; Luo, W.; Zhang, Y.; Cheng, X.; Deng, Y. Amphiphilic Block Copolymers Directed Synthesis of Mesoporous Nickel-Based Oxides with Bimodal Mesopores and Nanocrystal-Assembled Walls. *Chinese Chem. Lett.* **2019**, in press.

(13) Pan, J. H.; Lee, W. I. Preparation of Highly Ordered Cubic Mesoporous WO_3/TiO_2 Films and Their Photocatalytic Properties. *Chem. Mater.* **2006**, *18*, 847−853.

(14) Boissiere, C.; Grosso, D.; Lepoutre, S.; Nicole, L.; Bruneau, A. B.; Sanchez, C. Porosity and Mechanical Properties of Mesoporous Thin Films Assessed by Environmental Ellipsometric Porosimetry. *Langmuir* **2005**, *21*, 12362−12371.

(15) Ke, Y.; Lai, S. Y. Comparison of the Catalytic Benzene Oxidation Activity of Mesoporous Ceria Prepared via Hard-Template and Soft-Template. *Microporous Mesoporous Mater.* **2014**, *198*, 256−262.

(16) Zukalová, M.; Zukal, A.; Kavan, L.; Nazeeruddin, M. K.; Liska, P.; Grätzel, M. Organized Mesoporous TiO_2 Films Exhibiting Greatly Enhanced Performance in Dye-Sensitized Solar Cells. *Nano Lett.* **2005**, *5*, 1789−1792.

(17) Chiu, C. Y.; Chiang, A. S. T.; Chao, K. J. Mesoporous Silica Powders and Films-Pore Size Characterization by Krypton Adsorption. *Microporous Mesoporous Mater.* **2006**, *91*, 244−253.

(18) Brezesinski, T.; Wang, J.; Senter, R.; Brezesinski, K.; Dunn, B.; Tolbert, S. H. On the Correlation between Mechanical Flexibility, Nanoscale Structure, and Charge Storage in Periodic Mesoporous CeO_2 Thin Films. *ACS Nano* **2010**, *4*, 967−977.

(19) Suchomski, C.; Weber, D. J.; Dolcet, P.; Hofmann, A.; Voepel, P.; Yue, J.; Einert, M.; Möller, M.; Werner, S.; Gross, S.; et al. Sustainable and Surfactant-Free High-Throughput Synthesis of Highly Dispersible Zirconia Nanocrystals. *J. Mater. Chem. A* **2017**, *5*, 16296−16306.

(20) Ortel, E.; Fischer, A.; Chuenchom, L.; Polte, J.; Emmerling, F.; Smarsly, B.; Kraehnert, R. New Triblock Copolymer Templates, PEO-PB-PEO, for the Synthesis of Titania Films with Controlled Mesopore Size, Wall Thickness, and Bimodal Porosity. *Small* **2012**, *8*, 298−309.

(21) Brezesinski, T.; Smarsly, B.; Iimura, K. I.; Grosso, D.; Boissière, C.; Amenitsch, H.; Antonietti, M.; Sanchez, C. Self-Assembly and Crystallization Behavior of Mesoporous, Crystalline HfO_2 Thin Films: A Model System for the Generation of Mesostructured Transition Metal Oxides. *Small* **2005**, *1*, 889−898.

(22) Hartmann, P.; Brezesinski, T.; Sann, J.; Lotnyk, A.; Eufinger, J.-P.; Kienle, L.; Janek, J. Defect Chemistry of Oxide Nanomaterials with High Surface Area : Ordered Mesoporous Thin Films of the Oxygen Storage Catalyst. *ACS Nano* **2013**, *7*, 2999−3013.

(23) Eckhardt, B.; Ortel, E.; Bernsmeier, D.; Polte, J.; Strasser, P.; Vainio, U.; Emmerling, F.; Kraehnert, R. Micelle-Templated Oxides and Carbonates of Zinc, Cobalt, and Aluminum and a Generalized Strategy for Their Synthesis. *Chem. Mater.* **2013**, *25*, 2749−2758.

(24) Kraffert, K.; Karg, M.; Schmack, R.; Clavel, G.; Boissiere, C.; Wirth, T.; Pinna, N.; Kraehnert, R. Stabilization of Mesoporous Iron Oxide Films against Sintering and Phase Transformations via Atomic Layer Deposition of Alumina and Silica. *Adv. Mater. Interfaces* **2018**, *5*, 1800360.

(25) Innocenzi, P.; Malfatti, L. Mesoporous Thin Films: Properties and Applications. *Chem. Soc. Rev.* **2013**, *42*, 4198−4216.

(26) Reitz, C.; Leufke, P. M.; Hahn, H.; Brezesinski, T. Ordered Mesoporous Thin Film Ferroelectrics of Biaxially Textured Lead Zirconate Titanate (PZT) by Chemical Solution Deposition. *Chem. Mater.* **2014**, *26*, 2195−2202.

(27) Kirchberg, K.; Wang, S.; Wang, L.; Marschall, R. Mesoporous $ZnFe_2O_4$ Photoanodes with Template-Tailored Mesopores and Temperature-Dependent Photocurrents. *ChemPhysChem* **2018**, *19*, 2313−2320.

(28) Kirchberg, K.; Marschall, R. Sol-Gel Synthesis of Mesoporous $CaFe_2O_4$ Photocathodes with Hierarchical Pore Morphology. *Sustain. Energy Fuels* **2019**, *3*, 1150−1153.

(29) Li, Y.; Bastakoti, B. P.; Imura, M.; Hwang, S. M.; Sun, Z.; Kim, J. H.; Dou, S. X.; Yamauchi, Y. Synthesis of Mesoporous TiO_2/SiO_2 Hybrid Films as an Efficient Photocatalyst by Polymeric Micelle Assembly. *Chem. Eur. J.* **2014**, *20*, 6027−6032.

(30) Hartmann, P.; Lee, D.-K.; Smarsly, B. M.; Janek, J. Mesoporous TiO_2: Comparison of Classical Sol-Gel and Nanoparticle Based Photoelectrodes for the Water Splitting Reaction. *ACS Nano* **2010**, *4*, 3147−3154.

(31) Benkstein, K. D.; Semancik, S. Mesoporous Nanoparticle TiO_2 Thin Films for Conductometric Gas Sensing on Microhotplate Platforms. *Sensors Actuators, B Chem.* **2006**, *113*, 445−453.

DOI: 10.1021/acs.langmuir.9b02455
Langmuir 2019, 35, 16427−16437

(32) Yue, J.; Suchomski, C.; Voepel, P.; Ellinghaus, R.; Rohnke, M.; Leichtweiss, T.; Elm, M. T.; Smarsly, B. M. Mesoporous Niobium-Doped Titanium Dioxide Films from the Assembly of Crystalline Nanoparticles: Study on the Relationship between the Band Structure, Conductivity and Charge Storage Mechanism. *J. Mater. Chem. A* **2017**, *5*, 1978−1988.
(33) Brezesinski, T.; Wang, J.; Polleux, J.; Dunn, B.; Tolbert, S. H. Templated Nanocrystal-Based Porous TiO_2 Films for Next-Generation Electrochemical Capacitors. *J. Am. Chem. Soc.* **2009**, *131*, 1802−1809.
(34) Kozuka, H. Stress Evolution and Cracking in Sol-Gel-Derived Thin Films. In *Handbook of Sol-Gel Science and Technology*; Klein, L. C., Aparicio, M., Jitianu, A., Eds.; Springer International Publishing AG: Switzerland, 2018, pp 275−311.
(35) Keddie, J. L.; Braun, P. V.; Giannelis, E. P. Interrelationship between Densification, Crystallization, and Chemical Evolution in Sol-Gel Titania Thin Films. *J. Am. Ceram. Soc.* **1994**, *77*, 1592−1596.
(36) Ishikawa, Y.; Kozuka, H. Evolution of Stress in Alkoxide Derived Titania Gel Films under Heat Treatment : Effects of Polyvinylpyrrolidone and Acetic Acid in Coating Solutions. *J. Ceram. Soc. Japan* **2004**, *112*, 228−233.
(37) Cop, P.; Kitano, S.; Niinuma, K.; Smarsly, B. M.; Kozuka, H. In-Plane Stress Development in Mesoporous Thin Films. *Nanoscale* **2018**, *10*, 7002−7015.
(38) Janssen, G. C. A. M.; Abdalla, M. M.; van Keulen, F.; Pujada, B. R.; van Venrooy, B. Celebrating the 100th Anniversary of the Stoney Equation for Film Stress: Developments from Polycrystalline Steel Strips to Single Crystal Silicon Wafers. *Thin Solid Films* **2009**, *517*, 1858−1867.
(39) Ohno, K.; Uchiyama, H.; Kozuka, H. Understanding of the Development of In-Plane Residual Stress in Sol-Gel-Derived Metal Oxide Thin Films. *J. Appl. Phys.* **2012**, *111*, No. 014901.
(40) Mutin, P. H.; Vioux, A. Nonhydrolytic Processing of Oxide-Based Materials: Simple Routes to Control Homogeneity, Morphology, and Nanostructure. *Chem. Mater.* **2009**, *21*, 582−596.
(41) Niederberger, M.; Pinna, N. *Metal Oxide Nanoparticles in Organic Solvents: Synthesis, Formation and Application*; Springer Verlag: Heidelberg, Germany, 2009.
(42) Niederberger, M.; Bartl, M. H.; Stucky, G. D. Benzyl Alcohol and Titanium Tetrachloride - A Versatile Reaction System for the Nonaqueous and Low-Temperature Preparation of Crystalline and Luminescent Titania Nanoparticles. *Chem. Mater.* **2002**, *14*, 4364−4370.
(43) Patterson, A. L. The Scherrer Formula for X-Ray Particle Size Determination. *Phys. Rev.* **1939**, *56*, 978−982.
(44) Navrotsky, A. Energetics of Nanoparticle Oxides: Interplay between Surface Energy and Polymorphism. *Geochem. Trans.* **2003**, *4*, 34−37.
(45) Lide, D. R. *CRC Handbook of Chemistry and Physics*, 89th Edition; CRC Press/Taylor and Francis: Boca Raton, FL, 2009.
(46) Kingery, W. D.; Bowen, H. K.; Uhlmann, D. R. *Introduction to Ceramics*, 2nd Edition; John Wiley & Sons Inc.: New York, United States, 1976.
(47) Zhang, H.; Banfield, J. F. Thermodynamic Analysis of Phase Stability of Nanocrystalline Titania. *J. Mater. Chem.* **1998**, *8*, 2073−2076.
(48) Yoldas, B. E.; Partlow, D. P. Formation of Broad Band Antireflective Coatings on Fused Silica for High Power Laser Applications. *Thin Solid Films* **1985**, *129*, 1−2), 1−14.
(49) Bauccio, M. *ASM Engineered Materials Reference Book*, 2nd Edition; ASM International: Almere, the Netherlands, 1994.

DOI: 10.1021/acs.langmuir.9b02455
Langmuir 2019, 35, 16427−16437

3.5 Atomic Layer Deposition of Defined Thin CeO_2 Layers in Ordered ZrO_2 Films and Their Impact on the Ionic/Electronic Conductivity

to be submitted

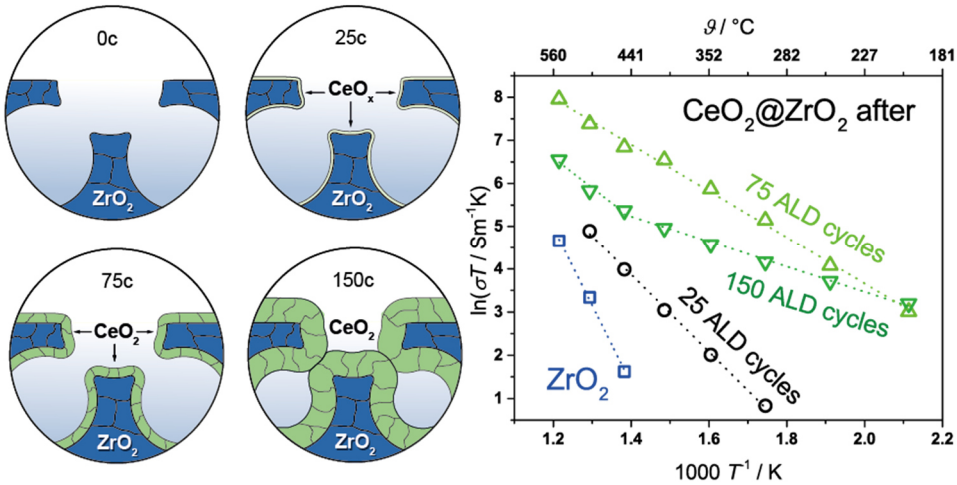

Adapted with permission from

P. Cop, E. Celik, K. Hess, Y. Moryson, P. Klement, M. T. Elm, B. M. Smarsly, Atomic Layer Deposition of Defined Thin CeO_2 Layers in Ordered ZrO_2 Films and Their Impact on the Ionic/Electronic Conductivity, *ACS Applied Nano Materials,* **2020**, *submitted.*

Atomic Layer Deposition of Defined Thin CeO_2 Layers in Ordered ZrO_2 Films and Their Impact on the Ionic/Electronic Conductivity

Pascal Cop[a,b], Erdogan Celik[b], Kevin Hess[a,b], Yannik Moryson[a,b], Philip Klement[b,c], Matthias T. Elm[a,b,c,], Bernd M. Smarsly[a,b,]**

a. Physikalisch-Chemisches Institut, Justus-Liebig University, Heinrich-Buff-Ring 17, D-35392 Giessen, Germany

b. Center of Materials Research, Justus-Liebig University, Heinrich-Buff-Ring 16, D-35392 Giessen, Germany.

c. Institute of Experimental Physics I, Justus-Liebig University, Heinrich-Buff-Ring 16, D-35392 Giessen, Germany.

KEYWORDS: ALD, mesoporous, ceria, zirconia, conductivity, core-shell

ABSTRACT

The physicochemical properties of thin metal oxide layers are strongly dependent on the deposited layer thickness and thus differ significantly from its bulk counterpart. In this work, we present the growth of defined thin layers of CeO_2 within mesostructured ZrO_2 thin films using atomic layer deposition (ALD). The prepared films consist of a cubic ordered arrangement of 15 nm spherical mesopores induced by the used diblock copolymer poly(isobutylene)-*block*-poly(ethylene oxide) (PIB_{50}-*b*-PEO_{45}), which allows studying the growth process and the successful coating of the interior pore surfaces via the combination of scanning electron microscopy (SEM), time-of-flight mass spectrometry (ToF-SIMS) and laser ellipsometry. These methods prove the CeO_2 layer growth and impregnation of the pores up to 100 ALD cycles, at which the interconnecting channels between the mesopores layers are filled completely impeding further transport of the gaseous CeO_2 precursors. X-Ray photoelectron spectroscopy (XPS) and diffractometry (XRD) measurements point out the increased amount of Ce^{3+} after a low amount of ALD cycles and show the presence of cubic CeO_2 with rising cycle counts, respectively. Impedance spectroscopic investigation further prove the formation of a continuous CeO_2 path through the entire porous network of the insulating ZrO_2 film and show a strong influence of the layer thickness on the conductivity. All in all, our work presents the preparation of novel hybrid CeO_2/ZrO_2 model systems, which enables to tailor their physicochemical properties by changing the thickness of the active oxide layer and promises improvements for their use as catalysts in oxidation reactions.

CeO_2 is well known for its unique redox trait to switch easily between Ce^{3+} and Ce^{4+}. It is therefore capable of catalyzing redox reactions as well as incorporating and releasing oxygen resulting in mixed ionic-electronic conductivity. Hence, CeO_2 is studied and industrially used as a solid oxide fuel cell (SOFC) electrolyte[1–3] and oxygen storage catalyst in automobiles, soot combustion and the HCl oxidation.[4–6] Yet, these mass technologies would still benefit from improved properties in terms of activity and stability of CeO_2-based catalysts. Recent studies on thin CeO_2 films indicated that the aforementioned properties can be tuned and potentially optimized. For instance, Sun *et al.* showed that thin layers of CeO_2 on ZrO_2 nanoparticles enhanced the catalytic activity as well as the stability in the corrosive $HCl/O_2/Cl_2$ atmosphere.[7] In addition, Gopal *et al.* revealed the impact of biaxial strain in ultrathin $CeO_{2-\delta}$ films on the oxygen storage properties.[8] These studies indicated that the physico-chemical properties of CeO_2 on a support material can be tailored by carefully adjusting the layer thickness on the nanometer scale.

In literature, the most prominent nanostructured examples are core-shell nanoparticles maximizing the interfacial area between two components, which lead to improvements in various applications. For instance, ZnO shells on SnO_2 nanorods improve the selectivity of the sensor in H_2 gas sensing.[9] Changing the thickness of γ-Fe_2O_3 layers on a Fe_3O_4 core tailors the magnetic properties used in hyperthermia treatment.[10] Promising properties of such core-shell nanostructures have already been discussed also for CeO_2. It was reported that the Ce^{3+}/Ce^{4+} ratio is adjusted by the CeO_x layer thickness on a TiO_2 nanoparticle core, thereby effecting its redox abilities.[11] Such dependence is supported by theoretical calculations revealing the influence of the substrate as well as the layer thickness on the formation of Ce^{3+} species[12] and thus the formation of oxygen vacancies. By increasing the film thickness and hence, decreasing the surface-to-bulk-ratio, the formation of Ce^{4+} is favored resulting in bulk-like redox properties of the mixed ion-electron conductor. Sayle *et al.*[13] as

well as Migani *et al.*[14] studied the influence of the particle size or layer thickness of CeO_2 on the activity in redox reactions by theoretical calculations of the oxygen vacancy formation energy. Both groups concluded a non-linear dependency on the particle size with Sayle *et al.* suggesting a minimum of the oxygen vacancy formation energy and highest oxygen depletion level for particles with a dimension of 3.5 nm .

However, most of the impregnation attempts concerning core-shell materials suffer from an inhomogeneous and non-conformal coating due to nanoparticle agglomeration or unpredictable movement of the particles during the deposition or impregnation procedure. These issues are avoided by using a more suitable substrate such as mesoporous metal oxide thin films possessing a defined and continuous porous framework, which allows to access the interior surface area. In comparison with nanoparticles, mesoporous structures provide a fundamentally better model system for its defined impregnation with a different material.

In order to cover the pore surfaces with the desired thickness, the layer growth using atomic layer deposition (ALD) has gained considerable scientific interest in the last years.[15–17] Thanks to its operation mode including the separation of the gas-solid reactions with inert gas purging step, the deposition of the desired metal oxide species is performed layer-by-layer. Hence, the ALD technique gives the possibility to impregnate even more complex substrates such as porous and mesoporous thin films with an atomic-level control of the formed layer and its thickness with significant reproducibility.[18–20] Thus, the ALD method classifies as superior in comparison with wet-chemical approaches such as wet-impregnation[21], co-condensation[22] and grafting[23] as well as physical attempts such as physical vapor or pulsed layer deposition.

Despite its benefits, the deposition in porous thin films with pore diameter below 50 nm remains challenging due to the difficulty of achieving and proving the conformal coating

of the interior pores. In order to overcome these issues, the deposition procedure was studied in detail with various characterization techniques elaborating the growth process and studying the effect of the active shell material on specific material properties.[24–27] For instance, Detavernier *et al.* presented comprehensively the combination of ellipsometric porosimetry (EP) and X-ray fluorescence studies to describe the growth process in porous substrates.[28] Also, this group demonstrated the "bottleneck" of the deposition procedure of TiO_2 and HfO_2 in Pluronic® F127-templated mesoporous SiO_2 and TiO_2 thin films, respectively, which is dependent on the size of interconnecting channels between the bigger pore layers.[17,28,29] The latter result was verified by our group using ordered mesoporous $Ce_{0.5}Zr_{0.5}O_2$ (CZO) thin films and depositing TiO_2 layers by ALD.[30] The films were synthesized using the diblock copolymer poly(isobutylene)-*block*-poly(ethylene) oxide referred to as PIB_{50}-*b*-PEO_{45}, which our group uses to fabricate different metal oxides including TiO_2[31,32], indium tin oxide[33], Al_2O_3[34] and $Ce_xZr_{1-x}O_2$[35] as it provides a 3D network of spherical mesopores with 15 nm in diameter connected by smaller channels. Hence, the defined pore size and their connection using this type of material allows studying the ALD-based deposition in greater detail and more accurately in comparison with non-ordered films, and thus the impact of the deposited layer on physicochemical properties can be investigated more deeply.

Following this strategy, in this study mesoporous ZrO_2 thin films with an ordered arrangement of around 15 nm are prepared and impregnated with CeO_2 using ALD. Based on our previous study[30], the coated mesoporous films are investigated by several state-of-the-art characterization techniques to understand the growth process inside the mesoporous network, using $Ce(thd)_4$ and O_3 as the corresponding precursors. X-ray photoelectron spectroscopy gives insight about the Ce^{3+}-content dependent on the thickness of the prepared CeO_2 layer. In order to elucidate the influence of the CeO_2 layer thickness on physico-

chemical properties, the conductivity is examined using impedance spectroscopy, to elaborate on its different transport mechanism occurring when varying thickness and pore clogging. Due to the low conductivity of ZrO_2, a deposition of CeO_2 layers is easily detectable by an increase in conductivity and delivers additional insight into covering the mesoporous network as well as the oxygen vacancy formation.

Results and Discussion

The mesoporous ZrO_2 thin films were prepared via the so-called EISA approach[36] using a solution containing $ZrOCl_2 \cdot 8\ H_2O$ and the structure-directing agent PIB_{50}-*b*-PEO_{45} in a mixture of ethanol and 2-methoxy-ethanol. The solutions were deposited on partially oxidized [110] silicon wafers using spin-coating in order to fabricate thin films of 40 nm thickness. The films were subsequently freed from the polymeric template by an annealing step

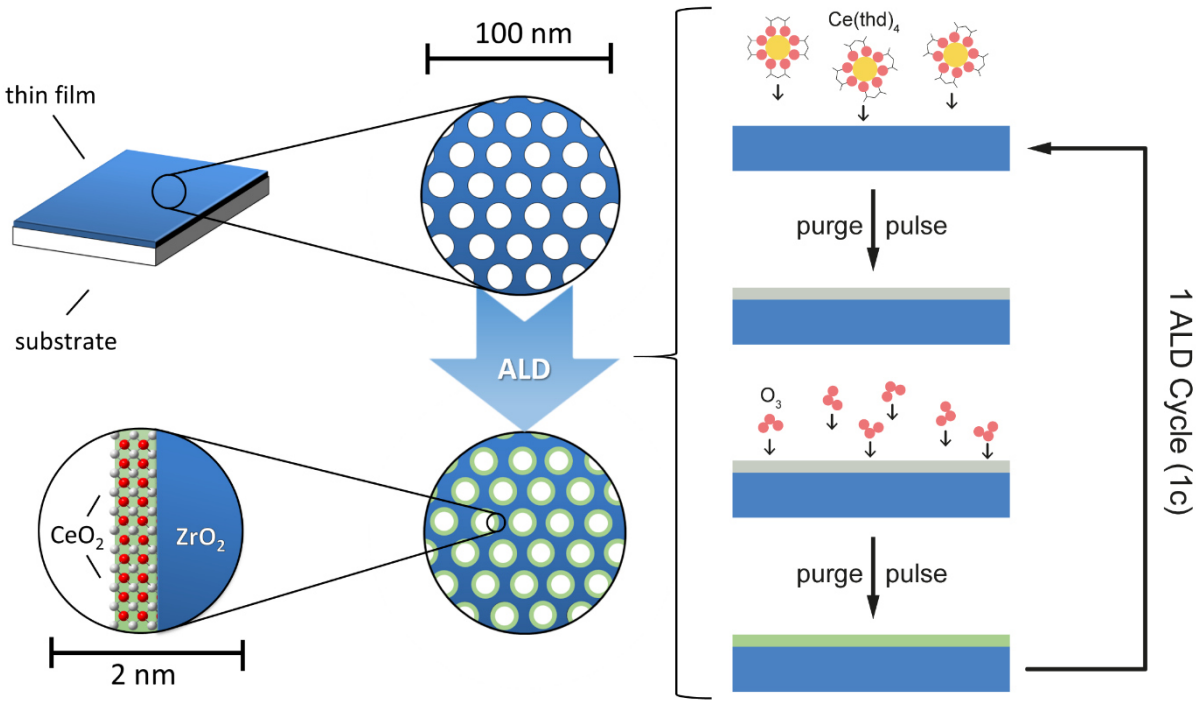

Figure 12: Schematic overview of the strategy for studying the atomic layer deposition (ALD) of thin layers of CeO_2 in the mesoporous matrix of ZrO_2 thin films with pore sizes of 15 nm.

at 600 °C leading to the crystallization into the tetragonal phase of ZrO_2 and the formation of a cubic arrangement of the mesopores. The obtained pore size of around 15 nm is determined by the used diblock copolymer PIB_{50}-*b*-PEO_{45}. In addition, the layers of the spherical mesopores are connected via small channels[37,38], which are essential for the gaseous ALD precursors to infiltrate the porous structure and reach every pores' surface. The characteristics of these films are described in more detail in previous works.[30,31]

The mesoporous ZrO_2 thin films were cut into 1x1 cm^2 pieces and transferred to the ALD instrument alongside blank Si[110] substrates as references. The latter were used to measure the CeO_2 film thickness and to determine the growth rate for the applied deposition parameters. The thickness was measured by laser ellipsometry and reveals a growth rate per cycle (GPC) of 0.029 nm / cycle (see Figure S1). However, only the thicknesses of 75 cycles and above were taken into account as the thickness of the CeO_2 layers after a lower number of ALD cycles is below the detection limit of the laser ellipsometer setup. The deposition rate is linear for higher number of ALD cycles and a non-linear trend occurs in the first ALD cycles. In the beginning, the growth is aggravated as the precursor connects to the Si-OH groups of the partially oxidized silicon wafer. After one cycle it reacts with Ce-OH groups assuming that the $Ce(thd)_4$ chemisorbs as a perfect monolayer on the whole substrate. In our previous work[30] we showed that a higher dwell time leads to a higher saturation per cycle of the substrate surface enhancing the growth rate. The higher dwell time during the procedure also facilitates the deposition on complex substrates just like the mesoporous ZrO_2 thin films used here. It provides enough time for the gaseous precursor to diffuse through the interconnecting channels into the porous structure and chemisorb on the inner pore surfaces. However, it has to be considered that the deposition rate may differ for the mesoporous ZrO_2 compared to the silicon wafers. On the one hand, the chemisorption process on different materials is dissimilar. On the other hand, the distinct roughness

of the substrates also exerts an impact on the number of sorption sites accompanied with steric hindrance influencing the growth rate.[39,40]

Figure 2 reveals that the refractive indices as well as the thickness of the mesoporous ZrO_2 substrate changes after a certain number of ALD cycles based on the ellipsometric measurements. Except the result after 15 cycles, the thickness increases linearly with rising amount of ALD cycles from originally 42.8 nm to 49.1 nm after 150 cycles resulting in a 6.3 nm thick CeO_2 layer, which is in good agreement with the obtained thickness results on Si substrates (see Figure S1). While this indicates the formation of a top layer growing on

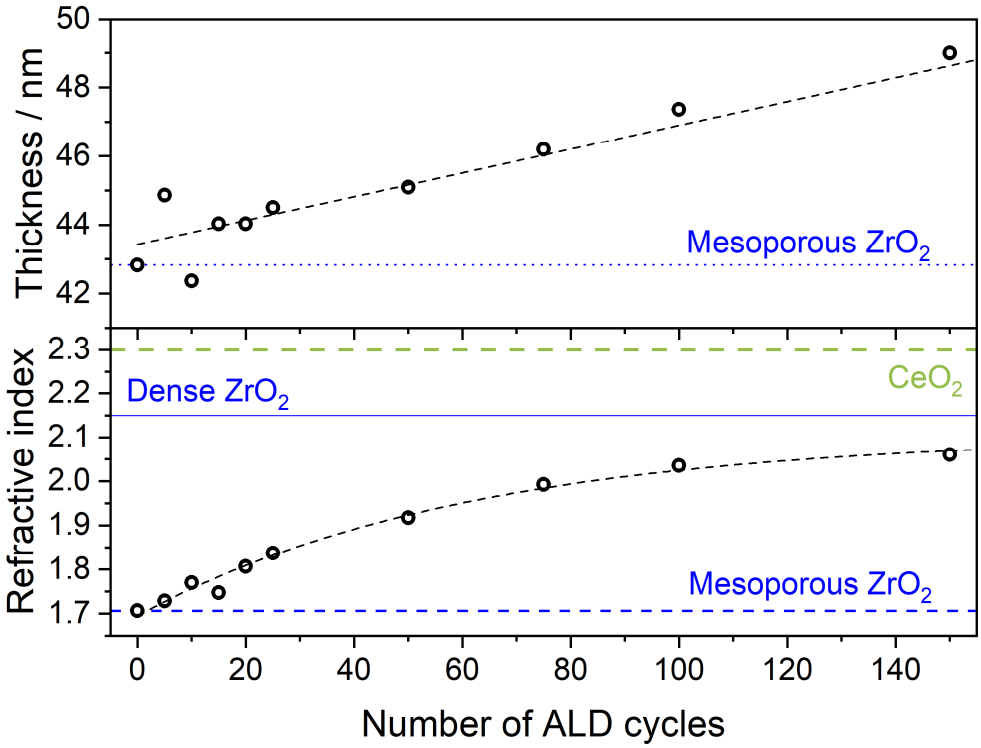

Figure 13: Thickness (top) and refractive index (bottom) of the mesoporous ZrO_2 film before and as a function of the number of ALD cycles, determined by laser ellipsometry performed using λ = 633 nm. The difference in size between the sample before and after the deposition via ALD as well as the refractive index of tetragonal dense (solid line), mesoporous (dashed line) ZrO_2 (blue) and CeO_2 (green) are also displayed. The latter is based on ellipsometric studies of the deposited CeO_2 film on Si[110] substrates.

the mesoporous ZrO_2 substrate, the enlarging refractive indices is assigned to a CeO_2 deposition inside the pores of the substrate. The saturation slope at higher cycles supports this assumption as the pores might diminish in size increasing the refractive index significantly after the first cycles due to the CeO_2 possessing a remarkably higher refractive index of 2.3[41] than the mesoporous ZrO_2 film. Hence, the porosity in the films decreases and the refractive index rises. After 75 cycles the increment of the refractive index is lowered due to the interconnecting channel being clogged so that the upcoming cycles only add a layer on top of the substrate. However, the resulting refractive index after 150 cycles is still smaller than the index of dense tetragonal ZrO_2 as well as a cubic CeO_2 layer indicating that the pores are not completely filled approving the theory of the clogged interconnected channels preventing further deposition in the pores at higher ALD cycle counts.

The films were investigated by ToF-SIMS using depth profiling and tracing the secondary ions CeO^-, ZrO^- and Si^- to evaluate the existence of CeO_x species inside the pores of the ZrO_2 matrix (see Figure 3). These measurements reveal two decisive results. First, the CeO^- species' signal increases with higher amount of ALD cycles indicating the formation of a small top layer of CeO_x before it reaches the porous ZrO_2 substrate after 100 cycles. Second, CeO_x is homogeneously distributed in the film accounted by the CeO^- count slope which is parallel to the ZrO^- one representing the mesoporous substrate. Furthermore, both

species decrease equally when reaching the silicon substrate marked by the Si^--signal. However, one has to consider the different ablation rates of the different ionic species preventing a precise calculation of the Ce and Zr content. A semiquantitative analysis can be performed nonetheless, as the same instrumental parameters including the same analysis current were used. Hence, the signal ratio of CeO^- and ZrO^- was determined after a sputter time of 100 s for all of the coated films. The results are also shown in Figure 3 illustrating the process of the pore coating, which is in good agreement with the ellipsometric studies of the refractive index and includes a saturation after 100 cycles. Here, the intensity of the CeO^- species remains nearly constant with respect to the ZrO^- signal showing that after 100 cycles only the top layers grow in thickness with further deposition cycles, while the pores in the sub-layers are not accessible anymore. This phenomenon is additionally visualized in Figure 4,

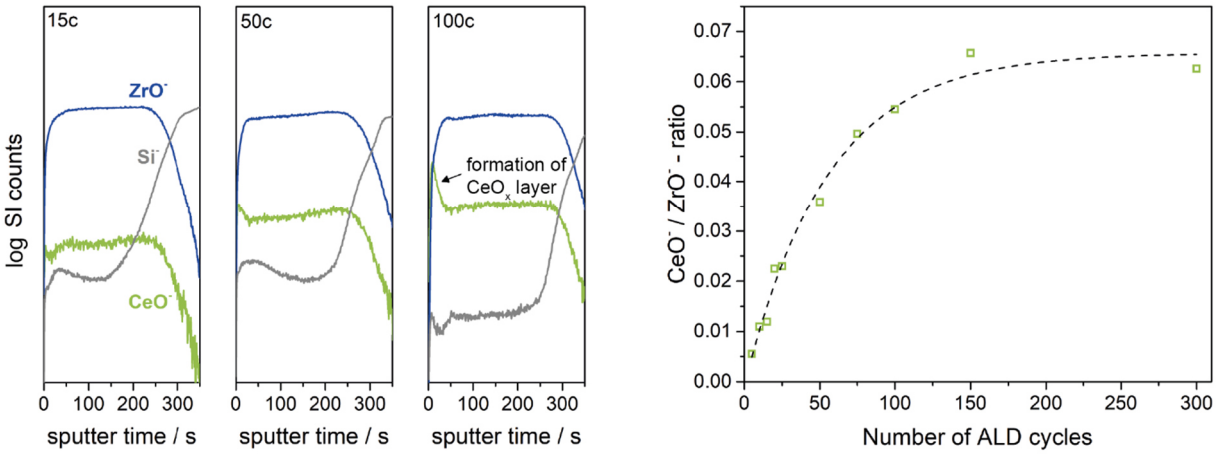

Figure 14: ToF-SIMS depth profiles of the mesoporous ZrO_2 film after 15, 50 and 100 ALD cycles. Next to the ions deriving from the thin film (ZrO^- and CeO^-) the signal from the utilized silicon substrate (Si^-) is depicted by plotting the secondary ion (SI) counts logarithmic as a function of the sputter time. In addition, the signal ratio of CeO^- and ZrO^- at 100 s of sputtering in relation to the ALD cycles is shown.

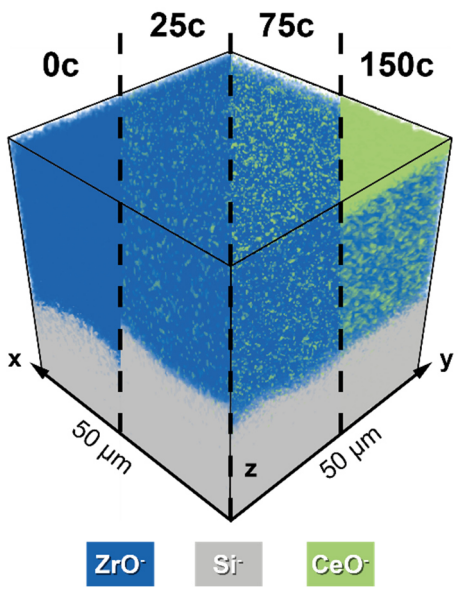

Figure 15: 3D topographic images based on the ToF-SIMS depth profiles are displayed for the untreated mesoporous ZrO_2 films as well as after 25, 75 and 150 ALD cycles. The *z*-axis corresponds to the sputter time.

showing the 3D profiles generated from the ToF-SIMS data. After a certain number of ALD cycles, only the top layer of CeO^- species grows in size while the interior of the mesoporous film maintains the same CeO^-/ZrO^- intensity ratio.

The pore morphology was investigated using SEM with a focus on the pore diameter changes with raising amount of ALD cycles. The results shown in Figure 5 point out a similar saturation slope like the ToF-SIMS study. The pores shrink faster in diameter within the first ALD cycles than after 75 cycles. This can be interpreted as a further evidence for the closing of the interconnected channels between the mesopore layers. The mesopores on top of the film are still observable deriving from the pillar growth of CeO_2 around the pores in the top layer and decreasing only slightly in their lateral diameters and thus, consolidating gradually. The EDS analyses (Figure 5) of the coated films show an increasing elemental Ce/Zr-ratio for growing number of ALD cycles. Due to the high penetration depth of EDS, the technique does not allow to determine whether the stronger signal derives from

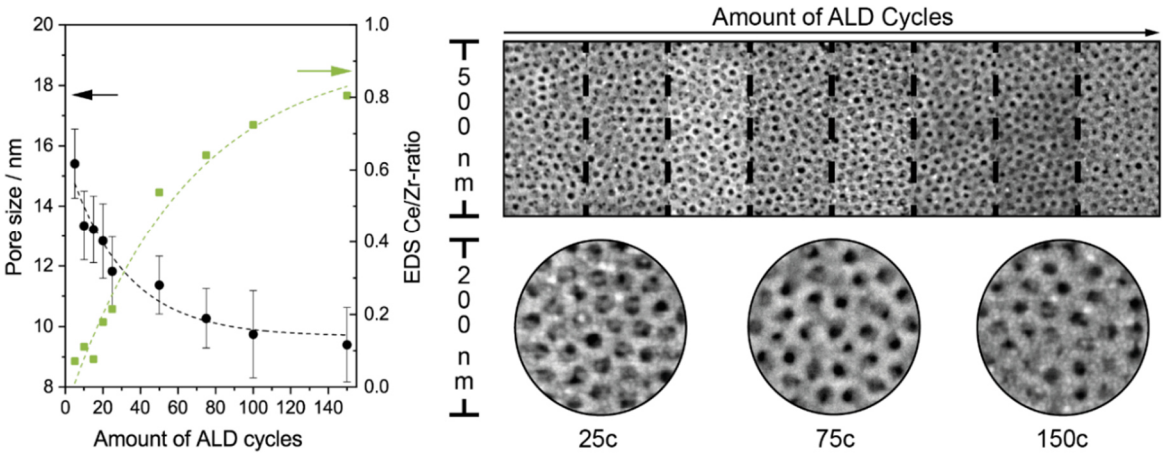

Figure 16: SEM and EDS investigations for the uncoated and coated mesoporous ZrO_2 films. (*left*) Pore size determination using the given SEM images (black) as well as EDS analyses to calculate the elemental Ce/Zr-ratio of the coated films in dependence of the amount of ALD cycles. (right) Top-view SEM recordings revealing the morphological changes of the porous structures.

the top layer or the coating of the pores. However, in combination with the ToF-SIMS investigations, the detected signals from Ce originate from CeO_2 deposited in the meso-pores. As Figure 5 also reveals a saturation curve but with a smaller slope compared to the results obtained by ellipsometry, SEM and ToF-SIMS, the increase in the EDS signal after 75 cycles is assigned to the growing top layer. When depositing CeO_2 on the pore surfaces as well as on the top of the mesoporous substrate, relatively more material is added on the film in comparison with covering solely the surface on a flat substrate after 100 cycles due to the difference of their respective specific surface area.

To conclude the structural investigations of the CeO_2-coated mesoporous ZrO_2 thin films, the deposition process after 5 and up to 150 cycles was successfully tracked by the combi-nation of ToF-SIMS, SEM, EDS as well as ellipsometric studies. After around 100 cycles, the interconnecting channels between two mesopore layers are completely filled preventing

the gaseous ALD precursor to reach the inner pore surfaces and therefore, only the top layer on the complex substrate is growing.

While these structural investigations prove the existence of CeO_x species inside the mesoporous network, the question remains, which crystal structure and how much Ce^{3+} is present in the ZrO_2 substrate in regards to the amount of ALD cycles. The first question can be answered by taking GI-XRD measurements into account (see Figure 6), revealing the tetragonal phase of ZrO_2. At 50 cycles, a small shoulder becomes visible in the diffraction pattern at 28°, which can be assigned to the (111) reflection of CeO_2. The signal sharpens and possesses a higher intensity with increasing number of ALD cycles deriving from the

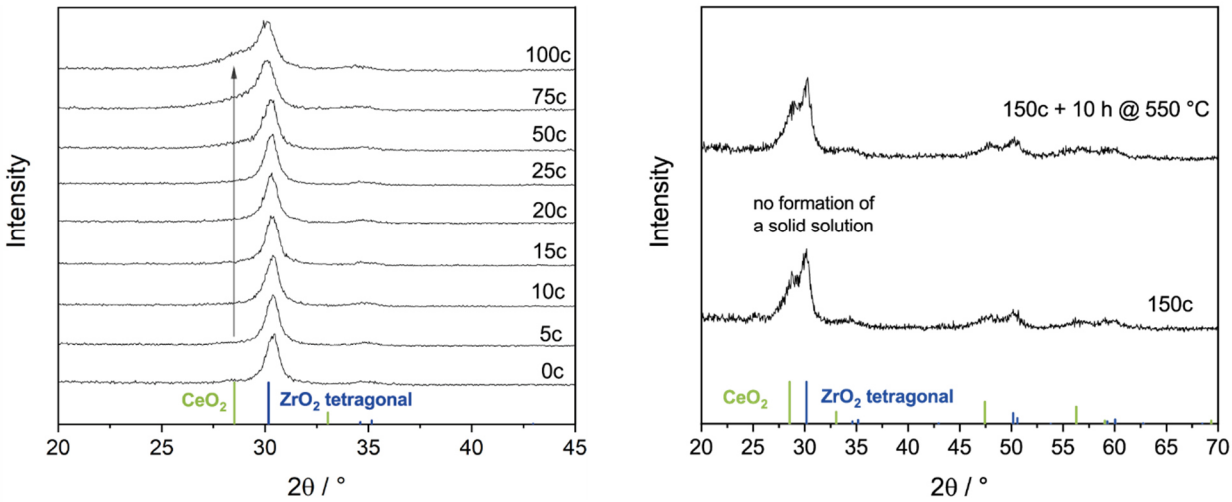

Figure 17: (*left*) XRD pattern of the mesoporous ZrO_2 thin films before and after the ALD deposition using different numbers of cycles. (*right*) XRD pattern of the mesoporous thin film after 150 ALD growth cycles followed by an annealing step at 550 °C for 10 h. In both cases the reference pattern for the cubic lattice of tetragonal ZrO_2 (ICDS 98-065-5671, blue) and cubic CeO_2 (JCPDS 98-016-7160, green) are also shown.

raising crystallite growth and the present amount of the deposited material. Due to the high

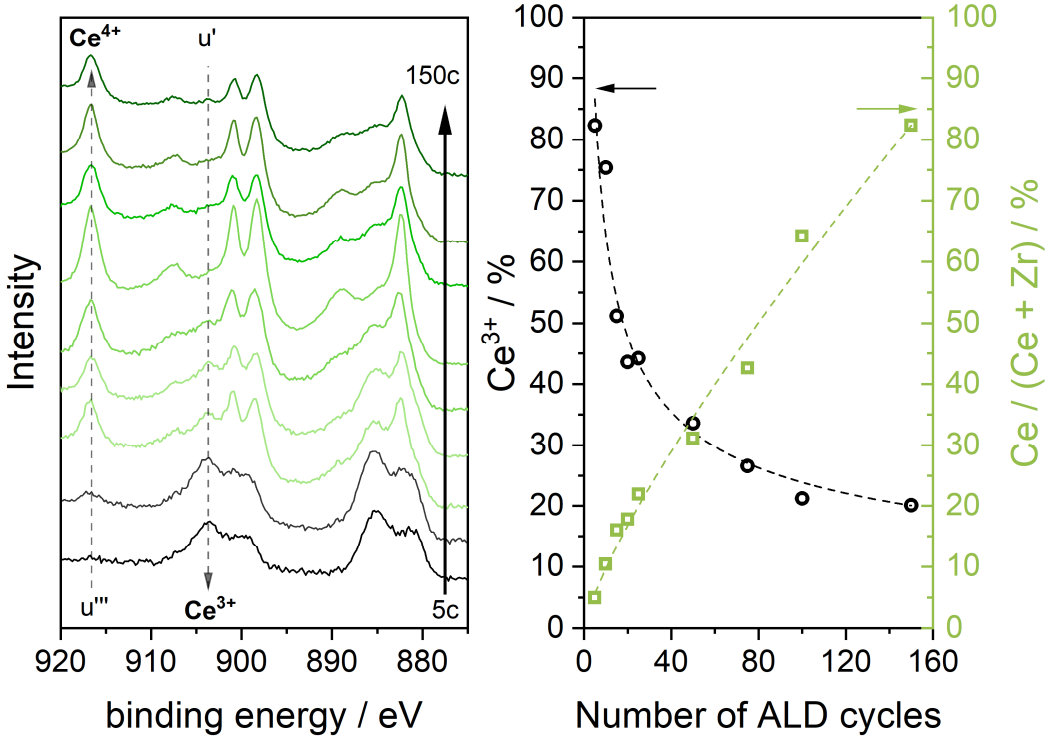

Figure 18: (*left*) XPS study of Ce3d spectra of the CeO_2-coated mesoporous ZrO_2 films. The u''' band correspond to Ce^{4+} while u' band can be assigned to the Ce^{3+} species. (*right*) Evaluation of the XPS study regarding the Ce^{3+} content (black) as well as the relative Ce content in the mesoporous ZrO_2 film (green) depending on the number of ALD cycles.

surface area of the mesoporous ZrO_2 substrate, the amount of deposited CeO_2 is multiplied and leads to the detectability of the cubic CeO_2 in and on the film. As no visible formation of a top layer is determined by ToF-SIMS at 25 cycles, we can conclude that the observed (111) reflection originates from CeO_2 inside the mesopores. Moreover, an additional annealing step of 550 °C (10 hours) refutes the formation of a possible CeO_2-ZrO_2 solid solution (see Figure 6). Thus, the CeO_2 layer is preserved even at elevated temperatures, which is essential for the interpretation of the temperature-dependent total conductivity experiments. Lastly, XPS studies show the Ce^{3+} content dependent on the number of ALD cycles used in the deposition procedure giving values ranging between 85% and 20%. In

Figure 7, we observe the expected bands in the Ce 3d region for CeO_2 for higher cycle counts. Next to the six signals deriving from CeO_2 (v, v'', v''' and u, u'', u'''), we also take the four additional signals from Ce_2O_3 (v0, v' and u0, u') into account. Based on the findings of Skala *et al.*[42] we used a combination of two signals to fit the observed asymmetry of *u* and *v* resulting in better fit conditions. After the first cycles only the band belonging to Ce_2O_3 is observable. Granozzi *et al.*[11] also showed this phenomenon on TiO_2 nanoparticles explaining this effect as interface stabilization of Ce^{3+}. With additional ALD cycles, the u''' band is observed indicating the formation of CeO_2 and increasing the amount of Ce^{4+}, respectively. Until 25 cycles, the Ce^{3+}/Ce^{4+}-ratio decreases significantly which is affected by the higher layer thickness according to Agnoli *et al.*.[12] Due to the low penetration depth of around 5 nm, the XPS recordings depict the Ce-content inside the mesoporous ZrO_2 structure. Taking the ellipsometric results into account revealing the top layer thickness to be around 5 nm after 100 cycles, the obtained value for Ce^{3+} considers also the layers in the inner pores. After 150 cycles, only the top layer is analyzed giving the lowest

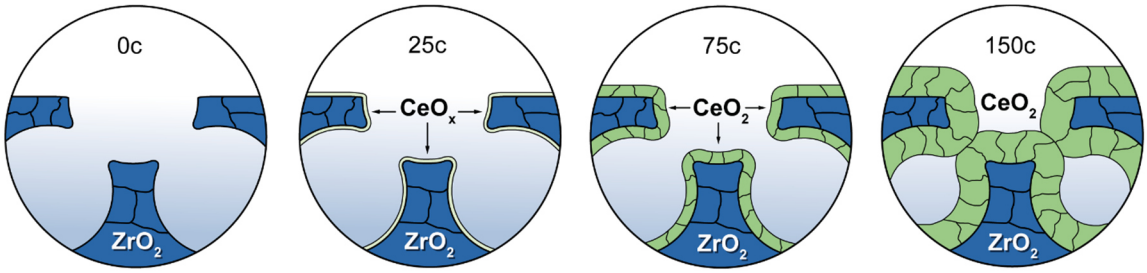

Figure 19: Schematic model of the CeO_2 deposition in the mesoporous ZrO_2 film using ALD. CeO_2 covers firstly the surface of the 15 nm mesopores as well as the smaller interconnecting channel leading to a decrease in the average pore size. The CeO_2 layer in the pores grows with increasing number of the ALD cycles leading to the closing of the channels and prevents the gaseous precursor to reach the inner pore layers. Hence, pores in the topmost pore layer remain and additional ALD cycles result in a thicker layer on top of the film.

relative content of Ce^{3+} with around 20%. Hence, we believe that the Ce^{4+} content inside the pores is higher but cannot be detected by XPS due to its small penetration depth. However, for the following interpretation of the conductivity measurements, this option needs to be considered.

Conductivity measurements

On the basis of the structural investigations of the mesoporous thin films coated with CeO_2, four of the acquired samples were chosen for impedance spectroscopy representing the different growth stages of the CeO_2 layer (see Figure 8). The shown scheme reveals that for every sample diverse causes have to be considered such as layer thickness, Ce^{3+}-content as well as interface effects. In addition, due to the low thickness of around 5 nm inside the

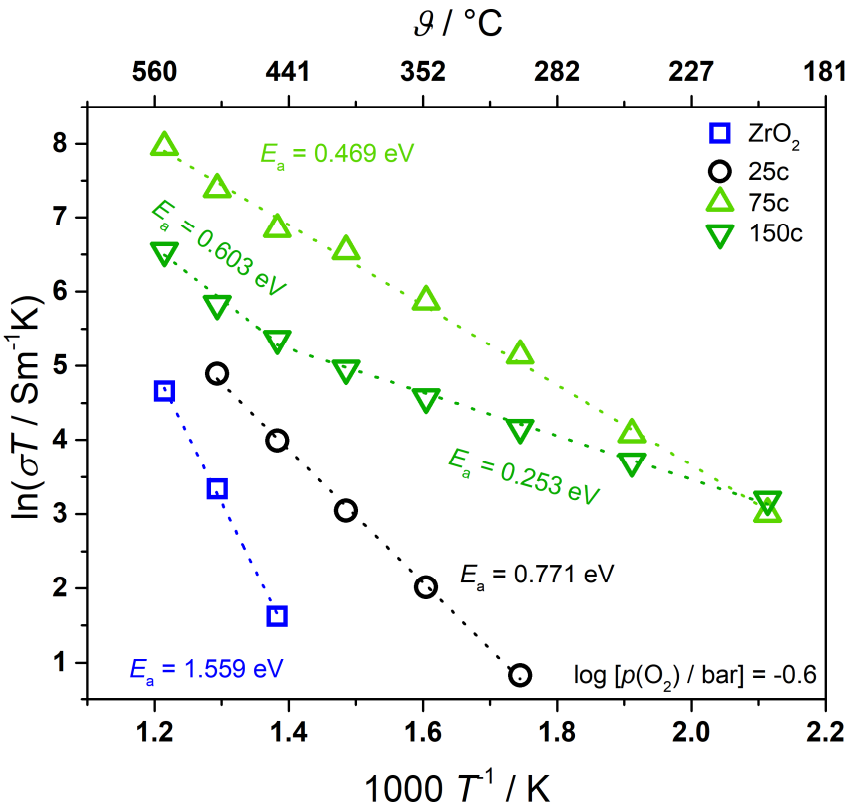

Figure 20: Arrhenius plots of the total conductivity for the uncoated ZrO_2 film (blue)), after 25 (black), 75 (green) and 150 ALD cycles (dark green).

pores as well as for the top layer, a comparison with the transport properties of CeO_2 in its bulk form is restricted. Figure 9 shows the measured total electrical conductivity for the samples investigated under dry conditions and a constant oxygen partial pressure of $\lg(p(O_2)/\mathrm{bar}) \approx -0.67$. The measurements were carried out in the temperature range between 200 and 500 °C. The tetragonal ZrO_2 sample shows the lowest electrical conductivity compared to the measured conductivity of the CeO_2-coated thin films. Using the Arrhenius equation, the activation energy is found to be approximately 1.55 eV, which is typically obtained for tetragonal ZrO_2 and characteristic for the transport of oxygen ions.[43–46] Coating the thin films with CeO_2 significantly changes the total conductivity. After 25 cycles, the conductivity of the mesoporous thin film coated with ceria is increased by at least two orders of magnitude compared to the pure ZrO_2 accompanied with a significant decrease in the activation energy to 0.77 eV. After 75 cycles, the ZrO_2-CeO_2 sample exhibits the highest value in conductivity and the activation energy is further decreased to about 0.47 eV. Finally, in the case of the CeO_2-ZrO_2 sample prepared by the deposition of 150 cycles, the total conductivity decreases again and two transport regimes are observed. At low temperatures the thin films reveal the lowest activation energy of about 0.25 eV, which increases to approximately 0.6 eV at temperatures above 450 °C. The increase in activation energy for this sample is attributed to a non-negligible conductivity contribution of the mesoporous ZrO_2 at high temperatures. While at low temperatures, the transport is dominated solely by the ceria layer with a low activation energy, at higher temperatures the conductivity of the ZrO_2 also contributes to the total conductivity of the CeO_2-ZrO_2 composite, i.e. $\sigma_{\mathrm{tot}} = \sigma_{\mathrm{CeO_2}} + \sigma_{\mathrm{ZrO_2}}$, and therefore results in an increase in activation energy.

The change in activation energy and total conductivity of the ceria coating can be understood qualitatively when considering that the deposited CeO_2 coatings show a large amount of Ce^{3+} which decreases with increasing cycle number as revealed by XPS measurements.

In undoped $CeO_{2-\delta}$ the concentration of Ce^{3+} is directly related to the amount of oxygen vacancies and thus to the non-stoichiometry δ by the following defect equilibrium written in Kröger-Vink notation (see Equation (1)):[47,48]

$$2\mathrm{Ce}_{\mathrm{Ce}}^{x} + \mathrm{O}_{\mathrm{O}}^{x} \leftrightarrow 2\mathrm{Ce}_{\mathrm{Ce}}^{\prime} + \mathrm{V}_{\mathrm{O}}^{\bullet\bullet} + \frac{1}{2}\mathrm{O}_{2(g)} \qquad (1)$$

It is well known from literature, that in non-stoichiometric ceria the conductivity is dominated by the transport of electrons, which occurs by a hopping mechanism.[48–50] Here, the electrons behave as small polarons jumping from a Ce^{3+} ion to neighboring Ce^{4+} ions. Thus, the electronic conductivity as well as the activation energy are strongly affected by the amount of the Ce^{3+} ions in the system and thus the non-stoichiometry x. As reported by Naik *et al.* and Tuller *et al.* the activation energy for the hopping process of the electrons in $CeO_{2-\delta}$ increases with increasing non-stoichiometry x.[48,49] Naik *et al.* determined an activation energy of about 0.2 eV at $x = 0.03$, which increases nonlinear to approximately 0.55 eV for highly non-stoichiometric ceria compounds with $\delta = 0.2$.[49] A comparable behavior is also found for our mesoporous ZrO_2-CeO_2 thin films. According to our XPS results the ceria thin film after 25 cycles exhibits a Ce^{3+} amount of about 40% corresponding to a non-stoichiometry of $\delta = 0.2$. The obtained activation energy of about 0.77 eV is therefore higher as the value of 0.55 eV reported by Naik *et al.* for $CeO_{2-\delta}$ with a comparable non-stoichiometry. This discrepancy is mainly attributed to a non-negligible ionic contribution of the mesoporous ZrO_2 film, which reveals a significantly higher activation energy of 1.56 eV. However, for the thin film after 75 cycles, XPS indicates a Ce^{3+} amount of about 30%, i.e. a non-stoichiometry $\delta = 0.15$. The corresponding activation energy of 0.47 eV is therefore in good agreement with the values of about 0.5 eV determined for highly non-stoichiometric ceria with comparable oxygen deficiency. Finally, for the ceria thin film after 150 cycles with an activation energy of 0.25 eV the non-stoichiometry of $\delta \approx 0.1$

estimated from the XPS results is slightly higher than the expected value of $\delta = 0.06$ according to the results Naik *et al.*. Not only the change of the activation energy can be correlated with the non-stoichiometry of the deposited ceria layer, but also the magnitude of the conductivity. Here, a maximum in conductivity was also observed for ceria with δ of about 0.15 in excellent agreement with our results.[48,49]

It is worth noting that the origin for the thickness dependence of the non-stoichiometry and thus the much higher Ce^{3+} amount in the ceria layer compared to bulk ceria at comparable oxygen partial pressure is not clear yet. One possible reason may be that the grain boundary density depends on the thickness of the ceria coating layer. As shown recently, ceria grows epitaxially on ZrO_2-based oxides with a grain size of a few nanometers when using ALD.[18] Thus, it is reasonable to assume that the coating layers exhibits a high grain boundary density, which can significantly affect the defect concentrations due to the formation of a space charge region at the boundary. As the formation of a space charge layer results in an accumulation of electrons and a depletion of oxygen ions in the space charge layer in the case of ceria,[51,52,53] a high grain boundary density may be responsible for the high Ce^{3+} concentration in the coating layer.

It is also possible that the observed thickness dependence of the electronic conductivity is due to variations of the surface area itself, where also a space charge layer is formed.[54,55] With increasing number of ALD cycles, the pore size shrinks accompanied with a reduction of the surface area and thus the electron concentration. However, further investigations are necessary to elucidate in detail the influence of the coating morphology and the surface area on the electrical transport properties in the CeO_2-ZrO_2 composites.

It is furthermore worth noting that compared to findings of Hartmann *et al.*,[56] who investigated the transport properties of mesoporous CeO_2-ZrO_2 thin films with a nearly identical

pore structure, all of our calculated activation energies are significant lower. They determined the lowest activation barrier of 0.86 eV for a pure mesoporous CeO_2 film, while the activation energies of the CeO_2-ZrO_2 solid solutions range from 1.0 to 1.3 eV. As these values were also found by Chiodelli *et al.*[57] using CeO_2-ZrO_2 ceramics with grain sizes of several micrometers, the herein reported low activation barriers are not directly due to the mesoporous structure, but caused by the composite character of the samples with different layer thicknesses of the CeO_2 coating deposited by ALD. As seen in Figure 9 the total conductivity maximum is measured for the sample after 75 ALD cycles with a thickness of around 3.4 nm according to the ellipsometric investigations (see Figure 2). This result agrees well with the postulated optimum CeO_2 particle size of 3.5 nm by Sayle *et al.*[13] who investigated the oxygen vacancy formation energy as a function of nanoparticle size. However, this comparison with theoretical calculations needs to be addressed more deeply by measuring additional CeO_2-coated mesoporous ZrO_2 samples after different amount of ALD cycles.

Conclusions

Our study presented the deposition of defined thin layer of CeO_2 into an ordered mesoporous ZrO_2 structure with 15 nm pores in diameter using a layer-by-layer approach using ALD. The impregnation of the interior of the porous structure and the accompanied growth process using $Ce(thd)_4$ and O_3 as precursors were followed by ToF-SIMS, SEM and ellipsometric investigations. The combination of these characterization methods reveal that the pores are filled up to 100 ALD cycles ensued by the formation of a CeO_2 top layer for upcoming ALD cycles. This limit corresponds well with previous results and is accompanied by pore clogging of the interconnecting channels between two mesopores layers. Based on XRD analyses, the existence of cubic CeO_2 after 50 ALD cycles derives from the high amount of CeO_2 owned to the high surface area of the given ZrO_2 substrate. In addition, XPS measurements indicate the transfer from the presence of Ce^{3+} ions at lower ALD cycles and hence, smaller layer thicknesses, to Ce^{4+} dominating the deposited CeO_x species with rising cycle counts. Impedance spectroscopy studies for the CeO_2-coated ZrO_2 samples after 25, 75 and 150 cycles exhibit a significant influence of the coating layer thickness on the total conductivity of the CeO_2/ZrO_2 composite accompanied with changes in the activation energy of the transport process. As the Ce^{3+} content correlates with the ceria layer thickness, the changes in conductivity are directly related to changes of the non-stoichiometry of the coating layer indicating an additional electronic conductivity contribution caused by small polaron hopping of electrons between Ce^{3+} and Ce^{4+} ions.

All in all, our work presents the preparation of novel hybrid CeO_2/ZrO_2 model systems, which allows to tailor their physicochemical properties by changing the thickness of the active oxide layer. In further studies, the influence of the layer thickness of CeO_2 on its catalytic properties such as the oxygen storage capacity as well as the catalytic performance

in oxidation reactions needs to be addressed. Furthermore, the deposition of CeO_2 on yttrium-stabilized ZrO_2 (YSZ), sharing the same cubic crystal structure, with a more detailed look on their performance in the impedance spectroscopy and its usage as SOFC will be studied.

Experimental Section

Preparation of mesoporous ZrO_2 films

The fabrication of mesoporous ZrO_2 thin films using an EISA approach[35,36] was based on a precursor solution of mole ratio, $ZrOCl_2 \cdot 8H_2O$:PIB_{50}-*b*-PEO_{45}:H_2O:2-methoxy-ethanol:ethanol of 1:0.005:18:10:35. 184 mg $ZrOCl_2 \cdot 8\ H_2O$ (99.9%, Alfa Aesar) were dissolved in 1 mL ethanol (99.8%, Merck) and 1 mL 2-methoxy-ethanol (99%, Alfa Aesar), while 100 mg was added to 1 mL ethanol. Afterwards, both solutions were treated in an ultrasonic bath at 35 °C and 80 kHz for 30 min. The solutions were cooled down to room temperature and mixed together. After 5 min of stirring, 0.1 mL distilled H_2O was added to the solution to start the hydrolysis process.

After a stirring time of 90 min the solution was freed from agglomerates using 0.2 µm syringe filters. 100 µL of this solution were taken and deposited on a 2-inch Si[110] wafer rotating at 1000 rpm for 60 s using a spin-coater-kit *SCK-200P* from *Instras Scientific*. The relative humidity inside the chamber was kept constant at 20 % utilizing a custom-made glass enclosure. The films were treated at such low relative humidity for additional 3 min and then transferred in a preheated furnace at 130 °C to force the solvent to evaporate. Afterwards, the films were aged at 300 °C in air for 12 h to remove the structure directing agent. In the final step, the coated thin films were annealed to 600 °C under air to obtain crystalline ZrO_2 thin films. In a final step, the films were cut into 1x1 cm^2 pieces for the ALD deposition procedure.

Atomic layer deposition of CeO_2

CeO_2 was deposited on Si[110] wafers and the mesoporous ZrO_2 thin films in a commercial ALD system (PicoSun R200 Standard) at a deposition temperature of 250 °C

A typical ALD cycle consists of a 2 s pulse of Tetrakis(2,2,6,6-tetramethyl-3,5-heptanedionato)cerium(IV) (97 %, abcr GmbH) with 150 sccm nitrogen carrier gas followed by a 60 s purging step with nitrogen. Then, ozone (produced by an *AC-2025 ozone generator-2000* from *Teledyne API*) was pulsed for 2 s, followed by a 60 s purging step with nitrogen. In order to enable access to every pore of the complex oxide, a dwell time of 60 s was introduced,before excess of the precursor as well as byproducts were flushed out of the chamber. The thin films were coated using 5, 10, 25, 50, 75, 100 and 150 cycles, which are labeled as 5c, 10c, ..., 150c in the text. Additionally, ALD deposition with 25 cycles was carried out with different dwell times of 30 s, 60 s and 120 s to evaluate the saturation of the substrate surface.

Preparation of the Microelectrodes

Gold electrodes with a thickness of 300 nm were fabricated on the (un-)coated mesoporous thin film cuts (1.5 x 1.5 cm^2) by thermal evaporation through a shadow mask. Previously, a thin layer of chromium of about 5 nm has been deposited to improve the adhesion of gold. The width and length of the electrodes were 1 and 7 mm, respectively. The distance between the adjacent electrodes was 1 mm.

Material Characterization

The crystalline phases of the mesoporous thin films were studied by grazing incidence X-ray diffraction (GI-XRD) acquired from a *PANalytical X'Pert³ MRD* diffractometer using an incidence angle of ω = 0.25° and a scanning range of 2θ = 20° till 70°. A scan speed of 0.6° min^{-1} and step size of 0.01° were set. The crystallite sizes were calculated applying the Scherrer equation[58] on the wide angle reflections. Scanning electron microscopy (SEM)

images were recorded using the model *Merlin* by *Zeiss* with an acceleration voltage of 2 keV and a current of 50 pA. For an increased conductivity of the samples, the films were sputtered with platinum for 10 s with an applied current of 40 mA. The thicknesses as well as the refractive indices of the films were determined using a *SE400adv* laser ellipsometry by *Sentech* equipped with a HeNe laser (633 nm). The samples were measured at the specific angle of 70° assuming a two-model system consisting of the ZrO_2 film and the Si[110] substrate. For the time-of-flight secondary ion mass spectrometry (ToF-SIMS) a *ToF-SIMS 5-100 model* by *IonTOF GmbH* was used. The depth profiles were recorded using Cs ions at 1 keV and a current of 50 nA generating a 100x100 μm^2 crater. However, only 50x50 μm^2 were analyzed with a resolution of 256x256 $pixels^2$ using a Bi(I) primary ion source with an acceleration voltage of 25 keV. The measurements were carried out under charged compensation.

X-Ray Photoelectron Spectroscopy analyses were performed by a *PHI 5000 VersaProbe II* from *Ulvac-Phi* employing an Al Kα radiation with 1486.6 eV. A spot with a diameter of 200 µm was measured utilizing 50 W, 15 kV and 20 ms per step. A pass energy of 93.90 eV were applied for survey spectra, while 23.53 eV were applied for the detailed spectra of Ce 3d and Zr 3d, respectively. Calibration was performed by defining the C1s peak at 284.8 eV. The software CasaXPS V2.3.17 was used for peak analysis. Next to the six signals deriving from CeO_2 (v, v'', v''' and u, u'', u'''), we also take the four additional signals from Ce_2O_3 (v0, v' and u0, u') into account.[59] Based on the findings of Skala *et al.*[42] we used a combination of two signals to fit the observed asymmetry of *u* and *v* resulting in better fit conditions.

Electrical Characterization

The electrochemical properties were investigated by impedance spectroscopy in the frequency range from 10 mHz to 3 MHz between 200 and 550 °C with a *Novocontrol Alpha-A* impedance bridge and an AC amplitude of 100 mV. The measured impedance spectra exhibit a single semicircle as typically observed for mesoporous thin films.[54,56] Thus, only the total conductivity of the samples was determined by evaluation of the impedance spectra with a single R-Q-element using *RelaxIS 3* software package. The oxygen partial pressure in the gas atmosphere was controlled by Ar/O_2 gas mixtures. Conductivity values were calculated using Equation (2):

$$\frac{1}{\sigma} = \frac{1}{R} \cdot \frac{l}{A}, \qquad (2)$$

where σ is specific conductivity, R is resistance, l is the thickness of the samples and A is area of active electrode.

ASSOCIATED CONTENT

The following files are available free of charge:

Laser ellipsometric studies of the CeO_2-coated silicon wafer; SEM and ToF-SIMS analyses of the CeO_2-coated ZrO_2 films dependent on different dwell times; ToF-SIMS depth profiles of all the coated mesoporous ZrO_2 films; XPS measurements - Ce3d spectra with fittings - of the CeO_2-coated films (PDF).

AUTHOR INFORMATION

Corresponding Authors

*(B.S.) E-mail: bernd.smarsly@phys.chemie.uni-giessen.de

*(M.T.E.) E-mail: matthias.elm@phys.chemie.uni-giessen.de

Author Contributions

The manuscript was written through contributions of all authors. All authors have given approval to the final version of the manuscript.

Notes

The authors declare no competing financial interest.

ACKNOWLEDGMENT

The authors thank Christian Sack for his supports regarding the XPS analyses. In addition, the authors would like to thank Jörg Schörmann for his service regarding the ALD instrument. E.C. and M.T.E. thank the German Research Foundation (DFG) for financial support (grant no. EL 863/3-1). M.T.E. thanks the German Federal Ministry of Education and Research (BMBF) for funding of the NanoMatFutur project NiKo (03XP0093). This

project was supported by the Center for Materials Research (LaMa) of the Justus-Liebig-University Giessen, Germany.

REFERENCES

(1) Marizy, A.; Roussel, P.; Ringuedé, A.; Cassir, M. Atomic Layer Deposition of Epitaxial CeO_2 Thin Layers for Faster Surface Hydrogen Oxidation and Faster Bulk Ceria Reduction/Reoxidation. *J. Mater. Chem. A* **2015**, *3* (19), 10498–10503.

(2) Marrocchelli, D.; Bishop, S. R.; Tuller, H. L.; Yildiz, B. Understanding Chemical Expansion in Non-Stoichiometric Oxides: Ceria and Zirconia Case Studies. *Adv. Funct. Mater.* **2012**, *22* (9), 1958–1965.

(3) Balĺee, E.; Ringuedé, A.; Cassir, M.; Putkonen, M.; Niinisẗo, L. Synthesis of a Thin-Layered Ionic Conductor, CeO_2-Y_2O_3, by Atomic Layer Deposition in View of Solid Oxide Fuel Cell Applications. *Chem. Mater.* **2009**, *21* (19), 4614–4619.

(4) Trovarelli, A. Catalytic Properties of Ceria and CeO_2-Containing Materials. *Catal. Rev.* **1996**, *38* (4), 439–520.

(5) Amrute, A. P.; Mondelli, C.; Moser, M.; Novell-Leruth, G.; López, N.; Rosenthal, D.; Farra, R.; Schuster, M. E.; Teschner, D.; Schmidt, T.; Pérez-Ramírez, J. Performance, Structure, and Mechanism of CeO_2 in HCl Oxidation to Cl_2. *J. Catal.* **2012**, *286*, 287–297.

(6) Li, C.; Sun, Y.; Djerdj, I.; Voepel, P.; Sack, C.-C.; Weller, T.; Ellinghaus, R.; Sann, J.; Guo, Y.; Smarsly, B. M.; Over, H. Shape-Controlled CeO_2 Nanoparticles: Stability and Activity in the Catalyzed HCl Oxidation Reaction. *ACS Catal.* **2017**, *7*, 6453–6463.

(7) Sun, Y.; Cop, P.; Djerdj, I.; Guo, X.; Weber, T.; Khalid, O.; Guo, Y.; Smarsly, B. M.; Over, H. CeO_2 Wetting Layer on ZrO_2 Particle with Sharp Solid Interface as Highly Active and Stable Catalyst for HCl Oxidation Reaction. *ACS Catal.* **2019**, *9*, 10680–10693.

(8) Balaji Gopal, C.; García-Melchor, M.; Lee, S. C.; Shi, Y.; Shavorskiy, A.; Monti, M.; Guan, Z.; Sinclair, R.; Bluhm, H.; Vojvodic, A.; Chueh, W. C. Equilibrium Oxygen Storage Capacity of Ultrathin $CeO_{2-\delta}$ Depends Non-Monotonically on Large Biaxial Strain. *Nat. Commun.* **2017**, *8*, 15360.

(9) Huang, H.; Gong, H.; Chow, C. L.; Guo, J.; White, T. J.; Tse, M. S.; Tan, O. K. Low-Temperature Growth of SnO_2 Nanorod Arrays and Tunable n-p-n Sensing Response of a ZnO/SnO_2 Heterojunction for Exclusive Hydrogen Sensors. *Adv. Funct. Mater.* **2011**, *21* (14), 2680–2686.

(10) Obaidat, I. M.; Nayek, C.; Manna, K. Investigating the Role of Shell Thickness and Field Cooling on Saturation Magnetization and Its Temperature Dependence in Fe_3O_4/γ-Fe_2O_3 Core/Shell Nanoparticles. *Appl. Sci.* **2017**, *7* (12), 1269–1283.

(11) Artiglia, L.; Agnoli, S.; Paganini, M. C.; Cattelan, M.; Granozzi, G. Core − Shell Nanoparticles as Artificial Enzymes with Peroxidase-Like Activity. *ACS Appl. Mater. Interfaces* **2014**, *6* (22), 20130–20136.

(12) Agnoli, S.; Reeder, A. E.; Senanayake, S. D.; Hrbek, J.; Rodriguez, J. A. Structure and Special Chemical Reactivity of Interface-Stabilized Cerium Oxide Nanolayers on TiO_2(110). *Nanoscale* **2014**, *6* (2), 800–810.

(13) Sayle, T. X. T.; Caddeo, F.; Zhang, X.; Sakthivel, T.; Das, S.; Seal, S.; Ptasinska, S.; Sayle, D. C. Structure-Activity Map of Ceria Nanoparticles, Nanocubes, and

Mesoporous Architectures. *Chem. Mater.* **2016**, *28* (20), 7287–7295.

(14) Migani, A.; Vayssilov, G. N.; Bromley, S. T.; Illas, F.; Neyman, K. M. Greatly Facilitated Oxygen Vacancy Formation in Ceria Nanocrystallites. *Chem. Commun.* **2010**, *46* (32), 5936–5938.

(15) Lu, J.; Elam, J. W.; Stair, P. C. Atomic Layer Deposition - Sequential Self-Limiting Surface Reactions for Advanced Catalyst "Bottom-up" Synthesis. *Surf. Sci. Rep.* **2016**, *71* (2), 410–472.

(16) Lee, J. W. J.; Lee, J. W. J.; Kim, C.; Cho, C.-Y.; Moon, J. H. Facile Fabrication of Sub-100 nm Mesoscale Inverse Opal Films and Their Application in Dye-Sensitized Solar Cell Electrodes. *Sci. Rep.* **2014**, *4*, 6804–6810.

(17) Dendooven, J.; Devloo-Casier, K.; Ide, M.; Grandfield, K.; Kurttepeli, M.; Ludwig, K. F.; Bals, S.; Van Der Voort, P.; Detavernier, C. Atomic Layer Deposition-Based Tuning of the Pore Size in Mesoporous Thin Films Studied by in Situ Grazing Incidence Small Angle X-Ray Scattering. *Nanoscale* **2014**, *6* (24), 14991–14998..

(18) Zscherp, M. F.; Glaser, J.; Becker, C.; Beyer, A.; Cop, P.; Schörmann, J.; Volz, K.; Elm, M. T. Epitaxial Growth and Structural Characterization of Ceria Deposited by Atomic Layer Deposition on High-Surface Porous Yttria-Stabilized Zirconia Thin Films. *Cryst. Growth Des.* **2020**, *20* (4), 2194–2201.

(19) Dubraja, L. A.; Boll, D.; Reitz, C.; Wang, D.; Belić, D.; Mazilkin, A.; Breitung, B.; Hahn, H.; Elm, M. T.; Brezesinski, T. Thin Films of Thermally Stable Ordered Mesoporous Rh_2O_3(I) for Visible-Light Photocatalysis and Humidity Sensing. *ACS Appl. Nano Mater.* **2019**, *2* (1), 7126–7133.

(20) Celik, E.; Negi, R. S.; Bastianello, M.; Boll, D.; Mazilkin, A.; Brezesinski, T.; Elm, M. T. Tailoring the Protonic Conductivity of Porous Yttria-Stabilized Zirconia Thin Films by Surface Modification. *Phys. Chem. Chem. Phys.* **2020**, *22*, 11519-11528.

(21) Jiang, S. P. A Review of Wet Impregnation - an Alternative Method for the Fabrication of High Performance and Nano-Structured Electrodes of Solid Oxide Fuel Cells. *Mater. Sci. Eng. A* **2006**, *418*, 199–210.

(22) Burkett, S. L.; Sims, S. D.; Mann, S. Synthesis of Hybrid Inorganic-Organic Mesoporous Silica by Co-Condensation of Siloxane and Organosiloxane Precursors. *Chem. Commun.* **1996**, *11*, 1367–1368.

(23) Aronson, B. J.; Blanford, C. F.; Stein, A. Solution-Phase Grafting of Titanium Dioxide onto the Pore Surface of Mesoporous Silicates: Synthesis and Structural Characterization. *Chem. Mater.* **1997**, *9* (12), 2842–2851.

(24) Pagán-Torres, Y. J.; Gallo, J. M. R.; Wang, D.; Pham, H. N.; Libera, J. A.; Marshall, C. L.; Elam, J. W.; Datye, A. K.; Dumesic, J. A. Synthesis of Highly Ordered Hydrothermally Stable Mesoporous Niobia Catalysts by Atomic Layer Deposition. *ACS Catal.* **2011**, *1* (10), 1234–1245.

(25) Berland, B. S.; Gartland, I. P.; Ott, A. W.; George, S. M. In Situ Monitoring of Atomic Layer Controlled Pore Reduction in Alumina Tubular Membranes Using Sequential Surface Reactions. *Chem. Mater.* **1998**, *10* (12), 3941–3950.

(26) Kraffert, K.; Karg, M.; Schmack, R.; Clavel, G.; Boissiere, C.; Wirth, T.; Pinna, N.; Kraehnert, R. Stabilization of Mesoporous Iron Oxide Films against Sintering and Phase Transformations via Atomic Layer Deposition of Alumina and Silica.

Adv. Mater. Interfaces **2018**, *5*, 1800360.

(27) Reitz, C.; Haetge, J.; Suchomski, C.; Brezesinski, T. Facile and General Synthesis of Thermally Stable Ordered Mesoporous Rare-Earth Oxide Ceramic Thin Films with Uniform Mid-Size to Large-Size Pores and Strong Crystalline Texture. *Chem. Mater.* **2013**, *25* (22), 4633–4642.

(28) Detavernier, C.; Dendooven, J.; Sree, S. P.; Ludwig, K. F.; Martens, J. A. Tailoring Nanoporous Materials by Atomic Layer Deposition. *Chem. Soc. Rev.* **2011**, *40* (11), 5242–5253.

(29) Dendooven, J.; Goris, B.; Devloo-Casier, K.; Levrau, E.; Biermans, E.; Baklanov, M. R.; Ludwig, K. F.; Voort, P. Van Der; Bals, S.; Detavernier, C. Tuning the Pore Size of Ink-Bottle Mesopores by Atomic Layer Deposition. *Chem. Mater.* **2012**, *24* (11), 1992–1994.

(30) Cop, P.; Göttlicher, M.; Schörmann, J.; Boissiere, C.; Beyer, A.; Becker, C.; Volz, K.; Over, H.; Smarsly, B. M. Atomic Layer Deposition of Titania in Ordered Mesoporous Cerium Zirconium Oxide Thin Films: A Case Study. *J. Phys. Chem. C* **2019**, *123* (20), 12851–12861.

(31) Cop, P.; Hess, K.; Werner, S.; Meinusch, R.; Smarsly, B. M.; Kozuka, H. Comparison of In-Plane Stress Development in Sol-Gel- And Nanoparticle-Derived Mesoporous Metal Oxide Thin Films. *Langmuir* **2019**, *35* (50), 16427–16437.

(32) Hartmann, P.; Lee, D.; Smarsly, B. M.; Janek, J. Mesoporous TiO_2 : Comparison of Splitting Reaction. *ACS Nano* **2010**, *4* (6), 3147–3154.

(33) Graberg, T. Von; Hartmann, P.; Rein, A.; Gross, S.; Seelandt, B.; Röger, C.; Zieba, R.; Traut, A.; Wark, M.; Janek, J.; Smarsly, B. M. Mesoporous Tin-Doped Indium Oxide Thin Films: Effect of Mesostructure on Electrical Conductivity. *Sci. Technol. Adv. Mater.* **2011**, *12* (2), 025005.

(34) Weidmann, C.; Brezesinski, K.; Suchomski, C.; Tropp, K.; Grosser, N.; Haetge, J.; Smarsly, B. M.; Brezesinski, T. Morphology-Controlled Synthesis of Nanocrystalline η-Al_2O_3 Thin Films, Powders, Microbeads, and Nanofibers with Tunable Pore Sizes from Preformed Oligomeric Oxo-Hydroxo Building Blocks. *Chem. Mater.* **2012**, *24* (3), 486–494.

(35) Cop, P.; Kitano, S.; Niinuma, K.; Smarsly, B.; Kozuka, H. In-Plane Stress Development in Mesoporous Thin Films. *Nanoscale* **2018**, *10*, 7002–7015.

(36) Brinker, C. J.; Lu, Y.; Sellinger, A.; Fan, H. Evaporation-Induced Self-Assembly : Nanostructures Made Easy. *Adv. Mater.* **1999**, *11* (7), 579–585.

(37) Sel, O.; Sallard, S.; Brezesinski, T.; Rathouský, J.; Dunphy, D. R.; Collord, A.; Smarsly, B. M. Periodically Ordered Meso- and Macroporous SiO_2 Thin Films and Their Induced Electrochemical Activity as a Function of Pore Hierarchy. *Adv. Funct. Mater.* **2007**, *17* (16), 3241–3250.

(38) Sel, O.; Brandt, A.; Wallacher, D.; Thommes, M.; Smarsly, B. Pore Hierarchy in Mesoporous Silicas Evidenced by In-Situ SANS during Nitrogen Physisorption. *Langmuir* **2007**, *23* (9), 4724–4727.

(39) Langner, A.; Knez, M.; Müller, F.; Gösele, U. TiO_2 Microstructures by Inversion of Macroporous Silicon Using Atomic Layer Deposition. *Appl. Phys. A Mater. Sci. Process.* **2008**, *93* (2), 399–403.

(40) Puurunen, R. L. Surface Chemistry of Atomic Layer Deposition: A Case Study for the Trimethylaluminum/Water Process. *J. Appl. Phys.* **2005**, *97* (12), 121301.

(41) Atanassov, G.; Thielsch, R.; Popov, D. Optical Properties of TiO_2, Y_2O_3 and CeO_2 Thin Films Deposited by Electron Beam Evaporation. *Thin Solid Films* **1993**, *223* (2), 288–292.

(42) Skála, T.; Šutara, F.; Prince, K. C.; Matolín, V. Cerium Oxide Stoichiometry Alteration via Sn Deposition: Influence of Temperature. *J. Electron Spectros. Relat. Phenomena* **2009**, *169* (1), 20–25.

(43) Kwon, O. H.; Jang, C.; Lee, J.; Jeong, H. Y.; Kwon, Y. il; Joo, J. H.; Kim, H. Investigation of the Electrical Conductivity of Sintered Monoclinic Zirconia (ZrO_2). *Ceram. Int.* **2017**, *43* (11), 8236–8245.

(44) Kofstad, P.; Ruzicka, D. J. On the Defect Structure of ZrO_2 and HfO_2. *J. Electrochem. Soc.* **1963**, *110* (3), 181–184.

(45) Gupta, T. K.; Grekila, R. B.; Subbarao, E. C. Electrical Conductivity of Tetragonal Zirconia below the Transformation Temperature. *J. Electrochem. Soc.* **1981**, *128* (4), 929–931.

(46) Kumar, A.; Rajdev, D.; Douglass, D. L. Effect of Oxide Defect Structure on the Electrical Properties of ZrO_2. *J. Am. Ceram. Soc.* **1972**, *55* (9), 439–445.

(47) Bishop, S. R.; Duncan, K. L.; Wachsman, E. D. Defect Equilibria and Chemical Expansion in Non-Stoichiometric Undoped and Gadolinium-Doped Cerium Oxide. *Electrochim. Acta* **2009**, *54* (5), 1436–1443.

(48) Tuller, H. L.; Nowick, A. S. Small Polaron Electron Transport in Reduced CeO_2

Single Crystals. *J. Phys. Chem. Solids* **1977**, *38* (8), 859–867.

(49) Naik, I. K.; Tien, T. Y. Small-Polaron Mobility in Nonstoichiometric Cerium Dioxide. *J. Phys. Chem. Solids* **1978**, *39* (3), 311–315..

(50) Michel, K.; Eufinger, J.-P.; Elm, M. T.; Ulbrich, G.; Lerch, M.; Janek, J. Combining Two Redox Active Rare Earth Elements for Oxygen Storage - Electrical Properties and Defect Chemistry of Ceria-Praseodymia Single Crystals. *Phys. Chem. Chem. Phys.* **2017**, *19*, 17661–17669.

(51) Tschöpe, A.; Sommer, E.; Birringer, R. Grain Size-Dependent Electrical Conductivity of Polycrystalline Cerium Oxide: I. Experiments. *Solid State Ionics* **2001**, *139* (3), 255–265.

(52) Kim, S.; Maier, J. On the Conductivity Mechanism of Nanocrystalline Ceria. *J. Electrochem. Soc.* **2002**, *149* (10), J73.

(53) Guo, X.; Sigle, W.; Maier, J. Blocking Grain Boundaries in Yttria-Doped and Undoped Ceria Ceramics of High Purity. *J. Am. Ceram. Soc.* **2003**, *86* (1), 77–87.

(54) Elm, M. T.; Hofmann, J. D.; Suchomski, C.; Janek, J.; Brezesinski, T. Ionic Conductivity of Mesostructured Yttria-Stabilized Zirconia Thin Films with Cubic Pore Symmetry - On the Influence of Water on the Surface Oxygen Ion Transport. *ACS Appl. Mater. Interfaces* **2015**, *7* (22), 11792–11801.

(55) Yue, J.; Suchomski, C.; Voepel, P.; Ellinghaus, R.; Rohnke, M.; Leichtweiss, T.; Elm, M. T.; Smarsly, B. M. Mesoporous Niobium-Doped Titanium Dioxide Films from the Assembly of Crystalline Nanoparticles: Study on the Relationship between the Band Structure, Conductivity and Charge Storage Mechanism. *J.*

Mater. Chem. A **2017**, *5* (5), 1978–1988.

(56) Hartmann, P.; Brezesinski, T.; Sann, J.; Lotnyk, A.; Eufinger, J.-P.; Janek, J. Defect Chemistry of Oxide Nanomaterials with High Surface Area : Ordered Mesoporous Thin Films of the Oxygen Storage Catalyst. *ACS Nano* **2013**, *7* (4), 2999–3013.

(57) Chiodelli, G.; Flor, G.; Scagliotti, M. Electrical Properties of the ZrO_2-CeO_2 System. *Solid State Ionics* **1996**, *91* (1), 109–121.

(58) Patterson, A. L. The Scherrer Formula for X-Ray Particle Size Determination. *Phys. Rev.* **1939**, *56* (10), 978–982.

(59) Romeo, M.; Bak, K.; El Fallah, J.; Le Normand, F.; Hilaire, L. XPS Study of the Reduction of Cerium Dioxide. *Surf. Interface Anal.* **1993**, *20* (6), 508–512.

4. Fazit und Ausblick

Ziel dieser Arbeit war die Entwicklung von mesoporösen CeO_2-Materialien als Modellsysteme für die heterogen katalysierte HCl-Oxidation (Deacon-Prozess). Insbesondere wurde der Einfluss von der Sauerstoffspeicherkapazität und Leerstellenkonzentration mithilfe von Seltenerddotierungen und Nanostrukturierung auf die katalytischen Eigenschaften aufgeklärt. Des Weiteren wurde die Präparation von neuartigen Modellsystemen in Form von definiert abgeschiedenen CeO_2-Dünnschichten in geordneten mesoporösen Substraten beschrieben, welche die Auswirkung der OSC auf zukünftige katalytische Messungen noch weiter aufklären werden.

Im ersten Teil der Arbeit wurden mit einem neuartigen Syntheseverfahren mesoporöse CeO_2-Materialien auf Basis der Sol-Gel-Synthese hergestellt, die über eine kubische Porenstruktur von ca. 12-14 nm Mesoporen verfügen. Die mesostrukturierten Katalysatoren besitzen im Gegensatz zu Nanopartikeln mit ähnlich großen Oberflächen eine deutlich bessere Zugänglichkeit für die gasförmigen Reaktanden des Deacon-Prozesses. Dadurch konnten morphologische Veränderungen in Folge der HCl-Oxidation anhand der beschädigten Mesoporenstruktur mittels Rasterelektronenmikroskopie (SEM) und Stickstoffphysisorption verfolgt werden. Mithilfe von alio-/isovalenten Dotierungselementen (Gd^{3+}, Zr^{4+}, $Pr^{3+/4+}$, $Tb^{3+/4}$) wurde gezeigt, dass keine direkte Korrelation zwischen der OSC und den katalytischen Eigenschaften im Deacon-Prozess besteht. Die hohe OSC(c) der Pr-dotierten Proben erzielte die geringste STY und die geringste Stabilität. Aus den Ergebnissen von Publikation 3.1. resultiert die Annahme, dass eine zu hohe Anzahl von Sauerstoffleerstellen, wie sie durch trivalente Ionen induziert wird, geeignete Adsorptionsplätze für die Chlorspezies darstellt und die Formation von katalytisch inaktiven $CeCl_3$ fördert. Wie in anderen katalytischen Prozessen zeigte das Zr-dotierte CeO_2 neben einer hohen Sauerstoffspeicherkapazität auch die beste katalytische Stabilität.

Aufgrund dieser Resultate wurde das Synthesekonzept erweitert, um CeO_2-ZrO_2-Nanopartikel mit wohldefinierten Stöchiometrien als Präkursoren für den Prozess der Mesostrukturierung einzusetzen. Ein Vergleich zwischen den hergestellten aber unbehandelten Nanopartikeln und den aus Nanopartikeln hergestellten Mesostrukturen demonstrierte, dass durch die Mesostrukturierung die Zugänglichkeit der katalytisch aktiven Stellen erhöht wird. Während die nicht-templatierten Nanopartikel in Agglomeraten mit zufälliger Anordnung vorliegen, ermöglicht die Mesoporenstruktur einen verbesserten Kontakt mit den Gasreaktanden pro Zeit, was die dynamische OSC und die STY im Deacon-Prozess im Vergleich zu den chemisch äquivalenten Nanopartikeln erhöhte. Die Konnektivität der Partikel spielt folglich eine entscheidende Rolle für die katalytischen Eigenschaften. Neben dem Einfluss des Zr-Gehaltes im CeO_2-Gitter auf die OSC, wurde im Vergleich mit nicht-templatierten CeO_2-ZrO_2-Nanopartikel eine verbesserte Stabilität für die mesostrukturierten Katalysatoren beobachtet. Zudem überstieg die bestimmte katalytische Stabilität der undotierten CeO_2-Mesostrukturen die der Zr-dotierten Nanostäbe von Li *et al.*[169] und der ebenfalls aus Nanopartikeln bestehenden Nanofasern von Möller *et al.*[170],

welche mit der gleichen Apparatur gemessen wurden. Erste Messungen zeigten zudem, dass die geringe Partikelanzahl pro Porenwand der mesostrukturierten Proben zu einer hohen katalytischen Stabilität im Deacon-Prozess führt. In zukünftigen Ansätzen sollten die Porenwände durch die Verwendung weiterer Softtemplate variiert werden, um den Einfluss der Konnektivität mehrerer Partikel pro Wand auf die Sauerstoffspeicherkapazität und die katalytische Stabilität zu untersuchen. Denn die hier verwendeten templatierten CeO_2-ZrO_2-Mesostrukturen werden lediglich von den abgeschiedenen CeO_2-Dünnschichten auf ZrO_2-Nanopartikeln von Sun *et al.*[11] hinsichtlich der katalytischen Stabilität im Deacon-Prozess überboten. Dies lässt sich vermutlich auf die stabilisierende Wirkung der CeO_2-ZrO_2-Grenzfläche anstelle der hergestellten festen Lösung aus CeO_2-ZrO_2 in diesem Projekt zurückführen.

Um eine definierte Grenzfläche zwischen CeO_2 und ZrO_2 zu erhalten, wurde im zweiten Teil der Arbeit die Deposition von definierten CeO_2-Schichten in mesoporösen ZrO_2-Substraten mithilfe der ALD entwickelt. Mit einer *conformality*-Studie auf hochgeordneten mesoporösen CeO_2-ZrO_2-Oxiden, wurden geeignete Charakterisierungsmethoden getestet. Eine Kombination aus gängigen Messmethoden wie ToF-SIMS, SEM, TEM, XRD und Ellipsometrie bewährten sich, um die komplette Bedeckung der Porenoberfläche ebenfalls in tieferen Porenschichten nachzuweisen. Die ermittelten Methoden sollen als Leitfaden für den Nachweis zukünftiger ALD-Experimente auf mesoporösen Substraten dienen. Die etablierten Messmethoden wurden auf die Abscheidung von CeO_2 auf mesoporöse ZrO_2-Substrate übertragen. Dabei wurde die Präparation sowohl von ZrO_2 als auch von TiO_2 mithilfe mechanischer Verspannungsstudien und auf Basis molekularer Präkursoren und Nanopartikeldispersionen optimiert. Poröse Dünnfilme basierend auf molekularer Präkursoren verfügen über eine erhöhte Periodizität der Mesoporen, weswegen das Aufwachsen von dünnen CeO_2-Schichten besser mit bildgebenden Methoden aufgelöst und verfolgt werden konnte. Basierend auf XPS-Untersuchungen sinkt die Ce^{3+}-Konzentration mit steigender Schichtdicke von 75 % bei 0,5 nm (10 ALD Zyklen) bis zu 20 % bei 6,8 nm (150 ALD Zyklen). Die Impedanzspektroskopie-Messungen der CeO_2@ZrO_2-Substrate zeigen jedoch ein Leitfähigkeitsmaximum nach 75 ALD-Zyklen mit einer Schichtdicke von 3,4 nm. Dies stimmt sehr gut mit den theoretischen Berechnungen der Sauerstoffvakanzbildungsenthalpien von Sayle *et al.*[137] (3,5 nm) überein.

Die vorliegende Promotionsstudie demonstriert folglich, dass die hier vorgestellten mesoporöse Katalysatoren nicht nur für katalytische Studien bestens geeignete Modellsysteme darstellen – um die Performance in katalytischen Prozessen systematisch zu studieren – sondern sie sind auch ideale Substrate für *conformality*-Studien zur Abscheidung von Metalloxiden mittels ALD. Zudem ist die experimentell bestimmte OSC eine komplexe Größe, die nicht unüberlegt mit der katalytischen Aktivität in Oxidationsreaktionen korreliert werden sollte. Da die OSC von mehreren Faktoren wie der Anzahl von Sauerstoffleerstellen und deren Mobilität abhängt, muss für die untersuchte Modellreaktion ermittelt werden, welche der genannten Einflussfaktoren eine Rolle im katalytischen Prozess spielt.

Im Falle der HCl-Oxidation ist eine zu hohe Anzahl von Sauerstoffleerstellen von Nachteil, da es gemäß der Publikation in Kapitel 3.1. die Bildung von $CeCl_3$ fördert. Dies stimmt sehr gut mit vorangegangen Studien[209] an einkristallinen CeO_x(111)/Ru(0001)-Schichten überein, die eine möglichst geringe Konzentration an Sauerstoffleerstellen an der Oberfläche vorschlägt, um die Chlorierung der aktiven Oberfläche zu vermeiden. Aus diesem Grund sind die CeO_2-ZrO_2-Oxide, welche lediglich die Bildungsenthalpie der Sauerstoffleerstellen absenken und keine direkten Vakanzen induzieren, der richtige Schritt um CeO_2-basierte Materialien für die HCl-Oxidation zu etablieren. Daher ist es keine Frage nach der optimalen Sauerstoffleerstellenkonzentration, sondern viel mehr nach der chemischen Umgebung der aktiv im Reaktionsmechanismus beteiligten Sauerstoffleerstelle. Der Einsatz von CeO_2-Einkristallen mit gezielter Dotierung von Zr nahe einer Sauerstoffleerstelle könnte den Einfluss ihrer chemischen Umgebung auf die HCl-Adsorption bzw. Cl_2-Desorption ermitteln. Auf Basis der mesostrukturierten Pulver können jedoch strukturelle Eigenschaften im Detail und unter realen Bedingungen betrachtet werden. Durch die Abscheidung wohldefinierter dünner CeO_2-Schichten auf die Mesoporenoberfläche mittels ALD können die Ergebnisse von Einkristalluntersuchungen in die realen katalytischen Bedingungen übertragen werden, da sich die aufzuwachsenden Schichten in den gleichen Größendimensionen (< 10 nm) befinden. Wie in dieser Arbeit gezeigt wurden, scheint unter realen katalytischen Bedingungen im Flussreaktor neben der Zugänglichkeit der Sauerstoffleerstellen an der Oberfläche auch die Mobilität der Sauerstoffionen aus dem Bulk eine essentielle Rolle für die OSC einzunehmen. Hierzu ist es notwendig, dass die Modellkatalysatoren auch elektrochemisch speziell hinsichtlich der ionischen und elektrischen Leitfähigkeit analysiert werden. Eine Verknüpfung der Elektrochemie und der Katalyse ist somit notwendig, um CeO_2-ZrO_2-Materialien für heterogen katalysierte Redoxreaktionen zu optimieren. Obwohl die impedanzspektroskopischen Messungen aus Kapitel 3.5 bereits den ersten Schritt darstellen, die Grenzfläche zwischen CeO_2 und ZrO_2 elektrochemisch näher zu untersuchen, fehlt es bei den CeO_2-ZrO_2-Oxiden noch an Verständnis, wie die Mobilität der Sauerstoffionen und folglich die OSC von der gemeinsamen Grenzfläche und der chemischen Umgebung beeinflusst wird.

Der nächste Schritt wäre nun die Kombination der beiden in der Promotion behandelten Teilziele: die Abscheidung der CeO_2-Schichten auf analog hergestellten porösen ZrO_2-Pulvern, um den Einfluss der Schichtdicke auf die OSC und die katalytischen Eigenschaften in der HCl-Oxidation aufzuklären. Dies wäre eine direkte Erweiterung der Studien von Sun *et al.*[11], da gleichzeitig wohldefinierte CeO_2-Schichtdicken eingesetzt werden und die Bildung von einzelnen Partikeln vermieden werden kann. Dabei würden Sol-Gel-basierte Pulver mit ausgeprägter Porenordnung für die Kontrolle des Abscheidungsprozesses verwendet werden, während auf Nanopartikeln basierende Systeme für höhere spezifische Produktbildungsraten und Stabilitätsuntersuchungen eingesetzt werden sollten. Um die Limitierung durch die Porengröße für die aufzuwachsenden CeO_2-Schichten aufzuheben, können Invers-Opal-Strukturen mit definierten Porendurchmessern von 100 – 300 nm mittels

hard templating Methoden verwendet werden. Ähnlich wie die hier berichteten mesoporösen Materialien verfügen die Invers-Opal-Strukturen über sphärische und untereinander verknüpfte Poren. Die erhöhte Porengröße und die damit einhergehende verkleinerte BET-Oberfläche würde die mesoporösen Dünnschichten und Pulver als Zwischenmodellsystem verbinden, um die bestimmten Abscheidungsparameter zu transferieren.

Weiterhin kann die entwickelte Synthese für mesoporöse CeO_2-ZrO_2-Pulver aus Nanopartikeldispersionen im Hinblick auf die gewünschte Porengröße und Porenwandstärke mithilfe unterschiedlicher Block-Copolymere der PIB-PEO-Reihe angepasst werden. Zudem können auch Dispersionen von CeO_2- und ZrO_2-Nanopartikeln verwendet werden, um mesoporöse Modellkatalysatoren mit einer großen Anzahl an CeO_2-ZrO_2-Grenzflächen zu erzeugen, welche einen entscheidenden Einfluss auf die katalytische Stabilität im Deacon-Prozess aufweist[11] und in zukünftigen Studien näher untersucht werden sollte.

Alles in allem, zeigt das vorgelegte Promotionsprojekt, dass sich mesoporöse CeO_2-Katalysatoren dank ihrer hohen spezifischen Oberfläche und guten Zugänglichkeit für gasförmige Reaktanden ideal als Modellsysteme für die HCl-Oxidation eignen, um die mit der OSC zusammenhängenden katalytischen Eigenschaften im Deacon-Prozess auf mikroskopischer Ebene aufzuklären. Auch in zukünftigen Studien sollten mesoporöse Materialien als Basis für CeO_2-basierte Katalysatoren dienen, um den Einfluss der OSC nicht nur auf die HCl-Oxidation, sondern auch auf andere Oxidationsreaktionen zu ermitteln. Insbesondere die Herstellung neuartiger MO_x/CeO_2 Kern-Schale-Modellkatalysatoren durch die ALD ist zukunftsweisend, um das Verständnis der OSC und der katalytischen Eigenschaften zu vertiefen. Schlussendlich sollen die erlangten Erkenntnisse der entwickelten CeO_2-Modellkatalysatoren dazu führen, RuO_2-basierten Katalysatoren für die heterogene HCl-Oxidation abzulösen, um mit CeO_2-Materialien die Rückgewinnung von Cl_2 aus HCl wirtschaftlich attraktiv zu gestalten.

5. Literaturverzeichnis

[1] J. Pérez-Ramírez, C. Mondelli, T. Schmidt, O. F. K. Schlüter, A. Wolf, L. Mleczko, T. Dreier, *Energy Environ. Sci.* **2011**, *4*, 4786–4799.
[2] "http://www.eurochlor.org/the-chlorine-universe/what-is-chlorine-used-for/the-chlorine-tree/chlorine-tree.aspx" (Stand: 20.04.2020)
[3] H. Deacon, *U.S. Patent 85, 370*, **1875**.
[4] K. Iwanaga, K. Seki, T. Hibi, *Sumitomo Kagaku* **2004**, *I*, 1–11.
[5] K. Seki, *Catal. Surv. from Asia* **2010**, *14*, 168–175.
[6] A. P. Amrute, C. Mondelli, M. Moser, G. Novell-Leruth, N. López, D. Rosenthal, R. Farra, M. E. Schuster, D. Teschner, T. Schmidt, et al., *J. Catal.* **2012**, *286*, 287–297.
[7] P. Li, X. Chen, Y. Li, J. W. Schwank, *Catal. Today* **2019**, *327*, 90–115.
[8] T. Montini, M. Melchionna, M. Monai, P. Fornasiero, *Chem. Rev.* **2016**, *116*, 5987–6041.
[9] S. Deshpande, S. Patil, S. V. Kuchibhatla, S. Seal, *Appl. Phys. Lett.* **2005**, *87*, 133113.
[10] L. Artiglia, S. Agnoli, M. C. Paganini, M. Cattelan, G. Granozzi, *ACS Appl. Mater. Interfaces* **2014**, *6*, 20130–20136.
[11] Y. Sun, P. Cop, I. Djerdj, X. Guo, T. Weber, O. Khalid, Y. Guo, B. M. Smarsly, H. Over, *ACS Catal.* **2019**, *9*, 10680–10693.
[12] H. Over, R. Schomäcker, *ACS Catal.* **2013**, *3*, 1034–1046.
[13] F. Hess, B. M. Smarsly, H. Over, *Acc. Chem. Res.* **2020**, *53*, 380–389.
[14] M. Moser, A. P. Amrute, J. Pérez-Ramírez, *Appl. Catal. B Environ.* **2015**, *162*, 602–609.
[15] A. P. Amrute, C. Mondelli, M. A. G. Hevia, J. Pérez-Ramírez, *J. Phys. Chem. C* **2011**, *115*, 1056–1063.
[16] Y. Dai, Z. Fei, X. Xu, X. Chen, J. Tang, M. Cui, X. Qiao, *Can. J. Chem. Eng.* **2016**, *94*, 1140–1147.
[17] Z. Fei, H. Liu, Y. Dai, W. Ji, X. Chen, J. Tang, M. Cui, X. Qiao, *Chem. Eng. J.* **2014**, *257*, 273–280.
[18] A. P. Amrute, C. Mondelli, M. A. G. Hevia, P. Javier, *ACS Catal.* **2011**, *4*, 583–590.
[19] N. López, J. Gómez-Segura, R. P. Marín, J. Pérez-Ramírez, *J. Catal.* **2008**, *255*, 29–39.
[20] M. A. G. Hevia, A. P. Amrute, T. Schmidt, J. Pérez-Ramírez, *J. Catal.* **2010**, *276*, 141–151.
[21] D. Crihan, M. Knapp, S. Zweidinger, E. Lundgren, C. J. Weststrate, J. N. Andersen, A. P. Seitsonen, H. Over, *Angew. Chemie - Int. Ed.* **2008**, *47*, 2131–2134.
[22] J. P. Hofmann, S. Zweidinger, A. P. Seitsonen, A. Farkas, M. Knapp, O. Balmes, E. Lundgren, J. N. Andersen, H. Over, *Phys. Chem. Chem. Phys.* **2010**, *12*, 15358–15366.
[23] R. Farra, M. Garcia-Melchor, M. Eichelbaum, M. Hashagen, W. Frandsen, J. Allan, F. Girgsdies, L. Szentmiklosi, N. Lopez, D. Teschner, *ACS Catal.* **2013**, *3*, 2256–2268.
[24] M. Möller, S. Urban, P. Cop, T. Weller, R. Ellinghaus, M. Kleine-Boymann, C. Fiedler, J. Sann, J. Janek, L. Chen, et al., *ChemCatChem* **2015**, *7*, 3738–3747.
[25] R. Prasad, G. Rattan, *Bull. Chem. React. Eng. Catal.* **2010**, *5*, 7–30.
[26] A. P. Amrute, C. Mondelli, M. Moser, G. Novell-Leruth, N. López, D. Rosenthal, R. Farra, M. E. Schuster, D. Teschner, T. Schmidt, et al., *J. Catal.* **2012**, *286*, 287–297.
[27] M. Moser, C. Mondelli, T. Schmidt, F. Girgsdies, M. E. Schuster, R. Farra, L. Szentmiklósi, D. Teschner, J. Pérez-Ramírez, *Appl. Catal. B Environ.* **2013**, *132–133*, 123–131.
[28] C. H. Kanzler, S. Urban, K. Zalewska-Wierzbicka, F. Hess, S. F. Rohrlack, C. Wessel, R. Ostermann, J. P. Hofmann, B. M. Smarsly, H. Over, *ChemCatChem* **2013**, *5*, 2621–2626.
[29] D. Teschner, R. Farra, L. Yao, R. Schlögl, H. Soerijanto, R. Schomäcker, T. Schmidt, L. Szentmiklósi, A. P. Amrute, C. Mondelli, et al., *J. Catal.* **2012**, *285*, 273–284.
[30] E. Aneggi, M. Boaro, C. De Leitenburg, G. Dolcetti, A. Trovarelli, *J. Alloys Compd.* **2006**, *408–412*, 1096–1102.
[31] A. Trovarelli, *Catal. Rev.* **1996**, *38*, 439–520.
[32] A. Trovarelli, *Comments Inorg. Chem.* **1999**, *20*, 263–284.
[33] A. Trovarelli, C. de Leitenburg, M. Boaro, G. Dolcetti, *Catal. Today* **1999**, *50*, 353–367.
[34] N. Guillén-Hurtado, A. García-García, A. Bueno-López, *Appl. Catal. B Environ.* **2015**, *174–175*, 60–66.
[35] M. Capdevila-Cortada, G. Vilé, D. Teschner, J. Pérez-Ramírez, N. López, *Appl. Catal. B Environ.* **2015**, *197*, 299–312.
[36] A. Trovarelli, J. Llorca, *ACS Catal.* **2017**, *7*, 4716–4735.
[37] N. Hickey, P. Fornasiero, R. Di Monte, J. Kaspar, M. Graziani, G. Dolcetti, *Catal. Letters* **2001**, *72*, 45–50.
[38] C. Descorme, Y. Madier, D. Duprez, *J. Catal.* **2000**, *196*, 167–173.
[39] R. J. D. Tilley, *Defects in Solids*, John Wiley & Sons Inc., Hoboken, New Jersey, **2008**.
[40] T. Zacherle, A. Schriever, R. A. De Souza, M. Martin, *Phys. Rev. B - Condens. Matter Mater. Phys.* **2013**, *87*, 1–11.
[41] F. Zhang, S. W. Chan, J. E. Spanier, E. Apak, Q. Jin, R. D. Robinson, I. P. Herman, *Appl. Phys. Lett.* **2002**, *80*, 127–129.
[42] A. Martinez-Arias, M. Fernandez-Garcia, O. Galvez, J. M. Coronado, J. A. Anderson, J. C. Conesa, J. Soria, G. Munuera, *J. Catal.* **2000**, *195*, 207–216.
[43] A. K. Lucid, P. R. L. Keating, J. P. Allen, G. W. Watson, *J. Phys. Chem. C* **2016**, *120*, 23430–23440.
[44] M. Balaguer, C. Solís, J. M. Serra, *J. Phys. Chem. C* **2012**, *116*, 7975–7982.
[45] S. Agarwal, X. Zhu, E. J. M. Hensen, B. L. Mojet, L. Lefferts, *J. Phys. Chem. C* **2015**, *119*, 12423–12433.
[46] Y. Nagai, T. Nonaka, A. Suda, M. Sugiura, *R&D Rev. Toyota CRDL* **2002**, *37*, 20–27.
[47] Y. Sakamoto, K. Kizaki, T. Motohiro, Y. Yokota, H. Sobukawa, M. Uenishi, H. Tanaka, M. Sugiura, *J. Catal.* **2002**, *211*, 157–164.
[48] S. H. Song, J. Moon, J. H. Kim, J. Hong, J. H. Lee, H. W. Lee, B. K. Kim, H. Kim, *Acta Mater.* **2016**, *113*, 206–212.
[49] M. P. Yeste, J. C. Hernández-Garrido, D. C. Arias, G. Blanco, J. M. Rodríguez-Izquierdo, J. M. Pintado, S. Bernal, J. A. Pérez-Omil, J. J. Calvino, *J. Mater. Chem. A* **2013**, *1*, 4836–4844.
[50] N. Laosiripojana, S. Assabumrungrat, *Appl. Catal. B Environ.* **2008**, *82*, 103–113.
[51] P. Fornasiero, R. Di Monte, G. R. Rao, J. Kaspar, S. Meriani, A. Trovarelli, M. Graziani, *J. Catal.* **1995**, *151*, 168–177.
[52] H. C. Yao, Y. F. Y. Yao, *J. Catal.* **1984**, *86*, 254–265.
[53] J. M. López, A. L. Gilbank, T. García, B. Solsona, S. Agouram, L. Torrente-Murciano, *Appl. Catal. B Environ.* **2015**, *174–175*, 403–412.
[54] H. Zhu, Z. Qin, W. Shan, W. Shen, J. Wang, *J. Catal.* **2004**, *225*, 267–277.
[55] Z. Wang, Q. Wang, Y. Liao, G. Shen, X. Gong, N. Han, H. Liu, Y. Chen, *ChemPhysChem* **2011**, *12*, 2763–2770.
[56] P. S. Lambrou, C. N. Costa, S. Y. Christou, A. M. Efstathiou, *Appl. Catal. B Environ.* **2004**, *54*, 237–250.
[57] Y. Sun, C. Li, I. Djerdj, O. Khalid, P. Cop, J. Sann, T. Weber, S. Werner, K. Turke, Y. Guo, et al., *Catal. Sci. Technol.* **2019**, *9*, 2163–2172.
[58] S. Meiqing, W. Xinquan, A. Yuan, W. Duan, Z. Minwei, W. Jun, *J. Rare Earths* **2007**, *25*, 48–52.
[59] L. Pastor-Pérez, T. R. Reina, S. Ivanova, M. Á. Centeno, J. A. Odriozola, A. Sepúlveda-Escribano, *Catalysts* **2015**, *5*, 298–309.
[60] J. Li, X. Liu, W. Zhan, Y. Guo, Y. Guo, G. Lu, *Catal. Sci. Technol.* **2016**, *6*, 897–907.
[61] P. P. Dholabhai, J. B. Adams, P. Crozier, R. Sharma, *J. Chem. Phys.* **2010**, *132*, 094104.
[62] M. Kuhn, S. R. Bishop, J. L. M. Rupp, H. L. Tuller, *Acta Mater.* **2013**, *61*, 4277–4288.
[63] M. Sanchez-Dominguez, L. F. Liotta, G. Di Carlo, G. Pantaleo, A. M. Venezia, C. Solans, M. Boutonnet, *Catal. Today* **2010**, *158*, 35–43.
[64] A. S. Deshpande, N. Pinna, B. Smarsly, M. Antonietti, M. Niederberger, *Small* **2005**, *1*, 313–316.
[65] S. Yang, L. Gao, *J. Am. Chem. Soc.* **2006**, *128*, 9330–9331.
[66] J. Zhang, S. Ohara, M. Umetsu, T. Naka, Y. Hatakeyama, T. Adschiri, *Adv. Mater.* **2007**, *19*, 203–206.
[67] C. Li, Y. Sun, I. Djerdj, P. Voepel, C. C. Sack, T. Weller, R. Ellinghaus, J. Sann, Y. Guo, B. M. Smarsly, et al., *ACS Catal.* **2017**, *7*, 6453–6463.
[68] J. C. Conesa, *Surf. Sci.* **1995**, *339*, 337–352.

[69] M. Nolan, S. Grigoleit, D. C. Sayle, S. C. Parker, G. W. Watson, *Surf. Sci.* **2005**, *576*, 217–229.
[70] M. M. Branda, R. M. Ferullo, M. Causá, F. Illas, *J. Phys. Chem. C* **2011**, *115*, 3716–3721.
[71] T. X. T. Sayle, S. C. Parker, C. R. A. Catlow, *Surf. Sci.* **1994**, *316*, 329–336.
[72] K. Zhou, X. Wang, X. Sun, Q. Peng, Y. Li, *J. Catal.* **2005**, *229*, 206–212.
[73] Z. Wu, M. Li, S. H. Overbury, *J. Catal.* **2012**, *285*, 61–73.
[74] M. Nolan, S. C. Parker, G. W. Watson, *Surf. Sci.* **2005**, *595*, 223–232.
[75] A. Bueno-López, *Appl. Catal. B Environ.* **2014**, *146*, 1–11.
[76] S. Tsunekawa, S. Ito, Y. Kawazoe, *Appl. Phys. Lett.* **2004**, *85*, 3845–3847.
[77] S. Tsunekawa, R. Sivamohan, S. Ito, A. Kasuya, T. Fukuda, *Nanostructured Mater.* **1999**, *11*, 141–147.
[78] X. D. Zhou, W. Huebner, *Appl. Phys. Lett.* **2001**, *79*, 3512–3514.
[79] D. R. Mullins, *Surf. Sci. Rep.* **2015**, *70*, 42–85.
[80] E. Özkan, P. Cop, F. Benfer, A. Hofmann, M. Votsmeier, J. M. Guerra, M. Giar, C. Heiliger, H. Over, B. M. Smarsly, *J. Phys. Chem. C* **2020**, *In Press*, DOI 10.1021/acs.jpcc.0c00010.
[81] A. Migani, G. N. Vayssilov, S. T. Bromley, K. M. Neyman, *J. Mater. Chem.* **2010**, *20*, 10535–10546.
[82] A. Migani, G. N. Vayssilov, S. T. Bromley, F. Illas, K. M. Neyman, *Chem. Commun.* **2010**, *46*, 5936–5938.
[83] N. D. Petkovich, A. Stein, *Chem. Soc. Rev.* **2013**, *42*, 3721–3739.
[84] V. Malgras, J. Tang, J. Wang, J. Kim, N. L. Torad, S. Dutta, K. Ariga, M. S. A. Hossain, Y. Yamauchi, K. C. W. Wu, *J. Nanosci. Nanotechnol.* **2019**, *19*, 3673–3685.
[85] A. Thomas, F. Goettmann, M. Antonietti, *Chem. Mater.* **2008**, *20*, 738–755.
[86] X. Deng, K. Chen, H. Tüysüz, *Chem. Mater.* **2017**, *29*, 40–52.
[87] A. Aranda, B. Puértolas, B. Solsona, S. Agouram, R. Murillo, A. M. Mastral, S. H. Taylor, T. Garcia, *Catal. Letters* **2010**, *134*, 110–117.
[88] J. Roggenbuck, H. Schäfer, T. Tsoncheva, C. Minchev, J. Hanss, M. Tiemann, *Microporous Mesoporous Mater.* **2007**, *101*, 335–341.
[89] X. Qu, D. Xie, L. Gao, F. Du, *Mater. Sci. Semicond. Process.* **2014**, *26*, 657–662.
[90] M. J. Pellin, P. C. Stair, G. Xiong, J. W. Elam, J. Birrell, L. Curtiss, S. M. George, C. Y. Han, L. Iton, H. Kung, et al., *Catal. Letters* **2005**, *102*, 127–130.
[91] A. F. Sierra-Salazar, A. Ayral, T. Chave, V. Hulea, S. I. Nikitenko, S. Abate, S. Perathoner, P. Lacroix-Desmazes, *Stud. Surf. Sci. Catal.* **2019**, *178*, 377–397.
[92] M. Marcos-Hernández, D. Villagrán, in *Compos. Nanoadsorbents* (Eds.: G.Z. Kyzas, A.C. Mitropoulos), Elsevier, Cambridge (United States), **2019**, 265–293.
[93] B. Eckhardt, E. Ortel, D. Bernsmeier, J. Polte, P. Strasser, U. Vainio, F. Emmerling, R. Kraehnert, *Chem. Mater.* **2013**, *25*, 2749–2758.
[94] D. Gu, F. Schüth, *Chem. Soc. Rev.* **2014**, *43*, 313–344.
[95] Y. Wan, D. Zhao, *Chem. Rev.* **2007**, *107*, 2821–2860.
[96] C. J. Brinker, Y. Lu, A. Sellinger, H. Fan, *Adv. Mater.* **1999**, *11*, 579–585.
[97] C. J. Brinker, G. W. Scherer, *The Physics and Chemistry of Sol-Gel Processing*, Elsevier Science Publishing Co Inc, Amsterdam, **1990**.
[98] P. Innocenzi, L. Malfatti, *Chem. Soc. Rev.* **2013**, *42*, 4198–4216.
[99] C. Y. Chiu, A. S. T. Chiang, K. J. Chao, *Microporous Mesoporous Mater.* **2006**, *91*, 244–253.
[100] B. Smarsly, G. Garnweitner, R. Assink, C. J. Brinker, *Prog. Org. Coatings* **2003**, *47*, 393–400.
[101] P. Cop, S. Kitano, K. Niinuma, B. Smarsly, H. Kozuka, *Nanoscale* **2018**, *10*, 7002–7015.
[102] T. Von Graberg, P. Hartmann, A. Rein, S. Gross, B. Seelandt, C. Röger, R. Zieba, A. Traut, M. Wark, J. Janek, et al., *Sci. Technol. Adv. Mater.* **2011**, *12*, 025005.
[103] P. Hartmann, T. Brezesinski, J. Sann, A. Lotnyk, J.-P. Eufinger, J. Janek, *ACS Nano* **2013**, *7*, 2999–3013.
[104] T. Brezesinski, J. Wang, R. Senter, K. Brezesinski, B. Dunn, S. H. Tolbert, *ACS Nano* **2010**, *4*, 967–977.
[105] N. Pinna, M. Niederberger, *Angew. Chemie* **2008**, *120*, 5372–5385.
[106] M. Niederberger, N. Pinna, *Metal Oxide Nanoparticles in Organic Solvents: Synthesis, Formation and Application*, Springer, Heidelberg, **2009**.
[107] C. Suchomski, D. J. Weber, P. Dolcet, A. Hofmann, P. Voepel, J. Yue, M. Einert, M. Möller, S. Werner, S. Gross, et al., *J. Mater. Chem. A* **2017**, *5*, 16296–16306.
[108] P. Hartmann, D. Lee, B. M. Smarsly, J. Janek, *ACS Nano* **2010**, *4*, 3147–3154.
[109] L. Guo, H. Hagiwara, S. Ida, T. Daio, T. Ishihara, *ACS Appl. Mater. Interfaces* **2013**, *5*, 11080–11086.
[110] P. Feng, X. Bu, D. J. Pine, *Langmuir* **2000**, *16*, 5304–5310.
[111] C. Boissiere, D. Grosso, S. Lepoutre, L. Nicole, A. B. Bruneau, C. Sanchez, *Langmuir* **2005**, *21*, 12362–12371.
[112] D. Zhao, J. Sun, Q. Li, G. D. Stucky, *Chem. Mater.* **2000**, *12*, 275–279.
[113] P. Djinović, J. Batista, J. Levec, A. Pintar, *Appl. Catal. A Gen.* **2009**, *364*, 156–165.
[114] W. Wang, R. Qi, W. Shan, X. Wang, Q. Jia, J. Zhao, C. Zhang, H. Ru, *Microporous Mesoporous Mater.* **2014**, *194*, 167–173.
[115] E. Ortel, A. Fischer, L. Chuenchom, J. Polte, F. Emmerling, B. Smarsly, R. Kraehnert, *Small* **2012**, *8*, 298–309.
[116] B. Smarsly, D. Grosso, T. Brezesinski, N. Pinna, C. Boissière, M. Antonietti, C. Sanchez, *Chem. Mater.* **2004**, *16*, 2948–2952.
[117] T. Brezesinski, M. Antonietti, M. Groenewolt, N. Pinna, B. Smarsly, *New J. Chem.* **2005**, *29*, 237–242.
[118] C. Weidmann, K. Brezesinski, C. Suchomski, K. Tropp, N. Grosser, J. Haetge, B. M. Smarsly, T. Brezesinski, *Chem. Mater.* **2012**, *24*, 486–494.
[119] B. Smarsly, M. Antonietti, *Eur. J. Inorg. Chem.* **2006**, 1111–1119.
[120] C. Reitz, J. Reinacher, P. Hartmann, T. Brezesinski, *Catal. Today* **2014**, *225*, 55–63.
[121] J. Rathouský, D. F. Rohlfing, M. Wark, T. Brezesinski, B. Smarsly, *Thin Solid Films* **2007**, *515*, 6541–6543.
[122] T. Brezesinski, B. Smarsly, K. I. Iimura, D. Grosso, C. Boissière, H. Amenitsch, M. Antonietti, C. Sanchez, *Small* **2005**, *1*, 889–898.
[123] D. Grosso, C. Boissiere, B. Smarsly, T. Brezesinski, N. Pinna, P. A. Albouy, H. Amenitsch, M. Antonietti, C. Sanchez, *Nat. Mater.* **2004**, *3*, 787–792.
[124] C. Suchomski, C. Reitz, C. T. Sousa, J. P. Araujo, T. Brezesinski, *Chem. Mater.* **2013**, *25*, 2527–2537.
[125] C. Reitz, C. Suchomski, J. Haetge, T. Leichtweiss, Z. Jagličić, I. Djerdj, T. Brezesinski, *Chem. Commun.* **2012**, *48*, 4471–4473.
[126] B. Smarsly, D. Grosso, T. Brezesinski, N. Pinna, C. Boissière, M. Antonietti, C. Sanchez, *Chem. Mater.* **2004**, *16*, 2948–2952.
[127] S. Sallard, M. Schröder, C. Boissière, C. Dunkel, M. Etienne, A. Walcarius, T. Oekermann, M. Wark, B. M. Smarsly, *Nanoscale* **2013**, *5*, 12316–12329.
[128] C. Gérardin, J. Reboul, M. Bonne, B. Lebeau, *Chem. Soc. Rev.* **2013**, *42*, 4217–4255.
[129] A. Birault, E. Molina, C. Carcel, J. Bartlett, N. Marcotte, G. Toquer, P. Lacroix-Desmazes, C. Gerardin, M. Wong Chi Man, *J. Sol-Gel Sci. Technol.* **2019**, *89*, 189–195.
[130] M. D. Tyona, *Adv. Mater. Res.* **2013**, *2*, 195–208.
[131] D. Grosso, *J. Mater. Chem.* **2011**, *21*, 17033–17038.
[132] L. Li, M. Krissanasaeranee, S. W. Pattinson, M. Stefik, U. Wiesner, U. Steiner, D. Eder, *Chem. Commun.* **2010**, *46*, 7620.
[133] T. Weller, L. Deilmann, J. Timm, T. S. Dörr, P. A. Beaucage, A. S. Cherevan, U. B. Wiesner, D. Eder, R. Marschall, *Nanoscale* **2018**, *10*, 3225–3234.
[134] W. Shen, X. Dong, Y. Zhu, H. Chen, J. Shi, *Microporous Mesoporous Mater.* **2005**, *85*, 157–162.
[135] M. Zabilskiy, B. Erjavec, P. Djinovi??, A. Pintar, *Chem. Eng. J.* **2014**, *254*, 153–162.
[136] H. Yen, Y. Seo, R. Guillet-Nicolas, S. Kaliaguine, F. Kleitz, *Chem. Commun.* **2011**, *47*, 10473.
[137] T. X. T. Sayle, F. Caddeo, X. Zhang, T. Sakthivel, S. Das, S. Seal, S. Ptasinska, D. C. Sayle, *Chem. Mater.* **2016**, *28*, 7287–7295.
[138] W. Y. Hernández, O. H. Laguna, M. A. Centeno, J. A. Odriozola, *J. Solid State Chem.* **2011**, *184*, 3014–3020.

[139] O. Mendiuk, M. Nawrocki, L. Kepinski, *Ceram. Int.* **2016**, *42*, 1998–2012.
[140] N. Yang, P. Orgiani, E. Di Bartolomeo, V. Foglietti, P. Torelli, A. V. Ievlev, G. Rossi, S. Licoccia, G. Balestrino, S. V. Kalinin, et al., *J. Phys. Chem. C* **2017**, *121*, 8841–8849.
[141] D. A. Andersson, S. I. Simak, N. V. Skorodumova, I. A. Abrikosov, B. Johansson, *PNAS* **2006**, *103*, 3518–3521.
[142] C. Balaji Gopal, M. García-Melchor, S. C. Lee, Y. Shi, A. Shavorskiy, M. Monti, Z. Guan, R. Sinclair, H. Bluhm, A. Vojvodic, et al., *Nat. Commun.* **2017**, *8*, 15360.
[143] U. Hennings, R. Reimert, *Appl. Catal. A Gen.* **2007**, *325*, 41–49.
[144] H. L. Tuller, S. R. Bishop, D. Chen, Y. Kuru, J. J. Kim, T. S. Stefanik, *Solid State Ionics* **2012**, *225*, 194–197.
[145] D. Marrocchelli, S. R. Bishop, H. L. Tuller, B. Yildiz, *Adv. Funct. Mater.* **2012**, *22*, 1958–1965.
[146] A. Trovarelli, F. Zamar, J. Llorca, C. De Leitenburg, G. Dolcetti, J. T. Kiss, *J. Catal.* **1997**, *169*, 490–502.
[147] Y. Madier, C. Descorme, a M. Le Govic, D. Duprez, *J. Phys. Chem. B* **1999**, *103*, 10999–11006.
[148] J. A. Rodriguez, J. C. Hanson, J. Y. Kim, G. Liu, A. Iglesias-Juez, M. Fernández-García, *J. Phys. Chem. B* **2003**, *107*, 3535–3543.
[149] A. E. Nelson, K. H. Schulz, *Appl. Surf. Sci.* **2003**, *210*, 206–221.
[150] J. Kaspar, P. Fornasiero, G. Balducci, R. Di Monte, N. Hickey, V. Sergo, *Inorganica Chim. Acta* **2003**, *349*, 217–226.
[151] J. Kašpar, P. Fornasiero, N. Hickey, *Catal. Today* **2003**, *77*, 419–449.
[152] L. Lan, S. Chen, Y. Cao, S. Wang, Q. Wu, Y. Zhou, M. Huang, M. Gong, Y. Chen, *J. Mol. Catal. A Chem.* **2015**, *410*, 100–109.
[153] B. Y. R. D. Shannon, M. H, N. H. Baur, O. H. Gibbs, M. Eu, V. Cu, *Acta Cryst* **1976**, *A 32*, 751.
[154] F. Lin, R. Delmelle, T. Vinodkumar, B. M. Reddy, A. Wokaun, I. Alxneit, *Catal. Sci. Technol.* **2015**, *5*, 3556–3567.
[155] T. Vinodkumar, B. G. Rao, B. M. Reddy, *Catal. Today* **2015**, *253*, 57–64.
[156] G. S. Otero, P. G. Lustemberg, F. Prado, M. V. Ganduglia-Pirovano, *J. Phys. Chem. C* **2019**, *124*, 625–638.
[157] C. Bozo, N. Guilhaume, E. Garbowski, M. Primet, *Catal. Today* **2000**, *59*, 33–45.
[158] J. I. Gutiérrez-Ortiz, B. De Rivas, R. López-Fonseca, J. R. González-Velasco, *Catal. Today* **2005**, *107–108*, 933–941.
[159] E. Díaz, B. de Rivas, R. López-Fonseca, S. Ordóñez, J. I. Gutiérrez-Ortiz, *J. Chromatogr. A* **2006**, *1116*, 230–239.
[160] A. J. De Abreu, A. F. Lucrédio, E. M. Assaf, *Fuel Process. Technol.* **2012**, *102*, 140–145.
[161] A. Remiro, A. Arandia, L. Oar-Arteta, J. Bilbao, A. G. Gayubo, *Energy and Fuels* **2018**, *32*, 3588–3598.
[162] W. Ruettinger, X. Liu, R. J. Farrauto, *Appl. Catal. B Environ.* **2006**, *65*, 135–141.
[163] A. Goguet, R. Burch, Y. Chen, C. Hardacre, P. Hu, R. W. Joyner, F. C. Meunier, B. S. Mun, D. Thompsett, D. Tibiletti, *J. Phys. Chem. C* **2007**, *111*, 16927–16933.
[164] C. M. Kalamaras, D. D. Dionysiou, A. M. Efstathiou, *ACS Catal.* **2012**, *2*, 2729–2742.
[165] L. G. Pinaeva, E. M. Sadovskaya, Y. A. Ivanova, T. G. Kuznetsova, I. P. Prosvirin, V. A. Sadykov, Y. Schuurman, A. C. Van Veen, C. Mirodatos, *Chem. Eng. J.* **2014**, *257*, 281–291.
[166] D. W. Jeong, H. S. Na, J. O. Shim, W. J. Jang, H. S. Roh, *Catal. Sci. Technol.* **2015**, *5*, 3706–3713.
[167] C. A. Neyertz, E. D. Banús, E. E. Miró, C. A. Querini, *Chem. Eng. J.* **2014**, *248*, 394–405.
[168] I. Atribak, A. Bueno-López, A. García-García, *J. Catal.* **2008**, *259*, 123–132.
[169] C. Li, Y. Sun, F. Hess, I. Djerdj, J. Sann, P. Voepel, P. Cop, Y. Guo, B. M. Smarsly, H. Over, *Appl. Catal. B Environ.* **2018**, *239*, 628–635.
[170] M. Möller, N. Tarabanko, C. Wessel, R. Ellinghaus, H. Over, B. M. Smarsly, *RSC Adv.* **2018**, *8*, 132–144.
[171] M. Möller, H. Over, B. Smarsly, N. Tarabanko, S. Urban, *Catal. Today* **2015**, *253*, 207–218.
[172] Y. Sun, P. Cop, I. Djerdj, X. Guo, T. Weber, O. Khalid, Y. Guo, B. M. Smarsly, H. Over, *ACS Catal.* **2019**, *9*, 10680–10693.
[173] E. Ahvenniemi, A. R. Akbashev, S. Ali, M. Bechelany, M. Berdova, S. Boyadjiev, D. C. Cameron, R. Chen, M. Chubarov, V. Cremers, et al., *J. Vac. Sci. Technol. A Vacuum, Surfaces, Film.* **2017**, *35*, 010801.
[174] R. L. Puurunen, *Chem. Vap. Depos.* **2014**, *20*, 332–344.
[175] V. Miikkulainen, M. Leskelä, M. Ritala, R. L. Puurunen, *J. Appl. Phys.* **2013**, *113*, 021301.
[176] R. W. Johnson, A. Hultqvist, S. F. Bent, *Mater. Today* **2014**, *17*, 236–246.
[177] V. Cremers, R. L. Puurunen, J. Dendooven, *Appl. Phys. Rev.* **2019**, *6*, 021302.
[178] J.-P. Correa-Baena, K. Artyushkova, C. Santoro, P. Atanassov, A. G. Agrios, *ACS Appl. Mater. Interfaces* **2016**, *8*, 9849–9854.
[179] C. Detavernier, J. Dendooven, S. P. Sree, K. F. Ludwig, J. a Martens, *Chem. Soc. Rev.* **2011**, *40*, 5242–53.
[180] M. Knez, K. Nielsch, L. Niinistö, *Adv. Mater.* **2007**, *19*, 3425–3438.
[181] Q. Peng, X. Y. Sun, J. C. Spagnola, G. K. Hyde, R. J. Spontak, G. N. Parsons, *Nano Lett.* **2007**, *7*, 719.
[182] S. O. Kucheyev, J. Biener, Y. M. Wang, T. F. Baumann, K. J. Wu, T. van Buuren, A. V. Hamza, J. H. Satcher, J. W. Elam, M. J. Pellin, *Appl. Phys. Lett.* **2005**, *86*, 083108.
[183] J. W. Elam, J. A. Libera, T. H. Huynh, H. Feng, M. J. Pellin, *J. Phys. Chem. C* **2010**, *114*, 17286–17292.
[184] J. A. Libera, J. W. Elam, M. J. Pellin, *Thin Solid Films* **2008**, *516*, 6158–6166.
[185] Z. Cai, B. Liu, X. Zou, H. M. Cheng, *Chem. Rev.* **2018**, *118*, 6091–6133.
[186] M. Reiners, K. Xu, N. Aslam, A. Devi, R. Waser, S. Hoffmann-Eifert, *Chem. Mater.* **2013**, *25*, 2934–2943.
[187] T. Kääriäinen, D. Cameron, M.-L. Kääriäinen, A. Sherman, *Atomic Layer Deposition* ¨, Scrivener Publishing, Hoboken, New Jersey, **2013**.
[188] S. M. Rossnagel, *J. Vac. Sci. Technol. A Vacuum, Surfaces, Film.* **2003**, *21*, S74–S87.
[189] A. Yanguos-Gil, *Growth and Transport in PVD, CVD and ALD*, Springer Verlag, Heidelberg, **2017**.
[190] Atomic Layer Deposition: An Overview, *Chem. Rev.* **2010**, *110*, 111–131.
[191] R. L. Puurunen, *J. Appl. Phys.* **2005**, *97*, 121301.
[192] S. T. Barry, A. V. Teplyakov, F. Zaera, *Acc. Chem. Res.* **2018**, *51*, 800–809.
[193] F. Zaera, *J. Phys. Chem. Lett.* **2012**, *3*, 1301–1309.
[194] R. G. Gordon, D. Hausmann, E. Kim, J. Shepard, *Chem. Vap. Depos.* **2003**, *9*, 73–78.
[195] D. M. King, X. Liang, Y. Zhou, C. S. Carney, L. F. Hakim, P. Li, A. W. Weimer, *Powder Technol.* **2008**, *183*, 356–363.
[196] J. Dendooven, K. Devloo-Casier, M. Ide, K. Grandfield, M. Kurttepeli, K. F. Ludwig, S. Bals, P. Van Der Voort, C. Detavernier, *Nanoscale* **2014**, *6*, 14991–14998.
[197] S. Mahurin, L. Bao, W. Yan, C. Liang, S. Dai, *J. Non. Cryst. Solids* **2006**, *352*, 3280–3284.
[198] R. L. Puurunen, A. Root, P. Sarv, M. M. Viitanen, H. H. Brongersma, M. Lindblad, A. O. I. Krause, *Chem. Mater.* **2002**, *14*, 720–729.
[199] J. W. Elam, J. A. Libera, T. H. Huynh, H. Feng, M. J. Pellin, *J. Phys. Chem. C* **2010**, *114*, 17286–17292.
[200] S. Pulinthanathu Sree, J. Dendooven, J. Jammaer, K. Masschaele, D. Deduytsche, J. D'Haen, C. E. A. Kirschhock, J. A. Martens, C. Detavernier, *Chem. Mater.* **2012**, *24*, 2775–2780.
[201] S. Boukhalfa, K. Evanoff, G. Yushin, *Energy Environ. Sci.* **2012**, *5*, 6872–6879.
[202] S. P. Sree, J. Dendooven, T. I. Korányi, G. Vanbutsele, K. Houthoofd, D. Deduytsche, C. Detavernier, J. A. Martens, *Catal. Sci. Technol.* **2011**, *1*, 218–221.
[203] J. E. Mondloch, W. Bury, D. Fairen-Jimenez, S. Kwon, E. J. Demarco, M. H. Weston, A. A. Sarjeant, S. T. Nguyen, P. C. Stair, R. Q. Snurr, et al., *J. Am. Chem. Soc.* **2013**, *135*, 10294–10297.
[204] J. Dendooven, K. Devloo-Casier, E. Levrau, R. Van Hove, S. Pulinthanathu Sree, M. R. Baklanov, J. A. Martens, C. Detavernier, *Langmuir* **2012**, *28*, 3852–3859.
[205] M. A. Cameron, I. P. Gartland, J. A. Smith, S. F. Diaz, S. M. George, *Langmuir* **2000**, *16*, 7435–7444.
[206] J. Dendooven, B. Goris, K. Devloo-Casier, E. Levrau, E. Biermans, M. R. Baklanov, K. F. Ludwig, P. Van Der Voort, S. Bals, C. Detavernier, *Chem. Mater.* **2012**, *24*, 1992–1994.
[207] E. Levrau, K. Devloo-Casier, J. Dendooven, K. F. Ludwig, P. Verdonck, J. Meersschaut, M. R. Baklanov, C. Detavernier, *Langmuir* **2013**, *29*,

12284–12289.
[208] G. Chiodelli, G. Flor, M. Scagliotti, *Solid State Ionics* **1996**, *91*, 109–121.
[209] C. C. Sack, CeOx(111)/Ru(0001) Als Modellkatalysator Für Die HCl-Oxidation, PhD Thesis, Justus-Liebig-University Giessen, **2019**.

6. Anhang

6.1 **ESI:** The Impact of Alio-/Isovalent Ions (Gd, Zr, Pr and Tb) on the Catalytic Stability of Mesoporous CeO_2 in the HCl Oxidation Reaction

The Impact of Alio-/Isovalent Ions (Gd, Zr, Pr and Tb) on the Catalytic Stability of Mesoporous Ceria in the HCl Oxidation Reaction

- Supporting Information -

Pascal Cop,[a,b] Ruben Maile,[a,b] Yu Sun,[a,c] Omeir Khalid,[a,b] Igor Djerdj,[d] Patrick Esch,[e] Sven Heiles,[e] Herbert Over,[a,b,] Bernd M. Smarsly[a,b,]**

a. Physikalisch-Chemisches Institut, Justus Liebig University, Heinrich-Buff-Ring 17, D-35392 Giessen, Germany

b. Center of Materials Research, Justus Liebig University, Heinrich-Buff-Ring 16, D-35392 Giessen, Germany.

c. Key Laboratory for Advanced Materials, Research Institute of Industrial Catalysis, School of Chemistry and Molecular Engineering, East China University of Science and Technology, Shanghai 200237, PR China.

d. Josip Juraj Strossmayer University of Osijek, Department of Chemistry, Cara Hadrijana 8/A, 31000 Osijek, Croatia

e. Institute of Inorganic and Analytical Chemistry, Justus Liebig University Giessen, 35392 Giessen, Germany

*(B.S.) E-mail: bernd.smarsly@phys.chemie.uni-giessen.de

*(H.O.) E-mail: herbert.over@phys.chemie.uni-giessen.de

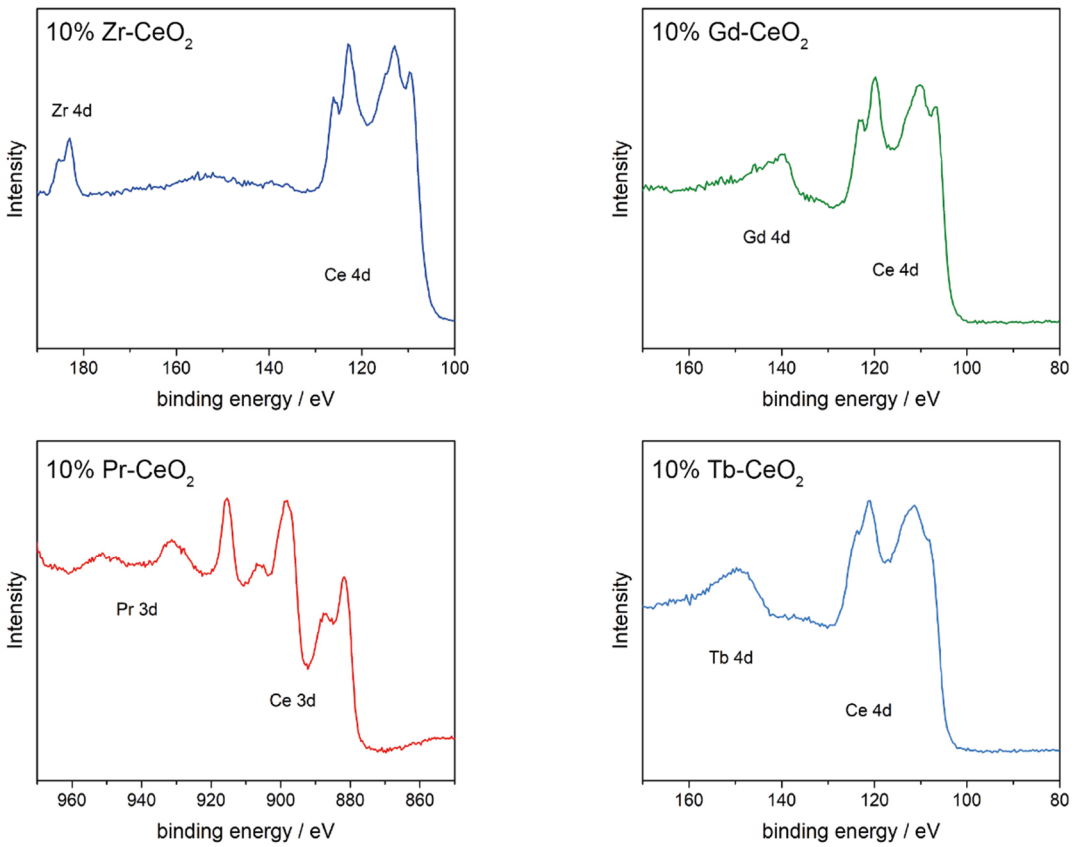

Figure S1: XPS spectra of the doped mesoporous CeO_2 powders to calculate the ratio of the dopant and cerium.

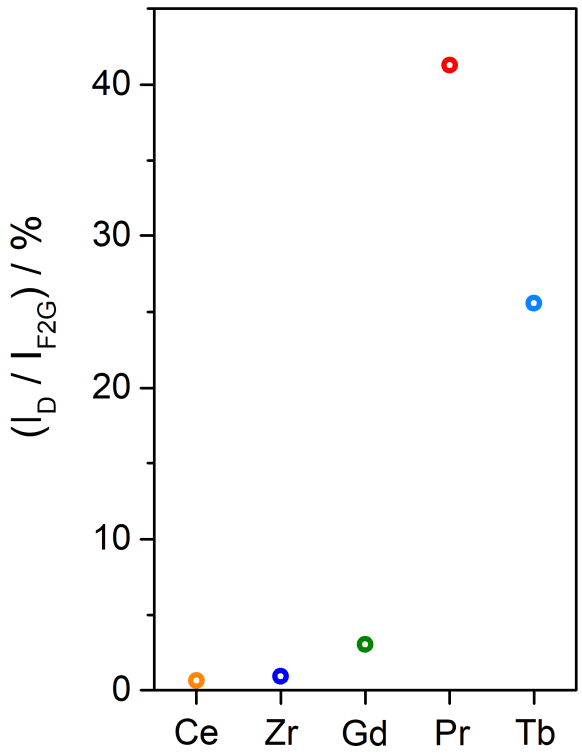

Figure S2: Comparison of the relative intensity ratio of the F_{2G} and defect mode D of the doped mesoporous CeO_2 catalysts.

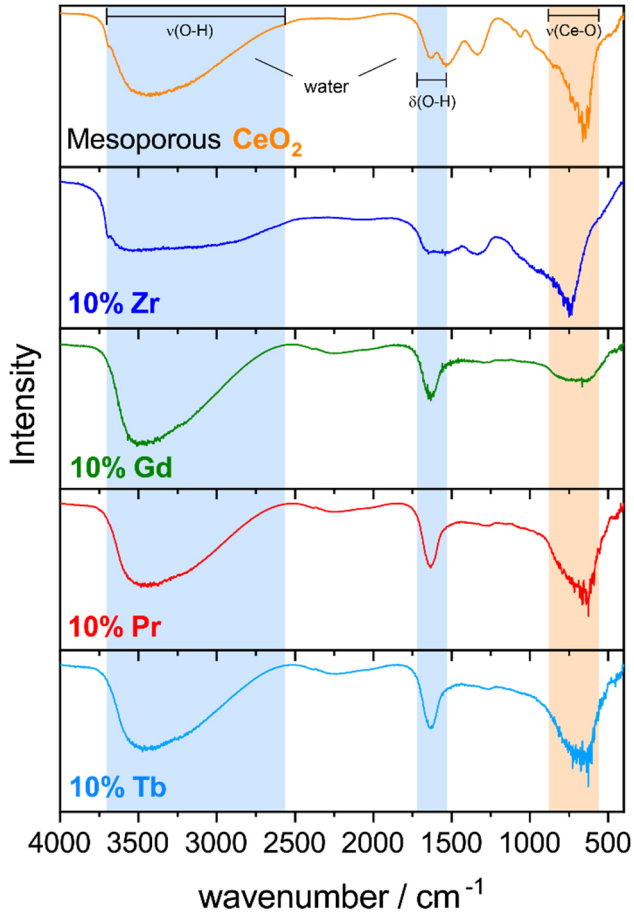

Figure S3: DRIFT measurements of the as-prepared mesoporous doped CeO_2 catalysts.

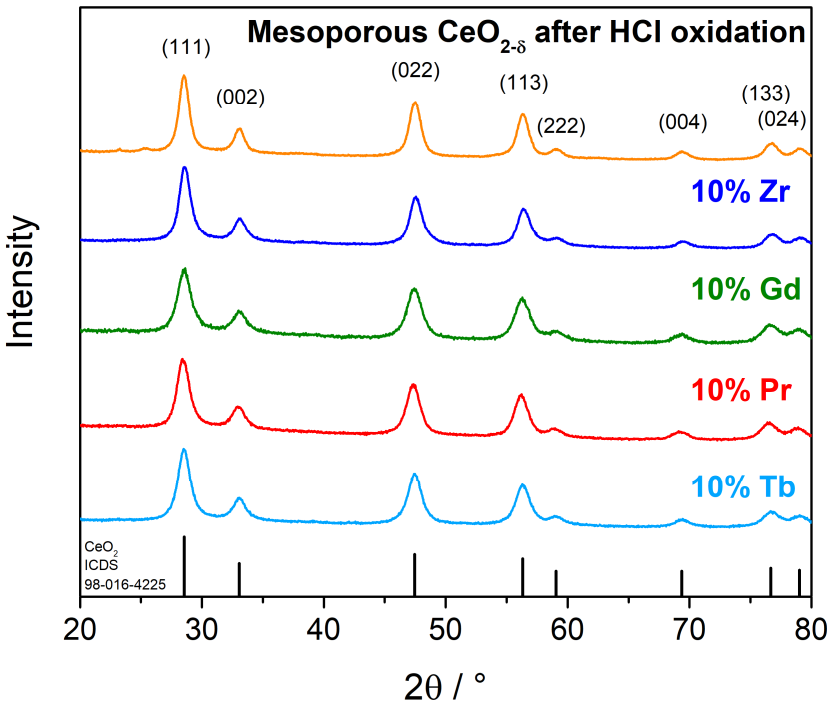

Figure S4: X-ray diffraction patterns of the mesoporous doped CeO_2 materials after the mild HCl oxidation. Additionally, the reference pattern of cubic CeO_2 (ICDS 98-016-4225) is displayed.

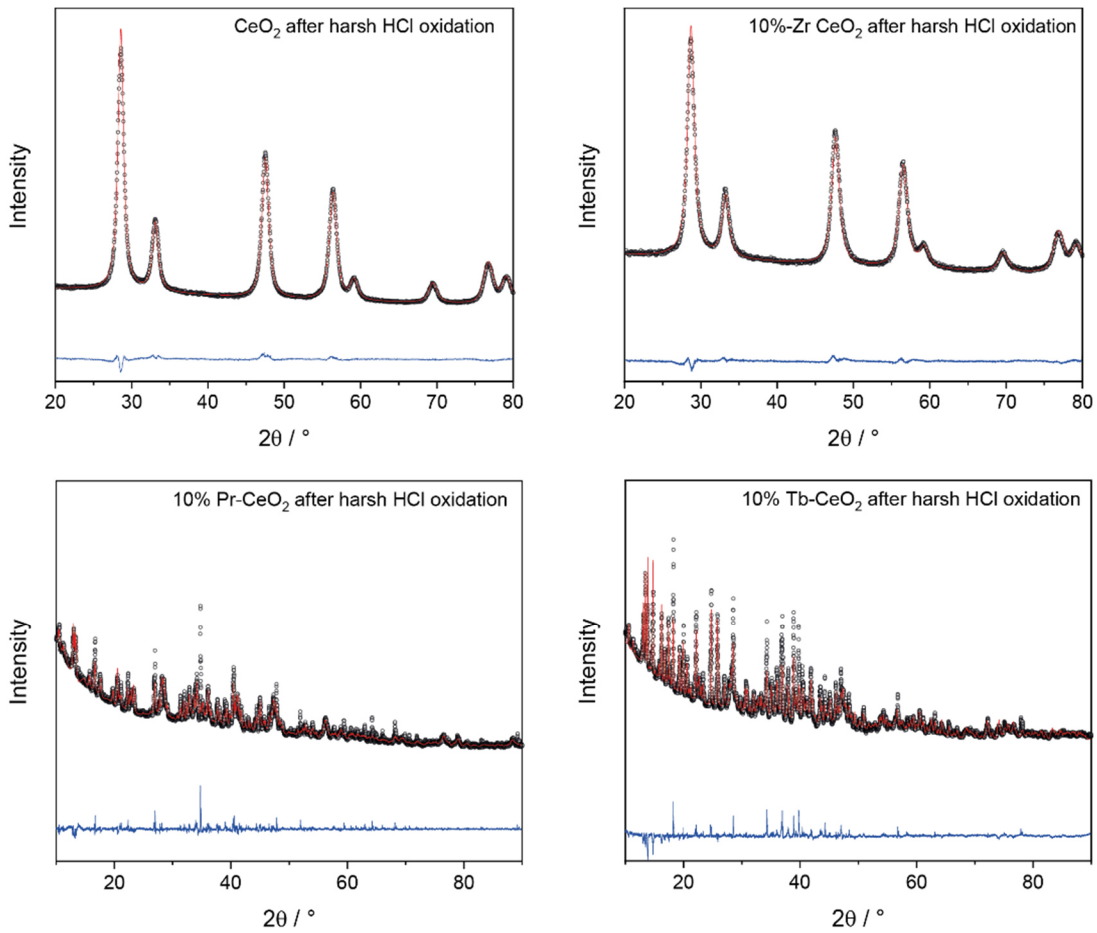

Figure S5: Rietveld output plots of the mesoporous doped CeO_2 after the harsh HCl oxidation.

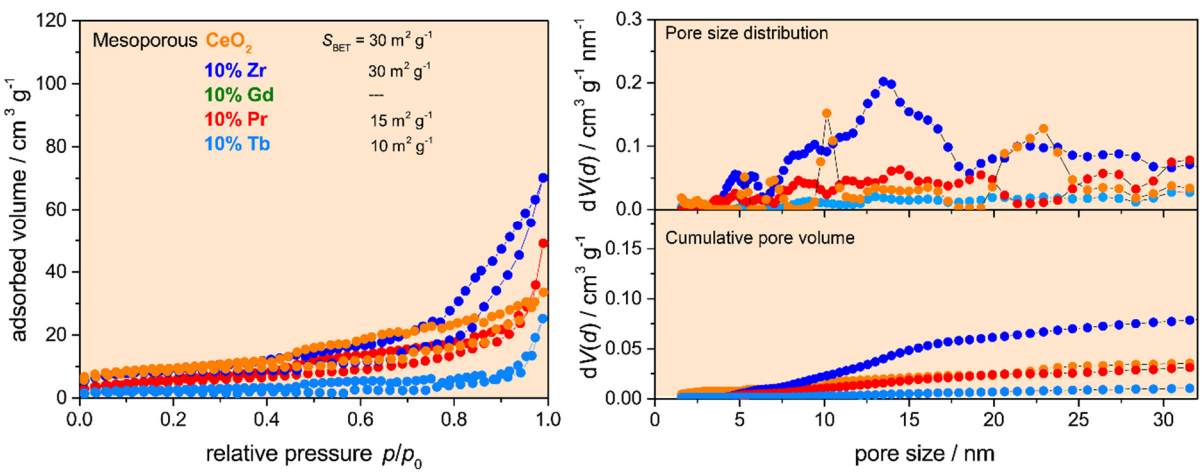

Figure S6: Nitrogen physisorption isotherms (left), the pore size distributions (top right) and cumulative pore volumes (bottom right) of the mesoporous doped CeO_2 catalysts after the harsh conditions of the HCl oxidation reaction.

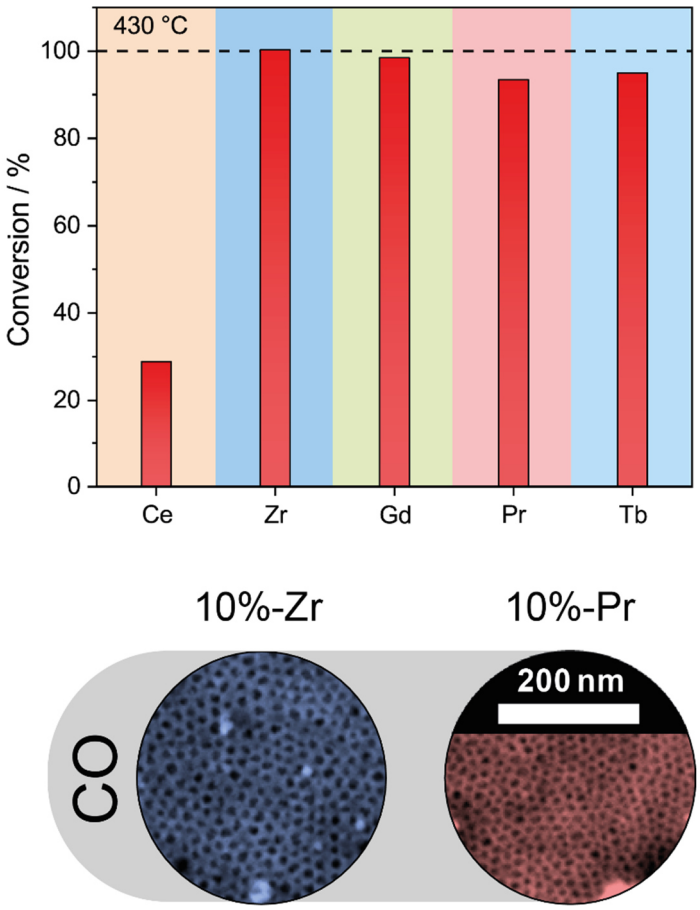

Figure S7: CO oxidation experiments under 430 °C for the doped mesoporous CeO_2 and the corresponding SEM images after the catalytic studies for 10%-Zr and 10%-Pr doped mesoporous powders. The latter shows the remaining presence of the mesopores.

6.2 **ESI:** Connectivity Matters: Comparison of Nanoparticle vs. Nanoparticle-Derived Mesoporous Ceria-Zirconia Structures in the HCl Oxidation Reaction

Connectivity Matters: Comparison of Nanoparticle vs. Nanoparticle-Derived Mesoporous Ceria-Zirconia Structures in the HCl Oxidation Reaction

Pascal Cop,[a,n] *Ruben Maile,*[a,b] *Yu Sun,*[c] *Felix Badaczewski,*[a,b] *Elifkübra Özkan,*[a,b] *Christian Sack,*[a,b] *Herbert Over,* [a,b] *Bernd M. Smarsly*[a,b] *

a. Physikalisch-Chemisches Institut, Justus Liebig University, Heinrich-Buff-Ring 17, D-35392 Giessen, Germany.

b. Center of Materials Research, Justus Liebig University, Heinrich-Buff-Ring 16, D-35392 Giessen, Germany.

c. Key Laboratory for Advanced Materials, Research Institute of Industrial Catalysis, School of Chemistry and Molecular Engineering, East China University of Science and Technology, Shanghai 200237, PR China.

Supporting Information

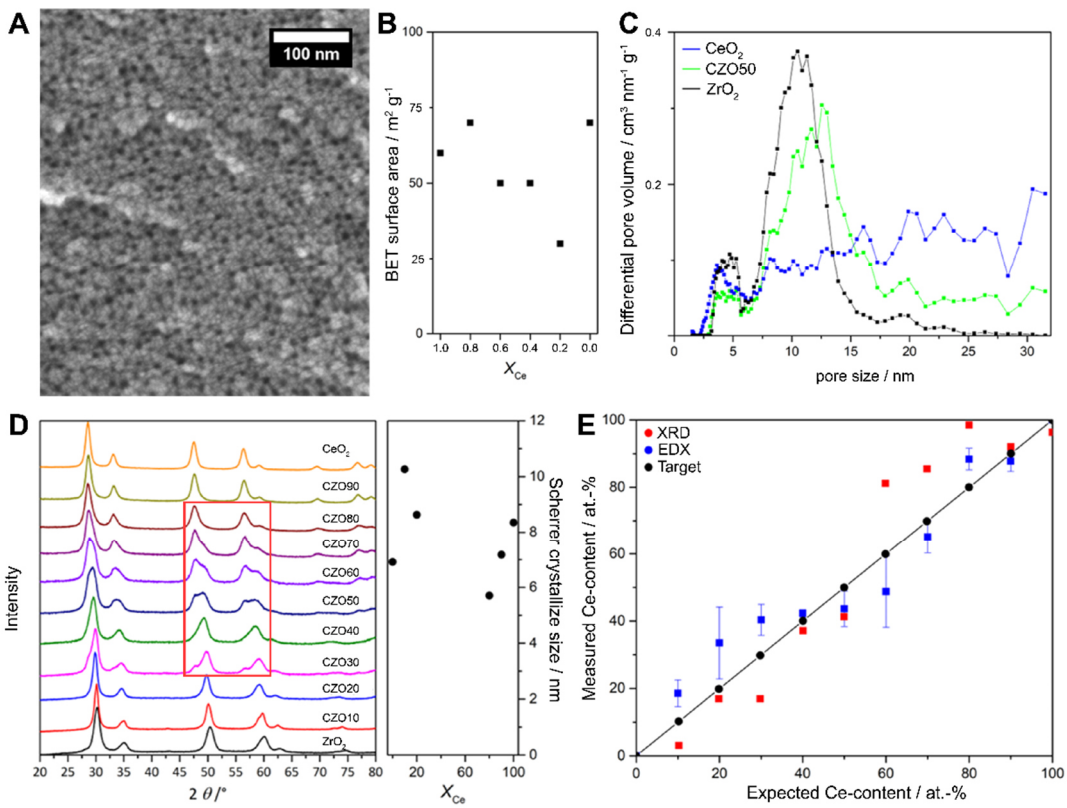

Figure S1: Overview of the results for the sol-gel-derived mesoporous $Ce_xZr_{1-x}O_2$ powders. (A) SEM; (B) BET surface area and (C) pore size distribution based on nitrogen physisorption experiments; (D) XRD results with the corresponding calculated Scherrer crystallite sizes; (E) Comparison of XRD (Vegard's rule) and EDS results regarding the Ce content.

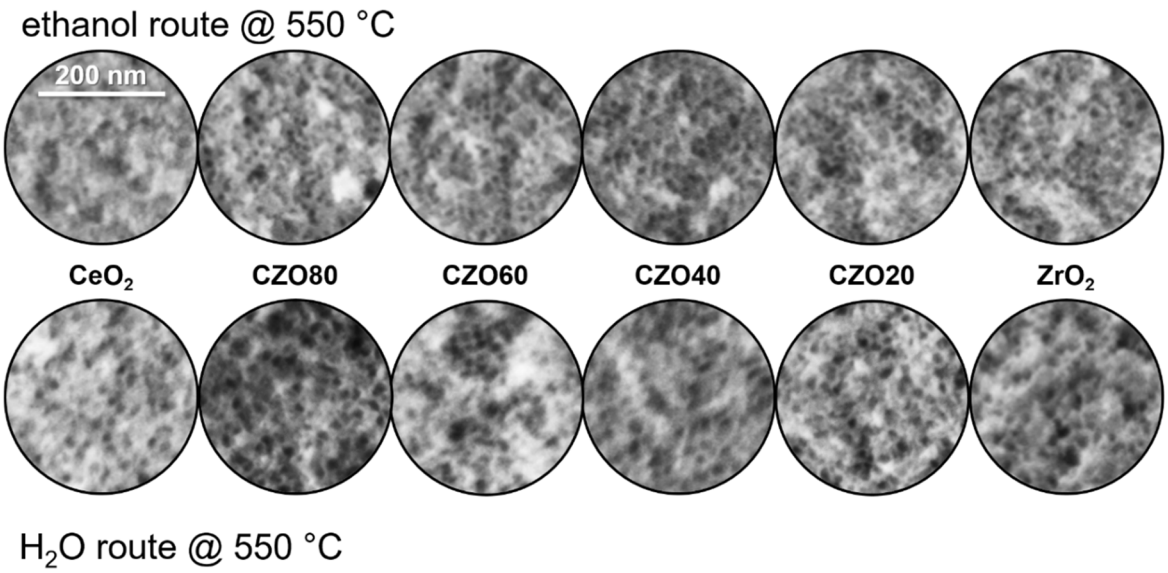

Figure S2: SEM images of the nanoparticle-derived mesoporous $Ce_xZr_{1-x}O_2$ powders using ethanol and H_2O. The existence of mesopores in the range of 12-17 nm are visible.

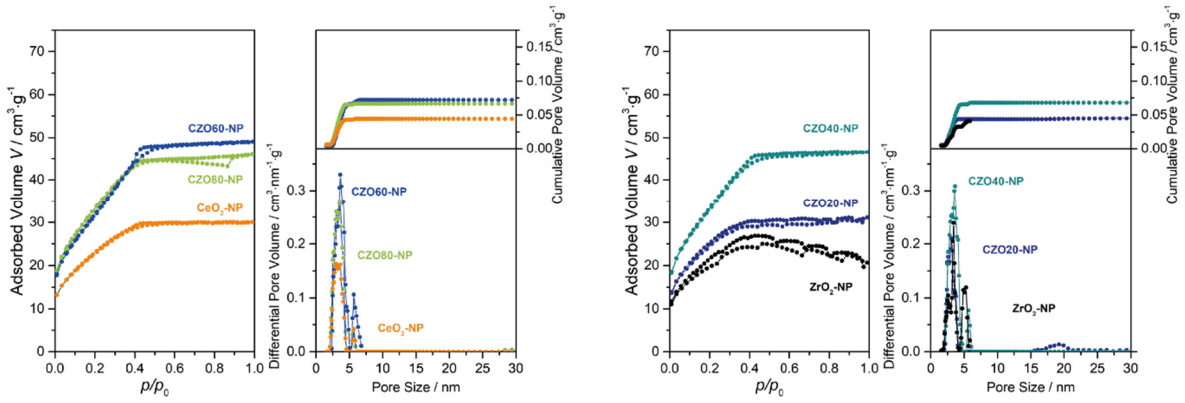

Figure S3: Nitrogen physisorption isotherms and pore size distribution including the cumulative and differential pore volume of the prepared CZO-NP after an annealing temperature of 550 °C (C).

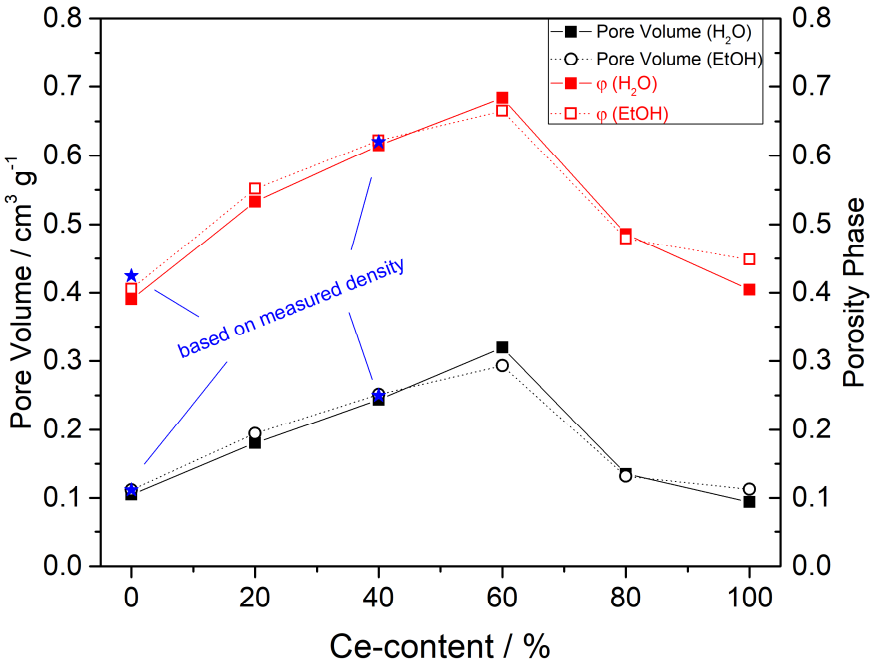

Figure S4: Comparison of pore volume and the porosity phase of the CZO-NP-Meso samples using EtOH and H_2O as the solvent. In addition, the blue points indicate values calculated with a measured density for the corresponding powders using pyknometry. The other porosity phase values were determined assuming a linear relationship between the densities of CeO_2 and ZrO_2.

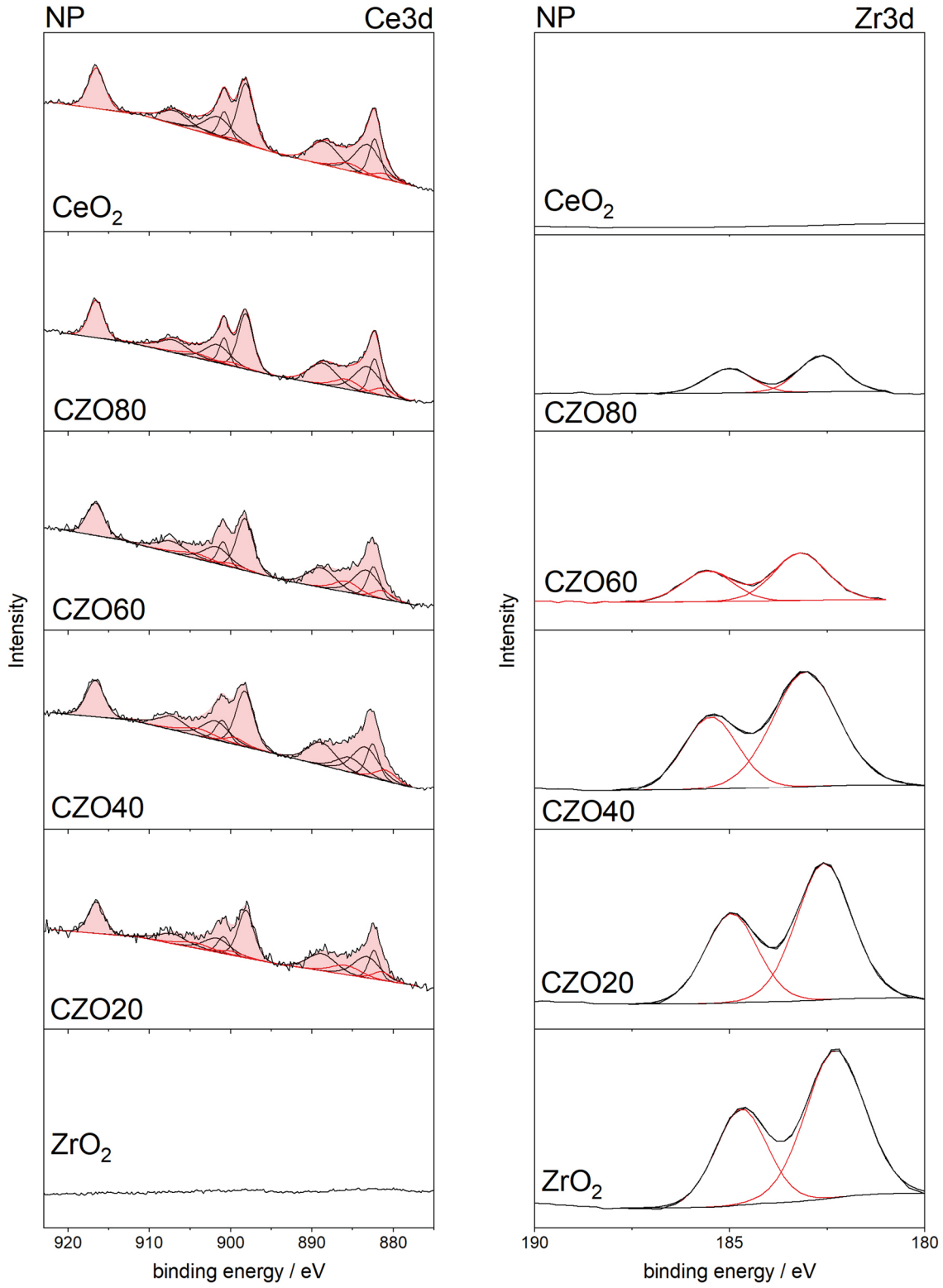

Figure S5: Ce3d and Zr3d spectra of the $Ce_xZr_{1-x}O_2$ nanoparticle. The Ce3d spectra is fitted using twelve Lorentz-Gaussian curves explained in more detail in the experimental section. The Ce^{3+} related bands (u',v',u_0 and v_0) are depicted in red.

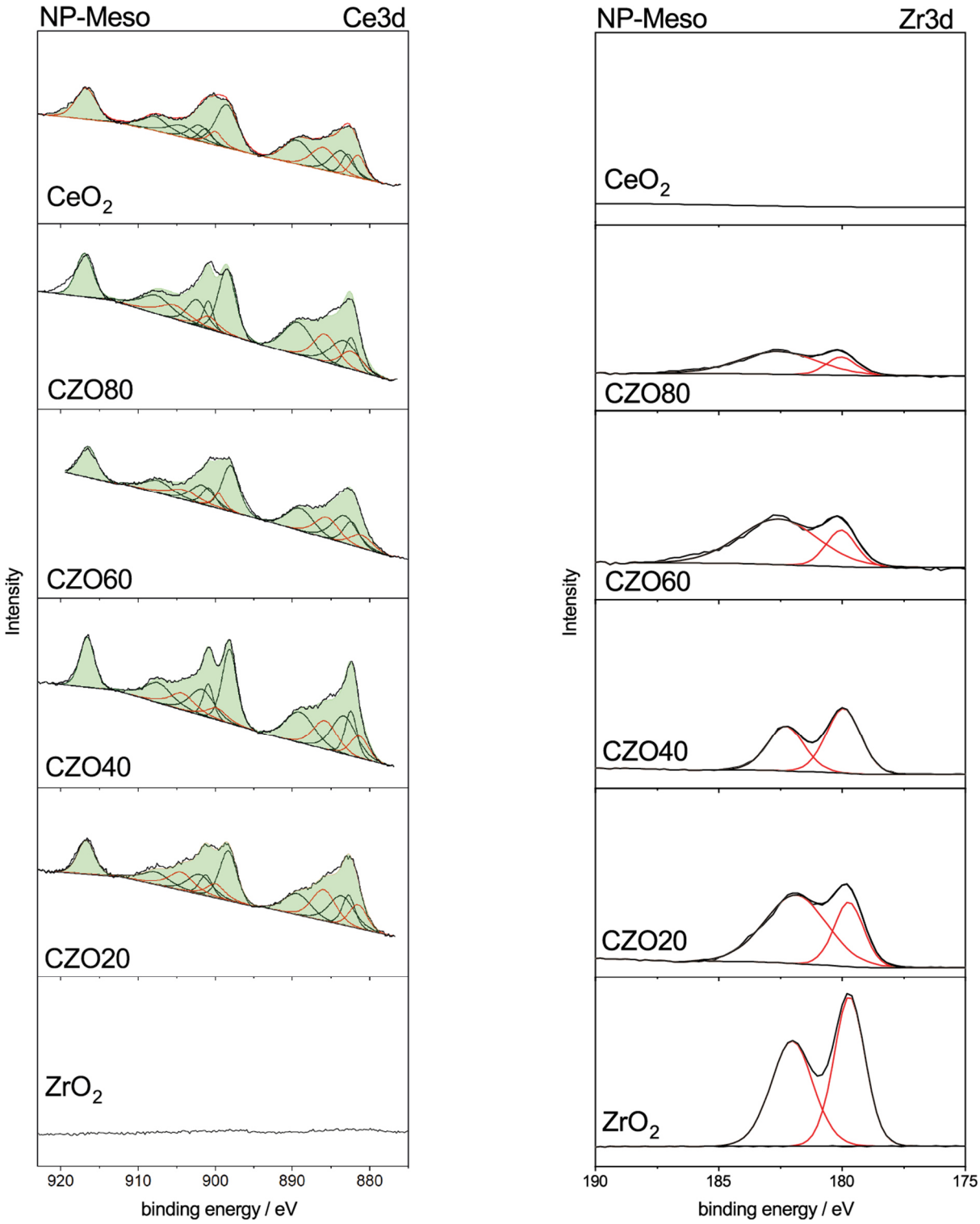

Figure S6: Ce3d and Zr3d spectra of the nanoparticle-derived mesoporous $Ce_xZr_{1-x}O_2$ powders. The Ce3d spectra is fitted using twelve Lorents-Gaussian curves explained in more detail in the experimental section. The Ce^{3+} related bands (u',v',u_0 and v_0) are depicted in red.

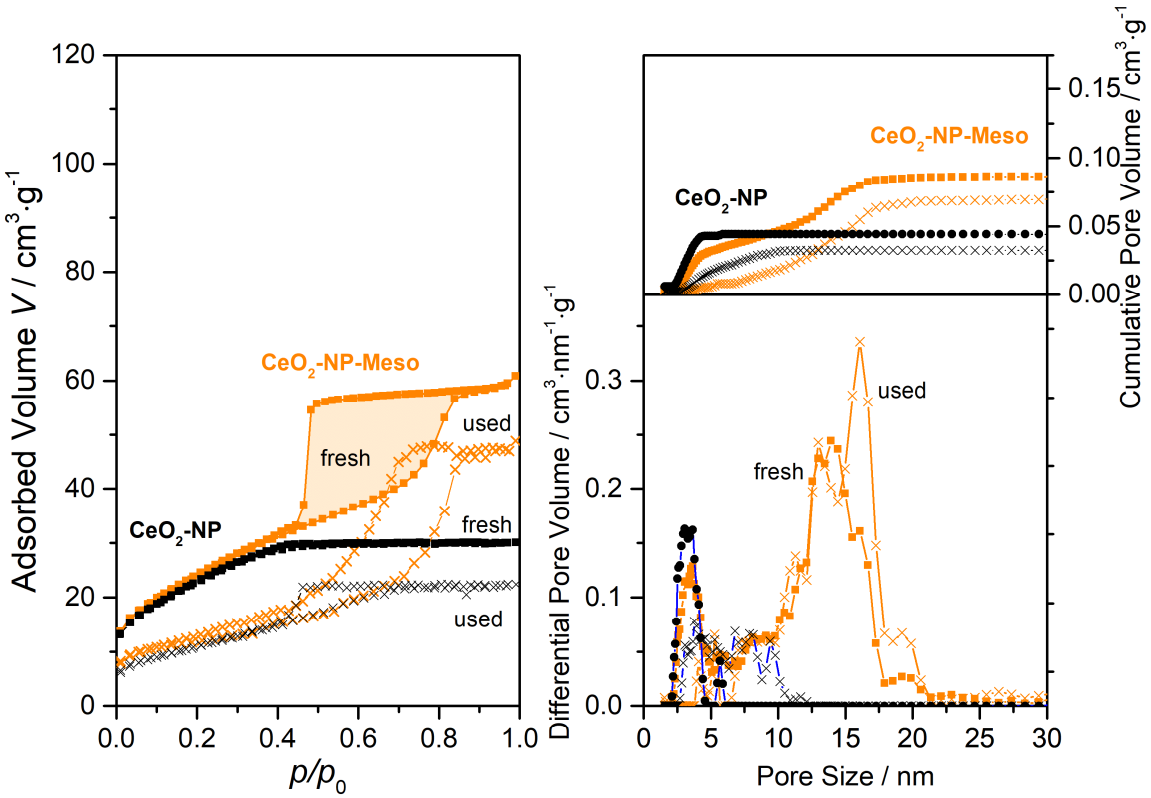

Figure S7: Nitrogen physisorption isotherms and pore size distribution including the cumulative and differential pore volume of the prepared CeO_2-NP compared to CeO_2-NP-Meso after 24 h in the HCl oxidation reaction ($HCl:O_2 = 3:1$).

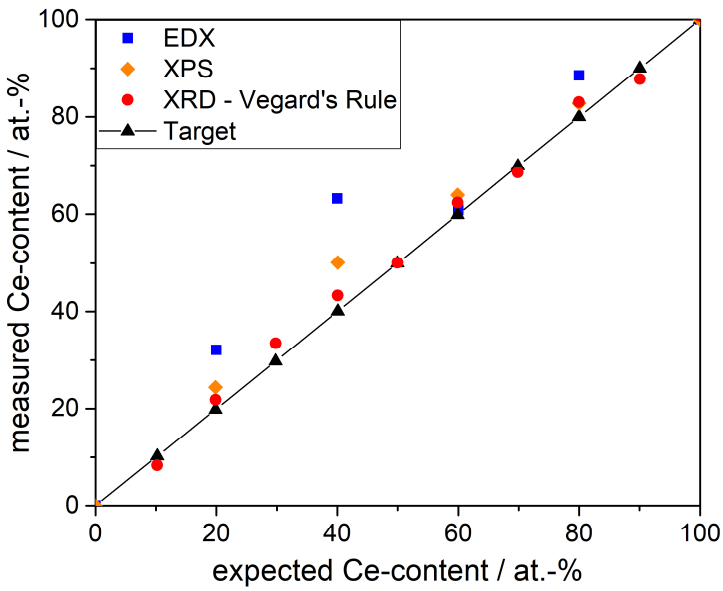

Figure S8: Summary of the composition analyses applying EDX, XPS and the Vegard's law on the XRD data of the nanoparticle-derived mesoporous powders.

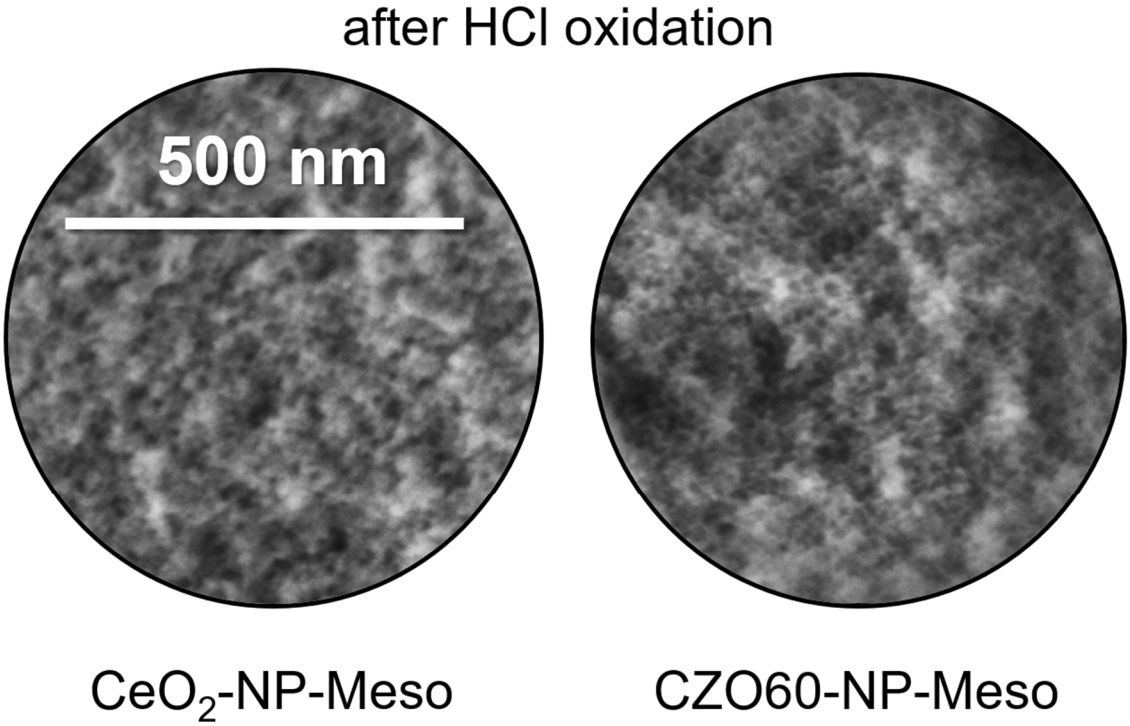

Figure S9: SEM images of the nanoparticle-derived mesoporous CeO_2 and CZO60 powder after the HCl oxidation proving the existence of the mesoporous structure.

6.3 **ESI:** Atomic Layer Deposition of Titania in Ordered Mesoporous Cerium Zirconium Oxide Thin Films: A Case Study

Atomic Layer Deposition of Titania in Mesoporous Cerium Zirconium Oxide Thin Films: A Case Study

P. Cop[a,b], M. Göttlicher[a,c], J. Schörmann[b,c], C. Boissiere[d], A. Beyer[e], C. Becker[e], K. Volz[e], H. Over[a,b], B. M. Smarsly[a, b*].*

a. Physikalisch-Chemisches Institut, Justus-Liebig-Universität, Heinrich-Buff-Ring 17, 35392 Giessen, Germany

b. Center for Materials Research, Heinrich-Buff-Ring 16, Justus-Liebig University, D-35392 Giessen, Germany.

c. I. Physikalisches Institut, Justus-Liebig-Universität, Heinrich-Buff-Ring 16, 35392 Giessen, Germany.

d. Laboratoire Chimie de la Matière Condensée de Paris Collège de France, 11 place, Marcelin Berthelot, 75005 Paris, France.

e. Department of Physics and Materials Science Center, Philipps-Universität Marburg, Hans-Meerwein-Straße 6, 35032 Marburg, Germany.

Supporting Information

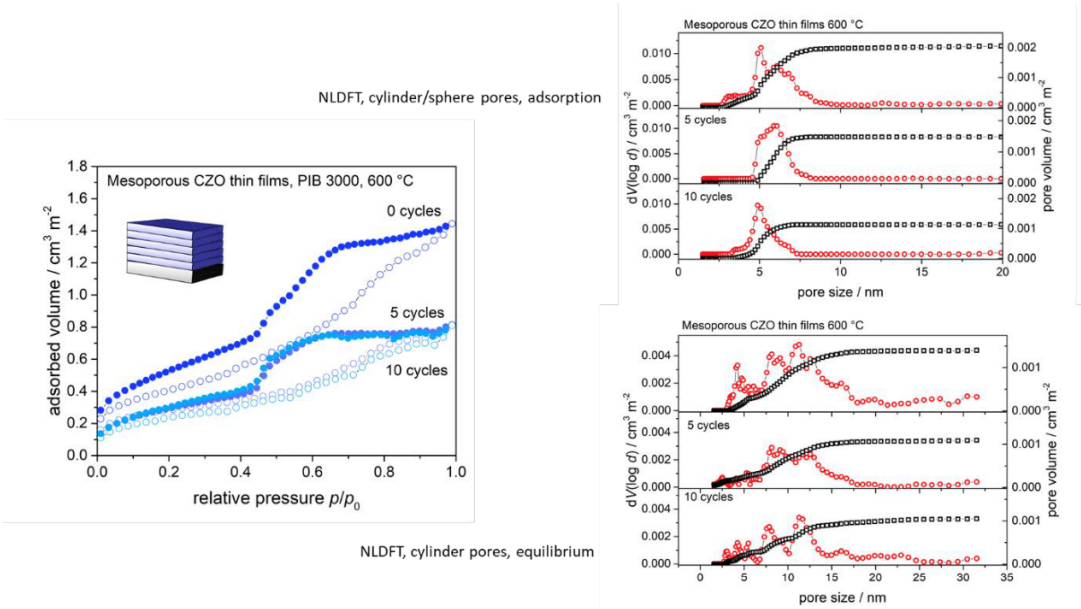

Figure S1: Nitrogen physisorption isotherm (left) of around 500 nm mesoporous CZO thin films before and after 5 and 10 ALD cycles. The higher thickness of the film in comparison with a single coated film was reached by repetitive coating. Furthermore, the pore size distribution of the measured films is displayed using only the adsorption branch (top right) and the desorption branch (bottom right).

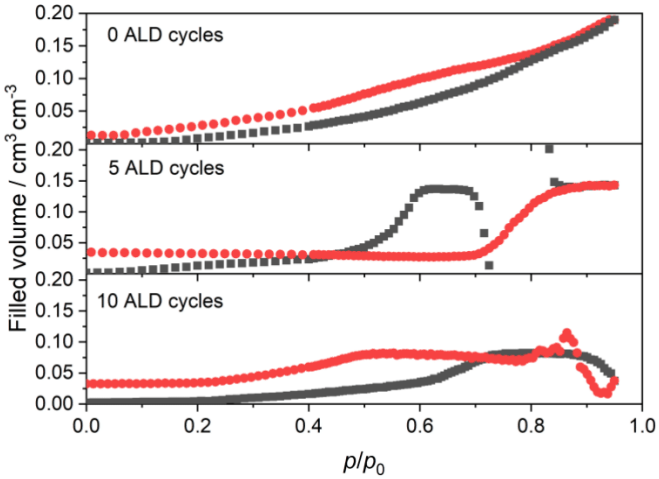

Figure S2: EEP isotherms for different numbers of ALD cycles. The data quality is not sufficient for determined a meaningful mesopore size distribution, but the mesopore volume can be extracted with reasonable precision.

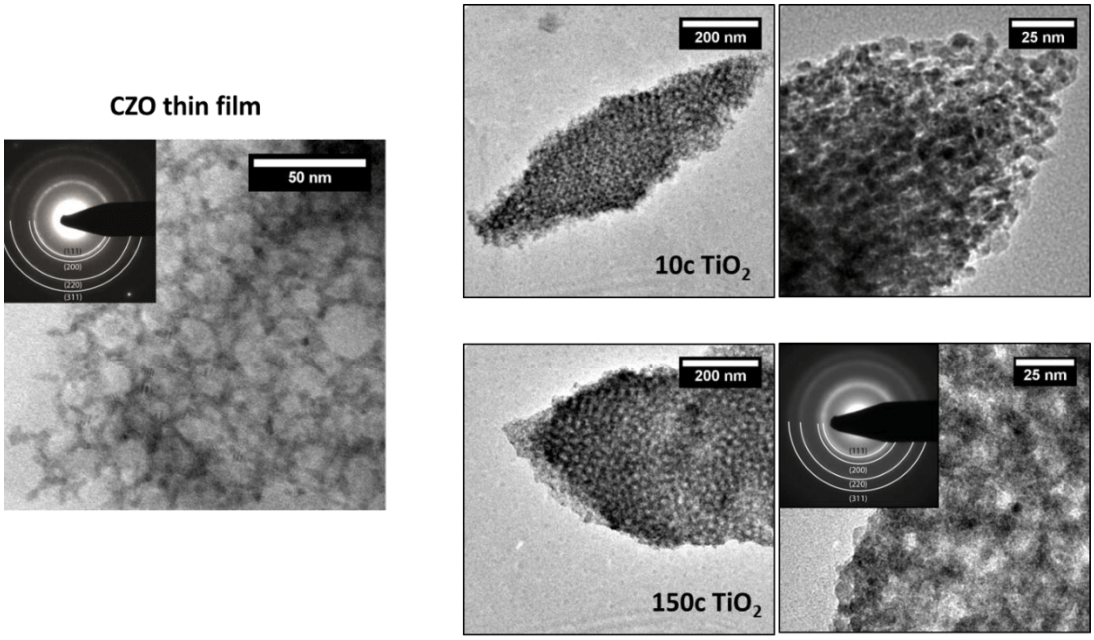

igure S3: TEM images of mesoporous CZO films before (left) and after the TiO_2 deposition of 10 and 150 ALD cycles (right) revealing the mesoporous network. In addition, the SAED pattern are displayed in the corresponding images implying that TiO_2 is not present.

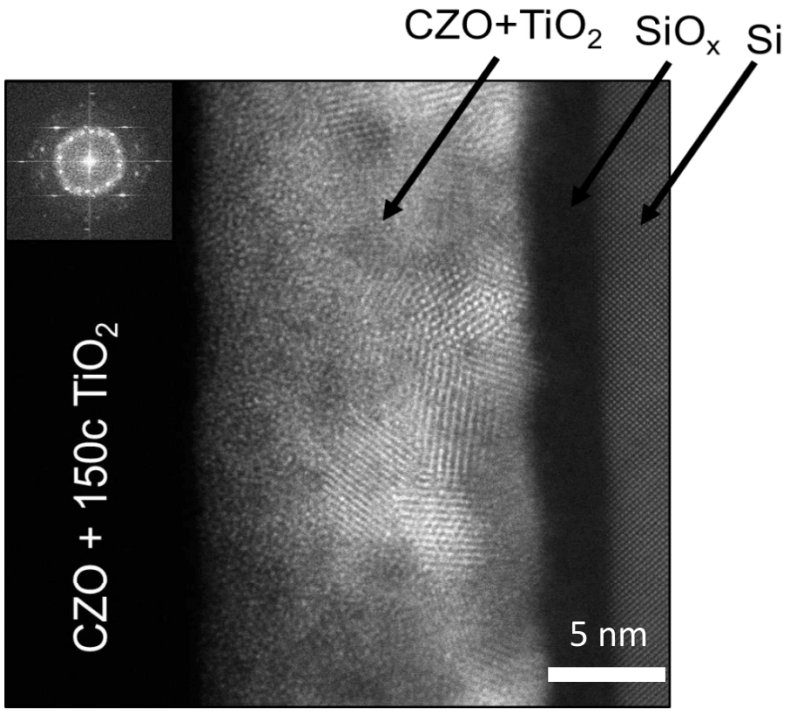

Figure S4: HRTEM cross-section images of the mesoporous CZO thin film after 150 TiO_2 ALD cycles. It reveals the presence of CZO and TiO_2 based on the atomic lattice and the followed FFT calculation.

6.4 **ESI:** Comparison of In-Plane Stress Development in Sol-Gel- and Nanoparticle-Derived Mesoporous Metal Oxide Thin Films

Comparison of In-Plane Stress Development in Sol-Gel- and Nanoparticle-Derived Mesoporous Metal Oxide Thin Films

Supplementary Information

Pascal Cop,[a,b] Kevin Hess,[a,b,c] Sebastian Werner[a,b], Bernd M. Smarsly,[a,b,*] Hiromitsu Kozuka[c,*]

a. Physikalisch-Chemisches Institut, Justus Liebig University, Heinrich-Buff-Ring 17, D-35392 Giessen, Germany

b. Center of Materials Research, Justus Liebig University, Heinrich-Buff-Ring 16, D-35392 Giessen, Germany.

c. Department of Chemistry and Materials Engineering, Kansai University, 3-3-35 Yamate-cho, Suita, Osaka 564-8680, Japan.

KEYWORDS: mesoporous, stress, nanoparticle, thin film, titania, zirconia

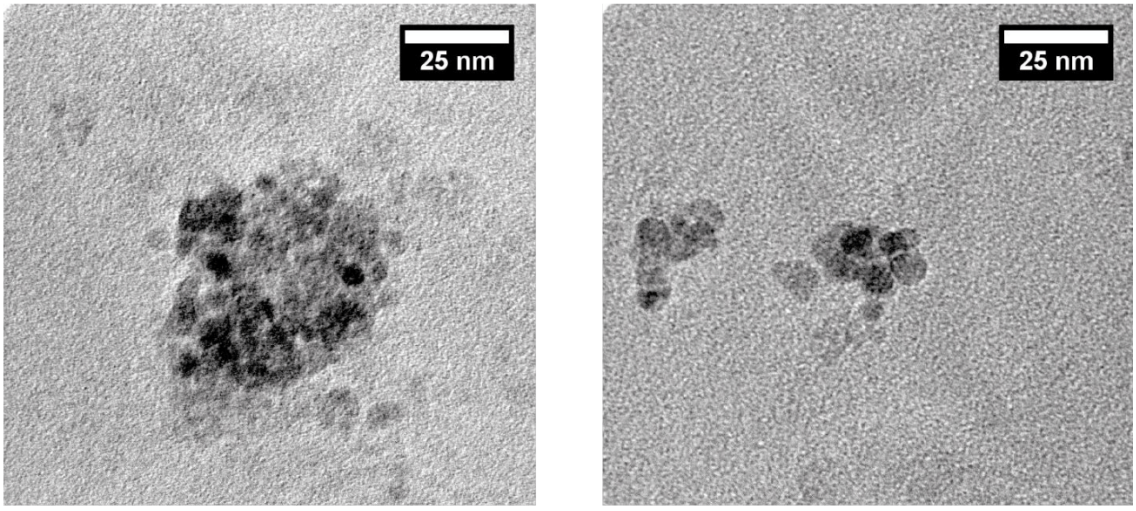

Figure S1: TEM images of the TiO_2 nanoparticles. The particles were heated up to 250 °C to ensure the evaporation of the utilized benzyl alcohol. The average particle size is 5.4±1.0 nm.

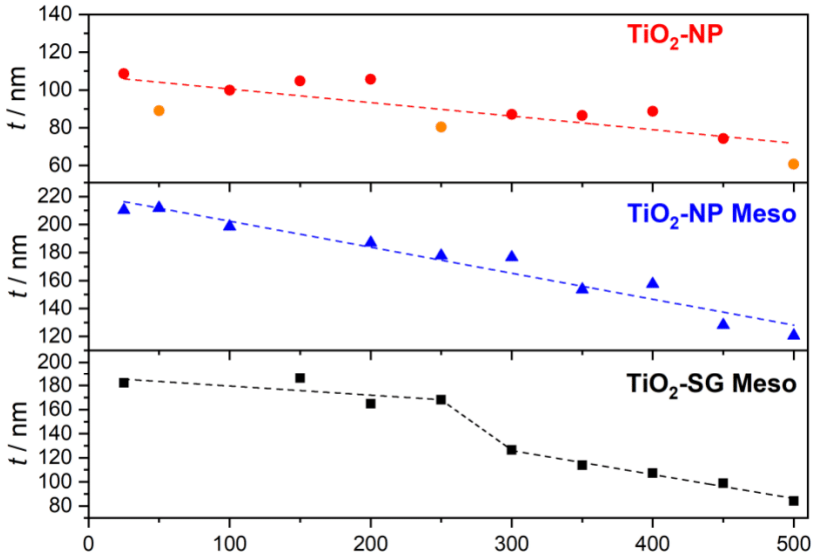

Figure S2: Thickness of the nanoparticle derived dense TiO_2 (red) as well as the mesoporous film based on a TiO_2 nanoparticle dispersion (blue) and sol-gel precursor solution (black) prepared using PIB_{50}-b-PEO_{45} in dependence of the heating temperature provided by spectroscopic ellipsometry. The fits were used to calculate the thickness every 5 °C.

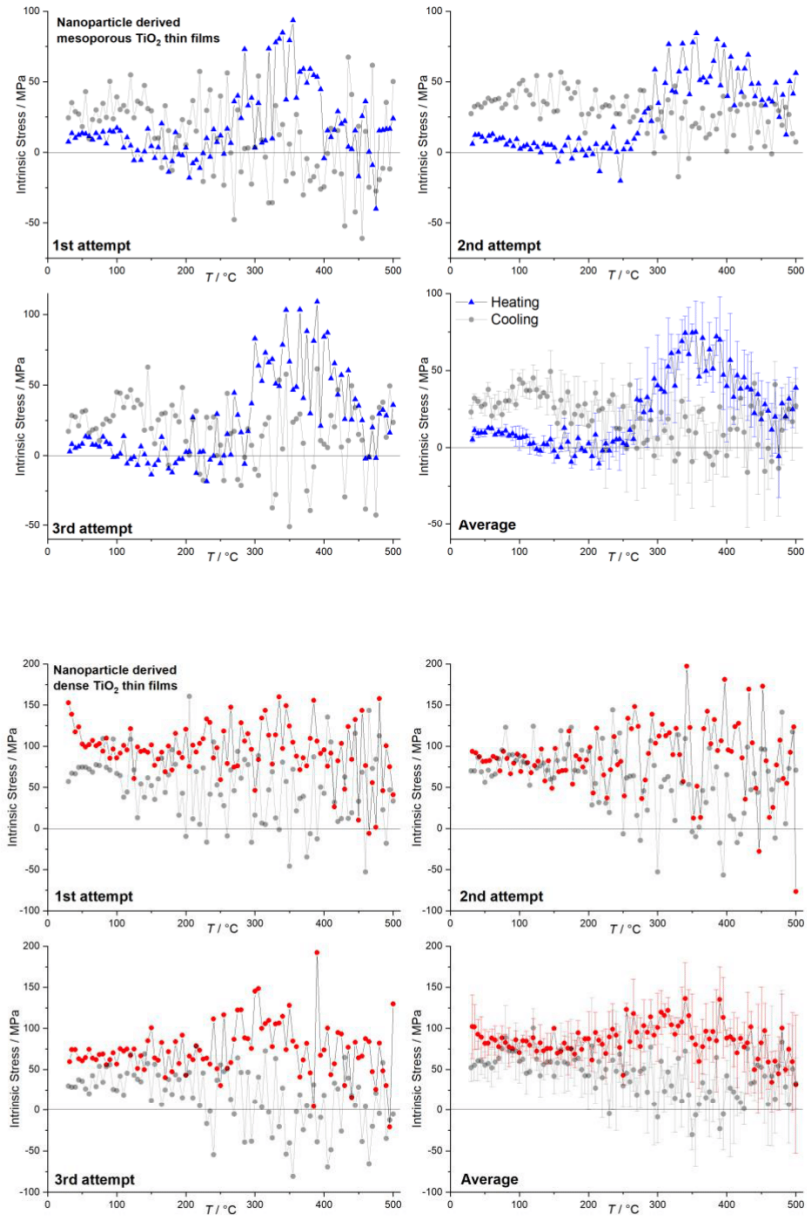

Figure S3: In-plane intrinsic stress of the nanoparticle derived TiO_2 thin films without (red) and with (blue) PIB_{50}-b-PEO_{45} as template during the heating and natural cooling process. The heating ramp was 5 °C per minute, while the data was recorded every 5 °C. Every measurement was repeated three times to ensure the validation of the obtained data. The bottom right image depicts the average of the three attempts including the error bars.

3

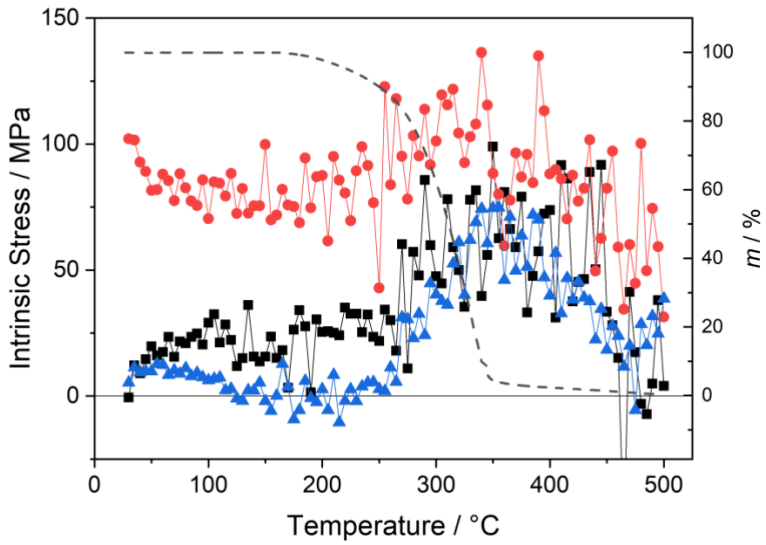

Figure S4: In-plane intrinsic stress of the dense (red) and mesoporous nanoparticle-derived (blue) as well as sol-gel-derived (black) TiO_2 thin film prepared using PIB_{50}-b-PEO_{45} during the heating up procedure. TGA data of the employed polymer PIB_{50}-b-PEO_{45} is depicted as dashed line.

6.5 **ESI:** Atomic Layer Deposition of Defined Thin CeO_2 Layers in Ordered ZrO_2 Films and Their Impact on the Ionic/Electronic Conductivity

Supporting Information

Atomic Layer Deposition of Defined Thin CeO_2 Layers in Ordered ZrO_2 Films and Their Impact on the Electronic/Ionic Conductivity

Pascal Cop[a,b], Erdogan Celik[a,b], Kevin Hess[a,b], Yannik Moryson[a,b], Philip Klement[b,c], Matthias T. Elm[a,b,], Bernd M. Smarsly[a,b,]**

a. Physikalisch-Chemisches Institut, Justus-Liebig University, Heinrich-Buff-Ring 17, D-35392 Giessen, Germany

b. Center of Materials Research, Justus-Liebig University, Heinrich-Buff-Ring 16, D-35392 Giessen, Germany.

c. Institute of Experimental Physics I, Justus-Liebig University, Heinrich-Buff-Ring 16, D-35392 Giessen, Germany.

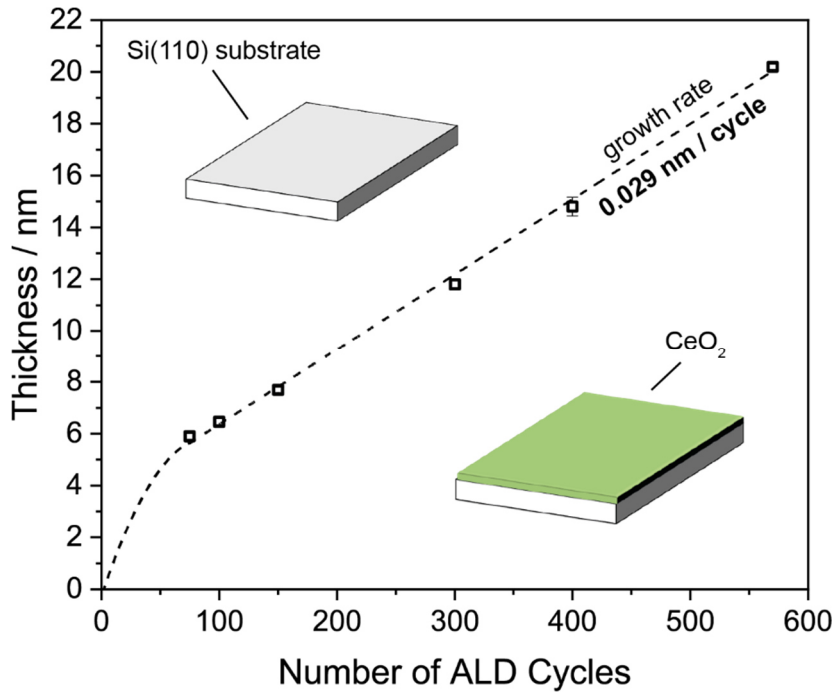

Figure S21: Thickness of the CeO_2-deposited Si[110] substrates in dependency of the number of ALD cycles. The dashed line illustrates the assumption concerning the growth rate.

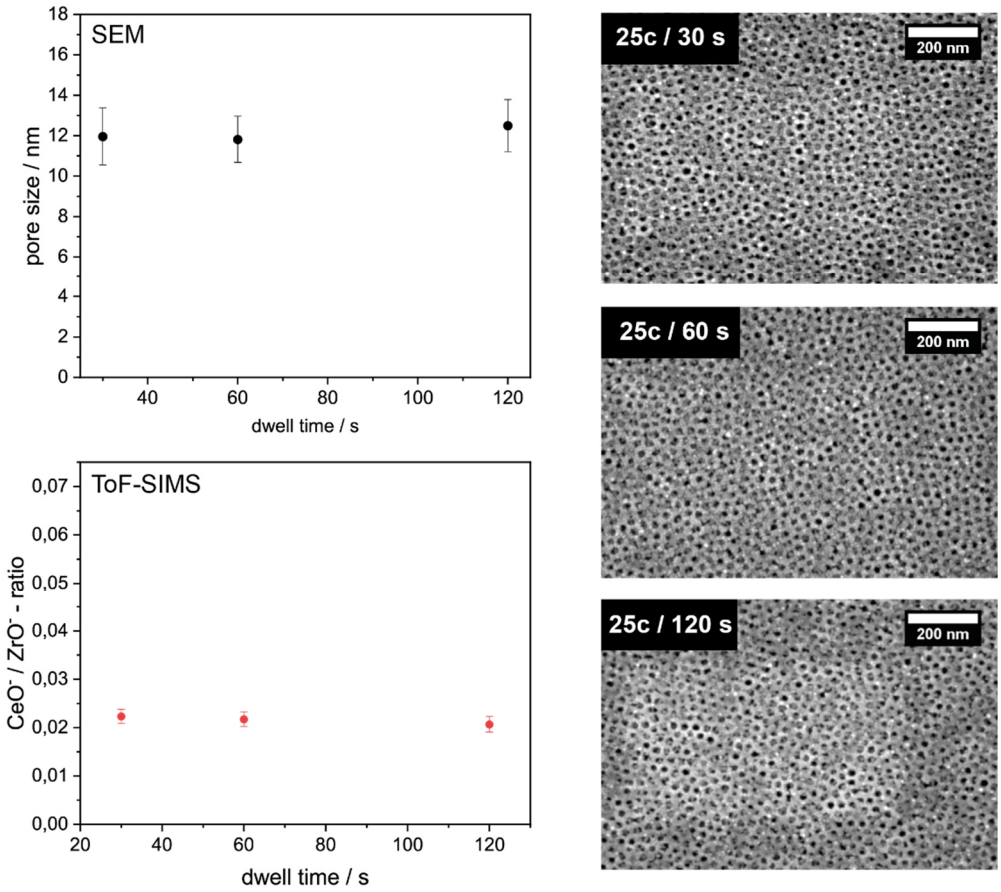

Figure S2: SEM and ToF-SIMS analyses of the CeO_2-coated ZrO_2 thin films after 25c with different dwell time. No significant differences are observed proving that the saturation of the precursor chem-isorption is already performed after 30s.

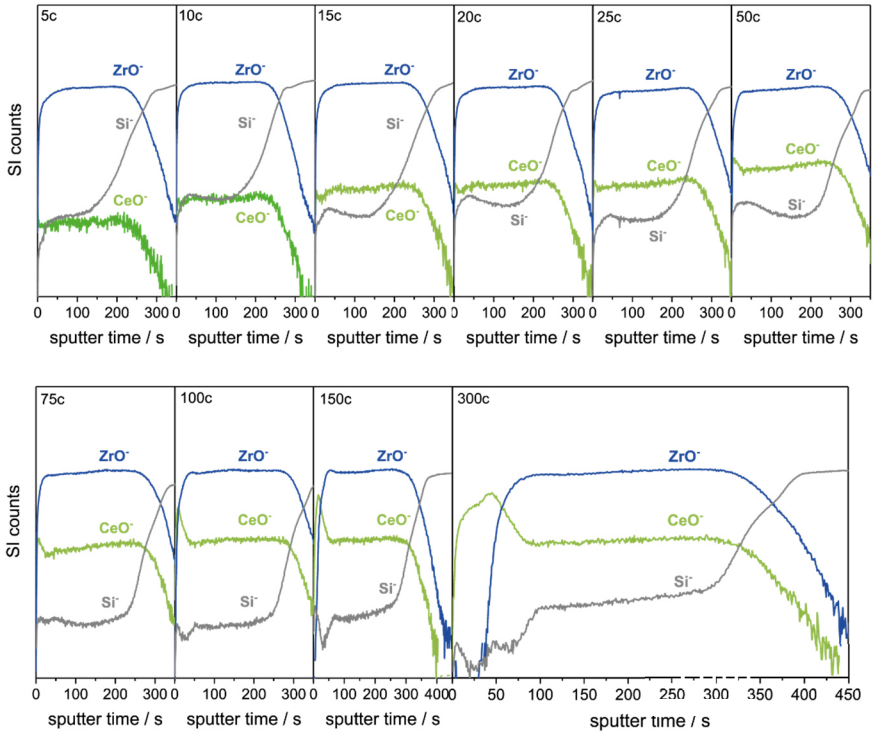

Figure S3: ToF-SIMS depth profiles of the mesoporous ZrO_2 film after different amount of ALD cycles. Next to the ions deriving from the thin film (ZrO^- and CeO^-) the signal from the utilized silicon substrate (Si^-) is depicted by plotting the secondary ion (SI) counts logarithmic dependent on the sputter time.

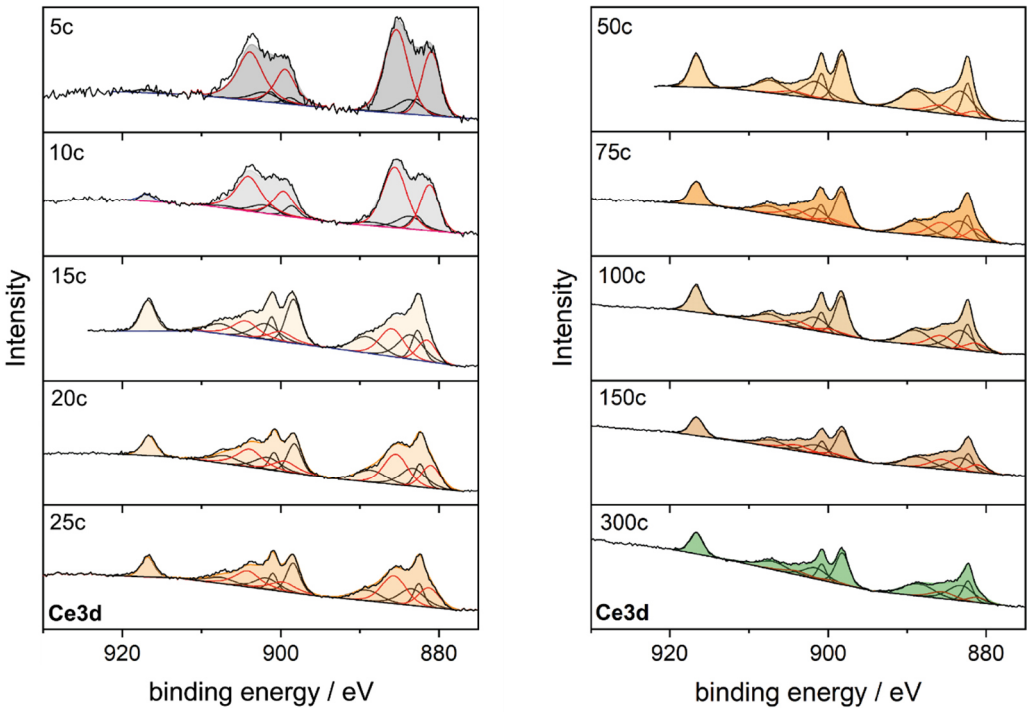

Figure S4: Ce3d spectra of the CeO_2-coated ZrO_2 thin films using XPS. Next to the six signals deriving from CeO_2 (v, v'', v''' and u, u'', u'''), the four additional signals from Ce_2O_3 (v0, v' and u0, u') were taken into account.